Université de Liège

ArGEnCo

MSM

Experimental and Numerical Characterization of Damage and Application to Incremental Forming

PhD thesis

Carlos Felipe Guzmán

November 2015

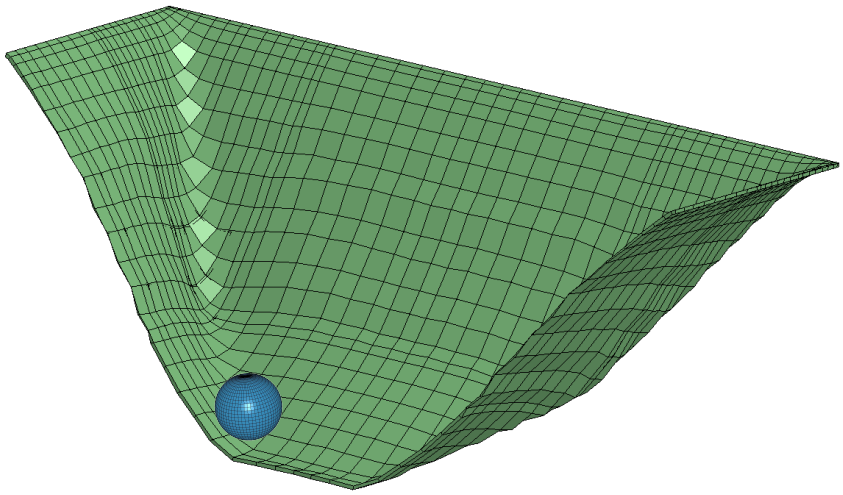

Experimental and Numerical Characterization of Damage and Application to Incremental Forming

By

Carlos Felipe Guzmán

A Thesis submitted to the University of Liège in partial fulfillment of the requirements for the degree of *Docteur en Sciences de l'Ingénieur*

November 2015

Jury members

Prof. Jacqueline Lecomte-Beckers, president of the jury
M&A Department, University of Liège, Belgium

Dr. Anne Marie Habraken, supervisor of the thesis
ArGEnCo Department, University of Liège, Belgium

Dr. Romain Boman
M&A Department, University of Liège, Belgium

Prof. Pierre-Olivier Bouchard
Cemef, École des Mines de Paris, France

Prof. Jian Cao
Department of Mechanical Engineering, Northwestern University, USA

Prof. Laurent Duchêne
ArGEnCo Department, University of Liège, Belgium

Prof. Joost Duflou
Department of Mechanical Engineering, Katholieke Universiteit Leuven, Belgium

Prof. Jeong-Whan Yoon
School of Engineering, Deakin University, Australia

Acknowledgments

The only guide to a man is his conscience, the only shield to his memory is the rectitude and sincerity of his actions.

Winston Churchill

The author would like to thank:

Dr. Anne Marie Habraken for her guidance, positive critics and patience during this four and a half years. I really appreciated her moral values on thoroughness, hard work and perseverance.

The members of the MSM team: Dr. Víctor Tuninetti, Chantal Bouffioux, Dr. Laurent Duchêne, Dr. Gaëtan Gilles, Amine Ben Bettaieb, Khalifa Marmi, Rúben Jardin and Hoang Son Tran for sharing personal and scientific views during the development of this thesis. Special thanks to my (occasional) office mate Dr. José Sena.

Je suis reconnaissant envers les techniciens du laboratoire des structures pendant la campagne d'essais expérimentaux. Notamment, Olivier Milis pour son dévouement et son engagement. Merci aussi á Hakan Paydas et Dr. Anne Mertens de l'équipe MMS pour les analyses microscopiques.

I enjoyed the SPIF meetings in Leuven with our project partners from the PMA department. Their broad experience allowed me to understand the SPIF process better. Bedankt aan prof. Joost Duflou, Hans Vanhove, Amirahmad Mohammadi en Amar Kumar Behera. Daarnaast, bedankt aan Philip Eyckens en Albert van Bael van het departement MTM.

The jury members, Dr. Romain Boman, Prof. Pierre Olivier Bouchard, Prof. Jian Cao, Prof. Laurent Duchêne, Prof. Joost Duflou, Prof. Jacqueline Lecomte-Beckers and Prof. Jeon-Whan Yoon for taking part of the public defense and the time spent reading this manuscript.

I am also grateful to my friends from all over Belgium for making me feel less homesick. Merci à tous! Dank u allen!

Special thanks to Juana Bianchini for her advises in the manuscript corrections.

Finalmente, me gustaría agradecer a mis padres y a mi hermano por su constante apoyo, confianza y amor en la lejanía. A ellos esta tesis va dedicada.

In addition, thanks to the F.R.S.-FNRS institution of the Belgian government for the financial support (PhD scholarship).

Abstract

Nowadays, product manufacturing can be divided into two groups: relatively simple products produced in a large production chain and complex (specialized) components produced in reduced batches. Within the second group, prototyping through incremental sheet forming (ISF) has been subject of several studies. ISF refers to processes where the plastic deformation occurs by repeated contact with a relatively small tool. A crucial aspect in the ISF processes is that the final shape is determined only by the tool movement. The focus of this research is the single point incremental forming (SPIF) process variant, where a clamped sheet metal is deformed by using a relatively small spherical tool.

SPIF has several advantages over traditional forming, such as the high formability attainable by the material. Different hypothesis haven been proposed to explain this behavior, but there is still not a clear and definitive understanding of the relation between the particular stress and strain state induced in the material during SPIF and the material degradation leading to localization or fracture.

In this thesis, a fundamental research is proposed using the finite element (FE) code LAGAMINE, developed within the University of Liège. Numerical implementation and validation of the Gurson-Tvergaard-Needleman (GTN) damage model into this FE code is performed. An experimental test campaign is developed to characterize plastic and damage behavior and to validate the damage model for the DC01 steel grade. Finally, this damage model is applied to simulate the SPIF process in order to verify if it is capable to predict failure. The thesis discusses the material parameter identification for classical plasticity models, describing the anisotropy and hardening behavior of the sheet metal. The derivation of the equations of the numerical damage model and the efficiency of the implementation is presented in great detail. A methodology for the numerical parameter identification of the damage model is proposed, including microscopic measurements by optical microscopy and strain and displacement field measurements by digital image correlation (DIC). The identified Gurson model is applied to simulate standard SPIF geometries, like the line, cone and pyramid tests. The simulations are performed using the solid-shell element formulation and validated in terms of shape and force prediction. Literature reviews of the Gurson model and the SPIF process are also included.

The experimental results show that the selected material (DC01 steel sheet) exhibits a slight anisotropic behavior and work-hardening stagnation

on cyclic tests. The performed microscopic measurements are not representative of the actual damage, but they give a qualitative estimation of the physical mechanism of fracture. The initial porosity of the material was determined using optical microscopy measurements in the base material.

The numerical implementation of the model is developed with all variables integrated in an implicit way, based on the backward Euler scheme. Nucleation, coalescence and shear extensions implementations are validated by results obtained from the literature. The macroscopic campaign allowed to identify the parameters for nucleation, coalescence and shear. An unique set of results matching all experiments was not possible to obtain, so different sets of parameters are retrieved following an approach that includes inverse modeling and sensitivity analysis. A numerical-experimental comparison of strain values in the loading direction shows that the model is able to correctly predict the strain distribution except during localization of the strain. Globally, the obtained set of material parameters is in good agreement with the experimental results.

For SPIF FE simulations, the results of the shape prediction are in good agreement with the experimental results, both for the line and pyramid test. Nevertheless, the force prediction is too high compared to reference values. On the other hand, the GTN model is capable to detect failure in a pyramid and a cone, but the prediction is too premature compared to the experimental failure angle for the same material and geometry.

An accurate prediction of failure for the SPIF process was not possible to achieve. The GTN model extended to shear presents inherent flaws that prevent an accurate prediction of the failure angle for the SPIF process. Hence, an extensive research on the damage mechanisms leading to fracture for SPIF cannot rely (only) on the GTN model. The classical coalescence model of the GTN model is insufficient to correctly predict failure. Hence, it is recommended that further analysis concentrates on the description of this particular stage of damage evolution.

During the development of this thesis, a robust implementation of the GTN model into the FE code LAGAMINE was done, including an extensive experimental database of microscopic and macroscopic measurements for the DC01 steel sheet. Other phenomena can be explored thanks to this model.

Contents

List of Figures

List of Tables

Nomenclature

Abbreviations, acronyms

A-F Armstrong and Fredrick, (1966)

ANS Assumed natural strain

AOI Area of interest

BCC Body-centered cubic

BM Base material

BUT Bending under tension

CAD Computer-aided design

CAM Computer-aided manufacturing

CCD Charged-coupled device

CNC Computer numerical control

CSA Classical simulated annealing

DIC Digital image correlation

DOF Degrees of freedom

EAS Enhanced assumed strain

FE Finite element

FFL Fracture forming limit

FHW Fraeijs de Veubeke-Hu-Washizu

FLC Forming limit curve

FLD Forming limit diagram

FSPIF Feature assisted single point incremental forming

GLD Gologanu-Leblond-Devaux

IP Integration point

ISF Incremental sheet forming

LASPIF Laser assisted single point incremental forming

MK Marciniak and Kuczynski, (1967)

MMS Métallurgie et science des matériaux

ODF Orientation distribution function

RD Rolling direction

SEM Scanning electron microscope

SMM Strain measurement method

SP Sampling points

SPIF Single point incremental forming

SSF Stress state fitting

TD Transverse direction

TPIF Two point incremental forming

VSG Virtual strain window

WEDM Wire electrical discharge machining

wt Percentage by weight

XRD X-ray diffraction

DP Dual phase

GTN Gurson-Tvergaard-Needleman

TTS Through thickness shear

Greek letters

α Angle between the sheet wall and the vertical axis (SPIF)

α_H Huang, (1991) correction constant

β_H Huang, (1991) correction constant

$\boldsymbol{\epsilon}$ Natural strain tensor

$\mathbf{\Gamma}$	Residual tensor
$\boldsymbol{\sigma}$	Cauchy stress tensor
χ	Scalar stress function from the Lode angle definition
δ	Kronecker delta
ϵ_f	Fracture strain
ϵ_N	Mean effective plastic strain of the matrix at incipient nucleation (Chu and Needleman, 1980)
ϵ_0	Material parameter of Swift's hardening law
ϵ_N	Critical value of the strain for which nucleation starts
κ	Coefficient from the anisotropic extension (Benzerga and Besson, 2001)
λ	Plastic multiplier
λ_f	Threshold value of inter-cavities distance value
μ_σ	Lode, (1926) parameter
ν	Poisson's ratio
$\overline{\theta}$	Normalized Lode angle (Bai and Wierzbicki, 2009)
$\overline{\theta}_V$	Lode parameter (Voyiadjis et al., 2012)
ρ	Material density
ρ_0	Specimen density
ρ_l	Liquid density
σ_c	Void evolution law material parameter (Landron et al., 2010)
σ_Y	Flow stress of the dense matrix medium (no voids)
Σ_1	Hardening function (Leblond et al., 1995)
Σ_2	Hardening function (Leblond et al., 1995)
σ_{eq}	Macroscopic effective stress (matrix plus voids)
σ_m	Macroscopic mean (hydrostatic) stress (matrix plus voids)
σ_{Y0}	Material parameter of Voce's hardening law
θ	Angle orientation of the void
υ	Isotropic hardening parameter

ϑ Yield locus shape

ξ Normalized third invariant (Wierzbicki et al., 2005)

ξ_L Lode parameter

$\boldsymbol{\epsilon}^{\text{com}}$ Strain tensor calculated from the compatibility equations

$\boldsymbol{\epsilon}^{\text{EAS}}$ Strain tensor calculated from the introduced EAS modes

$\boldsymbol{\epsilon}^p$ Plastic logarithmic strain tensor

ϵ_M^P Equivalent plastic strain in the matrix

σ_M Equivalent stress in the matrix

θ_B Void evolution law material parameter (Landron et al., 2010)

Latin letters

$\boldsymbol{C}$ Coefficient of the state variables derivatives

$\boldsymbol{u}$ Vector of nodal displacements

$\boldsymbol{X}$ Backstress tensor

$\boldsymbol{X}^*$ Backstress tensor function

Δh Scallop height (SPIF)

Δr Coefficient of planar anisotropy

$\mathbb{C}$ Elasticity tensor

$\mathbb{D}$ Tangent modulus tensor

$\mathbb{H}$ Hill's anisotropic tensor

$\mathbb{K}$ Coefficient tensor (Kim and Gao, 2005)

$\mathbb{L}$ Coefficient tensor (Kim and Gao, 2005)

$\mathcal{A}$ Nucleation law strain contribution (Needleman and Rice, 1978)

$\mathcal{B}$ Nucleation law stress contribution (Needleman and Rice, 1978)

$\mathfrak{A}$ Air mass

$\mathfrak{B}$ Liquid mass

$\overline{r}$ Coefficient of normal anisotropy

A_B Nucleation law material parameter (Bouaziz et al., 2008; Maire et al., 2008)

a_B Growth law material parameter (Bouaziz et al., 2008)

A_R Aspect ratio

A_{act} Actual area of the specimen's section

B_B Void evolution law material parameter (Landron et al., 2010)

c Nucleation law material parameter (Needleman and Rice, 1978)

C_R Circularity

C_X A-F model material parameter

D Finite element size

d_f Fracture displacement

d_t Tool diameter (SPIF)

d_x Average dimensions of the inclusions (X direction)

d_y Average dimensions of the inclusions (Y direction)

d_z Average dimensions of the inclusions (Z direction)

$d_{1,\dots,6}$ Parameters for the calculation of κ

E Elastic modulus

e Engineering strain

f Microvoid volume fraction (Porosity)

f_F Porosity at final failure (Tvergaard and Needleman, 1984)

f_N Nucleated void volume fraction (Chu and Needleman, 1980)

F_p Yield locus function

f_u Ultimate value of porosity at the occurrence of ductile rupture (Tvergaard and Needleman, 1984)

F_{hor} Horizontal force measured by the load cell

f_{inc} Void volume fraction of inclusions

F_{vert} Vertical force measured by the load cell

f_{cr} Critical void volume fraction at the onset of coalescence (Tvergaard and Needleman, 1984)

f_g Porosity (growth contribution)

f_n Porosity (nucleation contribution)

f_s Porosity (shear contribution)

Fz_p Peak force (SPIF)

Fz_s Steady force in SPIF

g_θ Stress measure (Xue, 2008)

G_s Shear modulus

K Material parameter of the isotropic hardening law

k Size of the yield locus

K_b Bulk modulus

K_p Penalty coefficient

k_ω Numerical constant (Nahshon and Hutchinson, 2008)

k_g Numerical constant (Xue, 2008)

N Void density (nucleated void per mm^3)

n Material parameter of the isotropic hardening law

N_0 Void evolution law material parameter (Landron et al., 2010)

N_ϵ Weight for the integration using sub-intervals

N_{intv} Variable for the integration using sub-intervals

P Engineering stress

p Tool step-down (SPIF)

q_1 Parameter from the GTN model (Tvergaard, 1981)

q_2 Parameter from the GTN model (Tvergaard, 1981)

q_3 Parameter from the GTN model (Tvergaard, 1981)

R Void radius

R_m Tensile strength

R_0 Mean radius of cavities after nucleation and before beginning of the growth phase

R_0^i Growth law material parameter (Bouaziz et al., 2008)

S_N Gaussian standard deviation of the normal distribution inclusions (Chu and Needleman, 1980)

S_R Spatial resolution

S_w Strain window size

SS	Subset size
ST	Step size
T	Triaxiality
t	Sheet thickness
t_f	Final thickness of the sheet
t_i	Initial thickness of the sheet
V_A	Volume of the cavity and the matrix
V_M	Volume of the cavity
X_{sat}	A-F model material parameter
F	Material parameter (Hill, 1948)
G	Material parameter (Hill, 1948)
H	Material parameter (Hill, 1948)
L	Material parameter (Hill, 1948)
M	Material parameter (Hill, 1948)
N	Material parameter (Hill, 1948)

Chapter 1

Introduction

1.1 Background and scope

The fabrication of metallic pieces can be achieved through different processes. For example, gluing two different pieces, cutting from a larger specimen (machining) or deforming the material plastically. This last process is called *metal forming* and has the particularity that the material attains large plastic deformation before obtaining the desired shape. This is how a metallic piece (usually a ductile material) is deformed by specific tools and transformed into a useful piece.

Nowadays, product manufacturing can be divided into two groups: relatively simple products produced in a large production chain and complex (specialized) components produced in reduced batches. Within the second group, prototyping through incremental sheet forming (ISF) has been subject of several studies. ISF refers to processes where the plastic deformation occurs by repeated contact with a relatively small tool. The small formed zone moves during the whole process, covering all the product and giving the final shape. The last decade has shown an increasing interest on ISF processes. After early developments in Japan during 1990s, the research moved towards Europe coinciding with an intense use of CNC machines and developments in CAD/CAM software products. A crucial aspect in the ISF processes is that the final shape is determined only by the tool movement. The focus of this research is the single point incremental forming (SPIF) process variant, where a clamped sheet metal is deformed by using a relatively small spherical tool, which follows a complex path in order to get the required shape. A schematic representation of the process can be seen in Fig. 1.1(a), where the tool follows a path depicted in Fig. 1.1(b) for a conical shape. One of the most prominent characteristics of the SPIF process is its flexibility. Since the shape is only given by the motion of the tool, no die is needed. Fig. 1.2 depicts two SPIF setups. Moreover, the toolpath can easily be controlled using a CAD/CAM software where a change of the final shape can be quickly and inexpensively done. This dieless nature makes the SPIF process appropriate for prototyping, highly personalized pieces and other shell-like structures, having a production cost lower than typical processes like deep drawing. Depending on the tool path length, the forming process can reach hours. It is, by consequence, adapted to small batch production and rapid prototyping. Applications range from large pieces like

automotive parts or dies, to small parts such as medical implants or prosthesis. The formability, which is higher than in the case of conventional forming processes (like stamping), has a high industrial interest but the poor geometrical accuracy of the final shape represents a major disadvantage of the process, preventing a massive industrial acceptance.

This process can be optimized by a numerical analysis and/or by experimental trials and errors. In this thesis, the numerical approach is chosen because of the practical usefulness of a virtual simulation of the forming process over a costly trial and error one. The numerical analysis needs the development and validation of the material models to simulate the sheet metal. Moreover, such information is accurate only if the simulation has been validated through experiments. Experimental validation is the first step towards prediction of the material rupture and numerical study of the process limits.

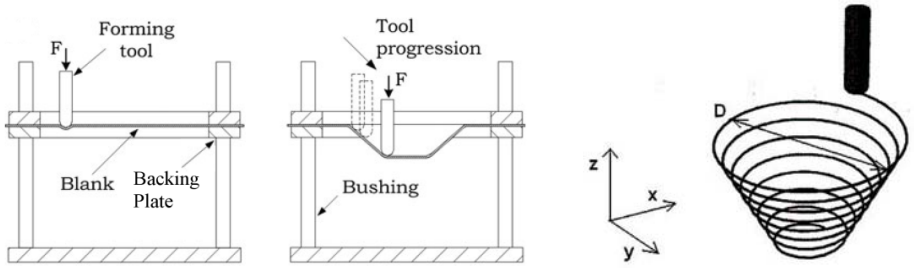

(a) SPIF setup (Jeswiet et al., 2005).

(b) SPIF spiral toolpath (Filice et al., 2002).

Figure 1.1: Schematic representation of the SPIF process.

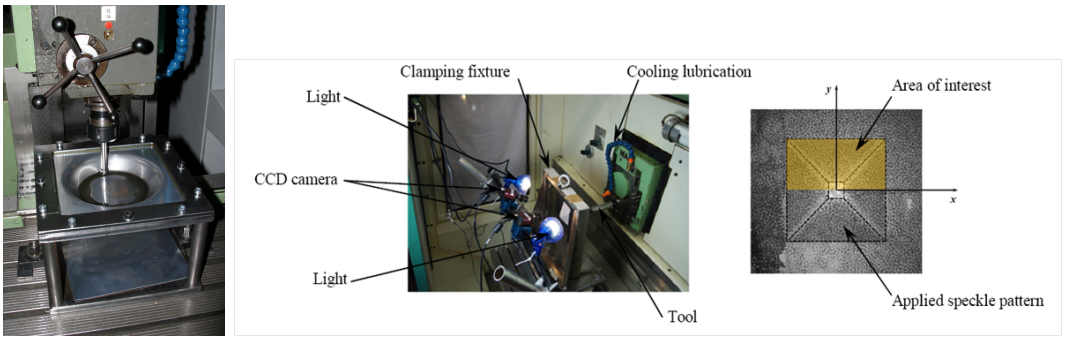

(a) Milling machine (Henrard, 2008)

(b) SPIF setup for DIC measurements (Guzmán et al., 2012b).

Figure 1.2: SPIF hardware setup.

1.2 Research objectives

Formability within SPIF process has been extensively studied using classical framework such as the forming limit curves (FLC). However, little has been done regarding the damage evolution leading to final fracture. Research on damage using a numerical approach requires a deeper knowledge of the material behavior and more complex material models. These aspects increase the difficulty of the research but on the contrary, their application range is not limited to a particular process (like SPIF). Hence, the results arising from this research can be applied to other investigations involving the same material or the same material model.

In this thesis, a fundamental research is proposed using the Finite Element (FE) code called Lagamine, developed since 1982 by AM Habraken's team in ULg. This code has a large library of finite elements and constitutive laws. The ULg team has a strong background on experimental material characterization (Flores, 2005; Gilles, 2015; Tuninetti, 2014), finite element technology (Ben Bettaieb et al., 2015; Duchêne et al., 2007; Li and Cescotto, 1997), damage modeling (Ben Bettaieb et al., 2011a; Fansi, 2013; Zhu, 1992) and incremental forming simulations (Henrard, 2008; Sena, 2015).

Collaborations with external teams have been activated within the thesis research, such as:

- The mechanical engineering department of the University of Aveiro, Portugal (within Grid team of Prof. Ricardo Alves de Sousa and Prof. Robertt Valente). Experience on finite element simulations applied to forming process (solid-shell elements and remeshing).

- The department of mechanical engineering (PMA division, Prof. Joost Duflou) and metallurgy and materials engineering (MTM, Prof. Albert Van Bael) of KULeuven. Wide knowledge on ISF experimental tests.

- The metallurgy and materials science division of the University of Liège (Prof. Jacqueline Lecomte-Beckers), dedicated to microscopic measurements of materials.

Finally, the research has the following objectives:

1. Numerical development, implementation and validation of a Gurson type damage model into the FE code Lagamine.

2. Development of a test campaign to characterize both plastic and damage behavior in a sheet metal under different types of loading.

3. Numerical validation of the damage model using the experimental results.

4. Application of the validated numerical damage model to SPIF FE simulations. Analysis of the results in terms of shape and force predictions.

1.3 Thesis outline

The body of this thesis is divided in seven chapters, the first one being the current introduction.

The second chapter deals with the material parameters identification of the DC01 steel, the chosen material for the research. The focus here is on the plastic behavior of the sheet. An experimental campaign designed to characterize the material is described and its results presented. Anisotropy and mixed (isotropic and kinematic) hardening parameters are identified for classical plasticity models.

The third chapter is a general review of the Gurson model. The Gurson model is a popular tool to simulate the damage behavior and several extensions have been proposed to cover different aspects of the phenomenon.

The fourth chapter covers the numerical implementation of the Gurson model into the FE code LAGAMINE. An implicit algorithm is described and then applied to the Gurson extensions that will be used in subsequent developments. A detailed derivation of the equations is presented and the efficiency of the implementation is assessed with results obtained from the literature.

The fifth chapter presents a methodology for the damage characterization of the DC01 steel sheet. It is important to remark that damage is harder to characterize than plasticity, both from a numerical and experimental point of view. Therefore, the chapter presents a methodology, which includes an experimental campaign involving microscopic and macroscopic measurements. A validation of the numerical model is given using the experimental results.

The sixth chapter is the application of the previous implemented and validated damage model to the SPIF process. Different SPIF geometries are simulated and their predictions analyzed to show the capabilities and limitations of the damage model.

Finally, the thesis ends with general conclusions and perspectives for future research.

1.4 Original contributions

Within the research, the following contribution were achieved:

- The material parameters for models describing the plasticity and damage behavior of the DC01 steel sheet were identified.
- Implementation of a Gurson damage model extended to matrix anisotropy, mixed hardening, void nucleation, void coalescence and shear loads into the LAGAMINE FE code.
- Analysis of the damage development undergone by the DC01 steel sheet, both from microscopic and macroscopic measurements.
- Reliable numerical tool to simulate SPIF. Good shape and strain prediction in the NUMISHEET 2013 benchmark.

- Concise literature review of the damage models applied on SPIF and rupture mechanisms acting on SPIF.
- An efficient parallel version of Lagamine code using the Walloon clusters available through ULg access was developed.

Chapter 2

Plasticity characterization of the DC01 steel sheet

For damage prediction involving coupled models, identifying the plasticity parameters is of crucial relevance due to the strong dependence of the damage variable evolution on the yield function and hardening. Based on methodologies presented in Flores, (2005) thesis and Gilles, (2015) thesis, the plastic behavior of the DC01 steel sheet including anisotropy and hardening, is characterized by using a test campaign involving homogeneous stress and strain fields. Since most of the preliminary numerical studies were carried on using classical plasticity models, the chapter begins by describing the material and the used mathematical models. This is followed by a description of the experimental setup and results from a set of different tests (tensile, shear and plane strain). A discussion of the identification procedure using optimization algorithms is followed. The obtained parameters are then analyzed with finite element simulations using the LAGAMINE software. The material exhibits large ductility, being able to reach large displacement before fracture and anisotropic behavior at 45° of the RD. Hardening stagnation in presence of reverse loadings is also observed, increasing the difficulty of modeling kinematic hardening.

2.1 Material presentation

In this section, the selected material for the current research is described qualitatively and quantitatively.

2.1.1 Material selection

The material was selected according to the following criteria:

- The existence of sufficient stock or insurance of renewed supply for long term availability.
- It should be relevant at industrial level.

- The thickness should be sufficiently large to allow the study of bending moments, but limited to SPIF platforms capacity.
- It should allow a relatively high formability.

In accordance with these criteria, the chosen material was the DC01 ferritic steel (EN 10330)[1] 1.0 mm thickness, a cold rolled low carbon steel commercially available for cold forming. In general, the carbon content for high-formable steels is very low (less than 0.10% C with a maximum of 0.4% Mn) as shown in Table 2.1, making them malleable and ductile.

2.1.2 Microstructure of the base material

The chemical composition of the DC01 steel is shown in Table 2.1. Its microstructure was obtained by Anne Mertens from the MMS team at the ULg and is shown in Fig. 2.1. It is mostly ferritic with a small amount of cementite, with a body-centered cubic (BCC) crystal system. Based on its carbon percentage, the DC01

Table 2.1: Chemical composition in percentages by weight (wt%) of the DC01 steel. Taken from Eyckens, (2010).

Mn	C	Al	Ni	Cu	Cr	P
0.21	0.049	0.029	0.024	0.017	0.016	0.008
S	N	Si	Ti	B	Fe	
0.008	0.003	0.002	0.001	2×10^{-4}	Bal.	

has an equivalent grade SAE/AISI 1005. It also has some amount of Al, meaning that this low carbon steel is of the *aluminium killed, drawing quality* type (Hosford and Caddell, 2007). The grain size of the base material is estimated

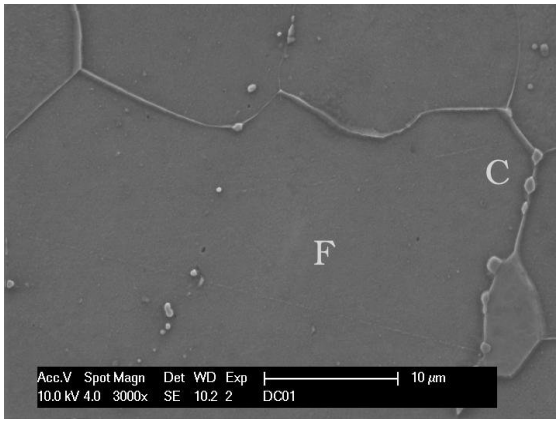

Figure 2.1: Microstructure of the DC01 steel. Two clear phases are visible with ferrite (α-Fe) being clearly dominant over cementite (Fe_3C).

[1]Within the standard: *EN 10130:2006 Cold rolled low carbon steel flat products for cold forming. Technical delivery conditions.*

using the ASTM norm E112-1998, taking into account the number of grains in a 1.0 in × 1.0 in area of chemically attacked sample (Fig. 2.2). The grain size and its associated index are shown in Table 2.2. The large grain size index (higher

Table 2.2: Grain characteristics of the DC01 steel.

Grain size index	*Average grain area* μm^2	*Average diameter* µm
10.5	89.1	9.4

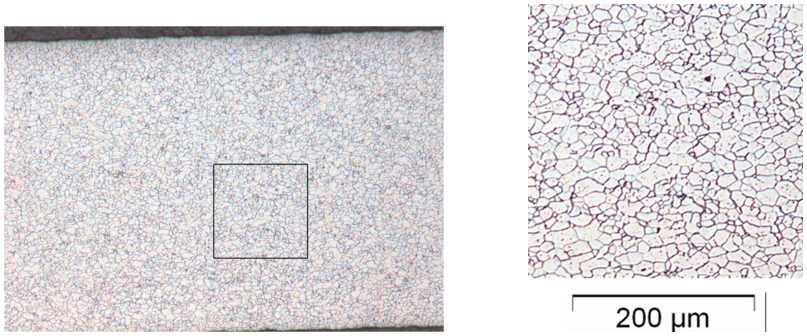

Figure 2.2: Analyzed zone for the estimation of the grain size. The left figure (100x) depicts a square, which is zoomed in the right figure (200x).

than ASTM n°7) could imply that an *orange peel effect* is to be expected for deep drawing operations (Hosford and Caddell, 2007).

The initial texture of the base material was measured by Philip Eyckens from the MTM team at KULeuven in 1 mm × 1 mm squared samples. The (incomplete) pole figures obtained from X-ray diffraction (XRD) measurement can be seen in Fig. 2.3, where the distribution functions have some preferred orientations implying some macroscopic anisotropy. The material also shows a strong α-fiber

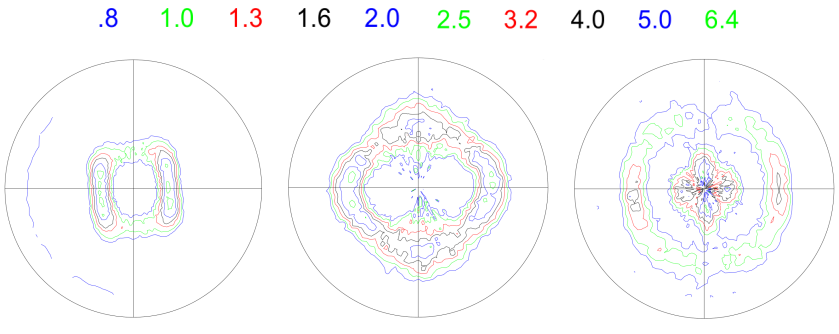

(a) (1 1 0) (b) (2 0 0) (c) (2 1 1)

Figure 2.3: Incomplete pole figures of the DC01 steel sheet at different crystal lattice planes. Obtained from XRD measurements in a 1 mm × 1 mm squared area with the normal direction coming out from the plane.

and a characteristic γ-fiber, contributing to the in-plane anisotropy of the sheet. More details on the crystallographic texture analysis of the base material can be found in the appendix C.

2.2 Constitutive modeling

The choice of the constitutive laws strongly depends on the material being analyzed and its mechanical behavior. However, irrespective of the constitutive laws selected three different aspects of the material should be identified: the elastic behavior, the initial yield surface and the work hardening regime.

2.2.1 Elastic part

The elastic part is described by the isotropic-linear version of the Hooke's law. The relation between the natural strain tensor $\boldsymbol{\epsilon}$ and the Cauchy stress tensor $\boldsymbol{\sigma}$ is given by:

$$\boldsymbol{\epsilon} = \frac{1}{2G_s}\boldsymbol{\sigma} - \frac{\nu}{E}\frac{1}{3}\mathrm{tr}\left(\boldsymbol{\sigma}\right)\boldsymbol{I} \tag{2.2.1}$$

where E is the elastic modulus, ν is the Poisson ratio and G_s is the shear modulus. The elastic material constants are related with each other by the relation:

$$G_s = \frac{E}{2\left(1+\nu\right)} \tag{2.2.2}$$

2.2.2 Initial yield surface

The yield surface divides the stress space in the elastic and plastic domains i.e., the yield surface is the boundary between these two domains. The general form of a yield function can be described by a surface function in the stress space:

$$F_p\left(\boldsymbol{\sigma}, \boldsymbol{X}, \upsilon\right) = 0 \tag{2.2.3}$$

where $\boldsymbol{X}$ is a *kinematic* hardening tensor commonly called *backstress* which defines the position of the center of the yield surface, and υ is an *isotropic* hardening parameter governing the size of the yield surface. The stress state $\boldsymbol{\sigma}$ is elastic if $F_p < 0$ and there is plastic deformation if $F_p = 0$. The surface function comprises the shape, displacement and size of the yield locus:

$$F_p\left(\boldsymbol{\sigma}, \boldsymbol{X}, \upsilon\right) = \vartheta\left(\boldsymbol{\sigma}, \boldsymbol{X}\right) - k\left(\upsilon\right) = 0 \tag{2.2.4}$$

where ϑ is the yield function shape and k is a function representing the size of the yield locus.

2.2.2.1 Isotropic yield surface

For the isotropic description of the yield surface the *maximum distorsional energy* criterion (von Mises, 1913)[2] is extensively used. It has the following form:

$$\vartheta\left(\boldsymbol{\sigma}, \boldsymbol{X}\right) := \sqrt{\frac{1}{2}\left(\boldsymbol{\sigma} - \boldsymbol{X}\right)_{\text{dev}} : \left(\boldsymbol{\sigma} - \boldsymbol{X}\right)_{\text{dev}}} \tag{2.2.5}$$

or in terms of the stress components without backstress:

$$2\vartheta^2 = \left(\sigma_y - \sigma_z\right)^2 + \left(\sigma_z - \sigma_x\right)^2 + \left(\sigma_x - \sigma_y\right)^2 + 6\sigma_{xy}^2 + 6\sigma_{yz}^2 + 6\sigma_{xz}^2 \tag{2.2.6}$$

where $(\cdot)_{\text{dev}}$ denotes the deviatoric part of the tensor.

2.2.2.2 Anisotropic yield surface

Considering the previous research into a similar material (Flores, 2005), the Hill, (1948) yield criterion is chosen because of its overall simplicity when describing the anisotropic behavior of a metallic material, over it well known limitations for BCC materials (viz. Bishop and Hill, 1951). Moreover, this quadratic model has been found to provide accurate predictions for steel sheets. The shape of this yield locus is given by the following equation:

$$\vartheta\left(\boldsymbol{\sigma}, \boldsymbol{X}\right) := \sqrt{\frac{1}{2}\left(\boldsymbol{\sigma} - \boldsymbol{X}\right) : \mathbb{H} : \left(\boldsymbol{\sigma} - \boldsymbol{X}\right)} \tag{2.2.7}$$

where $\mathbb{H}$ is a fourth-order tensor containing the anisotropic parameters. For this yield function the material is assumed to be *orthotropic*, having three orthogonal symmetry planes and three principal axes of anisotropy: x, y and z. Within the anisotropic axis frame and omitting the backstress:

$$\begin{aligned} 2\vartheta^2 := {} & F(\sigma_y - \sigma_z)^2 + G(\sigma_z - \sigma_x)^2 + H(\sigma_x - \sigma_y)^2 + \dots \\ & \dots + 2L\sigma_{yz}^2 + 2M\sigma_{zx}^2 + 2N\sigma_{xy}^2 \end{aligned} \tag{2.2.8}$$

where F, G, H, L, M and N are material parameters. For thin sheet metals, it is assumed that $L = M = N$ because of experimental restraints. Note that if $F = G = H = 1.0$ and $L = M = N = 3.0$, the Hill, (1948) yield locus recovers the isotropic von Mises yield locus.

2.2.3 Hardening

Hardening refers to the strengthening of the material due to both the dislocation movements and nucleation (annealing) of dislocations within the crystal structure. At the macroscopic level, this phenomenon can be mathematically represented through changes on the size and/or position of the yield locus using isotropic and/or kinematic hardening models.

[2]Including contributions by James Clerck Maxwell, Heinrich Hencky and Maximilian Huber, this criterion can be defined more precisely as Maxwell-Huber-Mises-Hencky criterion. In this thesis, we will use the name von Mises (VM) criterion in agreement to common engineering usage. For more historical references, see the book of Jones, (2009).

2.2.3.1 Isotropic hardening

In general, the isotropic hardening parameter υ has two different measures. One based on the equivalent plastic strain $\bar{\epsilon}^P$ (*strain hardening* hypothesis):

$$\upsilon := \bar{\epsilon}^P = \int d\bar{\epsilon}^P \tag{2.2.9}$$

and the other on the total plastic work W^P (*work hardening* hypothesis):

$$\upsilon := W^P = \int \boldsymbol{\sigma} : d\boldsymbol{\epsilon}^P \tag{2.2.10}$$

Hereafter, we use the *strain hardening* hypothesis because of its simplicity[3]. Therefore, the isotropic hardening behavior can be modeled by the Swift, (1952) law which shows neither saturation nor softening phenomenon:

$$\sigma_Y\left(\bar{\epsilon}^P\right) = K\left(\bar{\epsilon}^P + \epsilon_0\right)^n \tag{2.2.11}$$

where σ_Y is the actual yield stress, $\bar{\epsilon}^P$ the equivalent plastic strain and ϵ_0, K, n are material parameters. The Voce, (1948, 1955) law will also be used and it is expressed by:

$$\sigma_Y\left(\bar{\epsilon}^P\right) = \sigma_{Y0} + K(1 - \exp\left(-n\bar{\epsilon}^P\right)) \tag{2.2.12}$$

where σ_{Y0}, ϵ_0, K and n are material parameters. It is a phenomenological formula based on more physical models related to dislocations distributions. It predicts both hardening and softening effects.

2.2.3.2 Kinematic hardening

An evolution law for the backstress tensor was originally proposed by Prager, (1955) in a linear form:

$$\dot{\boldsymbol{X}} = c\dot{\boldsymbol{\epsilon}}^P \tag{2.2.13}$$

where c is a material constant. This was later modified by Armstrong and Fredrick, (1966) (herein referred to as the A-F model)[4], including a non-linear term:

$$\dot{\boldsymbol{X}} = C_X\left(X_{\text{sat}}\dot{\boldsymbol{\epsilon}}^P - \boldsymbol{X}\bar{\epsilon}^P\right) \tag{2.2.14}$$

where $\dot{\boldsymbol{X}}$ is the rate of the *backstress*, C_X (saturation rate) and X_{sat} (saturation value of the backstress) are material constants. The influence of each parameter on the stress-strain curve can be checked in Flores, (2005, chapter 5). The A-F model introduces $C_X\boldsymbol{X}\bar{\epsilon}^P$ as a *recall* term, which influences plastic flow differently for tensile or compressive loading depending on the accumulated plastic strain. In this way the model is able to predict both the Bauschinger, (1886) effect and accumulation of plastic strain (also called *ratcheting*) under an asymmetrical stress cycle.

[3]In LAGAMINE, the subroutine HILL3D uses the *work hardening* hypothesis while HILL3D_KI uses the *strain hardening* hypothesis.

[4]First referenced by Chaboche, (1977), the original report by Armstrong and Fredrick, (1966) was first made publicly available in Frederick and Armstrong, (2007).

2.3 Experimental setup

In this section we describe the experimental devices available to perform tests and measurements at the *Laboratoire de Mécanique des Matériaux et Structures* of the University of Liège.

2.3.1 Mechanical test equipment

Two machines are available to carry on the tests:

- An unixial Zwick machine shown in Fig. 2.4(a), with a load capacity of $\pm 100\,\mathrm{kN}$ with an integrated extensometer.
- A biaxial machine designed by Flores, (2003, 2005), shown in Fig. 2.4(b). It uses horizontal (**A**) and vertical (**C**) actuators to enable the displacement of the grips (**B**). Each actuator has a capacity of $\pm 100\,\mathrm{kN}$.

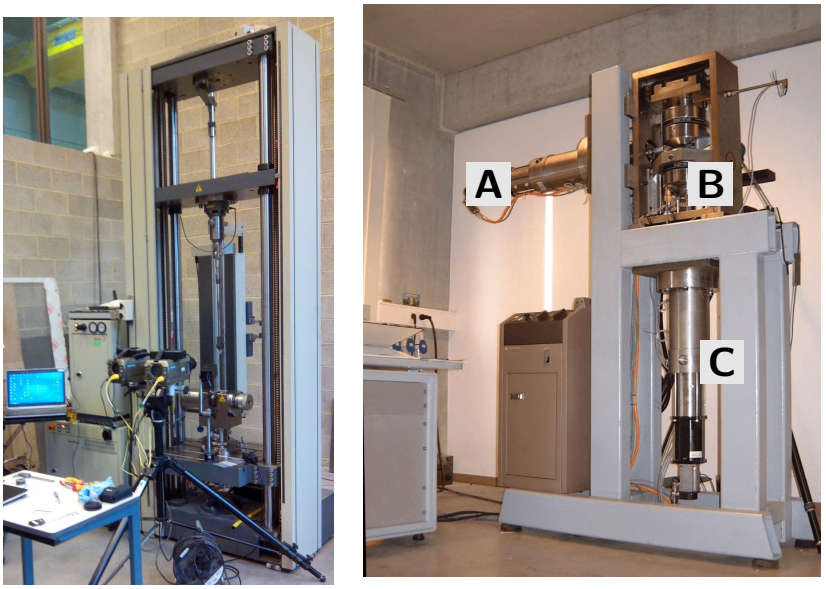

(a) Uni-axial Zwick machine and mounted optical system.

(b) Bi-axial testing machine depicting horizontal (**A**) and vertical (**C**) actuators and the grips (**B**).

Figure 2.4: Experimental equipment used to perform the tests.

All specimens were cut using *wire electrical discharge machining* (WEDM).

2.3.2 Optical measurements systems

Image analysis is a type of data extraction procedure which over the last decade, along with advances in digitalization techniques, has become very popular. The application range covers areas such as medical scans or video tracking. It basically consists in extracting meaningful information from images. One particular field

is the *image correlation*, a type of non-contacting measuring method. Here the images of an object are digitalized, and after an analysis is performed to extract full-field information such as shape, displacements and strains.

Digital Image Correlation (DIC) has several advantages over traditional measurement systems (like extensometers). Among these we found:

1. It is a contactless method.
2. It is independent on the geometry of the specimen,
3. It has the possibility of a wide range of loading conditions, from (very) small strains to large plastic deformations.
4. It measures full-field displacements and strains with sub-pixel accuracy.

Basically, DIC offers a wide range of applications with a limited hardware setup. The setup, besides the classical experimental devices, includes cameras, supports and a computer with a correlation software (Fig. 2.5). Hence, it is possible to couple the DIC measurement device to all laboratory test setups.

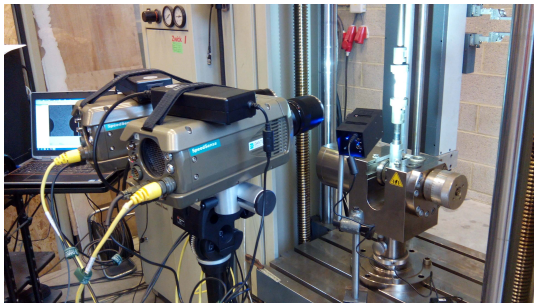

Figure 2.5: Mounted DIC hardware showing the cameras, supports, computer and part of the Zwick machine.

2.3.2.1 Principles

Two key DIC assumptions are generally used to convert images into experimental measurements of shape, displacements and strains:

- There is a direct correspondence between the image's motion of points of the image and the motion of points of the object.
- Each subregion has a suitable contrast (variation in light intensity) so that accurate matching can be performed to define local image motions.

However, situations may occur where these assumptions are broken. For instance, when correlating across a discontinuity (e.g., crack, hole) or when there is a loss of contrast during the loading process (separation of the painted speckle form the surface, change in diffuse reflectivity, etc.).

DIC is basically a *pattern tracking method*. To explore this concept, lets consider two images from the same surface of a specimen in two different situations

(Fig. 2.6). One situation will be taken as the reference image (usually the undeformed material) and the other after an applied load. To determine the displacement fields of the considered zone between both steps, the analyzed zone (area-of-interest, AOI) of the reference image (mxn pixels) is cut in different small zones (hereafter referred to as *subset*) (size lxl pixels). The goal of this method is look for each subset of the reference image and then for his counterpart in the deformed image. Here the concept of subset is introduced. Since each pixel value cannot

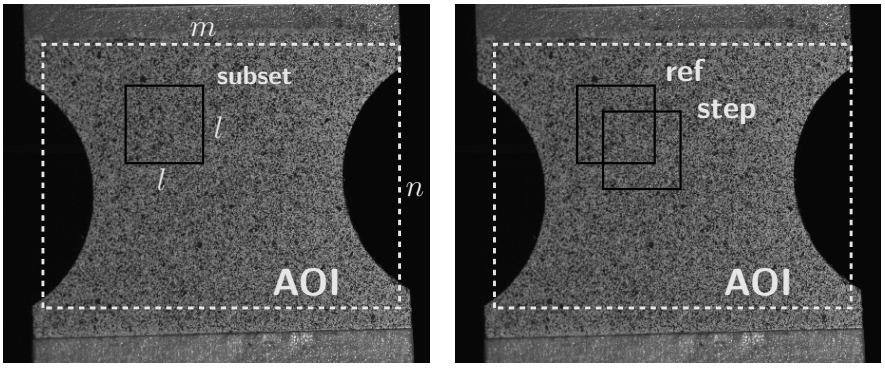

(a) AOI and subsets in the reference stage.

(b) Deformed image showing the same subset in a subsequent step.

Figure 2.6: Image correlation AOI and subset in a sample image.

be used as an unique signature within the AOI, the solution relies on the use of the pixel and its neighborhood (subset). Mathematically, a subset is uniquely identified as a 2D array of 8bit or 16bit grey intensity values[5]. In practice, the *uniqueness* of the subset is governed by its size and the quality of the applied speckle pattern, which should be as random as possible. In general, the image processing of subsets between two different steps has three main components:

- Matching the same pattern between these two images.
- Interpolation of the information between pixels.
- Give a shape function to all subsets.

Each process component is performed by the correlation software.

2.3.2.2 Practical considerations

In DIC analysis, both hardware and software play together to obtain accurate results. Hence, it is recommended to identify the hardware limitations which could eventually lead to uncertainties when performing the correlation. Among them, it is worth to mention:

- Identify the digital camera type (CMOS or CCD), gain, pixel size, aspect size, fill factor, blind area, active area, lenslets, etc.

[5]An histogram is another way to look at the image intensity

- Evaluate distorsion of lenses.
- Perform a noise evaluation by averaging a set of static images.

The experimental measurement setup for both the Zwick and biaxial machine is a Dantec Dynamics Q-450 optical acquisition system, which consists of:

- High speed CMOS cameras Vision research phantom V710Fast (max. resolution of 1280×800).
- Zeiss 50 mm f/2.0 Makro-Planar ZE Macro Lens F-mount.
- Sturdy tripod with mounting head.
- Istra4D v4.3.1 correlation software.

Camera noise is of particular importance because it is inversely proportional to the displacement accuracy. Moreover, strains (and velocities) are displacement derivatives, so they are very sensitive to noise. Since DIC is a nonlinear analysis based on function minimization, a single set of optimal parameters is practically impossible to obtain. Thus, defining a methodology can be helpful in order to find one set of hardware and software parameters that fulfills the user's requirements. In the following, we describe displacements and strains separately.

Displacements. A fundamental step to consider when measuring displacements with DIC is the *spatial* and *displacement resolution*. Resolution is defined as *the smallest distance between independent measurements* or *the smallest signal above noise*. Spatial resolution refers to how closed lines can be resolved in an image. In DIC it is defined by the subset (not step) size. This implies that a large subset size will have problems matching the shape. The displacement resolution on the other hand, is directly proportional to the subset size. Hence, a compromise between both should be considered with the lower limit being determined by the granularity of the speckle pattern and the upper limit by the desired spatial resolution. It is worth to mention that DIC is useful because of the subpixel accuracy i.e., the displacement resolution is hundreds times smaller than a pixel.

Strain measurements. Strains are defined within DIC software by a relative displacement over a gauge length:

$$\epsilon = \frac{\Delta L}{L} \tag{2.3.1}$$

Thus, it is straightforward to derive some important rules. For instance, in order to improve the resolution it is necessary to increase the relative displacement ΔL resolution (displacement resolution) or increase the gauge length L. Again, a trade-off between the spatial resolution and the strain resolution is needed. It is important to note that while displacement resolution scales with setup-related parameters (such as the field-of-view and camera resolution), strain resolution does not depend exclusively on the DIC software parameters.

Now we introduce the Virtual Strain Gauge (VSG):

$$VSG = (S_w - 1)\, ST + 1 \tag{2.3.2}$$

where S_w is the strain window size and ST the step size. The spatial (strain) resolution is defined as:

$$S_R = (S_w - 1)\, ST + SS \tag{2.3.3}$$

with SS as the subset size. Compared to displacement resolution, larger VSG improves strain resolution more dramatically. Overall, it is worthwhile to keep the following rules in mind:

1. Smaller subset capture the gradients better.
2. Smaller VSG have a higher noise.
3. Large subsets will mask strain gradients.

As a general rule, larger subsets and VSG when measuring uniforms strains should be used. If there are strong gradients, smaller subsets and VSG should be used in order to capture them. For all cases, in order to get useful strain results smoothing should be employed.

2.4 Tensile tests

The specimen shape is based on an European norm for tensile tests (ISO 6892-1:2009, 2009, See *Annexe B, éprouvettes pour produits mince, éprouvette type 1*). Taking the rolling direction (RD) as the reference direction, specimens were prepared in three orthogonal directions: at 0°, 45° and 90° (transverse) from the RD. Four tests in each direction were performed in the Zwick testing machine. An axial extensometer was mounted to measure the deformations.

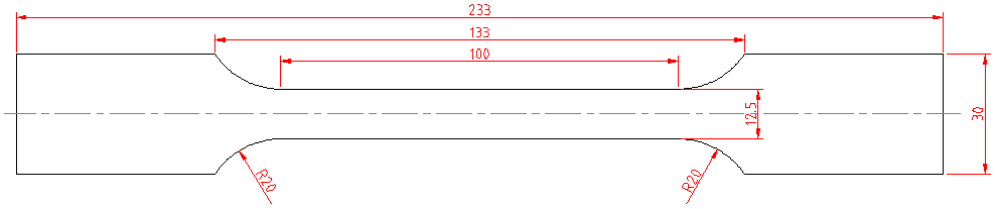

Figure 2.7: Tensile test specimen according to ISO 6892-1.

2.4.1 Mathematical description

In tensorial notation, the stress in a tensile test is given by:

$$\boldsymbol{\sigma} = \sigma_{11} \boldsymbol{e_1} \otimes \boldsymbol{e_1} \tag{2.4.1}$$

or in terms of tensor components:

$$[\boldsymbol{\sigma}] = \begin{bmatrix} \sigma_{11} & 0 & 0 \\ 0 & 0 & 0 \\ 0 & 0 & 0 \end{bmatrix} \tag{2.4.2}$$

$$\sigma_{11} = \frac{F_{\text{vert}}}{A_{\text{act}}} \tag{2.4.3}$$

where F_{vert} is the vertical force measured by the load cell while A_{act} is the actual area of the section of the specimen. The strain tensor is reduced to:

$$\boldsymbol{\epsilon} = \epsilon_{11}\boldsymbol{e_1} \otimes \boldsymbol{e_1} + \epsilon_{22}\boldsymbol{e_2} \otimes \boldsymbol{e_2} + \epsilon_{33}\boldsymbol{e_3} \otimes \boldsymbol{e_3} \tag{2.4.4}$$

or in matrix notation:

$$[\boldsymbol{\epsilon}] = \begin{bmatrix} \epsilon_{11} & 0 & 0 \\ 0 & \epsilon_{22} & 0 \\ 0 & 0 & \epsilon_{33} \end{bmatrix} \tag{2.4.5}$$

Assuming volume conservation:

$$\epsilon_{11} + \epsilon_{22} + \epsilon_{33} = 0 \tag{2.4.6}$$

the initial and actual area are related by:

$$A_{\text{act}} = A_0 \exp(-\epsilon_{11}) \tag{2.4.7}$$

Hence, A_{act} can be found using an extensometer according to the ISO 6892-1 norm. It is also possible to obtain an expression relating the true and engineering stress in one dimension:

$$e = \frac{\Delta l}{l_0}, \qquad P = \frac{F}{A_0} \tag{2.4.8}$$

$$\epsilon = \ln(1+e), \qquad \sigma = P(1+e) \tag{2.4.9}$$

where e is the engineering strain, ϵ is the logarithmic (natural) strain, P is the engineering stress[6] and σ is the true (Cauchy) stress.

2.4.2 Results

The output of the test is the loading versus displacement curve plotted in Fig. 2.8. It is possible to observe in the average curve of Fig. 2.8(a) that there is an anisotropic behavior, which is clearly noticeable for the test performed at 45° from the RD. During the homogeneous deformation, the maximal forces of tests performed at 45° are higher than those at RD and TD and it happens earlier. After this maximum seen in Fig. 2.8(c), 45° samples have a more dispersed behavior than RD and TD.

Because the tests were performed using an extensometer the stress/strain relations are only valid when the deformation is homogeneous i.e., before localized necking. The data from Fig. 2.8 were post-processed until the possible onset of localized necking (associated to the maximal force) was attained. It provides the true and engineering stress-strain curves, using both Eq. 2.4.8 and Eq. 2.4.9. The average curves are shown in Fig. 2.9.

[6] Also known as Piola-Kirchoff 1.

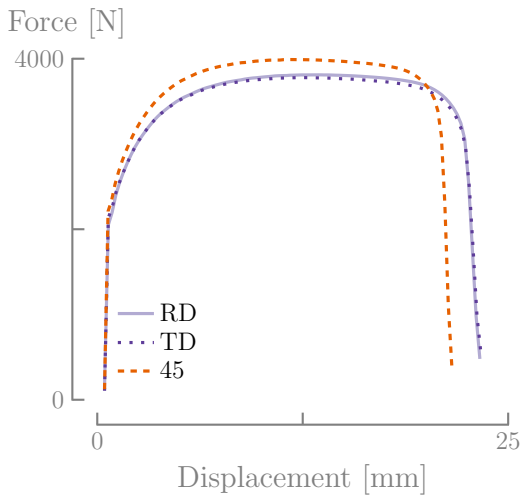

(a) Average values of the analog data.

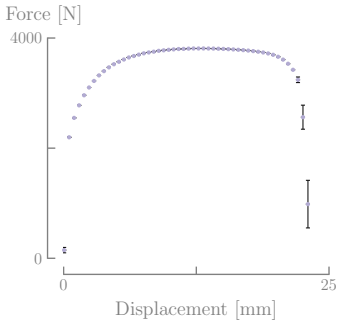

(b) Dispersion at the RD.

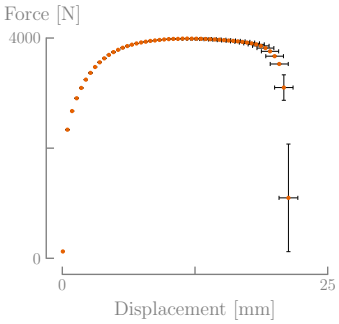

(c) Dispersion at 45°.

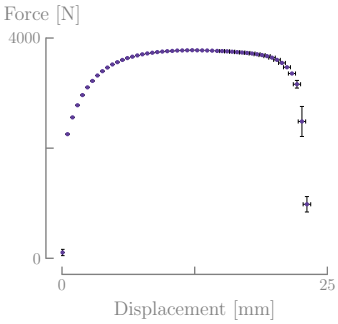

(d) Dispersion at the TD.

Figure 2.8: Force vs. displacement tensile test results showing the average values (Fig. 2.8(a)) and the dispersion in each direction (Fig. 2.8(b), 2.8(c) and 2.8(d)).

2.4.3 Analysis

2.4.3.1 Elasto-plastic transition

The serrated transition from the elastic to the plastic zone observed in Fig. 2.10 is similar to the well known *Portevin-Le Chatelier effect*. This effect is associated to a visco-plastic phenomena when the resistance to deformation increases with decreasing strain rate. Indeed, these characteristical *jerky flows* are usually found at displacement controlled tests for some materials (François et al., 2012), as for this case here.

2.4.3.2 Initial yield stress

The initial yield stress is taken from Fig. 2.9(a) using the offset method at different strain levels[7]. The curve at the RD is taken as the reference for the plastic work

[7] As the values of strain are very small at this point, we can use the true or the engineering stress indistinctly.

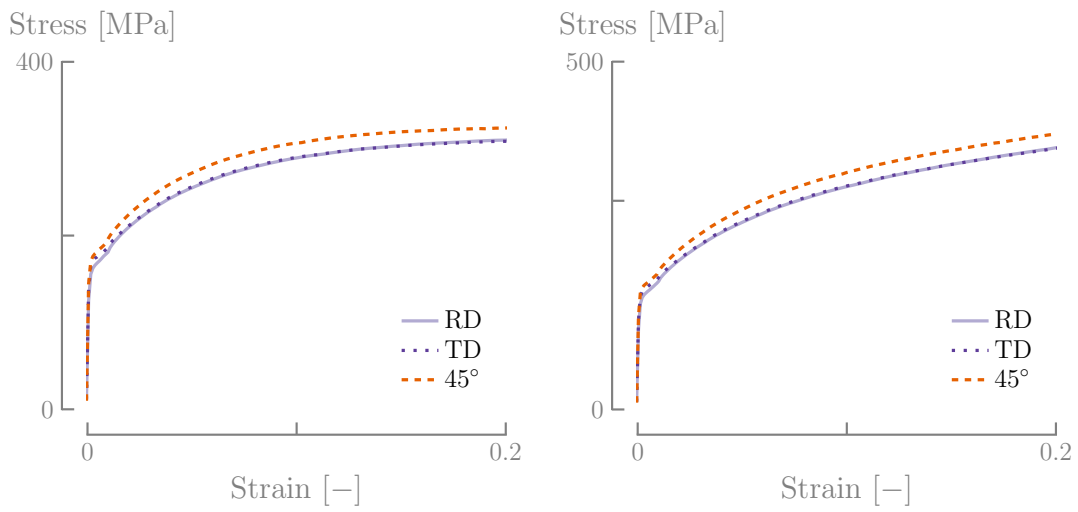

(a) Engineering stress P_{11} vs. engineering strain e_{11}.

(b) True stress σ_{11} vs. natural strain ϵ_{11}.

Figure 2.9: Engineering and natural stress vs. strain curves.

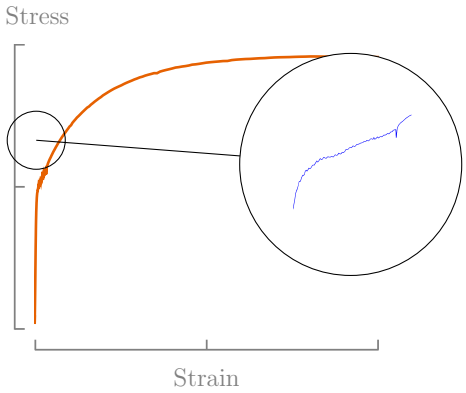

Figure 2.10: Zoom in transition between the elastic and plastic zone, showing the Portevin-Le Chatelier effect.

and calculated values are shown in Table 2.3 for different strain offsets. Regarding the general force-displacement curves, the 45° specimen presents higher scattering with higher initial yield stress and ultimate tensile strength (Table 2.4). For the determination of the yield stress for stress states other than tensile, it is useful to introduce the plastic work:

$$W^P = \int \boldsymbol{\sigma} : d\boldsymbol{\epsilon}^P \tag{2.4.10}$$

The use of this equation will be covered in subsequent sections.

2.4.4 Anisotropic coefficients

The anisotropic coefficient (also known as Lankford et al., (1950) coefficient) is a widely used approach to represent the anisotropy of a material. It is defined as

Table 2.3: Initial yield stress (in MPa) in the different directions based on different strain offsets. If the RD is taken as the reference, the relative difference with the 45° and the TD is 7.6% and 4.12% respectively. W^P is computed in the RD.

ϵ_0^P %	W_0^P MPa	*RD* MPa	45° MPa	*TD* MPa
0.20	0.422 ± 0.001	164.75 ± 0.73	177.14 ± 1.22	172.52 ± 0.83
0.50	0.943 ± 0.002	173.69 ± 1.43	185.42 ± 0.66	179.51 ± 0.47
0.75	1.397 ± 0.002	181.12 ± 0.75	192.17 ± 1.68	185.42 ± 0.71

Table 2.4: Ultimate tensile strength (in MPa) at different directions.

RD MPa	45° MPa	*TD* MPa
312.26 ± 1.10	324.18 ± 1.05	309.95 ± 0.42

the the ratio between the transversal plastic strain rate and the thickness plastic strain rate:

$$r := \frac{\dot{\epsilon}_{22}^P}{\dot{\epsilon}_{33}^P} \tag{2.4.11}$$

where ϵ_{22}^P and ϵ_{33}^P are the logarithmic plastic strain in the transversal and thickness direction respectively. By assuming volume conservation during the plastic deformation, we can express the strain in the thickness direction in terms of transversal and longitudinal strains:

$$\epsilon_{11}^P + \epsilon_{22}^P + \epsilon_{33}^P = 0 \tag{2.4.12}$$

$$\epsilon_{33}^P = -\epsilon_{11}^P - \epsilon_{22}^P \tag{2.4.13}$$

It is also possible to define the coefficient of *normal anisotropy* (or average Lankford):

$$\overline{r} := \frac{r_0 + 2r_{45} + r_{90}}{4} \tag{2.4.14}$$

and the coefficient of *planar anisotropy*:

$$\Delta r := \frac{r_0 - 2r_{45} + r_{90}}{4} \tag{2.4.15}$$

There are different ways to measure the anisotropic coefficient:

- By measuring the plastic strain rates in the transversal and thickness direction from the uni-axial tensile test (Fig. 2.11(a)).
- By measuring the slope of the transversal strain versus thickness strain from the uni-axial tensile test (Fig. 2.11(b)).
- Based on the crystallographic texture of the base material.

Here the focus is on values obtained from the tensile test, while the texture-based method is detailed in Appendix C. The plastic strain curves are shown within the range ϵ_{11}^P =10%-30% in Fig. 2.11, where a linear interpolation can be readily obtained. Fig. 2.12 shows that the evolution of the ratio $\epsilon_{22}^P/\epsilon_{33}^P$ falls within an acceptable range, despite not being constant. Values of the anisotropic

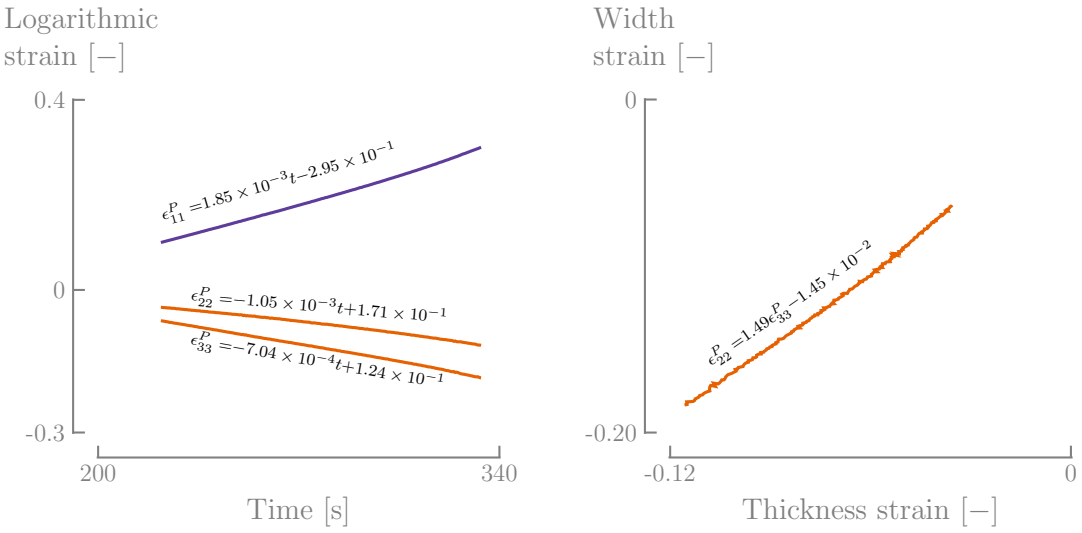

(a) Plastic strain rate measurements.

(b) Incremental plastic strain measurements.

Figure 2.11: Measured width (transversal) strain ϵ_{22}^P and thickness strain ϵ_{33}^P from one test in RD showing the linear interpolation equation.

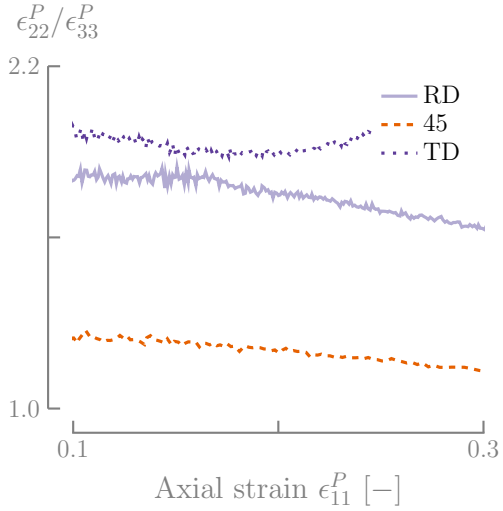

Figure 2.12: Plastic strain ratio $\epsilon_{22}^P/\epsilon_{33}^P$ evolution for one test in each direction.

coefficients are shown in Table 2.5. Anisotropic coefficients obtained from texture measurements are higher than those obtained from deformation measurements. The tensile test based values will be used hereafter because they are based on several tensile tests, while the texture based values are only taken at one thickness

Table 2.5: Anisotropic coefficients for the DC01 steel taken from the tensile test and texture measurements from Appendix C.

Direction	*Tensile test*		*Texture*
	$r = \frac{\dot{\epsilon}^P_{22}}{\dot{\epsilon}^P_{33}}$	$r = \frac{\Delta\epsilon^P_{22}}{\Delta\epsilon^P_{33}}$	
RD	1.513 ± 0.068	1.508 ± 0.067	2.237 ± 0.054
45°	1.141 ± 0.025	1.137 ± 0.025	1.478 ± 0.028
TD	1.854 ± 0.089	1.847 ± 0.090	2.166 ± 0.074
$\overline{r}$	1.4121	1.4076	1.840
Δr	0.2714	0.2701	0.724

depth. The results show a low dispersion (less than %5), with $\overline{r}$ =1.4 being a common value for low carbon steels of the *aluminium killed* type (Hosford and Caddell, 2007). As expected, the difference between the incremental and rate values of the Lankford coefficients is almost negligible because of the low strain insensitivity of steels (Eyckens, 2010).

2.5 Shear tests

The specimen geometry was selected according to Flores, (2005, annex C) in order to decrease the sliding influence on the results and is depicted in Fig. 2.13. The measurable zone (in gray) is covered with a special paint (Henkel Teroson mat, reference 155.64S) to get a stochastic speckle pattern for DIC measurements.

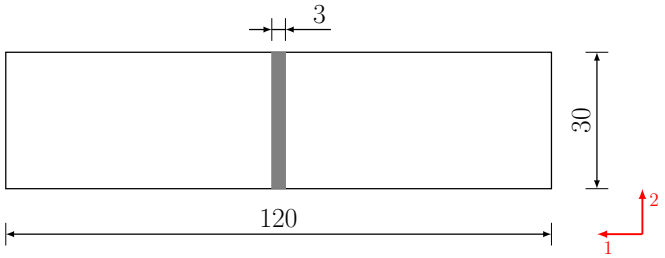

Figure 2.13: Shear test specimen. The speckle pattern for DIC measurements is applied on the gray zone.

2.5.1 Mathematical description

To define the shear strain, let us consider an initial square element subjected to simple shear as shown in Fig. 2.14. In tensorial notation, the stress state in a shear test is given by:

$$\boldsymbol{\sigma} = \sigma_{11}\boldsymbol{e_1} \otimes \boldsymbol{e_1} + \sigma_{22}\boldsymbol{e_2} \otimes \boldsymbol{e_2} + \sigma_{12}\boldsymbol{e_1} \otimes \boldsymbol{e_2} + \sigma_{21}\boldsymbol{e_2} \otimes \boldsymbol{e_1} \tag{2.5.1}$$

$$[\boldsymbol{\sigma}] = \begin{bmatrix} \sigma_{11} & \sigma_{12} & 0 \\ \sigma_{21} & \sigma_{22} & 0 \\ 0 & 0 & 0 \end{bmatrix} \tag{2.5.2}$$

with:

$$\sigma_{11} = \frac{F_{\text{vert}}}{A_{\text{act}}}, \qquad \sigma_{12} = \sigma_{21} = \frac{F_{\text{hor}}}{A_{\text{act}}} \tag{2.5.3}$$

where F_{hor} and F_{vert} are the forces measured using the horizontal and vertical actuator, respectively. Note that σ_{22} cannot be measured and that $\sigma_{12} = \sigma_{21}$ is assumed because of the symmetry of the Cauchy stress tensor. A_{act} is computed from the thickness reduction using a volume assumption. The strain tensor is given by:

$$\boldsymbol{\epsilon} = \epsilon_{11}\boldsymbol{e_1} \otimes \boldsymbol{e_1} + \epsilon_{22}\boldsymbol{e_2} \otimes \boldsymbol{e_2} + \epsilon_{33}\boldsymbol{e_3} \otimes \boldsymbol{e_3} + \epsilon_{12}\boldsymbol{e_1} \otimes \boldsymbol{e_2} + \epsilon_{21}\boldsymbol{e_2} \otimes \boldsymbol{e_1} \tag{2.5.4}$$

$$[\boldsymbol{\epsilon}] = \begin{bmatrix} \epsilon_{11} & \epsilon_{12} & 0 \\ \epsilon_{21} & \epsilon_{22} & 0 \\ 0 & 0 & \epsilon_{33} \end{bmatrix} \tag{2.5.5}$$

The deformation gradient helps to relate the geometry with the strain tensor. It is given by:

$$\boldsymbol{F} = \boldsymbol{I} + \gamma \boldsymbol{e_1} \otimes \boldsymbol{e_2} \tag{2.5.6}$$

$$[\boldsymbol{F}] = \begin{bmatrix} 1 & \gamma & 0 \\ 0 & 1 & 0 \\ 0 & 0 & 1 \end{bmatrix} \tag{2.5.7}$$

where γ is shown in Fig. 2.14, given by:

$$\gamma = \tan\theta = \frac{d}{a} \tag{2.5.8}$$

It can be shown using a strain definition of the deformation gradient that:

$$\epsilon_{12} = \frac{\gamma}{2} \tag{2.5.9}$$

known as the *shear strain*. Experimentally, this value is obtained as the average value of ϵ_{12} at the central part of the specimen (thus avoiding edge effects), obtained from DIC measurements.

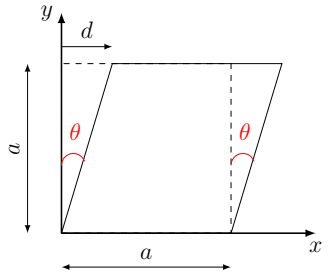

Figure 2.14: Simple shear acting over an element.

2.5.2 Monotonic shear test

Three tests were performed in the RD. The force-displacement curve of the horizontal actuator (**A** in Fig. 2.4(b)) is shown in Fig. 2.15(a). The figure shows low dispersion qualitatively. The stress-strain curve is obtained after applying Eq. 2.4.9 to F_{hor}, while the strain is obtained from DIC measurements. They are depicted in Fig. 2.15(b) while DIC software parameters for Istra4D are shown in Table 2.9. As expected, the rupture strain is larger than in the tensile test results in Fig. 2.9. A decrease on the force level is not noticed which confirms the lack of softening observed in the tensile curves before fracture. The determination of the

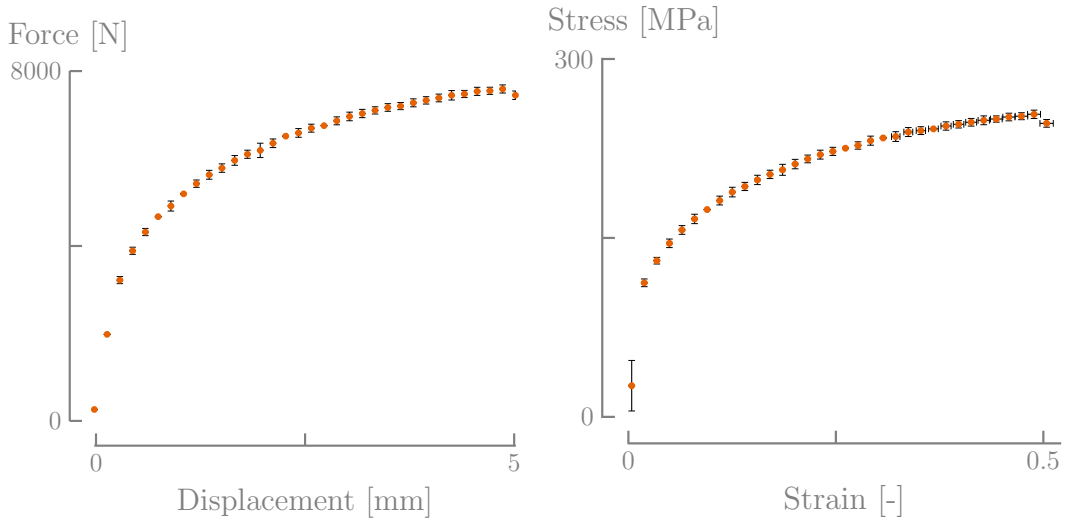

(a) Analog data from the horizontal actuator. (b) Shear stress σ_{12} vs. shear strain ϵ_{12}.

Figure 2.15: Monotonic shear test results in the RD. Three test are performed. Note that the final strain (obtained from DIC measurements) is larger than for the tensile test.

yield stress follows the work-equivalence principle, which states that the plastic work at a given strain offset W_0^P (Eq. 2.4.10) should be the same as the measured reference yield stress for the tensile test (Fig. 2.16). The obtained values are shown in Table 2.6.

Table 2.6: Shear yield stress at different contours of plastic work.

ϵ_0^P %	W_0^P MPa	*RD* MPa
0.20	0.422	93.30 ± 5.04
0.50	0.943	107.48 ± 2.71
0.75	1.397	112.59 ± 2.51

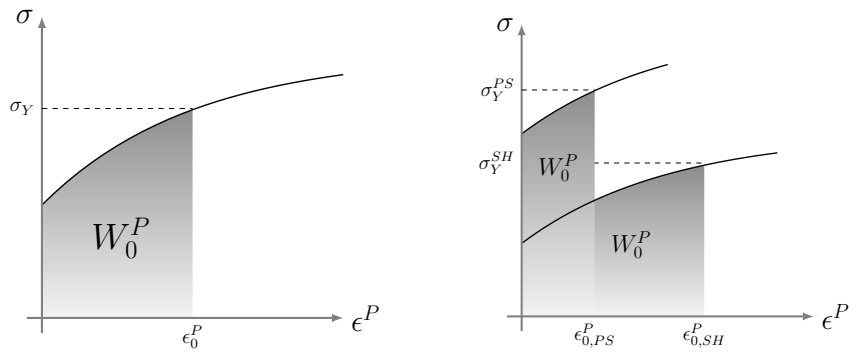

(a) Plastic work in the tensile test.

(b) Work equivalence for the shear and plane strain tests.

Figure 2.16: Determination of the yield stress for different stress states using the work-equivalence principle.

2.5.3 Bauschinger shear test

The objective of the Bauschinger test is to investigate the reverse loading effect in an easier way than in tension/compression tests. It also helps to identify material parameters for kinematic hardening models. Three different pre-strained tests (based on the strain data from the monotonic shear tests) are performed: approximately 10%, 20% and 30% of natural strain. After one of these values is reached, the specimen is loaded in the opposite direction until it breaks. These tests are repeated three times. The force-displacement curves measured from the horizontal actuator are depicted in Fig. 2.17(a). The results show a qualitatively low dispersion like the monotonic shear tests. From the stress-strain curve in Fig. 2.17(b) two phenomena can be noticed. The first is the presence of the Bauschinger effect, involving a significant variation of the flow stress when loading in the opposite direction. In order to clarify this point, refer to Fig. 2.18 and the values in Table 2.7, providing early yielding of the Bauschinger effect. The second

Table 2.7: Stress at the onset of plasticity, as indicated in Fig. 2.18.

	Stress MPa		*Stress* MPa
A	171.2	A'	−128.7
B	207.4	B'	−166.9
C	231.5	C'	−177.5

phenomenon observed is the work-hardening *stagnation*[8] (Hasegawa et al., 1975), after loading the specimen in the opposite direction. This phenomenon greatly complicates the modeling of kinematic hardening, thus needing large-strain cyclic plasticity models in order to obtain good results. Further discussion on this point will be given in section 2.7.4.2.

[8]Reported as a *plateau* in Bouvier et al., (2006).

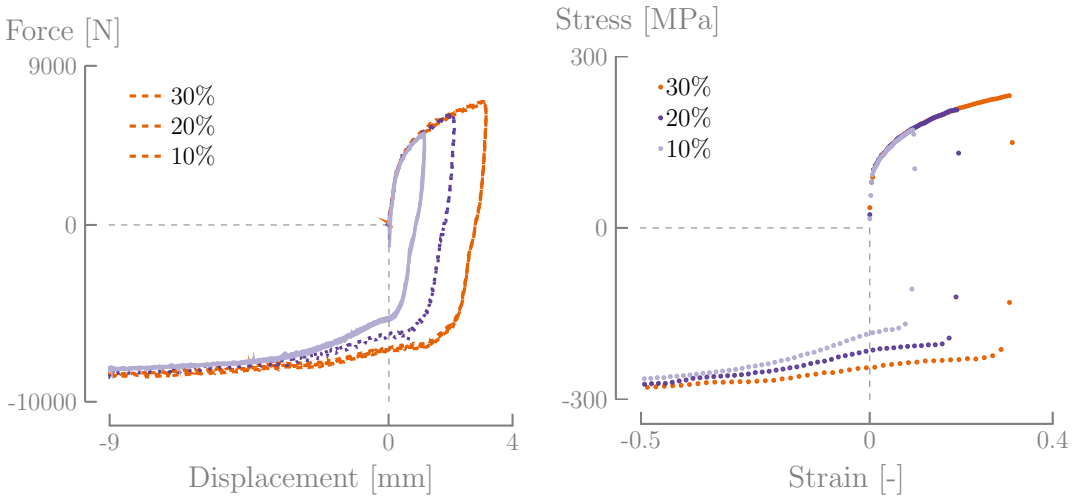

(a) Analog data from the horizontal actuator. (b) Shear stress σ_{12} vs. shear strain ϵ_{12}.

Figure 2.17: Results from the Bauschinger tests.

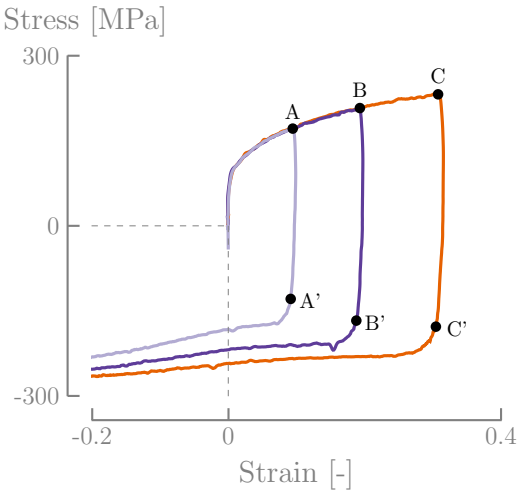

Figure 2.18: Bauschinger effect in the reversed shear test. For the values of each point, refer to Table 2.7.

2.5.4 Sliding evaluation

Sliding is an unwanted relative displacement between the specimen and the clamps. It can be estimated from the pressure of the clamps, the friction coefficient of the specimen's surface or geometry (Flores, 2005, annex C). Theoretically, the shear's strain value without sliding is given by Eq. 2.5.9. A simple way to evaluate sliding is to compare the strain based on the assumed clamp displacement and the observed strain on the specimen. The ideal case is when the shear strain reaches values predicted by Eq. 2.5.9. In practice, there is a displacement *gap* at the beginning of the test in which the specimen is not deformed. This gap is less than 0.20 mm in the present tests. In Fig. 2.19, a comparison between the mechanically adjusted theoretical and experimental values is presented i.e., the experimental displacement is shifted 0.20 mm. The difference in the slope is due to sliding which is low in comparison to the results presented in Flores, (2005, annex C).

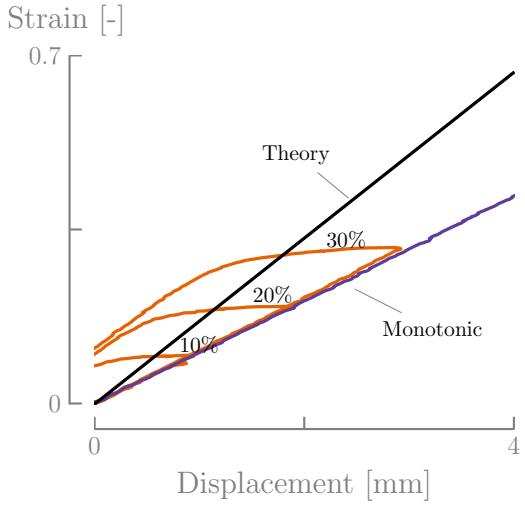

Figure 2.19: Sliding during the shear tests.

2.6 Plane strain tests

Simultaneously with the shear tests, plane strain tests were performed using the same experimental setup. The specimen geometry is depicted in Fig. 2.20 and selected according to Flores, (2005, annex C) and Gilles, (2015, chapter 4), in order to obtain an homogeneous distribution of strain in the specimen width. A speckle pattern is applied in the gray zone of Fig. 2.20 for DIC measurements.

2.6.1 Mathematical description

In tensorial notation, the stress state in the plane strain test is given by:

$$\boldsymbol{\sigma} = \sigma_{11}\boldsymbol{e_1} \otimes \boldsymbol{e_1} + \sigma_{22}\boldsymbol{e_2} \otimes \boldsymbol{e_2} \tag{2.6.1}$$

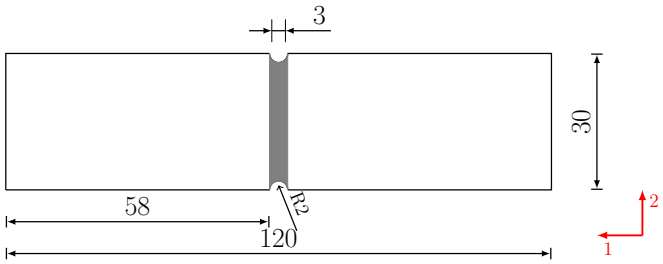

Figure 2.20: Plane strain specimen, showing the measurable zone (in gray).

In terms of tensor components:

$$[\boldsymbol{\sigma}] = \begin{bmatrix} \sigma_{11} & 0 & 0 \\ 0 & \sigma_{22} & 0 \\ 0 & 0 & 0 \end{bmatrix} \tag{2.6.2}$$

σ_{11} is calculated in the same fashion as Eq. 2.4.3 in the tensile test:

$$\sigma_{11} = \frac{F_{\text{vert}}}{A_{\text{act}}} \tag{2.6.3}$$

Unfortunately, under the current setup it is not possible to obtain σ_{22} experimentally. The strain tensor is represented by:

$$\boldsymbol{\epsilon} = \epsilon_{11}\boldsymbol{e_1} \otimes \boldsymbol{e_1} + \epsilon_{33}\boldsymbol{e_3} \otimes \boldsymbol{e_3} \tag{2.6.4}$$

or in matrix notation:

$$[\boldsymbol{\epsilon}] = \begin{bmatrix} \epsilon_{11} & 0 & 0 \\ 0 & 0 & 0 \\ 0 & 0 & \epsilon_{33} \end{bmatrix} \tag{2.6.5}$$

ϵ_{11} is measured from DIC measurements. It is safe to assume volume conservation (as numerically shown by Flores, (2005, chapter 4)), obtaining:

$$\epsilon_{11} = -\epsilon_{33} \tag{2.6.6}$$

The initial area and the actual area are related by:

$$A_{\text{act}} = A_0 \exp\left(-\epsilon_{11}\right) \tag{2.6.7}$$

2.6.2 Results

The tests were performed in three orthotropic directions: RD, 45° and TD. The results for the force-displacement curves are shown in Fig. 2.21 while Fig. 2.22 shows the stress/strain curves. It is clearly observed that the homogeneous part of the plastic deformation is isotropic under plane strain. Nevertheless, after localization there is a clear anisotropic behavior in the three orthotropic directions. In particular, it is again observed (as in the tensile tests) that the tests at 45° localize first, but at the RD and TD strain do not localize in the same way. The yield stress for the plane strain tests is calculated using the work equivalence principle at different strain offsets. The results are shown in Table 2.8 while the software parameters for Istra4D are shown in Table 2.9.

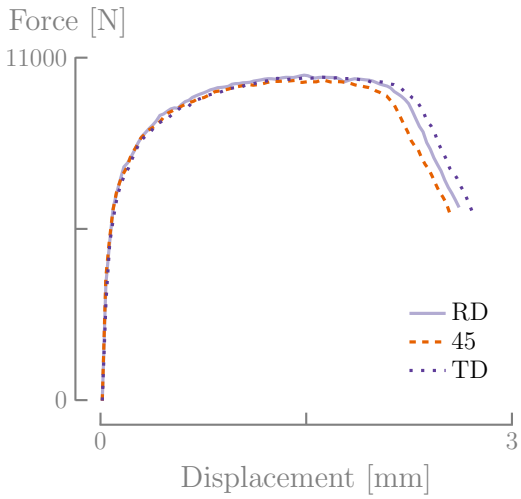

(a) Average values of the analog data.

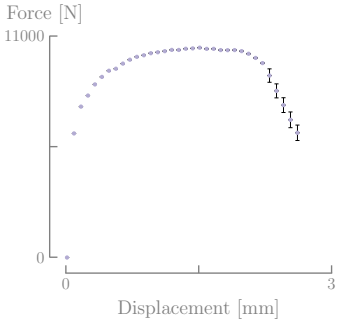

(b) Dispersion at the RD.

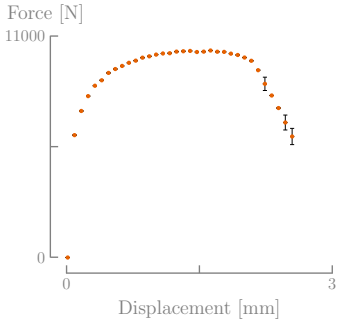

(c) Dispersion at 45°.

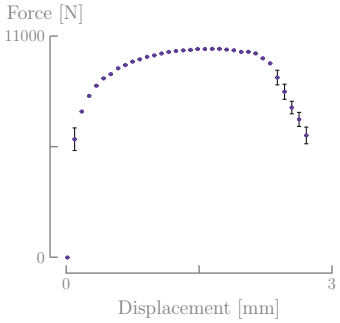

(d) Dispersion at the TD.

Figure 2.21: Force vs. displacement average curves for plane strain tests.

Table 2.8: Plane strain yield stress at different contours of plastic work.

ϵ_0^P %	W_0^P MPa	*RD* MPa	45° MPa	*TD* MPa
0.20	0.422	146.75 ± 3.36	155.58 ± 0.73	148.63 ± 1.56
0.50	0.943	192.28 ± 2.87	193.15 ± 0.76	187.07 ± 8.75
0.75	1.397	213.53 ± 0.36	210.72 ± 3.14	210.88 ± 5.77

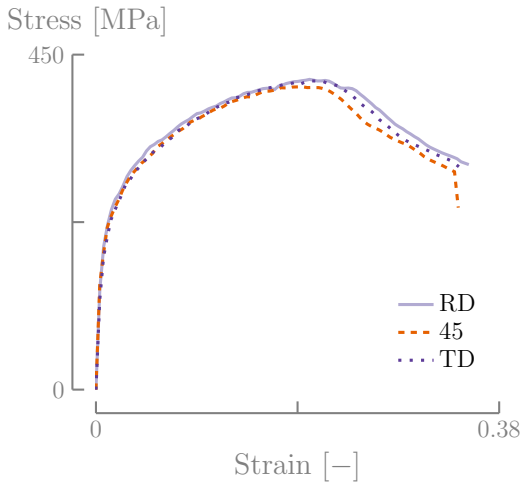

(a) Average values of the stress/strain.

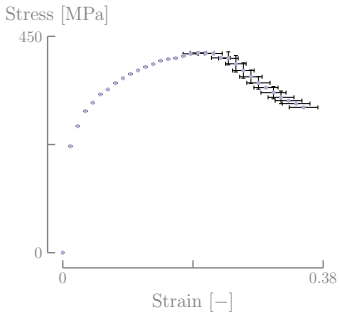

(b) Dispersion at the RD.

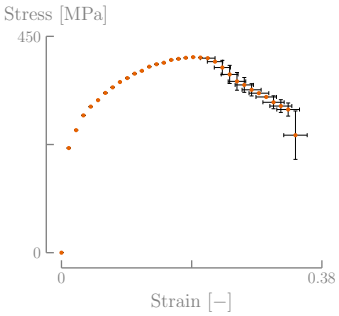

(c) Dispersion at 45°.

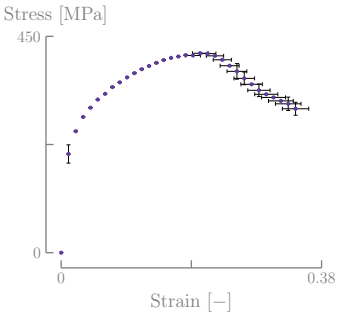

(d) Dispersion at the TD.

Figure 2.22: Stress σ_{11} vs. strain ϵ_{11} plane strain test results showing the average values (Fig. 2.21(a)) and the dispersion in each direction (Fig. 2.21(b), 2.21(c) and 2.21(d)).

Table 2.9: Istra4D parameters for image correlation for the different tests.

Parameter	*Shear*	*Plane strain*
Subset size	13	19
Step size	2	2
Outlier tolerance	low	low
Accuracy (pixel)	0.1	0.1
Residuum (gray values)	20	20
3D Residuum	0.2-0.8	0.4
Contour smoothing	-	ACSP 07x07
Displacement smoothing	-	2.5/−0.5

2.7 Identification of elastic and plastic material parameters

The DC01 steel mechanical characterization comprises:

1. Elasticity parameters (section 2.2.1).
2. Plasticity parameters:
   - Initial yield surface (section 2.2.2).
   - Isotropic hardening (section 2.2.3.1).
   - Kinematic hardening (section 2.2.3.2).

The methodology intends to be sequential but the use of an optimization software requires iterative calculations. The scope here is to identify 4 different set of parameters:

- Two different sets with the isotropic Von Mises yield locus, with and without kinematic hardening.
- Two different sets with the orthotropic Hill, (1948) yield locus, with and without kinematic hardening.

2.7.1 Elastic parameters

2.7.1.1 Stress-strain curve

The apparent elastic modulus is measured at different angles from the RD and is shown in Table 2.10. The average value of the elastic modulus is computed using the following relation:

$$\overline{E} = \frac{E_0 + 2E_{45} + E_{90}}{4} \tag{2.7.1}$$

The Poisson ratio is assumed equal to 0.3. Assuming an isotropic material, it is possible to use Eq. 2.2.2 to find G_s.

Table 2.10: Elastic modulus at different directions.

RD MPa	45° MPa	TD MPa	$\overline{E}$ MPa
$128\,247.2 \pm 1160.9$	$143\,396 \pm 3258$	$140\,355 \pm 7263$	138 848.8

2.7.1.2 Acoustic method

Since the tensile test is performed in a displacement driven fashion it allows little precision to characterize of the elastic zone. Moreover, the value of the elastic modulus computed above are very far from the common accepted value for commercial steel (≈210GPa). Based on this, further tests were perfomed using a

Grindosonic MK-2051 machine with a specimen of dimensions 70 mm × 20 mm. The results are not satisfactory as the thickness of the sheet is too small to obtain results without a large scattering. Hence, $\overline{E}$ =210GPa and ν =0.3 are assumed for this material.

Table 2.11: Elastic modulus from Grindsonic measurements. High dispersion is observed due to the small thickness of the sheet.

Specimen	*Weight* g	*Length* mm	*Thickness* mm	*Width* mm	*Frequency* kHz	*E. modulus* GPa
RD 1	10.8572	70.10	1.0	20.10	1.12	221.22
RD 2	10.8175	70.02	1.0	20.02	1.12	234.31
TD 1	10.8738	70.00	1.0	20.07	1.14	228.91
TD 2	10.7931	70.00	1.0	20.00	1.13	224.02

2.7.2 Optimization methods in plastic material identification

The plasticity equations of section 2.2 involved different material parameters. In principle, identifying these parameters can only rely on analytical relations but this choice is limited to the complexity of the constitutive equations and the desired accuracy. Using an optimization technique can solve this problem by comparing the experimental results and model predictions. In this work two methods are used:

Classical Simulated Annealing (CSA). An iterative global optimization algorithm based on the works of Metropolis et al., (1953) and Hastings, (1970). It distinguishes among different local minima/maxima and thus allowing the parameters space of the objective function to be explored through several possible solutions without being *freezed* in a particular local optimum. More details about this method and its application on yield locus identification can be found in Gilles, (2015).

Inverse method. This method is a gradient optimization technique which involves experimental and numerical results. Given a set of experimental tests (whose results are sensitive to the material parameters) and an initial FE solution (close enough to the real solution), an iterative procedure is then carried on to minimize the error norm of an objective function which is composed by two curves, an experimental one and another obtained from the simulations. The error norm is given by:

$$\text{error norm} = \sqrt{\sum_{i=1}^{N} \left(u_i^{\text{FE}} - u_i^{\text{exp}}\right)^2} \tag{2.7.2}$$

where u_i^{FE} is a point in the FE solution curve, u_i^{exp} is a point in the experimental curve and N is the total number of points to compare. After each iteration

a new set of material parameters is found. In our case, an optimization code called OPTIM (Mathonet, 2003), based on the Levenberg-Marquardt (Levenberg, 1944; Marquardt, 1963) algorithm, is coupled with LAGAMINE to obtain material parameters as schematically represented in Fig. 2.23.

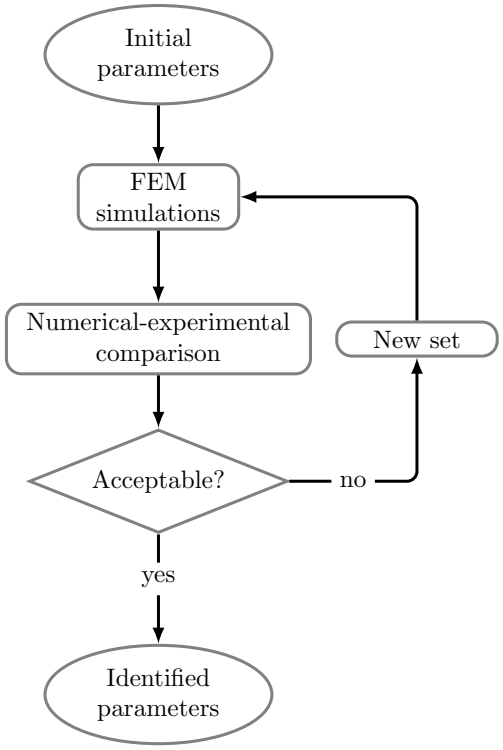

Figure 2.23: Flowchart of the parameter identification using OPTIM and LAGAMINE.

2.7.3 Plastic anisotropic parameters

In this section we discuss the characterization of the anisotropic behavior for the Hill, (1948) yield locus presented in section 2.2.2.

2.7.3.1 Hill, (1948)

There are two different approaches to obtain the Hill, (1948) parameters:

- By taking the initial yield stresses from several tests in different directions (*stress state fitting*, SSF).
- If associated plasticity is assumed (like in this case), the parameters can be found using the anisotropic coefficients (*strain measurements method*, SMM).

In both approaches the relation between experimental results and material parameters involves the theoretical equations defined by the Hill, (1948) yield surface.

For the case of the SSF, the stress in an uniaxial tensile test is given by (Flores, 2005, Eq. 5.40):

$$\sigma_{11} = \sqrt{\frac{2}{(H+G)\cos^4\alpha + (H+F)\sin^4\alpha + 2(N-H)\cos^2\alpha\sin^2\alpha}}\sigma_{Y,\text{ref}} \tag{2.7.3}$$

where α is the angle from the RD and $\sigma_{Y,\text{ref}}$ is the reference yield stress, commonly chosen to be at the RD. For the plane strain tests the stress has the following form (Flores, 2005, Eq. 5.41):

$$\sigma_{11} = \sqrt{\frac{2}{\begin{array}{r}\left[(1-k_\alpha)^2 H + G + k_\alpha^2 F\right]\cos^4\alpha + \left[(1-k_\alpha)^2 H + F + k_\alpha^2 G\right]\sin^4\alpha + \ldots \\ \ldots + \left[N(1-k_\alpha)^2 + k_\alpha(G+F) - (1-k_\alpha)^2 H\right] 2\cos^2\alpha\cos^2\alpha\end{array}}}\sigma_{Y,\text{ref}} \tag{2.7.4}$$

where:

$$k_\alpha = \frac{H + (2N - 4H - G - F)\cos^2\alpha\sin^2\alpha}{(H+G)\sin^4\alpha + (H+F)\cos^4\alpha + 2(N-H)\cos^2\alpha\sin^2\alpha} \tag{2.7.5}$$

For the simple shear test (Flores, 2005, Eq. 5.42), one has:

$$\sigma_{12} = \sqrt{\frac{2}{(4H+G+F)\sin^2 2\alpha + 2N\cos^2 2\alpha}}\sigma_{Y,\text{ref}} \tag{2.7.6}$$

In the case of the SMM, the anisotropic coefficients are given by (Flores, 2005, Eq. 5.11):

$$r_\alpha = \frac{H + (2N - F - G - 4H)\sin^2\alpha\cos^2\alpha}{G\cos^2\alpha + F\sin^2\alpha} \tag{2.7.7}$$

Hence, for eight experimental points there are eight relations (summarized in Table 2.12). Note that in general, and due to experimental constraints when measuring thickness reduction in thin metal sheets, $L = M = N$ can be assumed.

In practice, performing 8 different tests is time consuming so most of the researchers determine the material parameters based on certain assumptions. For the SSF approach, a *necessary and sufficient* condition is to perform 4 tests (tensile tests in the three directions plus a shear test) which is sufficient to obtain the Hill parameters. From Table 2.12, if $\sigma^{\text{UN}}_{Y,\text{RD}}$ is taken as the reference value $\sigma_{Y,\text{ref}}$, the equations become:

$$H + F = 2\left(\frac{\sigma_{Y,\text{ref}}}{\sigma^{\text{UN}}_{Y,\text{TD}}}\right)^2 \tag{2.7.8}$$

$$G + F + 2N = 8\left(\frac{\sigma_{Y,\text{ref}}}{\sigma^{\text{UN}}_{Y,45}}\right)^2 \tag{2.7.9}$$

$$L = M = N = \left(\frac{\sigma_{Y,\text{ref}}}{\sigma^{\text{SH}}_{Y,\text{RD}}}\right)^2 \tag{2.7.10}$$

Table 2.12: Equations relating the yield stress with the Hill, (1948) material parameters (adapted from Flores, 2005). $\sigma_{Y,\text{ref}}$ is the reference yield stress, chosen to be the yield stress of the tensile test at the RD.

Test	*SSF*
Uni-axial tensile RD	$\sigma^{\text{UN}}_{Y,\text{RD}} = \sqrt{\frac{2}{H+G}}\sigma_{Y,\text{ref}}$
Uni-axial tensile TD	$\sigma^{\text{UN}}_{Y,\text{TD}} = \sqrt{\frac{2}{H+F}}\sigma_{Y,\text{ref}}$
Uni-axial tensile 45°	$\sigma^{\text{UN}}_{Y,45} = \sqrt{\frac{8}{2N+G+F}}\sigma_{Y,\text{ref}}$
Plane strain RD	$\sigma^{\text{PS}}_{Y,\text{RD}} = \sqrt{\frac{2}{H(1-k_0)^2+k_Y^2F+G}}\sigma_{Y,\text{ref}}$
Plane strain TD	$\sigma^{\text{PS}}_{Y,\text{TD}} = \sqrt{\frac{2}{H(1-k_{90})^2+F+k_{90}^2G}}\sigma_{Y,\text{ref}}$
Plane strain 45°	$\sigma^{\text{PS}}_{Y,45} = \sqrt{\frac{8}{2N(1-k_{45})^2+(1+k_{45})^2(F+G)}}\sigma_{Y,\text{ref}}$
Simple shear RD	$\sigma^{\text{SH}}_{Y,\text{RD}} = \sqrt{\frac{1}{N}}\sigma_{Y,\text{ref}}$
Simple shear 45°	$\sigma^{\text{SH}}_{Y,45} = \sqrt{\frac{2}{4H+F+G}}\sigma_{Y,\text{ref}}$

$k_0 = \frac{H}{H+F}$, $k_{45} = \frac{2N-G-F}{2N+G+F}$, $k_{90} = \frac{H}{H+G}$

Table 2.13: Equations relating the anisotropic coefficients with the Hill, (1948) material parameters.

Test	*SMM*
Uni-axial tensile RD	$r_0 = H/G$
Uni-axial tensile TD	$r_{90} = H/F$
Uni-axial tensile 45°	$r_{45} = \frac{2N-F-G}{2(F+G)}$

The same applies for the SMM where the Hill, (1948) parameters are readily obtain from Table 2.13:

$$H = \frac{2r_0}{1+r_0} \tag{2.7.11}$$

$$F = \frac{H}{r_{90}} \tag{2.7.12}$$

$$G = \frac{H}{r_0} \tag{2.7.13}$$

$$L = M = N = (F+G)(r_{45}+0.5) \tag{2.7.14}$$

A third way to obtain the Hill parameters is to perform an optimization between SSF and SMM by minimizing the following error function (Flores, 2005, chapter 5):

$$\chi = \sum_{i=1}^{l}(1-\eta)\left(\frac{\sigma_{\text{Y,theo\_}i} - \sigma_{\text{Y,exp\_}i}}{\sigma_{Y,\text{ref}}}\right)^2 + \sum_{i=1}^{m}\eta\left(\frac{r_{\text{theo\_}i} - r_{\text{exp\_}i}}{\overline{r}}\right)^2 \tag{2.7.15}$$

where l is the number of tests performed to obtain stress points, m is the number of tests to obtain anisotropic coefficients, σ_{exp} and r_{exp} are experimental values

of stress and anisotropic coefficients obtained from section 2.4 to 2.6, σ_{theo} and r_{theo} are theoretical values of the stress and anisotropic coefficients obtained from Table 2.12 and Table 2.13. η is a weight factor meaning that η =0.0 retrieves the SSF while η =1.0 retrieves the SMM.

Based on the experimental campaign, Table 2.14 gathers the obtained yield stress at different strain offset using the work-equivalence principle. Note that there is no shear tests performed at 45°, so $\sigma^{\text{SH}}_{Y,\text{RD}} = \sigma^{\text{SH}}_{Y,45}$ is assumed. For each

Table 2.14: Yield stress for different tests performed in the experimental campaign at different strain offsets.

ϵ_0^P	W_0^P	σ_{11}^{UN} RD	σ_{11}^{UN} 45°	σ_{11}^{UN} TD	σ_{11}^{PS} RD	σ_{11}^{PS} 45°	σ_{11}^{PS} TD	σ_{12}^{SH} RD
%	MPa	MPa	MPa	MPa	MPa	MPa	MPa	MPa
0.20	0.422	164.75	177.14	172.52	146.75	155.88	148.63	98.30
0.50	0.943	173.69	185.46	179.51	192.28	193.15	187.07	107.48
0.75	1.397	181.12	192.17	185.42	213.53	210.72	210.88	112.59

strain offset varying η will lead to different Hill coefficients. After several optimizations, it was found that ϵ_0^P =0.50 leads to the most consistent values of predicted yield stress and anisotropic coefficients with the lowest value of error χ. Table 2.15 presents the final set of parameters.

Table 2.15: Hill coefficients obtained by varying the weight of the error function Eq. 2.7.15, using the yield stress at ϵ_0^P =0.50.

	SSF				*SMM*
η	0.0	0.25	0.50	0.75	1.00
H	0.7237	1.4225	1.4660	1.4814	1.4529
F	1.2093	0.8230	0.8103	0.8067	0.7853
G	1.2114	1.0030	0.9927	0.9885	0.9622
N	2.4354	2.9009	2.9246	2.9331	2.8659
χ	1.7872	0.3206	0.3086	0.3070	0.3158

2.7.3.2 Stress and strain directionality

The Hill, (1948) criterion is widely used because of its simple formulation, a relatively easy identification procedure and good predictions for weak anisotropic sheets, which is the case for some steels. Nevertheless, its efficiency depends on the identification procedure leading to different results if choosing the SSF or SMM approach. In order to evaluate the predictions of both methods, the yield stress and the anisotropic coefficients are calculated following the procedure depicted in Fig. 2.24. The results are shown in Fig. 2.25.

As expected, in Fig. 2.25(b) the r-values are well predicted using SMM but the SSF fails showing a very weak planar anisotropy. Conversely, in Fig. 2.25(a)

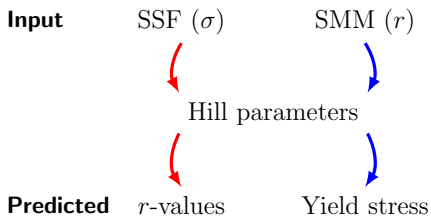

Figure 2.24: Scheme showing the stress and strain directionality analysis to obtain the theoretical yield stress and r-values from the Hill, (1948) parameters.

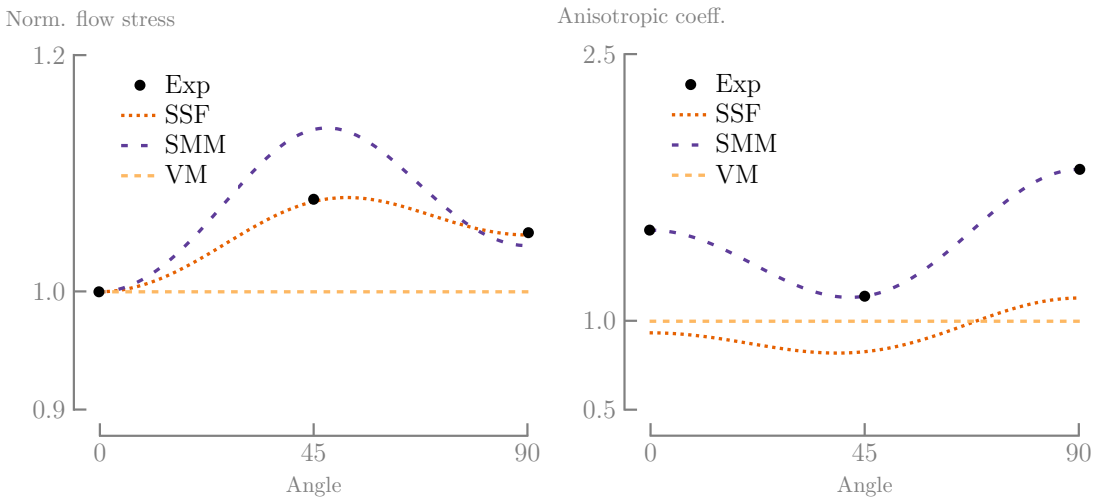

(a) Normalized flow stress $\sigma_{11}/\sigma_{0,\text{ref}}$ for the tensile test.

(b) Anisotropic coefficients.

Figure 2.25: Prediction of anisotropic coefficients and flow stresses by the Hill, (1948) yield surface identified either by SSF or by SMM. SSF has a weak planar anisotropy while SMM has a strong stress directionality.

the normalized yield stress is well predicted using the SSF but the SMM shows a very strong stress directionality. Qualitatively we can observe that the degree of weak planar anisotropy is much stronger than the stress directionality, which explains why in Table 2.15 the SMM is dominant over the SFF when optimizing the Hill coefficients.

These results expose a very well known limitation of the Hill, (1948) model. The initial yield surface is thus dependent on the identification method which is certainly not desired. In order to overcome this issue, several new yield surface models have been proposed, many of them evidently more complex involving several material parameters (thus complex experimental campaigns). Moreover, convexity is not always guaranteed[9]. It is not the goal of the current research to make a deep investigation of the anisotropic characteristics of the DC01 steel

[9]From the numerical standpoint, the yield surface should be convex which implies positive definiteness.

sheet, so these limitations are considered acceptable for sake of simplicity of the material model.

2.7.4 Work hardening

All the work-hardening parameters are found using the inverse method with Optim. A single reduced integration element called `BWD3D` is used because the stress/strain field is assumed homogeneous. The element is detailed in section 6.2. The Hill parameters correspond to η =0.5 of Table 2.15.

2.7.4.1 Isotropic hardening

Material parameters for the Swift (Eq. 2.2.11) and Voce (Eq. 2.2.12) law are fitted using results from the tensile and shear test at the RD. The obtained set of parameters are shown in Table 2.16 and Table 2.17, for the Swift law and Voce law, respectively. Fig. 2.26 compares simulations using the optimization with the experimental tensile test and shear test. In general, the agreement is good with both hardening laws with the sole exception of the tensile test performed at 45° in which the Hill, (1948) parameters are higher than the experimental results. This behavior is expected as shown in section 2.7.3.2, where the SMM predicts higher yield stress at 45° than the SSF.

2.7.4.2 Mixed hardening

As shown in Fig. 2.18, there is a clear Bauschinger effect so a kinematic hardening model should be used. Presence of work-hardening stagnation largely complicates the modeling requiring a large-strain cyclic plasticity model like the ones proposed by Yoshida and Uemori, (2002) and Teodosiu and Hu, (1995) (cf. Flores et al., 2007). These models fall out the scope of this thesis where a precise modeling of kinematic hardening is not needed. The classical A-F model referred in section 2.2.3.2 is used instead.

Obtaining a good set of parameters with this model is not easy as it does not predict stagnation. The optimization with Optim leads to several possible solutions, being some of them unrealistic. Hence, the parameters boundaries and the initial proposed solution should be carefully chosen. The used methodology was to optimize over tensile (RD), shear and Bauschinger (20%) tests, proving to be effective in terms of convergence and accuracy. The obtained set of parameters are shown in Table 2.16 and Table 2.17. Here, compared to the previous results in section 2.7.4.1, the influence of the kinematic hardening parameters over the isotropic hardening parameters (K and n) can be easily observed. The numerical results are depicted in Fig. 2.27. These show how difficult it is for the model to capture work-hardening stagnation. Interesting enough, the results for the tensile test at 45° (Fig. 2.27(b)) using the Hill, (1948) parameters are better predicted than when only using isotropic hardening (Fig. 2.26(b)).

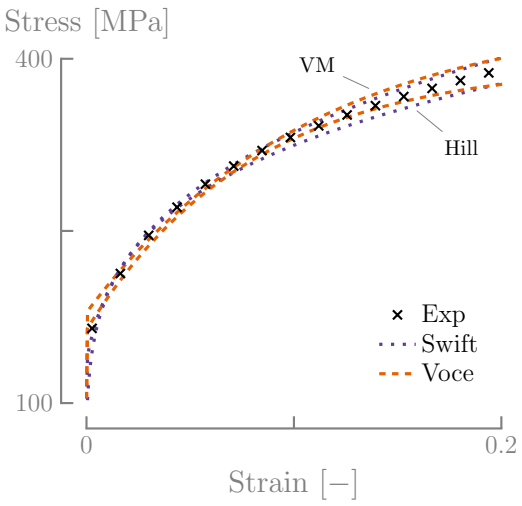

(a) True tensile stress σ_{11} vs. tensile strain ϵ_{11} in the RD.

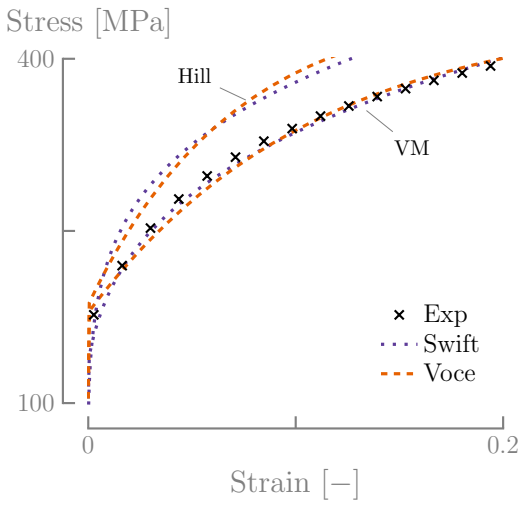

(b) True tensile stress σ_{11} vs. tensile strain ϵ_{11} at 45° from the RD.

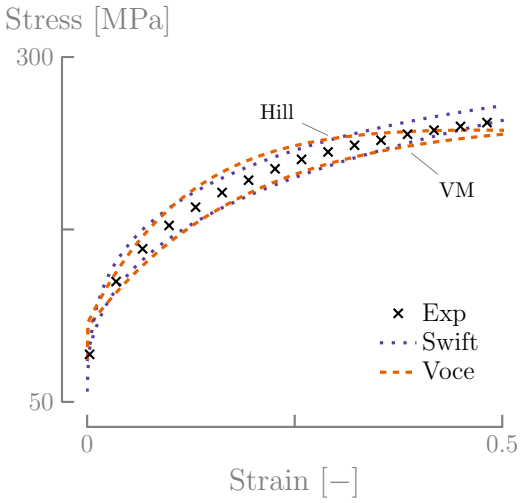

(c) True shear stress σ_{12} vs. shear strain in the RD.

Figure 2.26: Numerical optimization and experimental results comparison using the parameters from Tables 2.16 and 2.17 for pure isotropic hardening.

Table 2.16: Swift law model parameter s obtained using Optim in a tensile, shear and Bauschinger (20%) test. Note how K and n change compared to the pure isotropic hardening parameters.

	Swift		*Swift+A-F*	
Parameter	*Von Mises*	*Hill, (1948)*	*Von Mises*	*Hill, (1948)*
K [MPa]	605.60	601.88	399.48	542.49
ϵ_0	3.34×10^{-3}	9.48×10^{-6}	1.60×10^{-2}	1.78×10^{-2}
n	0.2589	0.2127	0.3712	0.4328
C_X	-	-	78.14	113.63
X_{sat} [MPa]	-	-	109.26	81.96
error	351.43	417.83	268.91	252.59

Table 2.17: Voce law parameters obtained using Optim in a tensile, shear and Bauschinger (20%) test.

	Voce		*Voce+A-F*	
Parameter	*Von Mises*	*Hill, (1948)*	*Von Mises*	*Hill, (1948)*
K [MPa]	259.59	255.03	233.91	264.36
σ_{Y0}	180.01	182.84	110.16	87.02
n	9.42	14.28	4.88	5.69
C_X	-	-	68.13	119.04
X_{sat} [MPa]	-	-	89.85	92.94
error	370.29	419.58	269.92	253.78

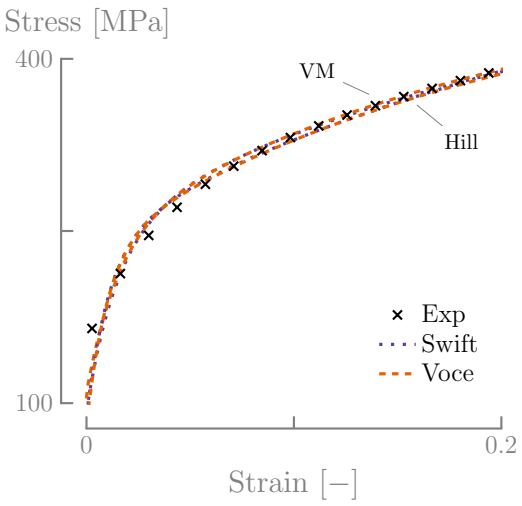

(a) Tensile test in the RD.

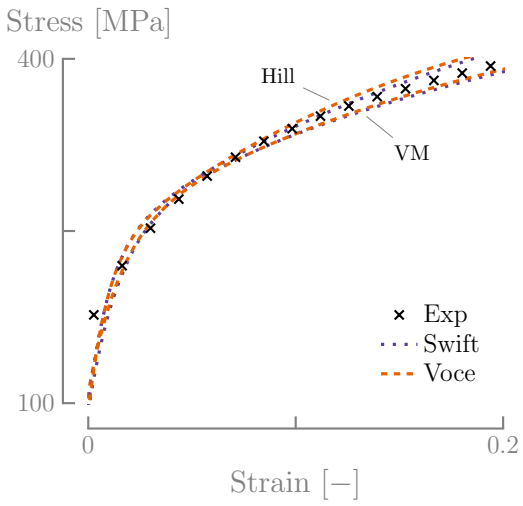

(b) Tensile test in the 45°.

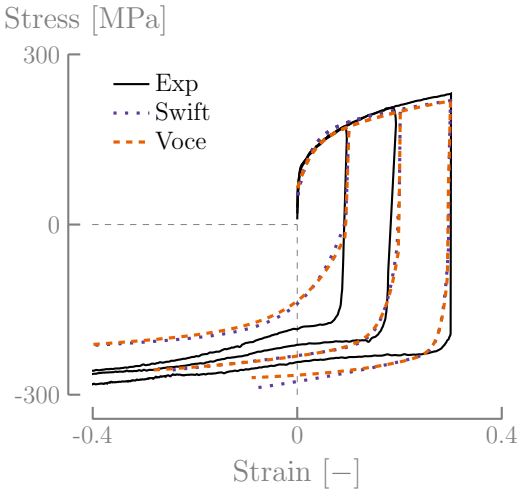

(c) Bauschinger tests for VM set of parameters.

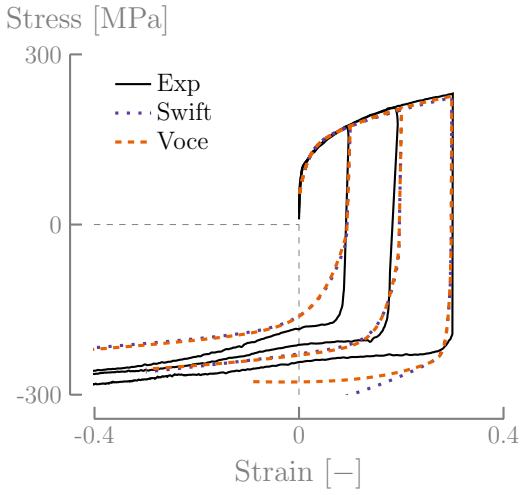

(d) Bauschinger tests for Hill, (1948) set of parameters.

Figure 2.27: Comparison of numerical optimization and experimental results comparison using the parameters from Tables 2.16 and 2.17 including kinematic hardening. Note that the Voce law leads to better results for the Bauschinger test at 30% than the Swift law.

2.8 Conclusions

In this chapter the plastic behavior of a DC01 steel sheet was investigated through mechanical tests and FE simulations. Plastic models including an isotropic (von Mises) and anisotropic (Hill, 1948) yield locus plus isotropic (Swift and Voce law) and kinematic (Armstrong and Fredrick, 1966) hardening were characterized using tensile, shear and plane strain tests at different directions from the RD. The material exhibits an anisotropic behavior at 45° of the RD during the tensile test, but it is isotropic during the plane strain tests. Two optimization algorithms, classical simulated annealing (CSA) and an inverse method, were used to find the Hill, (1948) parameters and strain hardening parameters respectively. The obtained set of parameters are in good agreement with the experimental results.

Chapter 3

About the Gurson model and its extensions

Ductile fracture is usually linked to the evolution of micro-cavities within the material, in the form of nucleation of new voids, growth and eventually coalescence, leading to final failure. In order to understand these physical phenomena, several theoretical developments have been proposed in last 40 years to describe void evolution and the associated macroscopic softening. Between them, we found the Gurson model which couples macroscopic yield criteria with micro-mechanical variables. His efficiency when dealing with mechanisms associated with stress triaxiality and equivalent plastic strain has attracted a great deal of attention. Here we present a concise summary of the Gurson model, giving an historical background and describing some important extensions. Among them, we find the Gurson-Tvergaard-Needleman extension, extensions to shear loads and others involving plastic anisotropy of the matrix and mixed hardening.

3.1 Introduction

The goal of the damage models is the prediction of fracture during forming processes or structural loading after a progressive deterioration of material properties. From all the types of damage (brittle, ductile, creep, fatigue, ...), we are particularly interested in the ductile damage, which is associated with large plastic deformation. The accurate prediction of the ductile fracture is very important because it is related with a damage mechanism that progressively modifies the material properties, after a certain level of plastic deformation. There are two common approaches:

1. *Uncoupled approach*, where the calculation of the rupture follows a criteria which has no effect into the classical constitutive behavior of the material.

2. *Coupled approach*, where the damage development is incorporated into the constitute equation to develop a brand new continuum damage theory with progressive decrease of material properties.

The coupled approach has some advantages over the uncoupled one, such as allowing the prediction of different fracture types and a better characterisation of the fracture zone. Nevertheless, the integration into a finite element code is more difficult than the uncoupled approach. The Gurson model belongs to the coupled approach group, and his strong physical roots has allowed a great increase of its use during the last 30 years.

This chapter is mainly focused in giving a literature review of the Gurson model used in current research. It begins by giving the roots which led to the development of the Gurson model in section 3.2. The model and its classical extensions are detailed in section 3.3. A special type of extensions covering shear loads with the introduction of the third stress invariant, is discussed in section 3.4. Section 3.5 presents two types of extensions of particular importance: anisotropy and mixed hardening in the matrix. Physically based fracture criteria are briefly presented in section 3.6. The chapter ends with some conclusions in section 3.7, regarding the description of each model.

3.2 Historical background

Physical observation regarding ductile fracture phenomena in metals dates back to the sixties (see early references by Garrison and Moody, (1987), Gurson, (1977a), and Rice and Tracey, (1969)), when it became more or less clear that the fracture phenomena in metal involved the generation, growth and coalescence of microscopic voids. Since the early work by Bridgman, (1952), the experimental evidence regarding the effect of the stress state on fracture has been studied by analyzing the effect of the external pressure in the development of plasticity and fracture. One of the main conclusions of this study is that external pressure has a significant effect on damage which leads to failure; eventually, failure can occur with or without damage development depending on the applied external pressure.

Based on these observations, the first micromechanical studies looked for a relation between the void growth and stress/strain fields. The pioneer work of McClintock, (1968) and Rice and Tracey, (1969), both studying the growth of isolated voids gave the first theoretical framework for ductile failure. In this respect, McClintock proposed a model for an isolated cylindrical cavity, where the growth rate is an increasing function of the stress triaxiality ratio[1]. This found that the void expansion increases exponentially with the transverse stress. This work was later extended by Rice and Tracey, (1969), who performed a variational analysis on a single spherical cavity within an infinite perfectly plastic medium under J_2-plasticity. The following evolution equation for the void radius was obtained:

$$\frac{\dot{R}}{R} = 0.283 \exp\left(\frac{1}{2}T\right)\dot{\epsilon}_M^P \tag{3.2.1}$$

Later, Huang, (1991) modified Eq. 3.2.1 based on the evidence (Huang et al., 1991) that the Rice and Tracey, (1969) equation significantly underestimates the

[1] In fact, triaxiality also affects nucleation of new voids (see Benzerga and Leblond, 2010).

dilatation rate of an isolated void subject to stress fields with moderate to high triaxiality. The following correction is proposed:

$$\frac{\dot{R}}{R} = \begin{cases} \alpha_H \exp(\beta_H T)\dot{\epsilon}_M^P & \text{if } T > 1 \\ \alpha_H T^{1/4} \exp(\beta_H T)\dot{\epsilon}_M^P & \text{if } T \leq 1 \end{cases} \tag{3.2.2}$$

choosing $\alpha_H = 0.427$ and $\beta_H = 1.5$. For high triaxiality values the solutions obtained by McClintock, (1968), Rice and Tracey, (1969) and Huang, (1991) are very similar, mainly because void shape effects are negligible at large values of triaxiality. It is interesting to present these results in their original forms as they give a simple relation for void growth. Moreover, these models can be used in post-processing stages of elastic-plastic calculations when using a threshold radius as a failure criteria.

3.3 General description of the Gurson model

The Gurson model is a mathematical representation of ductile damage based on the michromechanics of the material, using the continuum mechanics approach. It comes as a result of applying the homogenization theory in the analysis of the plastic stress field in a microscopic medium composed of a dense matrix and cavities. The model is expressed as a macroscopic yield criterion, introducing a micromechnical variable as its damage parameter: the *void volume fraction*. Herein, a brief explanation of the model and its parameters is presented. There is no intend to give a detailed description. For a more complete presentation of the model, the reader is encouraged to read the review papers of Tvergaard, (1989), Pardoen and Besson, (2004), Besson, (2009), Benzerga and Leblond, (2010) and François et al., (2013).

3.3.1 Gurson, (1977a)

The Gurson, (1975, 1977a) model has its root in the experimental evidence regarding the influence of microvoid growth on plastic deformation and the ductile fracture. Hence, the key feature of this model is the void volume fraction (porosity), which acts as an *imperfection* (Li et al., 2011) during the plastic flow. It is defined by:

$$f = \frac{V_A - V_M}{V_A} \tag{3.3.1}$$

where V_M is the volume of the matrix and V_A is the volume of the cavity and the matrix. One void is surrounded by an isotropic plastic matrix which is incompressible with no hardening (rigid plastic) and no viscosity. The resulting yield locus is shown in Eq. 3.3.2.

$$F_p(\boldsymbol{\sigma}, f, \sigma_Y) = \frac{\sigma_{eq}^2}{\sigma_Y^2} - 1 + \underbrace{2f\cosh\left(\frac{3}{2}\frac{\sigma_m}{\sigma_Y}\right) - f^2}_{\text{Damage}} = 0 \tag{3.3.2}$$

where σ_{eq} is the macroscopic effective stress (matrix plus voids), σ_m is the macroscopic mean (hydrostatic) stress (matrix plus voids) and σ_Y is the flow stress of the dense matrix medium (no voids). It is important to note that when $f = 0$, the Gurson yield locus recovers the classical isotropic von Mises yield locus. The growth of the void is considered by the following equation:

$$\dot{f} = \dot{f}_g = \frac{V_M \dot{V}_A}{V_A^2} = (1 - f)\, tr\dot{\boldsymbol{\epsilon}}^p \tag{3.3.3}$$

This equation comes from the apparent volume change, mass conservation and plastic incompressibility of the matrix, derived from Eq. 3.3.1.

In its original form, the Gurson model does not take into account the plastic anisotropy, mixed hardening of the dense matrix, appearance of new voids, coalescence leading to the crack and other phenomena involved in ductile fracture. Moreover, the voids are considered spherical or confined into a infinite cylinder, which is certainly a strict hypothesis. Even if by definition of the yield locus the macroscopic media is compressible (I_1-*dependent*), the fully dense matrix surrounding the voids is in fact incompressible, being governed by a J_2-flow theory. For these and other reasons, numerous extensions have been proposed in the literature.

3.3.2 Gurson-Tvergaard-Needleman extension

Several extensions have been introduced into original Gurson model and among them, the Gurson-Tvergaard-Needleman (hereafter called GTN model) is one of the first to robustly compile the three stages of damage development: void nucleation, growth and coalescence. In the following section, a brief description[2] of each of these mechanisms and the equations involved are presented.

3.3.2.1 Void nucleation

Within the nucleation of new microscopic voids, two main mechanisms are often found (Benzerga and Leblond, 2010; Tvergaard, 1989):

- Decohesion (debonding) of matrix-inclusion or matrix-second phase interfaces.
- Hard particle fracture.

They can be separately observed or as combination of both, since there are parameters favoring one or the other (see Fig. 3.1). A summary of these parameters can be found in Garrison and Moody, (1987) and Benzerga and Leblond, (2010). As a general rule, nucleation results from inhomogeneity of the plastic deformation between the matrix and the inclusions (Pineau, 2004). Sometimes nucleation is stress controlled and in other cases it is strain controlled. This is because of the energy condition for the separation of the interfaces can be met both by plastic

[2]No micromechanical models or cell studies are presented for the sake of simplicity. Refer to the reviewing papers for a more complete presentation of the topic.

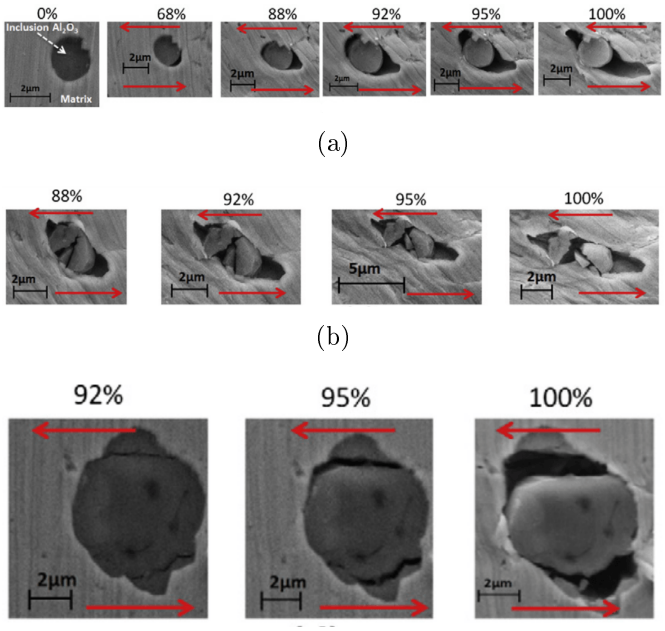

Figure 3.1: SEM images of different types of nucleation in a high-strength low-alloy steel. The percentages of displacement at fracture and the load direction (red arrows) are also depicted (Achouri et al., 2013).

deformation accumulation or stress applied to the interface. Nevertheless, the formulation of an adequate condition for void nucleation by interface fracture is difficult to obtain and usually another approach is used (François et al., 2013). This *continuum* approach will be described below.

Assuming that nucleation is a mechanism that is not linked with void growth[3], the total porosity can be decomposed in nucleated and growth parts (Gurson, 1977b):

$$\dot{f} = \dot{f}_g + \dot{f}_n \tag{3.3.4}$$

where f_n is the nucleated void volume fraction and f_g was already described in Eq. 3.3.3. Voids are also assumed to grow as spherical cavities once they nucleate. It is important to highlight that this assumption is more appropriate for particle debonding rather than particle fracture (Chu and Needleman, 1980). Nucleation can be correlated in terms of the equivalent plastic strain in the matrix, the equivalent stress or both. Needleman and Rice, (1978) proposed the following form:

$$\dot{f}_n = \underbrace{\mathcal{A}\dot{\epsilon}_M^P}_{\text{Strain}} + \underbrace{\mathcal{B}\left(\dot{\sigma}_{eq} + c\dot{\sigma}_M\right)}_{\text{Stress}} \tag{3.3.5}$$

with $\dot{\sigma}_{eq} + c\dot{\sigma}_M > 0$, c is a parameter adjusted by cell computations and ϵ_M^P equivalent (effective) plastic strain in the matrix. Later, Chu and Needleman, (1980) proposed a normal distribution for $\mathcal{A}$ to represent the nucleation phenomenon

[3]An assumption that has a micromechanical root (Benzerga and Leblond, 2010).

heterogeneity:

$$\mathcal{A}(\epsilon_M^P) = \frac{f_N}{S_N\sqrt{2\pi}} \exp\left[-\frac{1}{2}\left(\frac{\epsilon_M^P - \epsilon_N}{S_N}\right)^2\right]$$
$$\mathcal{B}(\boldsymbol{\sigma}) = 0 \tag{3.3.6}$$

where f_N is the maximum potential nucleated void volume fraction in relation with the inclusion volume fraction, ϵ_N is the mean effective plastic strain of the matrix at incipient nucleation and S_N is the Gaussian standard deviation of the normal distribution inclusions. To understand the meaning of each variable, refer to Fig. 3.2. The range over which the voids nucleate is controlled by S_N, while

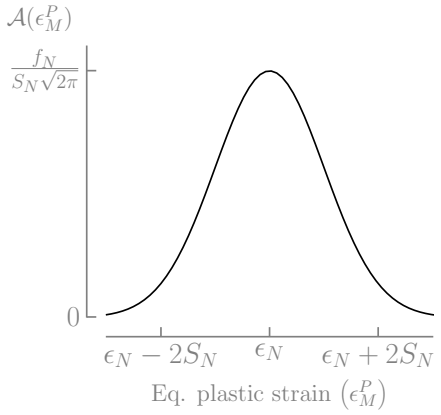

Figure 3.2: Distribution function for the nucleation law (Chu and Needleman, 1980).

ϵ_N determines the strain at which 50% of the inclusions are broken. As for f_N, the volume fraction which may nucleate is given by:

$$f_N = \int_{-\infty}^{\infty} \mathcal{A}\left(\epsilon_M^P\right) d\epsilon_M^P \tag{3.3.7}$$

which corresponds to the area under the curve in Fig. 3.2.

Many researches are based on nucleation models of the strain-based type as shown in Eq. 3.3.5 and Eq. 3.3.6 (e.g., Aravas, 1987; Besson, 2009; Dunand and Mohr, 2011a; Mühlich and Brocks, 2003), which is independent of the flow stress (Lievers et al., 2004)[4]. Stress controlled nucleation models are not often used because they are harder to implement numerically (François et al., 2013).

3.3.2.2 Void coalescence

In this phenomenon we can distinguish three different behaviors, sorted in chronological order of observations within the literature (viz., Benzerga and Leblond, 2010; Garrison and Moody, 1987):

[4]This can be helpful for large deformations laying beyond the tensile test fitting.

- Internal necking: the growth of the voids is large enough to create a neck in the space between cavities. Often observed at high stress triaxialities.
- Void sheeting: due to the formation of a secondary population of voids on small particles, creating shear bands. Dominant at low stress triaxialities.
- Necklace: due to formation of voided columns, prominent in steel containing elongated MnS inclusions (Benzerga, 2000) and favored at low triaxiality level.

Internal necking was studied by Thomason, (1968, 1993) based on limit-load analysis of the ligament between voids. Void sheeting was first described by Brown and Embury, (1973), in where it was observed that a 45° band can be formed when the distance between voids is approximately equal to their height. With the exception of the third mode, failure by internal necking or void sheeting seems to be mainly dependent on the stress triaxiality and the microstructure, but also on the void distribution (Weck and Wilkinson, 2008).

At the macroscopic level, the coalescence can be easily observed in a load-displacement curve after an abrupt change in the slope at the onset of a (macroscopic) crack, then descending as the crack propagates. According to the original Gurson, (1977a) model, loss of material stress carrying capacity occurs when the voids have grown so large that the Gurson yield surface becomes a point in the stress space i.e., $f_u = \frac{1}{q_1}$. Nevertheless, the experimental evidence shows that the material failure happens earlier. Indeed, experimental evidence by Brown and Embury, (1973) and Goods and Brown, (1979) revealed that coalescence between neighboring voids occurs when their length has grown to the order of magnitude of their spacing (Tvergaard and Needleman, 1984). The reason for this is that only an homogeneous deformation mode was considered when deriving the Gurson model.

Hence, and in order to incorporate coalescence into the Gurson model, Tvergaard and Needleman, (1984) proposed to modify the porosity evolution not as an additive part (like Eq. 3.3.4 or as in Tvergaard, (1982)), but as a specific coalescence function f^*, which replaces the porosity in the following way:

$$f^* = \begin{cases} f & \text{if } f < f_{cr} \\ f_{cr} + K_f(f - f_{cr}) & \text{if } f > f_{cr} \end{cases} \tag{3.3.8}$$

$$K_f = \frac{f_u - f_{cr}}{f_F - f_{cr}} \tag{3.3.9}$$

where f_u is the ultimate value of f^* at the occurrence of ductile rupture, f_{cr} is the critical void volume fraction at the onset of coalescence and f_F is the porosity at final failure. The relation between f and f^* is schematically shown in Fig. 3.3(a). The aim of f^* is to model the complete vanishing of the carrying stress capacity due to void coalescence. Both q_1, q_2 (correction factors described in section 3.3.2.3) and f^* allows recovering results from a mesoscopic approach near rupture. In their original research, Brown and Embury proposed a simple failure condition based on the distance between voids, obtaining $f_{cr} \approx 0.15$.

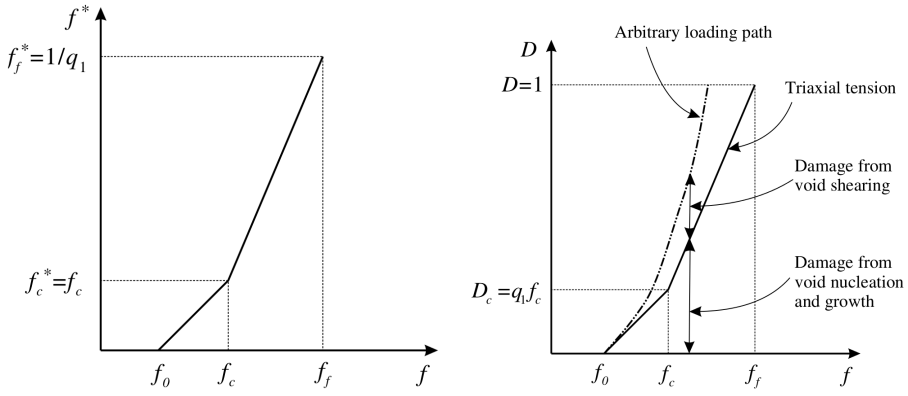

(a) GTN model. (b) Xue, (2008).

Figure 3.3: The effective porosity as function of the porosity as in Eq. 3.3.8 in both the GTN model and the shear extension by Xue, (2008). Taken from Xue, (2008).

Coalescence is associated to mechanisms of plastic flow localization[5] within the matrix, which is certainly harder to capture compared to diffuse plastic flow during void growth. For a detailed discussion of coalescence models and their physical roots, see Garrison and Moody, (1987) or Benzerga and Leblond, (2010).

3.3.2.3 Correction factors

Tvergaard, (1981) introduced the factors q_1 and q_2 (and a third one $q_3 = {q_1}^2$) to describe more accurately void growth kinematic assessed in unit cell calculations. A modified version of Eq. 3.3.2 is thus obtained:

$$F_p(\boldsymbol{\sigma}, f, \sigma_Y) = \frac{\sigma_{eq}^2}{\sigma_Y^2} - 1 + 2q_1 f \cosh\left(-\frac{3q_2}{2}\frac{\sigma_m}{\sigma_Y}\right) - q_3 f^2 = 0 \tag{3.3.10}$$

The original Gurson model gives too large localization strains if q_1 =1.0. Nevertheless, using a value of q_1 =1.5 allows the continuum model to be in good agreement with the localization strain for the cell analysis carried on by Tvergaard, (1981).

Some authors claim, wrongly motivated from these previous results, that q_1 and q_2 are parameters accounting for the void shape or the interactions between voids. The evidence, in this regard, is sparse and it is more likely that these parameters reflect the inner imperfections of the model (Benzerga and Leblond, 2010). For instance, cell analysis by Koplik and Needleman, (1988) and Gao et al., (1998) have shown that both parameters vary with the geometry and loading conditions. Faleskog et al., (1998) showed that these parameters also depend on the plastic hardening exponent and the ratio of the yield stress over the Young modulus. Ben Bettaieb et al., (2011b) mathematically demonstrated that fixing q_2 lead to an inconsistency with the volume conservation hypothesis of the dense matrix material. So, q_2 is integrated as a state variable with an evolution equation

[5]These mechanisms involve, for instance, void growth or void interactions.

which verifies this volume conservation. This type of inconsistency would be the price to pay for a simple model. However one can consider the volume conservation problem as equivalent as assuming that the void is an empty space where no inclusion is in the inside.

3.4 Shear extensions

The effect of stress invariants on the mechanical behavior of materials dates back with the first J_2-plasticity models developed in the early 20th century to describe yielding of metals. The mean stress was later included to describe porous media subjected to hydrostatic pressure (Drucker and Prager, 1952). Nevertheless, the study of the third invariant of the deviatoric stress is quite recent and it was mainly used in the civil engineering field. For instance, Bardet, (1990) studied the influence of the Lode angle over the yield surface of pressure insensitive materials.

The approach for ductile fracture has followed a different way. The effect of the mean stress in damage development and fracture is very well established and numerous studies exist. Nevertheless, the importance of the third invariant appeared when studying phenomena involving low triaxiality levels[6], such as metal forming processes. Some researchers have included these invariants into more general modified plasticity models to predict localization (Brünig et al., 2000) and fracture (Bai and Wierzbicki, 2008). The inherent complexity of damage phenomena hinder, even for a simple tensile test, distinguish between the softening induced by suppression of the dislocation motion and the softening due to porosity (Bai and Wierzbicki, 2008). In the following section, the effect of the Lode angle on plastic yield is not reviewed, and damage and fracture are considered to be mainly dependent on the nucleation, growth and coalescence of voids. The Lode angle and its definitions are introduced in annex A.

3.4.1 Developments

Since its formulation, the Gurson, (1977a) model and the GTN extension assumes that the voids are spherical during the deformation. Also, these models only include the triaxiality as the parameter describing the stress state. As mentioned by Pardoen, (2006), this historical view maybe come from the analysis of *crack-tip* problems, which are characterized by large stress triaxiality values, in which shape effects are usually not important. Nevertheless, one of the limitations of using only triaxiality and spherical voids became apparent when Gologanu et al., (1996) observed that the void expansion can vary in different directions under the same triaxiality. Following this point, Zhang et al., (2001) made a 3D numerical analysis of a spherical void to look for the influence of the Lode parameter into the directional expansion of the void. He considered a cubic cell, where the displacements at the boundaries were calculated from given values of triaxiality and Lode parameters. It was observed that both the deformation pattern of the void and the void volume fraction are influenced by the Lode parameter (Fig. 3.4).

[6]Usually, low triaxiality means $T < 1/3$.

Another interesting observation is that the influence of the Lode parameter seems to diminish with increasing triaxiality.

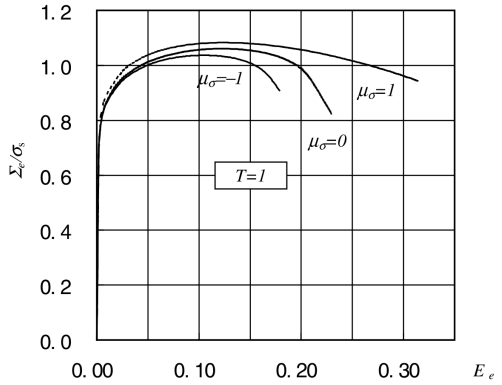

Figure 3.4: Equivalent stress-strain curves for different values of the Lode parameter (Zhang et al., 2001). If the triaxiality is kept constant, the load carrying capacity is inversely proportional to the Lode parameter.

Dealing with low values of triaxiality stress states could be problematic in the Gurson model. In some cases, like in shear-dominated deformations, triaxiality is near zero or even negative (Nahshon and Hutchinson, 2008) predicting almost no increase of damage (in the GTN extension of the Gurson model voids do not grow under pure shear). Pardoen, (2006) studies the effect of the void shape at low triaxiality, mentioning that the void elongates in the direction of maximum strain. By using a modified version of the Gurson model, which considers growth, coalescence of *spheroidal*[7] voids and void's aspect ratio [8], it is confirmed that shape effects on coalescence are significant, as in Fig. 3.5. **Barsoum2007b**; Barsoum and Faleskog, (2007) analysed the rupture mechanism of a mid and high strength steel in double notched axisymmetric specimens, subjected to combined tension and torsion. They found that when triaxiality is high, the specimens fail by *internal necking*, while for low triaxiality the crack is due to *plastic shear localization* (commonly referred to as *shear bands*). These two coalescense mechanisms were previously described by Pardoen and Brechet, (2004) and Bron and Besson, (2006) and they are shown in Fig. 3.6. At medium levels of triaxiality, these mechanisms may cooperate or even compete. **Barsoum2007b** performed a micromechanical study for an array of cells to investigate the transition between these two mechanisms. By using this approach, the array of voids can be seen as an initial imperfection inducing internal necking, shear localization or both, as in Fig. 3.7. The strain localization decreases when passing from tension to shear, and the softening rates decreases when increasing the Lode parameter. Gao et al., (2009) performed both experimental tests and micro-mechanics analyses in order to demonstrate that the Lode angle has an important effect on ductile fracture.

[7] Obtained by rotating an ellipse about one of its principal axes.

[8] Defined as the ratio between the diameter in the longitudinal direction and the diameter in the transverse direction.

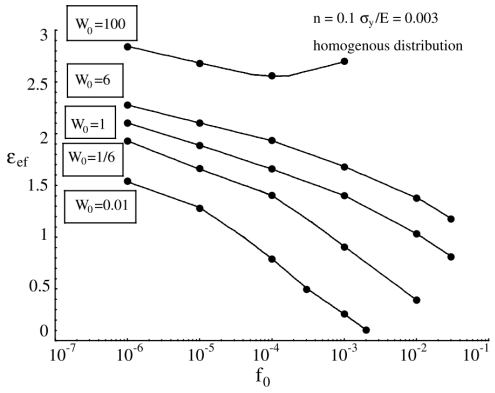

Figure 3.5: Influence of the initial void aspect ratio (W_0) in ductility (strain at fracture, ϵ_{ef}) vs. initial porosity f_0 of an ideal material (Pardoen, 2006). The two limiting cases, $W_0 \to 0$ and $W_0 \to \infty$ correspond, when $f_0 \to 0$, to the penny-shape crack and the infinitely thin needle, respectively, and, when the porosity is kept constant, to a *sandwich* and the infinitely long hollow cylinder, respectively (Pardoen and Hutchinson, 2000).

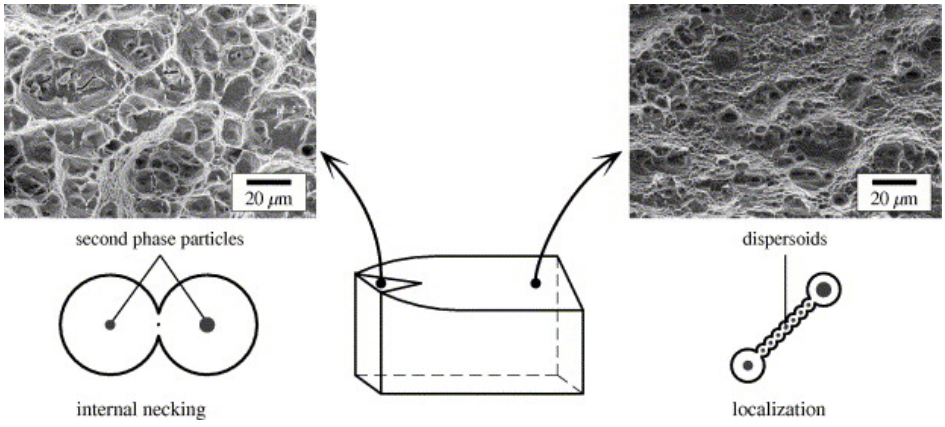

Figure 3.6: Two coalescence mechanisms (Bron and Besson, 2006). The internal necking of voids is dominant at high values of triaxiality, while the second characterised as a second population of voids (dispersoids or secondary dimples) that appeared between the primary voids, is dominant at low values.

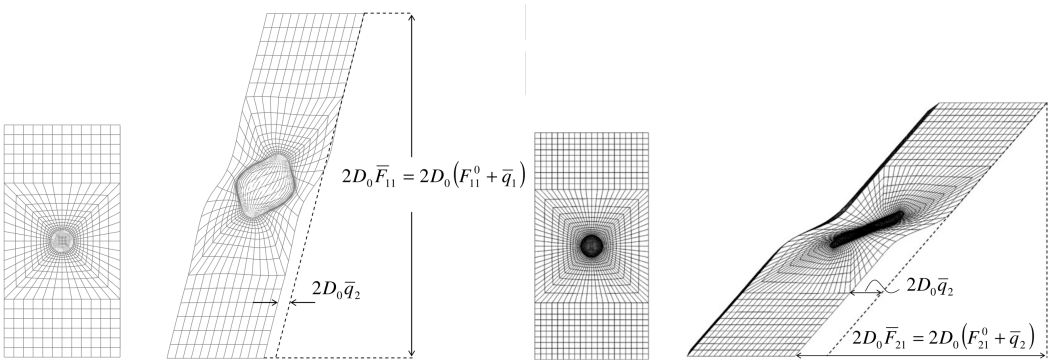

(a) Internal necking ($\mu_\sigma = -0.85$, $T = 1.0$). (b) Shear localization ($\mu_\sigma = -0.15$, $T = 0.5$).

Figure 3.7: Void coalescence mechanisms under different values of triaxiality and Lode parameter (**Barsoum2007b**). Internal necking arises at high values of triaxiality while shar localization appears at low values of triaxiality.

Prescribed boundary conditions are imposed to keep both the triaxiality or the Lode angle constant (similar as in Zhang et al., (2001)). Failure is assumed to happen when localization of plastic flow takes place in the inter-void ligament (uniaxial straining mode) (Koplik and Needleman, 1988). Fig. 3.8(a) shows that the Lode parameter has an important effect on the strain at coalescence and this effect is lower at high triaxiality, coinciding with the previous results from Zhang et al., (2001). Gao et al., (2009) also studied the effect of secondary voids, showing in Fig. 3.8(b) that the nucleation of secondary voids notables reduce the ductility of the material, but also reduce the effect of the Lode angle at low triaxiality.

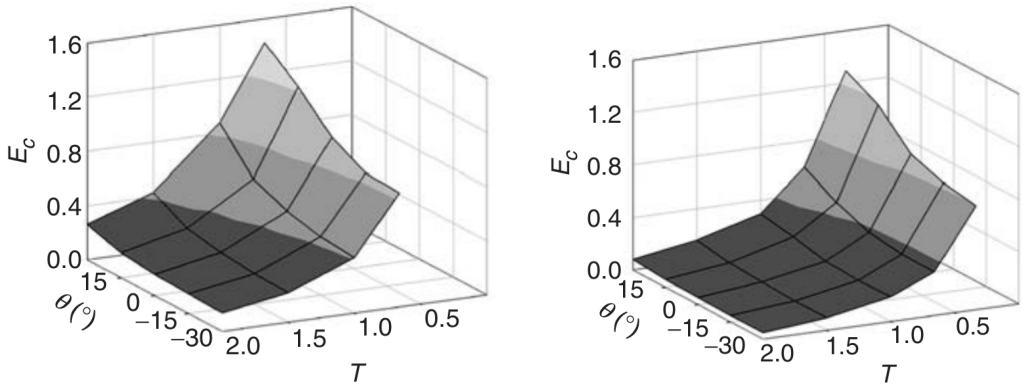

(a) Without secondary voids. (b) With secondary voids.

Figure 3.8: Strain at localization (E_c) as a function of the triaxiality (T) and the Lode angle (θ) (Gao et al., 2009). Note that the effect of the Lode parameter on ductility is higher at low values of triaxiality, but this effects diminish when considering the effect of nucleation of secondary voids.

Hereafter, a description is presented of the shear extensions implemented in the

Gurson/GTN model, based on the effect of the third invariant. It must be noted that like the coalescence extension, shear extensions are purely phenomenological and thus the *void porosity* loses its original meaning to a more general damage representation. Note that the Lode angle definition varies among authors, which are defined and compared in Annex A.

3.4.2 Xue, (2008)

The first shear extension of the Gurson model was developed by Xue, (2008) (cf. Xue, 2012), based on the void-shearing damage criterion from McClintock et al., (1966). In this criterion, void linkage occurs when a critical distance (void spacing in the shear direction) is reached. As pointed out by Xue, (2008), rotation of voids does not change the void volume fraction but damage is indeed happening. This can be seen in Fig. 3.9, where two different coalescence mechanisms are depicted.

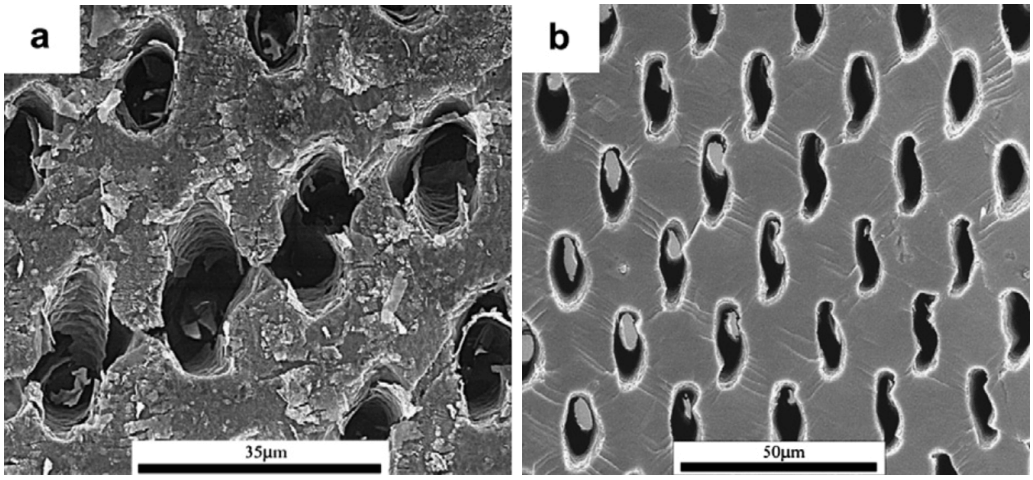

(a) Intervoid ligament. (b) Shear band formation.

Figure 3.9: Two different coalescence mechanisms (Weck et al., 2006).

In the Xue, (2008) extension, it is first recognized the phenomenological nature of the GTN model at coalescence, which replaces the void volume fraction by an *effective porosity*. The shear extension expands this concept by introducing a damage variable D, incorporating the effect of shear. In a broad way, the damage variable includes the effect of the third invariant of the deviatoric stress, thus considering stress states other than the axisymmetric case. The yield surface equation is written in terms of the damage variable D:

$$F_p(\boldsymbol{\sigma}, \sigma_Y, D) = \frac{\sigma_{eq}^2}{\sigma_Y^2} - 1 + 2D\cosh\left(-\frac{3q_2}{2}\frac{\sigma_m}{\sigma_Y}\right) - D^2 = 0 \tag{3.4.1}$$

with the trivial relation $D = q_1 f^*$. The related evolution equation for D:

$$\dot{D} = K_f\left(q_1\dot{f} + \dot{D}_{\text{shear}}\right) \tag{3.4.2}$$

where:

$$\dot{D}_{\text{shear}} = k_g f^{1/3} g_\theta(\boldsymbol{\sigma}) \epsilon_{eq} \dot{\epsilon}_{eq} \tag{3.4.3}$$

is the contribution due to shear. g_θ is a scalar stress function defined by:

$$g_\theta(\boldsymbol{\sigma}) = \frac{2}{\pi} \arccos \chi(\boldsymbol{\sigma}); \qquad \chi(\boldsymbol{\sigma}) = \frac{27}{2} \frac{J_3}{\sigma_{eq}^3}; \qquad 0 \leq g_\theta \leq 1$$

Coalescence is introduced through the term K_f:

$$K_f = \begin{cases} 1 & \text{if } D < D_{cr} \\ \frac{1/q_1 - f_{cr}}{f_F - f_{cr}} & \text{if } D > D_{cr} \end{cases} \tag{3.4.4}$$

which is slightly different from Eq. 3.3.8 in the GTN model, as can be seen in Fig. 3.3(b). In this formulation, k_g is material dependent. The nature of k_g is not further explored within Xue, (2008), but it seems to be material dependant.

3.4.3 Nahshon and Hutchinson, (2008)

Almost simultaneously, Nahshon and Hutchinson, (2008) proposed a different shear extension of the Gurson model. It seems that they were encouraged by the influence of the Lode angle in ductile fracture. The experimental evidence demonstrates that void distorsion and inter-void interaction give raise to shear softening and localization, which the GTN model is not able to capture. Under shearing, the voids increase their effective collective cross-sectional area parallel to the localization band without increasing the porosity. Hence, softening and then localization is expected solely due to deformation and rotation of voids.

The modification proposed by Nahshon and Hutchinson, (2008) only involves the void growth relation. Hence, the void evolution (without nucleation) is governed by the following equation:

$$\dot{f} = \dot{f}_g + \dot{f}_s$$

where:

$$\dot{f}_s = k_\omega f \omega(\boldsymbol{\sigma}) \frac{\widetilde{\boldsymbol{\sigma}}_{\text{dev}} : \dot{\boldsymbol{\epsilon}}^P}{\widetilde{q}} \tag{3.4.5}$$

k_ω is a material constant and $\omega(\boldsymbol{\sigma})$ a stress scalar function defined as:

$$\omega(\boldsymbol{\sigma}) = 1 - \chi(\boldsymbol{\sigma})^2 = 1 - \left(\frac{27}{2} \frac{J_3}{\sigma_{eq}} \right)^2; \qquad 0 \leq \omega \leq 1 \tag{3.4.6}$$

In Nielsen and Tvergaard, (2009, 2010) it has been noted the strong contribution of $\dot{f}_s$ in plane strain uni-axial tension, even if the triaxiality is high. As mentioned by the authors, the GTN model by itself is already a solid approach to deal with void based ductile damaging, so there is no need to add the shear contribution at this level. Moreover, in Nielsen and Tvergaard, (2010) the original model from Nahshon and Hutchinson, (2008) it is compared with micro-mechanical cell studies, leading to an earlier localization prediction. Hence, a triaxiality dependent

weight function $\Omega(T)$ is proposed. In Eq. 3.4.5, $\omega(\boldsymbol{\sigma})$ is replaced by ω_0 defined as:

$$\omega_0 := \omega(\boldsymbol{\sigma})\Omega(T) \tag{3.4.7}$$

whre $\Omega(T)$ is a function which linearly decreases depending on the triaxiality:

$$\Omega(T) = \begin{cases} 1 & \text{if } T < T_1 \\ (T - T_2)/(T_1 - T_2) & \text{if } T_1 \leq T \leq T_2 \\ 0 & \text{if } T > T_2 \end{cases} \tag{3.4.8}$$

3.5 Anisotropic plasticity and mixed hardening within the Gurson model

The original Gurson model is based in a development where the matrix surrounding the void is perfectly plasticity and obeying to von Mises type of yield criterion. This section present two important extensions covering anisotropy and mixed hardening in the matrix.

3.5.1 Anisotropy

Benzerga and Besson, (2001) incorporated anisotropy into the Gurson, (1977a) and the GTN model. Based on experimental evidence regarding the effect of matrix flow on particle debonding (and hence in void evolution), the main motivations behind this extension were:

- The inhomogenity of the matrix affecting void evolution and interaction.
- The practical problem observed in metal forming, in particular rolled sheets, where the strain at fracture can vary in a significant degree.

The approach considered the complete derivation of the (original) Gurson, (1977b) model for a hollow sphere and a hollow cylinder in the case of an orthotropic matrix, obeying the Hill, (1948) criteria.

It is shown in Benzerga and Besson, (2001, Eq. 32) that using the flow rule and the matrix incompressibility:

$$\frac{\dot{f}}{1-f} = \frac{\dfrac{\partial F_p}{\partial \sigma_m}}{\dfrac{\partial F_p}{\partial \sigma_{eq}}} \dot{\boldsymbol{\epsilon}}^P_{eq} \tag{3.5.1}$$

In this relation is evident that porosity rate is affected by plastic anisotropy, as plastic anisotropy appears both in $\dot{\boldsymbol{\epsilon}}^P_{eq}$ and σ_{eq}. Following an homogenization procedure using the Gurson, (1977a) approach, and later extended in the GTN model fashion[9], the following yield surface is obtained:

$$F_p(\boldsymbol{\sigma}, f, \sigma_Y) = \frac{\sigma^2_{eq}}{\sigma^2_Y} - 1 + 2q_1 f \cosh\left(-\frac{3\sigma_m}{\kappa\sigma_Y}\right) - q_3 f^2 = 0 \tag{3.5.2}$$

[9] With correction factors, strain hardening, etc.

which is the same as Eq. 3.3.2 but incorporates the effect of the anisotropy through σ_{eq} and κ.

It is remarked by the authors, that a so-called *scalar effect* and a *directional effect* are observed after the implementation. As for the scalar effect, it is clear from Eq. 3.5.1 that the evolution of damage is dependent on the anisotropy. An explicit relation is given in terms of the *anisotropy factor* κ, where $\kappa = 2$ stands for the isotropic Gurson/GTN model. Larger values of κ increase the porosity rate while lower values of κ decrease it. It is worth mentioning that due to the hyperbolic cosine in the GTN model, a small change on κ can induce notable change on the porosity evolution. Moreover, it is shown (Benzerga and Besson, 2001, section 7.1) that the value of κ is mainly determined by the *shear* Hill, (1948) coefficients (L, M and N). Unfortunately, these parameters are hard to obtain in thin sheets due to practical limitations.

This *scalar effect* (evolution of f) has of course, no relation with the observed damage anisotropy. In fact, damage induced anisotropy arises from the plastic anisotropy (*directional effect*), depending on the loading direction (Benzerga and Besson, 2001, section 6.2). Contrary to the *scalar effect*, in this case the *normal* Hill, (1948) coefficients (F, G and H) have more impact in the *directional effect* than the *shear* coefficients.

3.5.2 Mixed hardening

Originally, the Gurson, (1977a) model considered a perfectly plastic matrix, i.e. $\sigma_Y = \sigma_0$. In order to introduce an isotropic hardening, it is widely accepted that an evolution law like Swift or Voce can be used for the matrix and also within the cosine term of the Gurson, (1977a) yield function. For instance, taking the Swift law:

$$\sigma_Y = K\left(\epsilon_0 + \epsilon_M^P\right)^n \tag{3.5.3}$$

where ϵ_M^P is the equivalent plastic strain in the matrix. Nevertheless, Leblond et al., (1995) showed that incompatibilities can arise between model predictions and the analytical development by Gurson in the hollow sphere, when using this function in both the matrix and the yield surface. It is then proposed to replace σ_Y in the yield surface (Eq. 3.3.10) by two functions $\Sigma_1 = \Sigma_1(\epsilon_{eq}^P)$ and $\Sigma_2 = \Sigma_2(\epsilon_{eq}^P)$:

$$F_p(\boldsymbol{\sigma}, f, \sigma_Y) = \frac{\sigma_{eq}^2}{\Sigma_1^2} - 1 + 2q_1 f \cosh\left(-\frac{3q_2}{2}\frac{\sigma_m}{\Sigma_2}\right) - q_3 f^2 = 0 \tag{3.5.4}$$

which are nonetheless dependent only on the macroscopic plastic strain ϵ_{eq}^P and not in the equivalent plastic strain in the matrix ϵ_M^P, like Eq. 3.5.3. It is found that this new relation allows a better representation of the macroscopic hydrostatic stress-strain curve, which is however less significant when comparing the von Mises equivalent stress-strain curve. The expressions for functions Σ_1 and Σ_2 are more complex than Eq. 3.5.3 but, in terms of the integration of these equations into a FE code, using ϵ_{eq}^P instead of ϵ_M^P can reduce the number of equations to integrate.

In the other side, a kinematic hardening extension to the Gurson model is not commonly found in the literature, despite the clear effects of kinematic hardening on localization (see Tvergaard, 1989, section VII). This is probably due

to cumbersome derivatives arising when including the *backstress* term into the equations involving the stress. Anyway, there is no special development problems regarding kinematic hardening and classical evolution equations like Armstrong and Fredrick, (1966) have been used within the Gurson model family (Arndt et al., 1997; Ben Bettaieb et al., 2011c; Mühlich and Brocks, 2003).

3.6 Physically based extensions

The so-called physical models represent the evolution of voids based on physical (or direct) observation of voids within a material. Once they are integrated into the Gurson model, the nucleation and growth mechanisms are governed by equations fitted by experiments. Without the need to rely on the matrix plastic incompressibility to model the growth stage (Fansi et al., 2013), as is the case of the original void growth relation (Eq. 3.3.3).

3.6.1 Ben Bettaieb et al., (2011b)

From 3D X-ray tomography, two evolution laws for nucleation and growth of dual-phase (DP) steel were developed. Both evolution rules depend on the equivalent plastic strain and the triaxiality factor. These parameters were chosen because they can be measured from an experimental campaign. The nucleation criterion was initially proposed by Helbert et al., (1998) for biphasic titanium and later adapted to DP steels by Bouaziz et al., (2008) and Maire et al., (2008):

$$N = A_B \left(\frac{\epsilon_{eq}^P}{\epsilon_N} \right) \exp \left(\frac{\epsilon_{eq}^P}{\epsilon_N} \right) \tag{3.6.1}$$

where N is the void density nucleated per mm^3, ϵ_N is the critical value of the strain for which nucleation starts and A_B a material constant. The void growth kinetic is based on Rice and Tracey, (1969) and modified to incorporate the effect of the reduction of average radius R of cavities due to nucleation (Bouaziz et al., 2008; Maire et al., 2008), standing as follows:

$$\frac{dR}{d\epsilon_{eq}^P} = 0.283 \exp \left(\frac{3}{2} T \right) R - \frac{1}{N} \frac{dN}{d\epsilon_{eq}^P} \left(R - R_0(\epsilon_{eq}^P) \right) \tag{3.6.2}$$

where:

$$R_0 \left(\epsilon_{eq}^P \right) = R_0^i \exp \left(-a_B \epsilon_{eq}^P \right) \tag{3.6.3}$$

is the mean radius of cavities after nucleation and before beginning of the growth phase, R_0^i and a_B are material constants. Note that Eq. 3.6.2 reduces to the Rice and Tracey, (1969) model (Eq. 3.2.1) when there is no nucleation ($dN = 0$). Ben Bettaieb et al., (2011b) proposed two different approaches to integrate these evolution equations into the Gurson model:

- Replacement of the real population of voids by one single equivalent void.

- The classical approach by the additive decomposition of the porosity evolution (Eq. 3.3.4).

The first approach considers an homogenization of the population of nucleated void as a single void, characterized by the equivalent single void radius:

$$R_{eq} = \sqrt[3]{N} R \tag{3.6.4}$$

where N and R are defined by Eq. 3.6.1 and Eq. 3.6.2 respectively. Hence, the total void volume fraction evolution is given by:

$$f = \frac{(4/3)\pi R_{eq}^3}{V_m + (4/3)\pi R_{eq}^3} \tag{3.6.5}$$

with the following evolution law:

$$\frac{dR_{eq}}{R_{eq}} = \left(\frac{3q_2^2 \sigma_Y \sinh\left(\frac{3q_2\widetilde{\sigma}_m}{\kappa\sigma_Y}\right)}{2\kappa\widetilde{\sigma}_{eq}} \right) d\epsilon_{eq}^P \tag{3.6.6}$$

As the dependencies between variables are complex, q_2 is added as a new state variable and evaluated at each load increment while verifying Eq. 3.6.6. It is claimed that this approach allows to accurately reproduce experimental results.

The second approach considers an evolution equation for the nucleation:

$$\frac{df_n}{dN} = \frac{4}{3}\pi R_0^3 \tag{3.6.7}$$

where R_0 is defined by Eq. 3.6.3. The growth part evolution is given by:

$$\frac{dR}{R} = \left(\frac{q_1 q_2 \sigma_Y \sinh\left(\frac{3q_2\widetilde{\sigma}_m}{\kappa\sigma_Y}\right)}{\kappa\widetilde{\sigma}_{eq}} \right) d\epsilon_{eq}^P \tag{3.6.8}$$

Again, q_2 is added as an state variable verifying 3.6.8 at each load increment.

3.6.2 Fansi et al., (2013)

The work of Fansi et al., (2013) is based on experimental observations by Landron et al., (2010). It provides a new nucleation function introducing the triaxiality and kinematic hardening influence. Thus, the evolution of the nucleated void is now given by:

$$\frac{dN}{d\epsilon_{eq}^P} = \frac{B_B}{N_0 \sigma_c} \left(\sigma_{eq} + \theta\sigma_m\right)\left(N_0 + N\right) \tag{3.6.9}$$

where σ_c is the critical shear stress value that the martensite/ferrite interface can withstand without breaking, B_B is a material constant, while θ_B is given by:

$$\theta_B := \frac{\|\boldsymbol{\sigma}\|_{\mathbb{H}}}{\|\boldsymbol{\sigma} - \boldsymbol{X}\|_{\mathbb{H}}} \tag{3.6.10}$$

where $\|\cdot\|_{\mathbb{H}}$ is the energy norm of the (shifted) stress tensor. The void growth kinetics is the same as in Ben Bettaieb et al., (2011b), with the notable exception of introducing Huang, (1991) correction (Eq. 3.2.2) into the Rice and Tracey, (1969) term of Eq. 3.6.2. Another interesting result is the physical estimation of f_F, i.e. the porosity at final failure as described in section 3.3.2.2. Hence, for DP steels we have:

$$f_F = \frac{4\pi}{3}\left(\frac{R}{\lambda_f + 2R}\right)^3 \tag{3.6.11}$$

where λ_f is the average inter-cavities distance before the material fails.

3.7 Conclusions

Here a literature review is presented on the Gurson model and its extensions. It begins with early developments regarding cell studies and microscopic observations. Then, an explanation of the initial Gurson model and the GTN extension which covers nucleation, growth and coalescence of voids are given. The GTN model is widely used and is commonly found in FE software due to its robustness when describing the three stages of void evolution. Despite this fact, the model has been extended covering matrix anisotropy, mixed hardening and shear type of loads. The shear extension has attracted a great deal of attention over the last years because it covers a particular case where the initial GTN model did not predict stress softening. Extension based on microscopic observations are also briefly presented, directed towards specific materials.

Chapter 4

Numerical implementation of the Gurson model

Damage and fracture modeling deals with material softening and strain localization. These, usually lead to unwanted numerical features such as loss of the ellipticity of equilibrium equations, bifurcation into a shear band, etc. The first step before dealing with these issues is for the damage model to already have a stable, accurate integration scheme. In this chapter, the numerical integration of an extended version of the Gurson model (incorporating plastic anisotropy and mixed isotropic-kinematic hardening) proposed by Ben Bettaieb et al., (2011c), is revised and further extended to include nucleation, coalescence and shear. The main feature of this scheme is that all the variables are integrated in an implicit way based on the projection algorithm, while the consistent tangent matrix is analytically obtained. A detailed derivation of the equations used to extend the model is presented and a link with the developed subroutine is made. The efficiency of the implementation is assessed by comparing the numerical results of homogeneous cases with those obtained from the literature. Both results are in good agreement implying that the model can be used in more complex simulations which include heterogeneous strain paths.

4.1 Tensor and matrix-vector notation

The vectors and second order tensors are denoted by boldface letters, while the scalars are plain letters and $\mathbb{C}$ is a fourth order tensor. The capitals letters represent the material coordinates whilst the minuscules the spacial coordinates. Hence, $\boldsymbol{X}$ is a tensor in the material (*lagrangian*) coordinates while $\boldsymbol{x}$ represents a tensor in the spacial (*eulerian*) coordinates. The second and fourth order unity tensors are denoted by $\boldsymbol{I}$ and $\mathbb{I}$ respectively. The double contraction is represented by $\boldsymbol{A} : \boldsymbol{B} = \left[\boldsymbol{A}^T \boldsymbol{B}\right]$, while the tensorial product with the symbol $\otimes$.

The programmed equations are slightly different from the ones presented here since they had to be adapted for the programming language[1] and to decrease

[1]The LAGAMINE code is programmed using Fortran.

the computational effort, and at the same time using the advantages of the symmetry properties of some tensors. The tensor *storage schemes* are not as trivial as they could appear, since a vector can have a non-unique representation and a matrix representation of the tensor components can not recover the full integrity of the former tensor. Moreover, little information is found in the literature regarding this point. In order to use a consistent and unequivocal notation, a distinction between *covariant* and *contravariant* tensors representations in the $\mathbb{R}^6$ vector space is briefly presented following the analysis by Helnwein, (2001). The particular choice of an ortho-normal basis in $\mathbb{R}^3$ makes the covariant and contravariant representation equal, which is often the case. Nevertheless, generally the matrix representation in $\mathbb{R}^6$ associated with this space is usually related to *non normalized* vector space, making the distinction necessary. To simplify the discussion, no rigorous distinction in terms of superscript and underscripts will be made between the covariants and contravariant's tensor and only the covariant representation (underscript) will be used throughout the text.

To clarify this point, let's consider the symmetry of the Cauchy stress tensor $\boldsymbol{\sigma}$, arising from the angular momentum conservation principle:

$$\sigma_{ij} = \sigma_{ji} \tag{4.1.1}$$

Hence, the initial 9 components of the tensor in the $\mathbb{R}^3 \times \mathbb{R}^3$ space can be reduced to 6 different components in form of a vector in the $\mathbb{R}^6$ space. Therefore, we can express the stress tensor $\boldsymbol{\sigma}$ as:

$$\{\boldsymbol{\sigma}\} = \{\sigma_{11} \quad \sigma_{22} \quad \sigma_{33} \quad \sigma_{12} \quad \sigma_{13} \quad \sigma_{23}\}^T \tag{4.1.2}$$

which is the *contravariant* representation of the Cauchy stress tensor according to Helnwein, (2001). This representation is often used in the literature and referred to as the Voigt notation (Wikipedia, 2014). However, we can also express the stress tensor as:

$$\{\boldsymbol{\sigma}\} = \left\{\sigma_{11} \quad \sigma_{22} \quad \sigma_{33} \quad \sqrt{2}\sigma_{12} \quad \sqrt{2}\sigma_{13} \quad \sqrt{2}\sigma_{23}\right\}^T \tag{4.1.3}$$

which is a *normalized* representation, also called the Mandel notation. This representation is based on an *ortho-normal* basis, so no distinction between covariant and contravariant is needed.

For the strain tensor representation, it is often found that the strain tensor can be written in two different ways:

$$\{\boldsymbol{\epsilon}\} = \{\epsilon_{11} \quad \epsilon_{22} \quad \epsilon_{33} \quad 2\epsilon_{12} \quad 2\epsilon_{13} \quad 2\epsilon_{23}\}^T \tag{4.1.4}$$

$$\{\boldsymbol{\epsilon}\} = \{\epsilon_{11} \quad \epsilon_{22} \quad \epsilon_{33} \quad \gamma_{12} \quad \gamma_{13} \quad \gamma_{23}\}^T \tag{4.1.5}$$

where $\gamma_{ij} = 2\epsilon_{ij}$. Eq. 4.1.4 is the covariant representation of the strain tensor while Eq. 4.1.5 corresponds to the contravariant representation of the strain tensor. These distinctions can be regarded as highly academic, but are of practical importance as exemplified in Helnwein, (2001). This distinction also applies

to other tensors i.e. fourth order tensors are mapped onto a 6x6 matrix. The elasticity tensor[2] $\mathbb{C}$ has the following symmetry:

$$C_{ijkl} = C_{jikl} = C_{klij} = C_{ijlk} \tag{4.1.6}$$

Thus, we express the linear isotropic elasticity tensor $\mathbb{C}$ as:

$$[\mathbb{C}] = \begin{bmatrix} \lambda+2G & \lambda & \lambda & 0 & 0 & 0 \\ & \lambda+2G & \lambda & 0 & 0 & 0 \\ & & \lambda+2G & 0 & 0 & 0 \\ & & & 2G & 0 & 0 \\ & & & & 2G & 0 \\ & & & & & 2G \end{bmatrix} \tag{4.1.7}$$

which corresponds to the *normalized* description of $\mathbb{C}$.

In the implemented equations and in the following text, the contravariant representations of Eq. 4.1.2 and 4.1.5 are used. The fourth order tensors is represented in the *ortho-normal* basis, so the elasticity matrix can be used with both covariant and contravariant representations.

In terms of the operations between tensors, contraction between second order tensors are replaced by a dot product, and the fourth order tensors are replaced by a matrix transformation:

$$\boldsymbol{\sigma} : \boldsymbol{\epsilon}^e = \sigma_{ij}\epsilon^e_{ij} \Longleftrightarrow \{\boldsymbol{\sigma}\} \cdot \{\boldsymbol{\epsilon}^e\} = \{\boldsymbol{\sigma}\}^T \{\boldsymbol{\epsilon}^e\}$$

$$\boldsymbol{\sigma} = \mathbb{C} : \boldsymbol{\epsilon}^e \Longleftrightarrow \{\boldsymbol{\sigma}\} = [\mathbb{C}] \{\boldsymbol{\epsilon}^e\} \tag{4.1.8}$$

$$\tag{4.1.9}$$

Careful attention must be given when expressing the double contraction between a fourth and a second order tensor expressed in vector components. For example:

$$[\mathbb{H}]^{-1} \cdot \{\boldsymbol{\sigma}\} = \begin{Bmatrix} \dot{\epsilon}_{11} \\ \dot{\epsilon}_{22} \\ \dot{\epsilon}_{33} \\ \dot{\gamma}_{12} \\ \dot{\gamma}_{13} \\ \dot{\gamma}_{23} \end{Bmatrix} = \begin{Bmatrix} \dot{\epsilon}_{11} \\ \dot{\epsilon}_{22} \\ \dot{\epsilon}_{33} \\ 2\dot{\epsilon}_{12} \\ 2\dot{\epsilon}_{13} \\ 2\dot{\epsilon}_{23} \end{Bmatrix} \tag{4.1.10}$$

Hence, the shear terms must be divided by 2 to be in agreement with the tensor contraction. Inside the implemented subroutine, this is done by modifying the $[\mathbb{H}]$ matrix shear terms through the variable `HMAT2`.

4.2 Previous versions available in Lagamine

In its current state, Lagamine has different versions of the Gurson model, summarized in Table 4.1. We look at them in chronological order.

[2]The Hill anisotropic tensor $\mathbb{H}$ has the same symmetric properties.

Table 4.1: Implemented versions of the GTN model and their characteristics.

	`GUR3D` GTN model	`GUR3Dclas` Gurson model	`GUR3Dani` Physically based	`GUR3Dext` GTN plus shear
Anisotropy		√	√	√
Isotropic	√	√	√	√
Kinematic	√	√	√	√
Nucleation	√		√	√
Coalescence	√			√
Shear				√

4.2.1 GUR3D

This implementation is due to Wang, (1993, chapter 3)[3]. It corresponds to the classical GTN model, thus it includes nucleation, growth and coalescence of voids. The yield surface is given by:

$$F_p(\boldsymbol{\sigma}, \boldsymbol{X}, f, \sigma_Y) = \frac{\widetilde{\sigma}_{eq}^2}{\sigma_Y^2} - 1 + 2q_1 f^* \cosh\left(\frac{q_2 \widetilde{\sigma}_m}{2\sigma_Y}\right) - q_3 f^{*2} = 0 \tag{4.2.1}$$

which incorporates the effect of the kinematic hardening through the *shifted* stress:

$$\widetilde{\boldsymbol{\sigma}} := \boldsymbol{\sigma} - \boldsymbol{X} \tag{4.2.2}$$

$\widetilde{\sigma}_{eq}$ is the (macroscopic) *effective* stress tensor defined by:

$$\widetilde{\sigma}_{eq} := \sqrt{\frac{3}{2}\widetilde{\boldsymbol{\sigma}}_{\text{dev}} : \widetilde{\boldsymbol{\sigma}}_{\text{dev}}} \tag{4.2.3}$$

It must be noted that there is no relation between this definition regarding the kinematic hardening and the effective stress concept in the Lemaitre and Chaboche type of damage models.

Equivalence between the rates of tensorial macroscopic plastic work and physical plastic work within the matrix (computed on the entire matrix volume) is assumed:

$$\widetilde{\boldsymbol{\sigma}} : \dot{\boldsymbol{\epsilon}}^P = (1-f)\sigma_Y \dot{\epsilon}_M^P \tag{4.2.4}$$

where ϵ_M^P is the equivalent plastic strain in the matrix. σ_Y is the flow stress in the matrix, given by:

$$\sigma_Y = (1-\beta)\,\sigma_0 + \beta\sigma_M \tag{4.2.5}$$

where σ_M is the von Mises equivalent stress in the matrix, σ_0 is a material parameters representing the initial yield stress and β is the hardening coefficient representing the percentage of isotropic hardening i.e. β =1.0 is pure isotropic hardening and β =0.0 is pure kinematic hardening (Mear and Hutchinson, 1985).

[3]Further detailed in Wang, (1989).

4.2.2 GUR3Dclas

This version was introduced by Ben Bettaieb et al., (2011c). The essential difference from the `GUR3D` version is the introduction of the dense matrix's anisotropy, thus requiring a new integration scheme. In terms of the material law, it corresponds to the classic Gurson, (1977a) model modified by plastic anisotropy and using mixed isotropic (Swift) and kinematic (Armstrong and Fredrick, (1966)) hardening laws. The growth of cavities is classical and it is implicitly integrated. Void shape effects are not considered and the initial spherical shape is kept constant. Nucleation and coalescence are also neglected.

The anisotropy is incorporated into the Gurson/GTN model with the Benzerga and Besson, (2001) approach. The yield surface is then given by:

$$F_p(\boldsymbol{\sigma}, \boldsymbol{X}, f, \sigma_Y) = \frac{\widetilde{\sigma}_{eq}^2}{\sigma_Y^2} - 1 + 2q_1 f \cosh\left(\frac{3q_2\widetilde{\sigma}_m}{\kappa\sigma_Y}\right) - q_3 f^2 = 0 \tag{4.2.6}$$

where κ is a coefficient reflecting the plastic anisotropy effect. The Hill equivalent (effective) stress is defined by:

$$\widetilde{\sigma}_{eq} = \sqrt{\frac{1}{2}\widetilde{\boldsymbol{\sigma}} : \mathbb{H} : \widetilde{\boldsymbol{\sigma}}} \tag{4.2.7}$$

where $\mathbb{H}$ is the fourth order Hill tensor containing the anisotropic coefficients of the Hill, (1948) yield criterion, which components are:

$$[\mathbb{H}] = \begin{bmatrix} G+H & -H & -G & 0 & 0 & 0 \\ -H & H+F & -F & 0 & 0 & 0 \\ -G & -F & F+G & 0 & 0 & 0 \\ 0 & 0 & 0 & 2N & 0 & 0 \\ 0 & 0 & 0 & 0 & 2L & 0 \\ 0 & 0 & 0 & 0 & 0 & 2M \end{bmatrix} \tag{4.2.8}$$

The damage anisotropic parameter κ is a function of the Hill/Lankford coefficients:

$$\kappa = \sqrt{\frac{8}{5}\left(\frac{d_1+d_2+d_3}{d_1d_2+d_2d_3+d_3d_1}\right) + \frac{4}{5}\left(\frac{1}{d_4}+\frac{1}{d_5}+\frac{1}{d_6}\right)} \tag{4.2.9}$$

where:

$$\begin{aligned} d_1 &= -\frac{2}{3}\frac{r_0r_{90}-2r_0-2}{r_0+1} \\ d_2 &= d_1\left[1-\frac{3\left(r_0r_{90}-1\right)}{r_0r_{90}-2r_0-2}\right] \\ d_3 &= d_1\left[1-\frac{3r_0\left(r_{90}-1\right)}{r_0r_{90}-2r_0-2}\right] \\ d_4 &= d_1\left[-\frac{1}{2}\frac{3\left(r_0+1\right)}{r_0r_{90}-2r_0-2}\right] \\ d_5 &= d_1\left[-\frac{1}{2}\frac{3r_0\left(r_{90}+1\right)}{r_0r_{90}-2r_0-2}\right] \\ d_6 &= d_1\left[-\frac{1}{2}\frac{\left(2r_{45}+1\right)\left(r_0r_{90}+1\right)}{r_0r_{90}-2r_0-2}\right] \end{aligned}$$

It is important to highlight that these equations (which are those implemented in LAGAMINE code) are slightly different from those of original article by Benzerga and Besson, (2001). In the aforementioned article, the analysis is more general involving thick plates where deformations can be measured through the thickness. In this work however, case the main applications are thin plates where the thickness gradients are hard to capture and it is usually assumed that the shear Hill coefficients (L, M and N) are equal.

4.2.3 GUR3Dani

It is a model specifically developed for Dual-Phase (DP) steels by Ben Bettaieb et al., (2012). It can be decomposed in two mains parts:

- The modeling of the matrix, using mixed hardening as in the `GUR3DCLAS` implementation.
- The evolution of the porosity, neglecting the morphological distribution and shape evolution of the voids (which are assumed spherical).

The algorithm is explicit in regards to porosity and implicit regarding other variables (equivalent plastic strain in the matrix). In practical terms, it means that the jacobian matrix of `GUR3DCLAS` is calculated for all unknowns except for the porosity, which is calculated at the end of the step. See Ben Bettaieb et al., (2011b) for further details.

4.3 Integration algorithm description

In this thesis, the GTN model presented in chapter 3 is integrated into the FE code LAGAMINE. The previous integration scheme developed by Ben Bettaieb et al., (2011c) was found to be inadequate, leading to bad results and convergence issues compared to the literature. Globally, the new integration scheme is largely based on the one of Ben Bettaieb et al., (2011c) but significant changes have been introduced such as:

- New derivatives to improve convergence and accuracy.
- Improved integration of the kinematic hardening.
- The programmed subroutine underwent a complete *makeover*, in terms of the Fortran intrinsic functions and syntax, greatly simplifying their understanding.

Herein, we detail the integration scheme keeping Ben Bettaieb et al., (2011c) notation for sake of simplicity.

Integration of the rate constitutive equations into the finite element method requires obtaining the non-linear response of the material (in terms of the stress state) over a discrete sequence of time steps. This implies *linearization* of the non-linear discretized problem, thus treating it as an equivalent elastic problem. For

the case of rate-independent plasticity, the classical return mapping by Wilkins, (1964) is widely used because of its effectiveness and robustness. It was originally designed to satisfy the yield function at the end of the current step, and such introducing a constraint (*consistency condition*) into the discretized equations. The original version of the return mapping algorithm is applied to the isotropic Von Mises yield criterion, which can be represented as an hypersphere in the deviatoric stress space. Thus, the *return* to the yield surface is performed in a *radial* direction, hence the name of the method being the *radial return* (Fig. 4.1(a)). In general, the return mapping method may also be viewed as a two-step algorithm, involving:

1. Predictor step, used to compute the trial stress state.

2. Yield function evaluation:

   - If $F_p < 0$, set the current stress state equal to trial stress value.
   - If $F_p > 0$, apply a *plastic corrector* iteratively until $F_p = 0$.

As mentioned, the plastic corrector should be iteratively applied therefore a Newton's method is implemented at the element integration point level. Including an extra loop at this point could notoriously increase the calculation time so attention should be given to the number of unknowns.

A particular case of the return mapping algorithm arises when using an implicit scheme. In this case, and for perfectly plastic materials, the return mapping can be regarded as the *closest point projection* of the trial stress onto the set defined by the plastically admissible stresses (Simo and Hughes, 1998; de Souza Neto et al., 2008). This can be seen in Fig. 4.1(b).

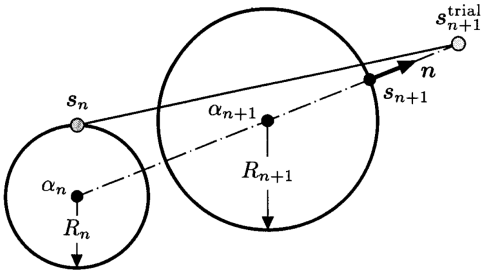

(a) Radial return for a mixed (isotropic and kinematic) hardening material, in the deviatoric stress space.

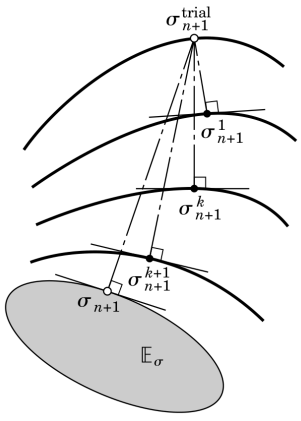

(b) Closest point projection representation for a nonlinear hardening material.

Figure 4.1: Geometrical representation of the return mapping algorithms. The closest point projection arises when applying an implicit scheme to the return mapping. Adapted from Simo and Hughes, (1998).

More references on the return mapping algorithms applied to plasticity can be found in the classical books by Crisfield, (1991, chapter 6) and Zienkiewicz and Taylor, (2006, chapter 4). For a deeper and more general presentation of the integration algorithms for different constitutive models, the books of Simo and Hughes, (1998) and de Souza Neto et al., (2008) are recommended.

4.3.1 Elastoplastic constitutive equations

For the following equations, we consider the decomposition of a tensor into an *hydrostatic* and a *deviatoric* part:

$$\boldsymbol{\sigma} = \boldsymbol{\sigma}_{\text{hyd}} + \boldsymbol{\sigma}_{\text{dev}}, \qquad \boldsymbol{X} = \boldsymbol{X}_{\text{hyd}} + \boldsymbol{X}_{\text{dev}} \tag{4.3.1}$$

where:

$$\boldsymbol{\sigma}_{\text{hyd}} = \frac{1}{3}\operatorname{tr}(\boldsymbol{\sigma})\boldsymbol{I}, \qquad \boldsymbol{X}_{\text{hyd}} = \frac{1}{3}\operatorname{tr}(\boldsymbol{X})\boldsymbol{I} \tag{4.3.2}$$

$$\boldsymbol{\sigma}_{\text{dev}} = \mathbb{P} : \boldsymbol{\sigma}, \qquad \boldsymbol{X}_{\text{dev}} = \mathbb{P} : \boldsymbol{X} \tag{4.3.3}$$

$\mathbb{P}$ is the deviatoric (projection) tensor defined as:

$$\mathbb{P} := \mathbb{I} - \frac{1}{3}\boldsymbol{I} \otimes \boldsymbol{I} \tag{4.3.4}$$

Note that $\mathbb{P} : \boldsymbol{\sigma}_{\text{hyd}} = 0$. Neglecting kinematic hardening (cf. Eq. 4.2.7), Aravas, (1987) also introduced the following variables:

$$p := -\frac{1}{3}\operatorname{tr}(\boldsymbol{\sigma}) \tag{4.3.5}$$

$$q := \|\boldsymbol{\sigma}\|_{\mathbb{H}} = \sqrt{\frac{1}{2}\boldsymbol{\sigma} : \mathbb{H} : \boldsymbol{\sigma}} = \sigma_{eq} \tag{4.3.6}$$

where $\|\cdot\|_{\mathbb{H}}$ is the energy norm induced by $\mathbb{H}$. Therefore, the Cauchy stress tensor can be expressed in the following way:

$$\boldsymbol{\sigma} = -p\boldsymbol{I} + 2q\left(\mathbb{H}^{-1} : \boldsymbol{n}\right) \tag{4.3.7}$$

while the plastic strain rate can be written as:

$$\dot{\boldsymbol{\epsilon}}^P = \frac{1}{3}\dot{\epsilon}_p\boldsymbol{I} + \dot{\epsilon}_q\boldsymbol{n} \tag{4.3.8}$$

where $\boldsymbol{n}$ denotes the unit normal to the yield surface. The yield function with straightforward extension to kinematic hardening $(\widetilde{q}, \widetilde{p})$ is therefore given by:

$$F_p\left(p, q, \boldsymbol{X}, \epsilon_M^P, f\right) = \frac{\widetilde{q}^2}{\sigma_Y^2} - 1 + 2q_1 f \cosh\left(-3\frac{q_2\widetilde{p}}{\kappa\sigma_Y}\right) - q_3 f^2 \tag{4.3.9}$$

which is equivalent to Eq. 4.2.6.

The set of governing equations of the material behavior are described hereafter. As in the classical theory of plasticity *additive decomposition* of the (total) infinitesimal strain tensor is assumed:

$$\dot{\boldsymbol{\epsilon}} = \dot{\boldsymbol{\epsilon}}^e + \dot{\boldsymbol{\epsilon}}^p \tag{4.3.10}$$

It is very well known that this assumption is valid for the infinitesimal strain only. For finite elasto-plastic deformations, a coupling exists between the elastic and plastic part and the *additive decomposition* is no longer valid. Nevertheless, it can be shown that for cases where the elastic strain is negligible compared to plastic strain (like metal forming operations), this assumption is acceptable (see Khan and Huang, 1995, chapter 7). This approach has successfully been used in Lagamine by Li, (1995) and Hoferlin, (2001). Therefore, in this section no discussion will be given on objectivity rates, keeping the classical infinitesimal theory notation. The infinitesimal strain field $\boldsymbol{\epsilon}$ can be defined in terms of the displacement field $\boldsymbol{u}$ as:

$$\boldsymbol{\epsilon} := \frac{1}{2}\left(\nabla \boldsymbol{u} + (\nabla \boldsymbol{u})^T\right) \tag{4.3.11}$$

where $\nabla(\bullet)$ is the (material) gradient operator. This expression is useful in FE implementations as it will be seen later.

The definition of a constitutive equation for both $\dot{\boldsymbol{\epsilon}}^e$ and $\dot{\boldsymbol{\epsilon}}^p$ is required in this case. For the elastic part, the constitutive equation is given by an *hyperelastic law* for linear, elastic, homogeneous (in time) and isotropic materials:

$$\dot{\boldsymbol{\sigma}} = \mathbb{C} : (\dot{\boldsymbol{\epsilon}} - \dot{\boldsymbol{\epsilon}}^p) \tag{4.3.12}$$

also known as Hooke's law, where $\mathbb{C}$ is the fourth-order (constant) elasticity tensor which can also be written as:

$$\mathbb{C} = K_b \boldsymbol{I} \otimes \boldsymbol{I} + 2G_s \mathbb{P} \tag{4.3.13}$$

where K_b and G_s are the bulk and shear modulus respectively. The constitutive relation for $\dot{\boldsymbol{\epsilon}}^p$ in the original Gurson, (1977a) is given by the associated flow rule. The normality of the plastic flow rule for the matrix implies macroscopic normality (Bishop and Hill, 1951):

$$\dot{\boldsymbol{\epsilon}}^p = \dot{\lambda}\frac{\partial F_p}{\partial \boldsymbol{\sigma}} \tag{4.3.14}$$

Here λ represents the plastic multiplier. To find $\dot{\boldsymbol{\epsilon}}^P$, it is necessary to develop Eq. 4.3.14:

$$\frac{\partial F_p}{\partial \boldsymbol{\sigma}} = \frac{\mathbb{H} : \widetilde{\boldsymbol{\sigma}}}{\sigma_Y^2} + 2\frac{q_1 q_2}{\kappa \sigma_Y} f \sinh\left(-3\frac{q_2 \widetilde{p}}{\kappa \sigma_Y}\right)\boldsymbol{I} \tag{4.3.15}$$

The identification of the hydrostatic and deviatoric parts gives:

$$\dot{\boldsymbol{\epsilon}}^p_{\text{hyd}} = \dot{\lambda}\frac{1}{3}\,\text{tr}\left(\frac{\partial F_p}{\partial \boldsymbol{\sigma}}\right)\boldsymbol{I} = 2\dot{\lambda}\frac{q_1 q_2}{\kappa \sigma_Y} f \sinh\left(-3\frac{q_2 \widetilde{p}}{\kappa \sigma_Y}\right)\boldsymbol{I} \tag{4.3.16}$$

$$\dot{\boldsymbol{\epsilon}}^p_{\text{dev}} = \dot{\lambda}\mathbb{P} : \frac{\partial F_p}{\partial \boldsymbol{\sigma}} = \dot{\lambda}\frac{\mathbb{H} : \widetilde{\boldsymbol{\sigma}}_{\text{dev}}}{\sigma_Y^2} \tag{4.3.17}$$

In terms of Aravas, (1987) notation (Eq. 4.3.5 and 4.3.6) we can write:

$$\dot{\epsilon}_p = -\dot{\lambda}\left(\frac{\partial F_p}{\partial \widetilde{p}}\right) \qquad \text{and} \qquad \dot{\epsilon}_q = \dot{\lambda}\left(\frac{\partial F_p}{\partial \widetilde{q}}\right) \tag{4.3.18}$$

Eliminating λ we obtain:

$$\dot{\epsilon}_p \left(\frac{\partial F_p}{\partial \widetilde{q}} \right) + \dot{\epsilon}_q \left(\frac{\partial F_p}{\partial \widetilde{p}} \right) = 0 \tag{4.3.19}$$

This equation can be regarded as equivalent to the *consistency condition*. We can calculate the plastic multiplicator λ using the definition of the equivalent plastic strain associated with $\mathbb{H}$:

$$\dot{\epsilon}_q = \|\dot{\boldsymbol{\epsilon}}\|_{\mathbb{H}^{-1}} = \sqrt{2\dot{\boldsymbol{\epsilon}} : \mathbb{H}^{-1} : \dot{\boldsymbol{\epsilon}}} \tag{4.3.20}$$

Replacing Eq. 4.3.17 or 4.3.18 in Eq. 4.3.20, we obtain the plastic multiplier:

$$\dot{\lambda} = \frac{\dot{\epsilon}_q \sigma_Y^2}{2\widetilde{q}} \tag{4.3.21}$$

By definition (Eq. 4.3.8), $\dot{\boldsymbol{\epsilon}}^p_{\text{dev}} := \dot{\epsilon}_q \boldsymbol{n}$. Hence, replacing 4.3.21 in 4.3.17 we finally obtain:

$$\boldsymbol{n} = \frac{\mathbb{H} : \widetilde{\boldsymbol{\sigma}}_{\text{dev}}}{2\widetilde{q}} \tag{4.3.22}$$

which fulfills the following property:

$$\|\boldsymbol{n}\|_{\mathbb{H}^{-1}} = \sqrt{2\left(\boldsymbol{n} : \mathbb{H}^{-1} : \boldsymbol{n}\right)} = 1 \tag{4.3.23}$$

The components of $\boldsymbol{n}$ can be expressed in following way (Ben Bettaieb et al., 2011c):

$$[\boldsymbol{n}] = \begin{bmatrix} n_1 & n_3 & n_4 \\ n_3 & n_2 & n_5 \\ n_4 & n_5 & -n_1 - n_2 \end{bmatrix} \tag{4.3.24}$$

The hardening relations for the dense matrix are given by an isotropic and kinematic relation. For the isotropic hardening, an evolution equation in terms of the equivalent plastic strain of the matrix is used:

$$\sigma_Y = \sigma_Y \left(\epsilon_M^P \right) \tag{4.3.25}$$

For the case of the kinematic hardening, the evolution of the backstress $\boldsymbol{X}$ is determined by:

$$\boldsymbol{X} = \boldsymbol{X} \left(\dot{\boldsymbol{\epsilon}}^P, f \right) \tag{4.3.26}$$

$$\boldsymbol{X} = (1 - q_1 f)\, \boldsymbol{X}^* \left(\dot{\boldsymbol{\epsilon}}^P \right) \tag{4.3.27}$$

where $\boldsymbol{X}^*$ is a function that evolves with the macroscopic plastic strain rate. In this case, we use the A-F model (Eq. 2.2.14):

$$\boldsymbol{X}^* = C_X \left(X_{\text{sat}} \dot{\boldsymbol{\epsilon}}^P - \boldsymbol{X} \bar{\epsilon}^P \right) \tag{4.3.28}$$

Finally, the set of internal variables representing the isotropic hardening and the porosity are defined as:

$$H_1 := \epsilon_M^P \qquad H_2 := f \tag{4.3.29}$$

With the related incremental equation defined as:

$$h_1 := \dot{\epsilon}_M^p = \frac{-\widetilde{p}\dot{\epsilon}_p + \widetilde{q}\dot{\epsilon}_q}{(1-f)\sigma_Y} \tag{4.3.30}$$

$$h_2 := \dot{f} = (1-f)\dot{\epsilon}_p \tag{4.3.31}$$

All the model equations are summarized in box 4.3.1.

Box 4.3.1: Equations involved in the implemented GTN model.

1. Elastoplastic split of the strain tensor

$$\dot{\boldsymbol{\epsilon}} = \dot{\boldsymbol{\epsilon}}^e + \dot{\boldsymbol{\epsilon}}^p$$

2. Elastic law (uncoupled from damage)

$$\boldsymbol{\sigma} = \mathbb{C} : \boldsymbol{\epsilon}^e$$

3. GTN yield function

$$F_p\left(p, q, \boldsymbol{X}, \boldsymbol{H}\right) = 0$$

where $\sigma_Y = \sigma_Y\left(\epsilon_M^p\right)$ and $\boldsymbol{X} = \boldsymbol{X}\left(\dot{\boldsymbol{\epsilon}}^P, f\right)$

4. Flow rule

$$\dot{\epsilon}_p \left(\frac{\partial F_p}{\partial \widetilde{q}}\right) + \dot{\epsilon}_q \left(\frac{\partial F_p}{\partial \widetilde{p}}\right) = 0$$

5. Normal to the yield surface

$$\boldsymbol{n} = \frac{\mathbb{H} : \widetilde{\boldsymbol{\sigma}}_{\text{dev}}}{2\widetilde{q}}$$

6. State variables

$$h_1 := \dot{\epsilon}_M^p = \frac{-\widetilde{p}\dot{\epsilon}_p + \widetilde{q}\dot{\epsilon}_q}{(1-f)\sigma_Y}$$
$$h_2 := \dot{f} = (1-f)\dot{\epsilon}_p$$

4.3.2 Aravas, (1987) approach

The extension of the return mapping algorithms to elastoplastic pressure-dependent (I_1-dependent) constitutive relations was first proposed by Aravas, (1987). The main feature added in this approach is the introduction of the hydrostatic part of the strain, meaning that $\dot{\boldsymbol{\epsilon}}^p_{\text{hyd}}$ (Eq. 4.3.16) is no longer zero, as in the J_2-plasticity models. Subsequently, Ben Bettaieb et al., (2011c) extended this approach to consider the plastic anisotropy and kinematic hardening. In this section, both the approaches of Aravas, (1987) and Ben Bettaieb et al., (2011c) are revised, based on the equations detailed in the previous section 4.3.1.

The backward Euler implicit scheme is chosen based on the work of Ortiz and Popov, (1985). They showed that for a J_2-plasticity model this algorithm gives better accuracy for strain increments several times bigger that the yield strain. Moreover, it is unconditionally stable independently of the smoothness of the yield criterion. Within an incremental problem for a step defined as $[t_n, t_{n+1}]$, the (current) strain can be globally represented in an implicit scheme as:

$$\boldsymbol{\epsilon}_{n+1} = \boldsymbol{\epsilon}_n + \Delta t \dot{\boldsymbol{\epsilon}}_{n+1}, \qquad \Delta t = t_{n+1} - t_n \tag{4.3.32}$$

or equivalently:

$$\boldsymbol{\epsilon}_{n+1} = \boldsymbol{\epsilon}_n + \Delta\boldsymbol{\epsilon}, \qquad \Delta\boldsymbol{\epsilon} = \Delta t \dot{\boldsymbol{\epsilon}}_{n+1} \tag{4.3.33}$$

where Δt represents the time increment, n denotes the time at the beginning of the step and $n+1$ the time at the end of the step. Since viscosity effects are neglected, the rate and incremental form of the constitutive equations are equivalent and therefore we can safely replace $\dot{\boldsymbol{\epsilon}}$ by $\Delta\boldsymbol{\epsilon}$. In the context of the FE simulation, the incremental strain field $\Delta\boldsymbol{\epsilon}$ is assumed to be given at the beginning of the time step in terms of the displacements field $\boldsymbol{u}$. Hence, the infinitesimal strain increment can be defined from Eq. 4.3.11 as:

$$\Delta\boldsymbol{\epsilon} := \frac{\Delta t}{2}\left(\nabla\dot{\boldsymbol{u}}_{n+1} + (\nabla\dot{\boldsymbol{u}}_{n+1})^T\right) \tag{4.3.34}$$

Then we can define the elastic predictor by assuming a *freezed plastic flow* ($\boldsymbol{\epsilon}^P_{n+1} = \boldsymbol{\epsilon}^P_n$):

$$\boldsymbol{\sigma}^{\text{trial}}_{n+1} := \mathbb{C} : \left(\boldsymbol{\epsilon}_{n+1} - \boldsymbol{\epsilon}^P_n\right) = \boldsymbol{\sigma}_n + \mathbb{C} : \Delta\boldsymbol{\epsilon} \tag{4.3.35}$$

Using Aravas, (1987) notation:

$$p^{\text{trial}}_{n+1} := \frac{1}{3}\,\text{tr}\left(\boldsymbol{\sigma}^{\text{trial}}_{n+1}\right) \qquad \text{and} \qquad q^{\text{trial}}_{n+1} := \|\boldsymbol{\sigma}^{\text{trial}}_{n+1}\|_{\mathbb{H}} \tag{4.3.36}$$

The main difference between the algorithm proposed by Aravas, (1987) and Ben Bettaieb et al., (2011c) is the introduction of the anisotropy tensor $\mathbb{H}$, implying that q^{trial}_{n+1} is no longer coaxial with q_{n+1} and, as a consequence, the normal tensor $\boldsymbol{n}$ cannot be explicitly determined from the trial state and must be considered as an unknown. The elastic trial state is evaluated using the yield function:

$$F_p\left(p^{\text{trial}}_{n+1}, q^{\text{trial}}_{n+1}, \boldsymbol{X}_n, \boldsymbol{H}_n\right) = 0 \tag{4.3.37}$$

If the yield condition is not fulfilled, the plastic corrector is applied to the trial state:

$$\widetilde{\boldsymbol{\sigma}}_{n+1} = \boldsymbol{\sigma}^{\text{trial}}_{n+1} - K_b\Delta\epsilon_{p_n}\boldsymbol{I} - 2G_s\Delta\epsilon_{q_n}\boldsymbol{n}_n - \boldsymbol{X}_n \tag{4.3.38}$$

Analogously, using Eq. 4.3.13, Eq. 4.3.35 and 4.3.36:

$$p_{n+1} = p^{\text{trial}}_{n+1} + K_b\Delta\epsilon_{p_n} \tag{4.3.39}$$

$$q_{n+1} = q^{\text{trial}}_{n+1} - 2G_s\Delta\epsilon_{q_n} \tag{4.3.40}$$

Hence, the plastic corrector is fully determined knowing $\Delta\epsilon_p$, $\Delta\epsilon_q$ and $\boldsymbol{n}$. Adding the state variables, the problem involves finding the following set of unknowns:

$$\{\boldsymbol{Y}\} = \left\{\Delta\epsilon_p, \Delta\epsilon_q, n_1, n_2, n_3, n_4, n_5, \Delta\epsilon^P_M, f\right\}^T \tag{4.3.41}$$

Having 9 unknowns, 9 equations should be available through the residual vector (tensor) $\boldsymbol{\Gamma}$. As presented hereafter, these 9 relations are indeed possible to find from Box 4.3.1. Starting with the yield surface:

$$\Gamma_1 = F_p\left(\widetilde{p}, \widetilde{q}, H_\alpha\right) = \frac{\widetilde{q}^2}{\sigma_Y^2} - 1 + 2q_1 f\cosh\left(-3\frac{q_2\widetilde{p}}{\kappa\sigma_Y}\right) - q_3 f^2 \tag{4.3.42}$$

The flow rule:

$$\Gamma_2 = \Delta\epsilon_p \left(\frac{\partial F_p}{\partial \widetilde{q}} \right) + \Delta\epsilon_q \left(\frac{\partial F_p}{\partial \widetilde{p}} \right) \tag{4.3.43}$$

The normal to the yield surface:

$$\Gamma_{3,\ldots,7} = \left\{ \boldsymbol{n} - \frac{\mathbb{H} : \widetilde{\boldsymbol{\sigma}}_{\text{dev}}}{2\widetilde{q}} \right\}_i, \quad i = 1, 2, 4, 5, 6 \tag{4.3.44}$$

where the subscript i denotes the vector (tensor) component of the contravariant representation of tensor $\boldsymbol{n}$ (cf. Eq. 4.3.24). The equations involving the state variables $\Delta\epsilon_M^P$ and f are defined as:

$$\Gamma_8 = (1 - f)\Delta\epsilon_M^P \sigma_Y - \widetilde{q}\Delta\epsilon_q + \widetilde{p}\Delta\epsilon_p \tag{4.3.45}$$

$$\Gamma_9 = f - \frac{f^t + \Delta\epsilon_p}{1 + \Delta\epsilon_p} \tag{4.3.46}$$

where f^t is the porosity from the last (converged) step. The jacobian matrix is calculated within the function `JACMOD` and the detailed implemented derivatives are listed in Appendix B. The programmed integration scheme is summarized in the (pseudo) algorithm 1 while the Newton scheme to solve the problem is shown in the (pseudo) algorithm 2. `NTRIAL` is an integer parameter that limits the number of loop iterations. `NTRIAL`=40 is found to give good results in terms of convergence.

An important characteristic of the Newton-Rhapson scheme is the choice of the initial solution[4]. The following solution is proposed:

$$Y_1^{(0)} = \Delta\epsilon_p^{(0)} = \text{tr}\,(\Delta\boldsymbol{\epsilon}) \tag{4.3.47}$$

$$Y_2^{(0)} = \Delta\epsilon_q^{(0)} = \sqrt{2\,(\Delta\boldsymbol{\epsilon} : \mathbb{H}^{-1} : \Delta\boldsymbol{\epsilon})} \tag{4.3.48}$$

$$Y_{3,\ldots,7}^{(0)} = n_i^{(0)} = \left\{ \frac{\mathbb{H} : \widetilde{\boldsymbol{\sigma}}_{\text{dev}}}{2q^{\text{trial}}} \right\}_i; \quad i = 1, 2, 4, 5, 6 \tag{4.3.49}$$

$$Y_8^{(0)} = \Delta\epsilon_M^{P\,(0)} = \frac{\widetilde{q}Y_2^{(0)} - \widetilde{p}Y_1^{(0)}}{(1 - f^t)\,\sigma_Y} \tag{4.3.50}$$

$$Y_9^{(0)} = f^{(0)} = (1 - f^t)Y_1^{(0)} \tag{4.3.51}$$

This proposed initial solution is similar to the one proposed by Ben Bettaieb et al., (2011c) but without the need to introduce *damping* parameter β for $\Delta\epsilon_p$ and $\Delta\epsilon_q$. Numerical tests performed in Lagamine using a single element showed that the influence of this parameter is small.

In summary, the described approach is similar to that of Ben Bettaieb et al., (2011c) in terms of formulation but with important changes in the implementation. An important (and useful) characteristic of this algorithm is the generality, including the effect of anisotropy and kinematic hardening which are not often

[4]Convergence is not guaranteed at least if provided an initial solution *close enough* to the real solution.

seen. In terms of CPU time it was shown by Ben Bettaieb et al., (2011c) that the described algorithm shows a better performance compared to the Aravas, (1987) and Kojic et al., (2002) approaches. This characteristic comes from the fact that all the variables within Ben Bettaieb et al., (2011c) are implicitly integrated and calculated in a single loop while in Aravas, (1987) and Kojic et al., (2002) an additional loop is added to calculate the state variables. Adding a loop has a significant impact on the CPU time but reduces the complexity of the algorithm.

4.3.3 Integration using sub-intervals

The above described algorithm was developed for plasticity models in order to use large time steps. For the damage model this scheme is also useful but using large time steps in the localization regime does not guarantee good convergence. To simulate damage, small time steps are needed which implies high simulations times. A simple and convenient way to improve accuracy without a significant loss of CPU performance is using sub-intervals. This consists in dividing every time step with a given fraction:

$$\delta t = \frac{\Delta t}{N_{\text{intv}}} \tag{4.3.52}$$

where δt is the time step of the sub-interval and N_{intv} is a variable defined within the simulations files which is kept constant during the simulation. In LAGAMINE, this method was initially implemented by Charlier, (1987, section 5.2.2.4) for each material subroutine, thus circumventing the need of small time steps at the FE loop level.

As it was explained, sub-intervals are useful in particular cases but using a fixed value of N_{intv} all along the simulations will not result in an improved accuracy in most situations. Thus, Charlier, (1987) proposed to use an automatically adjusted N_{intv}. Wang, (1993, section 3.2.5.3) used a criterion based on the deformation level, where the number of sub-intervals is proportional to the equivalent strain. In the current implementation of the GTN model the following criterion is used:

$$N_{\text{intv}} = \max\left\{N_{\text{intv}}, N_\epsilon \Delta\boldsymbol{\epsilon}\right\} \tag{4.3.53}$$

where N_ϵ is weight of the strain increment $\Delta\boldsymbol{\epsilon}$. The relation between Δt (or δt) and $\Delta\boldsymbol{\epsilon}$ is given in Eq. 4.3.34. Wang, (1993) showed that the use of N_{intv} allowed to improve the results when the strain increments $\Delta\boldsymbol{\epsilon}$ are high without an important CPU cost.

Algorithm 1 Return-mapping algorithm applied to the GTN model. $\boldsymbol{Y}_n^{(k)}$ and k are the solution vector and iteration index respectively, from the Newton method described in algorithm 2.

procedure JACEXT

Initial data: $\dot{\boldsymbol{u}}_{n+1}$,$\boldsymbol{\sigma}_n$,$\boldsymbol{X}_n$,$\boldsymbol{Y}_n^{(k)}$,$k$

Compute the infinitesimal strain

$$\Delta\boldsymbol{\epsilon} := \frac{\Delta t}{2}\left(\nabla\dot{\boldsymbol{u}}_{n+1} + (\nabla\dot{\boldsymbol{u}}_{n+1})^T\right)$$

Compute elastic trial stress

$$\boldsymbol{\sigma}_{n+1}^{\text{trial}} := \boldsymbol{\sigma}_n + \mathbb{C} : \Delta\boldsymbol{\epsilon}$$

$$p_{n+1}^{\text{trial}} = \frac{1}{3}\,\text{tr}\left(\boldsymbol{\sigma}_{n+1}^{\text{trial}}\right); \qquad q_{n+1}^{\text{trial}} = \|\boldsymbol{\sigma}_{n+1}^{\text{trial}}\|_{\mathbb{H}}$$

Compute isotropic hardening: $\sigma_Y = \sigma_Y\left(H_{1n}\right)$ from Eq. 2.2.11 or Eq. 2.2.12

Test for plastic loading:

if $F_p\left(p_{n+1}^{\text{trial}}, q_{n+1}^{\text{trial}}, \boldsymbol{X}_n, \boldsymbol{H}_n\right) \leq 0$ **then**

Elastic step: $(\bullet)_{n+1} = (\bullet)_{n+1}^{\text{trial}}$

exit.

else

if $k = 0$ **then**

Calculate $\{\boldsymbol{Y}\}^{(0)}$ from Eq. 4.3.47-4.3.51

end if

Update variables $\Delta\epsilon_{p_n}$,$\Delta\epsilon_{q_n}$,$\boldsymbol{n}_n$,$\boldsymbol{H}_n$ from $\boldsymbol{Y}^{(k)}$

Update plastic strain, stress and backstress

$$\begin{aligned}
\Delta\boldsymbol{\epsilon}_{n+1}^P &= \frac{1}{3}\Delta\epsilon_{p_n}\boldsymbol{I} + \Delta\epsilon_{q_n}\boldsymbol{n}_n \\
\widetilde{\boldsymbol{\sigma}}_{n+1} &= \boldsymbol{\sigma}_{n+1}^{\text{trial}} - K_b\Delta\epsilon_{p_n}\boldsymbol{I} - 2G_s\Delta\epsilon_{q_n}\boldsymbol{n}_n - \boldsymbol{X}_n \\
\widetilde{p}_{n+1} &= \frac{1}{3}\,\text{tr}\left(\widetilde{\boldsymbol{\sigma}}_{n+1}\right); \qquad \widetilde{q}_{n+1} = \|\widetilde{\boldsymbol{\sigma}}_{n+1}\|_{\mathbb{H}} \\
\boldsymbol{X}_{n+1} &= (1 - q_1 H_{2n})\left(\frac{\boldsymbol{X}_n + C_X X_{\text{sat}}\Delta\boldsymbol{\epsilon}_{n+1}^P}{1 + C_X\Delta\epsilon_{q_n}}\right)
\end{aligned}$$

Compute residual $\boldsymbol{\Gamma}_{n+1}$ from Eq. 4.3.42-4.3.46

Compute jacobian matrix $\mathbb{J}$ in subroutine JACMOD (Appendix B)

Compute consistent tangent matrix $\mathbb{D}$ in subroutine TANMOD

end if

end procedure

Algorithm 2 Newton scheme used to solve the return-mapping algorithm 1. TOL is a tolerance value for convergence and NTRIAL is the maximum number of iterations.

Given $\{\boldsymbol{Y}\}^{(0)} \in \mathbb{R}^9$,
for $k = 0, 1, \ldots,$ NTRIAL **do**
  JACEXT($\{\boldsymbol{Y}\}^{(k)}$,$\{\boldsymbol{\Gamma}\}^{(k)}$,$[\mathbb{J}]^{(k)}$)
  if $\left\|\boldsymbol{\Gamma}^{(k)}\right\|_\infty <$ TOL **then**
    exit.
  else
    Solve $[\mathbb{J}]^{(k)}\{\Delta\boldsymbol{Y}\}^{(k)} = -\{\boldsymbol{\Gamma}\}^{(k)}$,
    $\{\boldsymbol{Y}\}^{(k+1)} := \{\boldsymbol{Y}\}^{(k)} + \{\Delta\boldsymbol{Y}\}^{(k)}$.
  end if
end for

4.4 Consistent tangent matrix calculation

In the context of the FE framework, it is often necessary to find a relation of the following type:

$$\boldsymbol{\sigma} = \boldsymbol{\sigma}(\boldsymbol{\epsilon}) \tag{4.4.1}$$

Despite particular cases (such as linear isotropic elasticity), this expression is usually given by a non-linear constitutive equation. Linearization[5] of this expression leads to:

$$d\boldsymbol{\sigma} = \frac{\partial \boldsymbol{\sigma}(\boldsymbol{\epsilon})}{\partial \boldsymbol{\epsilon}} : d\boldsymbol{\epsilon} \qquad \text{or} \qquad d\boldsymbol{\sigma} = \mathbb{D} : d\boldsymbol{\epsilon} \tag{4.4.2}$$

where $d\boldsymbol{\sigma}$ and $d\boldsymbol{\epsilon}$ are the total derivatives of the Cauchy stress tensor and natural strain tensor respectively. Here, we define $\mathbb{D}$ as the tangent modulus. In an implicit time integration scheme the stiffness matrix should be calculated at the end of the present step. It is clear that in order to find $\mathbb{D}$ it is necessary to find expressions including both total derivatives. To do so two common approaches are usually used:

- *Continuum approach*, through differentiation of the continuum equations of Box 4.3.1.
- *Algorithm approach*, through differentiation of the return-mapping equations of algorithm 1.

The continuum approach was firstly used because it arises naturally by enforcing the consistency condition from the set of governing equations (Box 4.3.1). This method however, is not ideal since the asymptotic quadratic convergence of the Newton method (at element level) is lost when the time step is not infinitesimally small, thus requiring small time steps elsewhere in the simulation. This observation was first noted by Nagtegaal, (1982). Based on this observation, Simo and

[5]Linearization is the approximation of a given (non-linear) function at a given point using a linear function. In this case, the tensor function $\boldsymbol{\sigma}$ is approximated at $\boldsymbol{\epsilon}$ using a Taylor's expansion. Higher order terms are omitted.

Taylor, (1985) proved that a *consistent* tangent matrix derived by linearizing the set of *incrementally* formulated equations keeps the quadratic convergence rate. This crucial difference allows to use bigger time steps. Note that when the *continuum approach* is used with infinitesimal time steps it should converge to the *algorithm approach*. In practical terms, this is not feasible and both approaches differ if large time steps are used as depicted in Fig. 4.2.

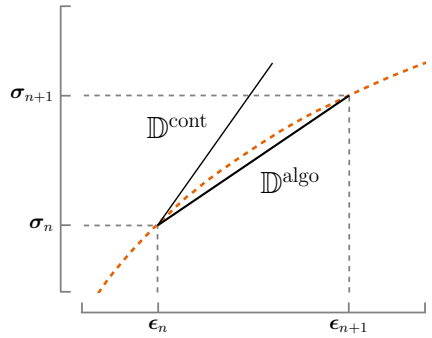

Figure 4.2: Comparison between the *continuum approach* and the *algorithm approach* to calculate the tangent modulus. In the *algorithm approach* the consistency condition is enforced at $n+1$.

For cases without kinematic hardening, the *classical* algorithm approach to obtain the consistent tangent modulus involves linearization of Eq. 4.3.38:

$$d\boldsymbol{\sigma} = \mathbb{C} : \left(d\Delta\boldsymbol{\epsilon} - d\Delta\epsilon_p \boldsymbol{I} - d\Delta\epsilon_q \boldsymbol{n} - d\Delta\epsilon_q \frac{\partial \boldsymbol{n}}{\partial \boldsymbol{\sigma}} : d\boldsymbol{\sigma} \right) \tag{4.4.3}$$

Subsequently, a system is solved to find $d\Delta\epsilon_p$ and $d\Delta\epsilon_q$ by enforcing the consistency condition. Note that formulating the plastic corrector in terms of $\Delta\epsilon_p$ and $\Delta\epsilon_q$ avoids calculating $d\lambda$ as in the original continuum or algorithmic approach by Simo and Taylor, (1985). Kim and Gao, (2005) highlighted that $d\lambda$ can be hard to evaluate when the constitutive equations are complex. Hence, they proposed a new way to obtain the tangent modulus based on the linearization procedure of Aravas, (1987) but using $d\Delta\boldsymbol{\epsilon}^P$ instead of $d\Delta\epsilon_p$ and $d\Delta\epsilon_q$ as primary unknowns. This choice has the following implications:

- A more generalized procedure for models which are not developed in terms of p and q (or $\Delta\epsilon_p$ and $\Delta\epsilon_q$). For instance, Kim and Gao, (2005) took the Gologanu-Leblond-Devaux model (Gologanu et al., 1993) as an application of this approach.
- Less analytical derivatives evaluations ($\frac{\partial(\bullet)}{\partial\boldsymbol{\sigma}}$ instead of $\frac{\partial(\bullet)}{\partial p}$ and $\frac{\partial(\bullet)}{\partial q}$).
- Instead of the two scalar unknowns ($d\Delta\epsilon_p$ and $d\Delta\epsilon_q$), now there are 9 unknowns corresponding to the components of $d\Delta\boldsymbol{\epsilon}^p$ (reduced to 6 unknowns if the Cauchy stress tensor is used).

Below we describe a generalization of the Kim and Gao, (2005) approach proposed by Ben Bettaieb et al., (2011c) which extended the above approach to kinematic

hardening. Hence, the yield function is also dependent on the backstress, which itself depends on the plastic strain.

4.4.1 Kim and Gao, (2005) approach

The procedure starts with the elastic relation which in terms of the increments is expressed as:

$$\boldsymbol{\sigma}_{n+1} = \mathbb{C} : \left(\boldsymbol{\epsilon}_{n+1} - \boldsymbol{\epsilon}^P_{n+1}\right) = \mathbb{C} : \left(\boldsymbol{\epsilon}_{n+1} - \boldsymbol{\epsilon}^P_{n} - \Delta\boldsymbol{\epsilon}^P_{n+1}\right) \tag{4.4.4}$$

Note that here the plastic flow is not *freezed* as for the trial elastic state in Eq. 4.3.35. Linearizing this equation leads to:

$$d\boldsymbol{\sigma} = \mathbb{C} : d\boldsymbol{\epsilon} - \mathbb{C} : d\Delta\boldsymbol{\epsilon}^P \tag{4.4.5}$$

As all variables are referred to step $n+1$ the subscript is removed for the sake of simplicity. It is easy to observe that finding a relation between $d\Delta\boldsymbol{\epsilon}^P$ and $d\boldsymbol{\epsilon}$ will define the tangent modulus. In order to achieve this some previous mathematical manipulations are needed. It will be shown throughout this section that $d\Delta\boldsymbol{\epsilon}^P$ can be conveniently related to $d\boldsymbol{\sigma}$ with:

$$\mathbb{K} : d\Delta\boldsymbol{\epsilon}^P = \mathbb{L} : d\boldsymbol{\sigma} \tag{4.4.6}$$

where $\mathbb{K}$ and $\mathbb{L}$ are coefficient tensors. Substituting $d\boldsymbol{\sigma}$ of Eq. 4.4.5 in Eq. 4.4.6, we obtain:

$$d\Delta\boldsymbol{\epsilon}^P = (\mathbb{K} + \mathbb{L}\mathbb{C})^{-1} : (\mathbb{L}\mathbb{C} : d\boldsymbol{\epsilon}) \tag{4.4.7}$$

Replacing Eq. 4.4.7 in Eq. 4.4.5, the tangent modulus can be expressed as:

$$\mathbb{D} = \mathbb{C} - \mathbb{C}(\mathbb{K} + \mathbb{L}\mathbb{C})^{-1}\mathbb{L}\mathbb{C} \tag{4.4.8}$$

Thus, the determination of the tangent modulus $\mathbb{D}$ is reduced to find the coefficient tensors $\mathbb{K}$ and $\mathbb{L}$. Given the symmetry of the Cauchy stress tensor, six equations are needed to express the tensor coefficients from the total derivatives of the yield surface and the flow rule:

$$F_p\left(\boldsymbol{\sigma}, \boldsymbol{\epsilon}^P, H_\alpha\right) = 0 \tag{4.4.9}$$

$$\Delta\boldsymbol{\epsilon}^P = \Delta\lambda \frac{\partial F_p}{\partial \boldsymbol{\sigma}} \tag{4.4.10}$$

The first equation for $[\mathbb{K}]$ and $[\mathbb{L}]$ is given by the total derivative of the yield condition dF_p:

$$dF_p = \frac{\partial F_p}{\partial \boldsymbol{\sigma}} : d\boldsymbol{\sigma} + \frac{\partial F_p}{\partial \Delta\boldsymbol{\epsilon}^P} : d\Delta\boldsymbol{\epsilon}^P + \frac{\partial F_p}{\partial H_\alpha} : dH_\alpha = 0 \tag{4.4.11}$$

where:

$$dH_\alpha = C_{\alpha\beta}\left(\frac{\partial h_\beta}{\partial \boldsymbol{\sigma}} : d\boldsymbol{\sigma} + \frac{\partial h_\beta}{\partial \Delta\boldsymbol{\epsilon}^P} : d\Delta\boldsymbol{\epsilon}^P\right) \tag{4.4.12}$$

and:

$$C_{\alpha\beta} = \left(\delta_{\alpha\beta} - \frac{\partial h_\alpha}{\partial H_\beta}\right)^{-1}; \qquad \alpha,\beta = 1,2 \tag{4.4.13}$$

as there are two state variables. δ is the Kronecker delta. Factorization in terms of the total derivatives leads to:

$$\left(\frac{\partial F_p}{\partial \Delta\boldsymbol{\epsilon}^P} + \frac{\partial F_p}{\partial H_\alpha} C_{\alpha\beta} \frac{\partial h_\beta}{\partial \Delta\boldsymbol{\epsilon}^P}\right) : d\Delta\boldsymbol{\epsilon}^P + \left(\frac{\partial F_p}{\partial \boldsymbol{\sigma}} + \frac{\partial F_p}{\partial H_\alpha} C_{\alpha\beta} \frac{\partial h_\beta}{\partial \boldsymbol{\sigma}}\right) : d\boldsymbol{\sigma} = 0 \tag{4.4.14}$$

Hence, the first line of the coefficient tensor is given by:

$$[\mathbb{K}]_{1j} = \frac{\partial F_p}{\partial \Delta\boldsymbol{\epsilon}^P} + \frac{\partial F_p}{\partial H_\alpha} C_{\alpha\beta} \frac{\partial h_\beta}{\partial \Delta\boldsymbol{\epsilon}^P}; \qquad \alpha,\beta = 1,2 \tag{4.4.15}$$

$$[\mathbb{L}]_{1j} = \frac{\partial F_p}{\partial \boldsymbol{\sigma}} + \frac{\partial F_p}{\partial H_\alpha} C_{\alpha\beta} \frac{\partial h_\beta}{\partial \boldsymbol{\sigma}}; \qquad \alpha,\beta = 1,2 \tag{4.4.16}$$

The remaining equations are derived from the flow rule. However, the form of Eq. 4.4.10 is not useful as the plastic multiplicator is included. Rearranging the flow rule in terms of the components and removing $\Delta\lambda$:

$$\frac{\Delta\epsilon^P_{11}}{\left(\frac{\partial F_p}{\partial \sigma_{11}}\right)} = \frac{\Delta\epsilon^P_{22}}{\left(\frac{\partial F_p}{\partial \sigma_{22}}\right)} = \frac{\Delta\epsilon^P_{33}}{\left(\frac{\partial F_p}{\partial \sigma_{33}}\right)} = \frac{\Delta\epsilon^P_{12}}{\left(\frac{\partial F_p}{\partial \sigma_{12}}\right)} = \frac{\Delta\epsilon^P_{13}}{\left(\frac{\partial F_p}{\partial \sigma_{13}}\right)} = \frac{\Delta\epsilon^P_{23}}{\left(\frac{\partial F_p}{\partial \sigma_{23}}\right)} = \Delta\lambda \tag{4.4.17}$$

Five linearly independent equations are obtained:

$$\begin{aligned}
\Upsilon_1 &= \Delta\epsilon^P_{11}\left(\frac{\partial F_p}{\partial \sigma_{22}}\right) - \Delta\epsilon^P_{22}\left(\frac{\partial F_p}{\partial \sigma_{11}}\right) = 0 \\
\Upsilon_2 &= \Delta\epsilon^P_{11}\left(\frac{\partial F_p}{\partial \sigma_{33}}\right) - \Delta\epsilon^P_{33}\left(\frac{\partial F_p}{\partial \sigma_{11}}\right) = 0 \\
\Upsilon_3 &= \Delta\epsilon^P_{11}\left(\frac{\partial F_p}{\partial \sigma_{12}}\right) - \Delta\epsilon^P_{12}\left(\frac{\partial F_p}{\partial \sigma_{11}}\right) = 0 \\
\Upsilon_4 &= \Delta\epsilon^P_{11}\left(\frac{\partial F_p}{\partial \sigma_{13}}\right) - \Delta\epsilon^P_{13}\left(\frac{\partial F_p}{\partial \sigma_{11}}\right) = 0 \\
\Upsilon_5 &= \Delta\epsilon^P_{11}\left(\frac{\partial F_p}{\partial \sigma_{23}}\right) - \Delta\epsilon^P_{23}\left(\frac{\partial F_p}{\partial \sigma_{11}}\right) = 0
\end{aligned} \tag{4.4.18}$$

The total derivative of, for instance Υ_1 leads to:

$$d\Upsilon_1 = \Delta\epsilon^P_{11}\partial\left(\frac{\partial F_p}{\partial \sigma_{22}}\right) + \left(\frac{\partial F_p}{\partial \sigma_{22}}\right)\partial\left(\Delta\epsilon^P_{11}\right) - \Delta\epsilon^P_{22}\partial\left(\frac{\partial F_p}{\partial \sigma_{11}}\right) - \left(\frac{\partial F_p}{\partial \sigma_{11}}\right)\partial\left(\Delta\epsilon^P_{22}\right) = 0 \tag{4.4.19}$$

which applies to Υ_2, Υ_3, Υ_4 and Υ_5 too. After some mathematical manipulations we have the rest of the equations completing the system in the form:

$$\begin{aligned}
[\mathbb{K}]_{ij} =& -\frac{\partial^2 F_p}{\partial\sigma_i\partial\Delta\boldsymbol{\epsilon}^P}\Delta\epsilon_{11}^P + \frac{\partial^2 F_p}{\partial\sigma_{11}\partial\Delta\boldsymbol{\epsilon}^P}\Delta\epsilon_i^P + \dots \\
& \left(-\frac{\partial^2 F_p}{\partial\sigma_i\partial H_\beta}\Delta\epsilon_{11}^P + \frac{\partial^2 F_p}{\partial\sigma_{11}\partial H_\beta}\Delta\epsilon_i^P\right) C_{\alpha\beta}\frac{\partial h_\alpha}{\partial\Delta\boldsymbol{\epsilon}^P} + \dots \\
& \frac{\partial F_p}{\partial\sigma_{11}}\Delta\epsilon_i^P - \frac{\partial F_p}{\partial\sigma_i}\Delta\epsilon_{11}^P; \qquad i = 2,\dots,6, \quad \alpha,\beta = 1,2
\end{aligned} \tag{4.4.20}$$

$$\begin{aligned}
[\mathbb{L}]_{ij} =& \frac{\partial^2 F_p}{\partial\sigma_i\partial\boldsymbol{\sigma}}\Delta\epsilon_i^P - \frac{\partial^2 F_p}{\partial\sigma_{11}\partial\boldsymbol{\sigma}}\Delta\epsilon_{11}^P + \dots \\
& \left(\frac{\partial^2 F_p}{\partial\sigma_i\partial H_\beta}\Delta\epsilon_{11}^P - \frac{\partial^2 F_p}{\partial\sigma_{11}\partial H_\beta}\Delta\epsilon_i^P\right) C_{\alpha\beta}\frac{\partial h_\alpha}{\partial\boldsymbol{\sigma}}; \qquad i = 2,\dots,6, \quad \alpha,\beta = 1,2
\end{aligned} \tag{4.4.21}$$

In order to avoid the abuse of notation $\sigma_i = \{\boldsymbol{\sigma}\}_i$ in the contravariant representation. The full set of derivatives can be found in appendix B.3. In the implemented subroutine the consistent tangent matrix is calculated within the function `TANMOD`.

4.5 New extensions

In the previous sections, the equations and algorithms of the implemented Gurson model in LAGAMINE were presented. This review was largely based on the works of Aravas, (1987), Kim and Gao, (2005) and Ben Bettaieb et al., (2011c). None of them, however, include the nucleation and coalescence as in the GTN model. Taking the already presented basis and notations, a new subroutine called `GUR3Dext` is developed combining the *classical* GTN model (i.e., nucleation and coalescence) with shear extensions. A comparison of the implemented subroutines[6] with the new subroutine is shown in Table 4.1. Herein, the (incrementally formulated) equations involved in the extensions are detailed. The step subscript n is dropped from the subsequent developments. For further details about the GTN extensions, see section 3.3.2.

4.5.1 GTN extension

As in Chu and Needleman, (1980), nucleation is added to void growth:

$$\Delta f = \Delta f_g + \Delta f_n \tag{4.5.1}$$

If strain-driven nucleation is assumed, we have:

$$\Delta f_n = \mathcal{A}\Delta\epsilon_M^P \tag{4.5.2}$$

[6]It is worth to note that despite being similar to the previous versions the new subroutine GUR3Dext was entirely reprogrammed.

and:

$$\mathcal{A}\left(\epsilon_M^P\right) = \frac{f_N}{S_N\sqrt{2\pi}} \exp\left[-\frac{1}{2}\left(\frac{\epsilon_M^P - \epsilon_N}{S_N}\right)^2\right]$$

Hence, Eq. 4.3.46 and Eq: 4.3.31 are modified within `GURD3EXT`:

$$\Gamma_9 = f - \frac{f^t + \Delta\epsilon_p + \mathcal{A}\Delta\epsilon_M^P}{1 + \Delta\epsilon_p} \tag{4.5.3}$$

$$h_2 := (1-f)\Delta\epsilon_p + \mathcal{A}\Delta\epsilon_M^P \tag{4.5.4}$$

The coalescence follows the yield condition modification proposed by Tvergaard and Needleman, (1984):

$$F_p\left(p, q, \boldsymbol{X}, \epsilon_M^P, f\right) = 0 \quad \rightarrow \quad F_p\left(p, q, \boldsymbol{X}, \epsilon_M^P, f^*\right) = 0 \tag{4.5.5}$$

where f^* is the so-called *effective porosity* which changes during the onset of coalescence:

$$f^* = \begin{cases} f & \text{if } f < f_{cr} \\ f_{cr} + K_f(f - f_{cr}) & \text{if } f > f_{cr} \end{cases} \tag{4.5.6}$$

Thus, new derivatives involving F_p should be obtained. This extension only modifies the yield condition, so the state variable equations (Eq. 4.3.30 and Eq. 4.3.31) with porosity f as a variable, remain unchanged. Box 4.5.1 summarizes the equations needed for this extension.

4.5.2 Extension by Xue, (2008)

This shear extension expands the concept of void volume fraction by introducing a damage variable D, which replaces the effective porosity acting in the coalescence phase (see section 3.4.2). Xue, (2008) expresses the yield surface equation in terms of the damage variable D in the following way:

$$F_p = \frac{\widetilde{q}^2}{{\sigma_Y}^2} - 1 + 2D\cosh\left(-\frac{3q_2\widetilde{p}}{\kappa\sigma_Y}\right) - D^2 = 0 \tag{4.5.7}$$

where $D = q_1 f^*$. Hence, a new internal variable is introduced into the integration scheme:

$$H_3 := D \tag{4.5.8}$$

with the related evolution equations:

$$h_3 := \Delta D = K_D\left(q_1\Delta f + \Delta D_{\text{shear}}\right) \tag{4.5.9}$$

where ΔD_{shear} is the contribution due to shear:

$$\Delta D_{\text{shear}} = k_g f^{q_4} g_\theta(\boldsymbol{\sigma})\epsilon_q\Delta\epsilon_q \tag{4.5.10}$$

k_g is a material parameter and $q_4 = 1/3$ for 3D problems. $g_\theta(\boldsymbol{\sigma})$ is a function dependent on the third deviatoric stress invariant:

$$g_\theta(\boldsymbol{\sigma}) = \frac{2}{\pi}\arccos\left(\frac{27}{2}\frac{J_3}{q^3}\right) \tag{4.5.11}$$

Box 4.5.1: New equations for the GTN extension indicating the modified subroutine.

- Initial guess (JACEXT)

$$Y_9^{(0)} = f^{(0)} = (1 - f^t)Y_1^{(0)} + \mathcal{A}Y_8^{(0)}$$

- Extension of Jacobian derivatives (JACMOD)

  Nucleation:

$$\begin{aligned}
\frac{\partial \Gamma_9}{\partial \Delta\epsilon_p} &= \frac{-1 + f^t + \mathcal{A}\Delta\epsilon_M^P}{(1 + \Delta\epsilon_p)^2} \\
\frac{\partial \Gamma_9}{\partial \Delta\epsilon_q} &= \frac{\partial \Gamma_9}{\partial \Delta n_i} = 0; \quad i = 1, \ldots, 5 \\
\frac{\partial \Gamma_9}{\partial \Delta\epsilon_M^P} &= -\frac{\mathcal{A}}{1 + \Delta\epsilon_p} \\
\frac{\partial \Gamma_9}{\partial f} &= 1
\end{aligned}$$

  Coalescence:

$$\begin{aligned}
\alpha_1 &= -3\frac{q_2\widetilde{p}}{\kappa\sigma_Y} \\
\frac{\partial \Gamma_1}{\Delta f} &= 2q_1K_f\cosh(\alpha_1) - 2q_3f^*K_f \\
\frac{\partial \Gamma_2}{\Delta f} &= \Delta\epsilon_q\left(-\frac{6K_fq_1q_2\sinh(\alpha_1)}{\kappa\sigma_Y}\right)
\end{aligned}$$

- Extension of tangent matrix derivatives (TANMOD)

  Nucleation:

$$\begin{aligned}
\frac{\partial h_2}{\partial \Delta\boldsymbol{\epsilon}^P} &= (1 - f)\boldsymbol{I} \\
\frac{\partial h_2}{\partial \boldsymbol{\sigma}} &= \mathcal{A}\frac{\Delta\boldsymbol{\epsilon}^P}{(1 - f)\sigma_Y} \\
\frac{\partial h_2}{\partial f} &= -\Delta\epsilon_p \\
\frac{\partial h_2}{\partial \sigma_Y} &= -\mathcal{A}\frac{\widetilde{\boldsymbol{\sigma}} : \Delta\boldsymbol{\epsilon}^P}{(1 - f)\sigma_Y^2}
\end{aligned}$$

  Coalescence:

$$\begin{aligned}
\frac{\partial F_p}{\partial f} &= -\frac{\widetilde{\boldsymbol{\sigma}} : \mathbb{H} : \dfrac{\partial \boldsymbol{X}}{\partial f}}{\sigma_Y^2} + 2q_1K_f\cosh(\alpha_1) + 2q_1f^*\frac{\partial \alpha_1}{\partial f} - 2q_3f^*K_f \\
\frac{\partial^2 F_p}{\partial \boldsymbol{\sigma}\partial f} &= -\frac{\mathbb{H} : \dfrac{\partial \boldsymbol{X}}{\partial f}}{\sigma_Y^2} + 2q_1K_f\frac{\partial \alpha_1}{\partial \boldsymbol{\sigma}}\sinh(\alpha_1) + 2q_1f^*\frac{\partial \alpha_1}{\partial \boldsymbol{\sigma}}\frac{\partial \alpha_1}{\partial f}\cosh\alpha_1
\end{aligned}$$

Coalescence is introduced through the term K_D, defined as in the GTN model:

$$K_D = \begin{cases} 1 & \text{if } D < D_{cr} \\ \frac{1/q_1 - f_c}{f_F - f_c} & \text{if } D > D_{cr} \end{cases} \tag{4.5.12}$$

To implement this proposal in the existent integration scheme, the unknown vector is now defined by:

$$Y_i = \{\Delta\epsilon_p, \Delta\epsilon_q, n_1, n_2, n_3, n_4, n_5, H_\alpha\} \tag{4.5.13}$$

$$H_1 = \Delta\epsilon_M^P, \quad H_2 = f, \quad H_3 = D \tag{4.5.14}$$

With this newly defined set of equations the modifications of the previous set of equations are:

$$\Gamma_1 = F_p = \frac{\widetilde{q}^2}{{\sigma_Y}^2} - 1 + 2q_1 f \cosh\left(-\frac{3q_2\widetilde{p}}{\kappa\sigma_Y}\right) - q_3 f^2 = 0 \tag{4.5.15}$$

$$\Gamma_9 = f - \frac{f^t + \Delta\epsilon_p}{1 + \Delta\epsilon_p} = 0 \tag{4.5.16}$$

$$\Gamma_{10} = D - D^t - K_D\left(q_1\Delta f + \Delta D_{\text{shear}}\right) = 0 \tag{4.5.17}$$

Box 4.5.2 summarizes the equations needed for this extension.

4.5.3 Extension by Nahshon and Hutchinson, (2008)

In the extension from Nahshon and Hutchinson, (2008) the only modification in the original Gurson model comes from the void evolution relation. Thus, the void function is governed by the following equation:

$$\Delta f = \Delta f_n + \Delta f_g + \Delta f_s \tag{4.5.18}$$

where:

$$\Delta f_s = k_\omega f \omega(\boldsymbol{\sigma}) \frac{\widetilde{\boldsymbol{\sigma}}_{\text{dev}} : \Delta\boldsymbol{\epsilon}^P}{\widetilde{q}} \tag{4.5.19}$$

k_ω is a material constant and $\omega(\boldsymbol{\sigma})$ a stress measure defined as:

$$\omega(\boldsymbol{\sigma}) = 1 - \chi(\boldsymbol{\sigma})^2 = 1 - \left(\frac{27}{2}\frac{J_3}{q}\right)^2; \qquad 0 \leq \omega \leq 1 \tag{4.5.20}$$

Box 4.5.3 resumes the equations needed for this extension.

Box 4.5.2: New equations for the Xue, (2008) shear extension indicating the modified subroutine.

- Initial guess (JACEXT)

$$\begin{aligned} Y_9^{(0)} =& f^{(0)} = (1-f^t)Y_1^{(0)} + \mathcal{A}Y_8^{(0)} \\ \Delta D_{\text{shear}}^{(0)} =& k_g \left(Y_9^{(0)}\right)^{q_4} g_\theta(\boldsymbol{\sigma})\epsilon_q Y_2^{(0)} \\ Y_{10}^{(0)} =& D^{(0)} = K_D \left[q_1 \left(Y_9^{(0)} - f^t\right) + \Delta D_{\text{shear}}^{(0)}\right] \end{aligned}$$

- Extension of Jacobian derivatives (JACMOD)

$$\begin{aligned} \frac{\partial \Gamma_1}{\partial D} &= 2\cosh\left(-3\frac{q_2\widetilde{p}}{\kappa\sigma_Y}\right) - 2D \\ \frac{\partial \Gamma_2}{\partial D} &= -6\frac{q_2}{\kappa\sigma_Y}\sinh\left(-3\frac{q_2\widetilde{p}}{\kappa\sigma_Y}\right)\Delta\epsilon_q \\ \frac{\partial \Gamma_j}{\partial D} &= 0, \qquad j = 3,\ldots,9 \end{aligned}$$

$$\begin{aligned} \frac{\partial \Gamma_{10}}{\partial \Delta\epsilon_p} &= -K_D q_1 (1-f) \\ \frac{\partial \Gamma_{10}}{\partial \Delta\epsilon_q} &= -K_D k_g f^{q_4} g_\theta(\boldsymbol{\sigma})\epsilon_q \\ \frac{\partial \Gamma_{10}}{\partial n_i} &= -K_D k_g f^{q_4}\epsilon_q \Delta\epsilon_q \frac{\partial g_\theta(\boldsymbol{\sigma})}{\partial n_i}; \quad i = 1,\ldots,5 \\ \frac{\partial \Gamma_{10}}{\partial \Delta\epsilon_M^P} &= -K_D q_1 \mathcal{A} \\ \frac{\partial \Gamma_{10}}{\partial f} &= K_D q_1 \Delta\epsilon_p - K_D k_g q_4 f^{q_4-1} g_\theta(\boldsymbol{\sigma})\epsilon_q \Delta\epsilon_q \\ \frac{\partial \Gamma_{10}}{\partial D} &= 1 \end{aligned}$$

$$\frac{\partial g_\theta}{\partial n_i} = \frac{27}{k_g \pi\sqrt{1-\chi^2}}\left(\frac{\partial J_3}{\partial n_i} - 3\frac{J_3}{q}\frac{\partial q}{\partial n_i}\right); \quad i = 1,\ldots,5$$

where:

$$\chi = \frac{27}{2}\frac{J_3}{q^3}$$

- Extension of tangent matrix derivatives (TANMOD)

$$\frac{\partial h_1}{\partial H_3} = \frac{\partial h_2}{\partial H_3} = \frac{\partial h_3}{\partial H_3} = 0$$

$$\begin{aligned}
\frac{\partial h_3}{\partial H_1} =& K_D q_1 \frac{\partial \Delta f}{\partial f} + K_D k_g q_4 f^{q_4 - 1} g_\theta(\boldsymbol{\sigma}) \epsilon_q \Delta \epsilon_q \\
\frac{\partial h_3}{\partial H_2} =& - K_D q_2 \frac{\widetilde{\boldsymbol{\sigma}} : \Delta \boldsymbol{\epsilon}^P}{(1-f)\sigma_Y^2} \\
\frac{\partial h_3}{\partial \boldsymbol{\sigma}} =& K_D k_g f^{q_4} \epsilon_q \Delta \epsilon_q \frac{\partial g_\theta(\boldsymbol{\sigma})}{\partial \boldsymbol{\sigma}} \\
\frac{\partial h_3}{\partial \Delta \boldsymbol{\epsilon}^P} =& K_D q_1 (1-f) \frac{\partial \Delta \epsilon_p}{\partial \Delta \boldsymbol{\epsilon}^P} + K_D k_g q_4 f^{q_4 - 1} g_\theta(\boldsymbol{\sigma}) \epsilon_q \frac{\partial \Delta \epsilon_q}{\partial \Delta \boldsymbol{\epsilon}^P}
\end{aligned}$$

$$\frac{\partial g_\theta}{\partial \boldsymbol{\sigma}} = \frac{27}{k_g \pi \sqrt{1-\chi^2}} \left(\frac{\partial J_3}{\partial \boldsymbol{\sigma}} - 3 \frac{J_3}{q} \frac{\partial q}{\partial \boldsymbol{\sigma}} \right)$$

Box 4.5.3: New equations for the Nahshon and Hutchinson, (2008) shear extension indicating the modified subroutine.

- Initial guess (JACEXT)

$$Y_9^{(0)} = f^{(0)} = \mathcal{A}Y_8^{(0)} + (1-f^t)Y_1^{(0)} + k_\omega f^t \omega(\boldsymbol{\sigma}^{\text{trial}}) \frac{\widetilde{\boldsymbol{\sigma}}_{\text{dev}}^{\text{trial}} : \Delta\boldsymbol{\epsilon}^P}{\widetilde{q}^{\text{trial}}}$$

- Extension of Jacobian derivatives (JACMOD)

$$\Gamma_9 = f - \frac{f^t + \Delta\epsilon_p + \mathcal{A}\Delta\epsilon_M^P}{\Delta\epsilon_{\text{smod}}} = 0$$

where:

$$\Delta\epsilon_{\text{smod}} = 1 + \Delta\epsilon_p - \Delta\epsilon_\omega$$

$$\Delta\epsilon_\omega = \frac{k_\omega \omega(\boldsymbol{\sigma})\widetilde{\boldsymbol{\sigma}}_{\text{dev}}}{\widetilde{q}} \left(\frac{1}{3}\Delta\epsilon_p \boldsymbol{I} + \Delta\epsilon_q \boldsymbol{n} \right)$$

$$\begin{aligned}
\frac{\partial\Gamma_9}{\partial\Delta\epsilon_p} &= -\frac{1}{\Delta\epsilon_{\text{smod}}} - \frac{f^t + \Delta\epsilon_p + \mathcal{A}\Delta\epsilon_M^P}{\Delta\epsilon_{\text{smod}}^2}\left(1 - \frac{\partial\Delta\epsilon_\omega}{\partial\Delta\epsilon_p}\right) \\
\frac{\partial\Gamma_9}{\partial\Delta\epsilon_q} &= -\frac{f^t + \Delta\epsilon_p + \mathcal{A}\Delta\epsilon_M^P}{\Delta\epsilon_{\text{smod}}^2}\frac{\partial\Delta\epsilon_\omega}{\partial\Delta\epsilon_q} \\
\frac{\partial\Gamma_9}{\partial n_i} &= -\frac{f^t + \Delta\epsilon_p + \mathcal{A}\Delta\epsilon_M^P}{\Delta\epsilon_{\text{smod}}^2}\frac{\partial\Delta\epsilon_\omega}{\partial n_i}; \qquad i = 1,\ldots,5 \\
\frac{\partial\Gamma_9}{\partial\Delta\epsilon_M^P} &= -\frac{\mathcal{A}}{\Delta\epsilon_{\text{smod}}} \\
\frac{\partial\Gamma_9}{\partial f} &= 1 - \frac{f^t + \Delta\epsilon_p + \mathcal{A}\Delta\epsilon_M^P}{\Delta\epsilon_{\text{smod}}^2}\frac{\partial\Delta\epsilon_\omega}{\partial f}
\end{aligned}$$

where:

$$\begin{aligned}
\frac{\partial\Delta\epsilon_\omega}{\partial\Delta\epsilon_p} &= \frac{k_\omega\omega(\widetilde{\boldsymbol{\sigma}})}{\widetilde{q}}\left(\widetilde{\boldsymbol{\sigma}}_{\text{dev}}\frac{\partial\Delta\boldsymbol{\epsilon}^P}{\partial\Delta\epsilon_p} + \frac{\partial\widetilde{\boldsymbol{\sigma}}_{\text{dev}}}{\partial\Delta\epsilon_p}\Delta\boldsymbol{\epsilon}^P + \frac{\widetilde{\boldsymbol{\sigma}}_{\text{dev}}\Delta\boldsymbol{\epsilon}^P}{\widetilde{q}}\frac{\partial\widetilde{q}}{\partial\Delta\epsilon_p}\right) \\
\frac{\partial\Delta\epsilon_\omega}{\partial\Delta\epsilon_q} &= \frac{k_\omega\omega(\widetilde{\boldsymbol{\sigma}})}{\widetilde{q}}\left(\widetilde{\boldsymbol{\sigma}}_{\text{dev}}\frac{\partial\Delta\boldsymbol{\epsilon}^P}{\partial\Delta\epsilon_q} + \frac{\partial\widetilde{\boldsymbol{\sigma}}_{\text{dev}}}{\partial\Delta\epsilon_q}\Delta\boldsymbol{\epsilon}^P + \frac{\widetilde{\boldsymbol{\sigma}}_{\text{dev}}\Delta\boldsymbol{\epsilon}^P}{\widetilde{q}}\frac{\partial\widetilde{q}}{\partial\Delta\epsilon_q}\right) \\
\frac{\partial\Delta\epsilon_\omega}{\partial n_i} &= \frac{k_\omega}{\widetilde{q}}\left(\widetilde{\boldsymbol{\sigma}}_{\text{dev}}\Delta\boldsymbol{\epsilon}^P\frac{\partial\omega(\boldsymbol{\sigma})}{\partial n_i} + \omega(\boldsymbol{\sigma})\Delta\boldsymbol{\epsilon}^P\frac{\partial\widetilde{\boldsymbol{\sigma}}_{\text{dev}}}{\partial n_i} + \ldots\right. \\
&\qquad \left. \cdots + \omega(\boldsymbol{\sigma})\widetilde{\boldsymbol{\sigma}}_{\text{dev}}\frac{\partial\Delta\boldsymbol{\epsilon}^P}{\partial n_i} - \frac{\omega(\boldsymbol{\sigma})\widetilde{\boldsymbol{\sigma}}_{\text{dev}}\Delta\boldsymbol{\epsilon}^P}{\widetilde{q}}\frac{\partial\widetilde{q}}{\partial n_i}\right); \quad i = 1,\ldots,5 \\
\frac{\partial\Delta\epsilon_\omega}{\partial f} &= \frac{k_\omega\omega(\boldsymbol{\sigma})}{\widetilde{q}}\left(\frac{\partial\widetilde{\boldsymbol{\sigma}}_{\text{dev}}}{\partial f}\Delta\boldsymbol{\epsilon}^P - \frac{\widetilde{\boldsymbol{\sigma}}_{\text{dev}}\Delta\boldsymbol{\epsilon}^P}{\widetilde{q}}\frac{\partial\widetilde{q}}{\partial f}\right)
\end{aligned}$$

and:

$$\frac{\partial\omega(\boldsymbol{\sigma})}{\partial n_i} = \frac{27\sqrt{1-\omega(\boldsymbol{\sigma})}}{q}\left(\frac{1}{q^2}\frac{\partial J_3}{\partial\boldsymbol{\sigma}}\frac{\partial\boldsymbol{\sigma}}{\partial n_i} - \frac{2\sqrt{1-\omega(\boldsymbol{\sigma})}}{9}\frac{\partial q}{\partial n_i}\right); i = 1,...,5$$

- Extension of tangent matrix derivatives (TANMOD)

$$\frac{\partial h_2}{\Delta\boldsymbol{\epsilon}^P}, \frac{\partial h_2}{\boldsymbol{\sigma}}, \frac{\partial h_2}{\partial H_\beta}, \quad \beta = 1, 2,$$

with,

$$h_2 = \mathcal{A}\Delta\epsilon_M^P + (1-f)\Delta\epsilon_p + k_\omega f\omega(\boldsymbol{\sigma})\frac{\widetilde{\boldsymbol{\sigma}}_{\text{dev}} : \Delta\boldsymbol{\epsilon}^P}{\widetilde{q}}$$

$$\begin{aligned}
\frac{\partial h_2}{\partial\Delta\boldsymbol{\epsilon}^P} &= (1-f)\boldsymbol{I} + \dots \\
&\quad \dots + \frac{k_\omega f\omega(\boldsymbol{\sigma})}{\widetilde{q}}\left(\widetilde{\boldsymbol{\sigma}}_{\text{dev}} + \frac{\partial\widetilde{\boldsymbol{\sigma}}_{\text{dev}}}{\partial\Delta\boldsymbol{\epsilon}^P}\Delta\boldsymbol{\epsilon}^P - \frac{\widetilde{\boldsymbol{\sigma}}_{\text{dev}}\Delta\boldsymbol{\epsilon}^P}{\widetilde{q}}\frac{\partial\widetilde{q}}{\partial\Delta\boldsymbol{\epsilon}^P}\right) \\
\frac{\partial h_2}{\partial\boldsymbol{\sigma}} &= \mathcal{A}\frac{\Delta\boldsymbol{\epsilon}^P}{(1-f)\sigma_Y} + \frac{k_\omega f}{\widetilde{q}}\left(\frac{\partial\omega(\boldsymbol{\sigma})}{\partial\boldsymbol{\sigma}}\widetilde{\boldsymbol{\sigma}}_{\text{dev}} : \Delta\boldsymbol{\epsilon}^P + \dots\right. \\
&\quad \left.\dots - \omega(\boldsymbol{\sigma})\frac{\partial\widetilde{\boldsymbol{\sigma}}_{\text{dev}}}{\partial\boldsymbol{\sigma}}\Delta\boldsymbol{\epsilon}^P - \omega(\boldsymbol{\sigma})\frac{\widetilde{\boldsymbol{\sigma}}_{\text{dev}} : \Delta\boldsymbol{\epsilon}^P}{\widetilde{q}}\frac{\partial\widetilde{q}}{\partial\boldsymbol{\sigma}}\right) \\
\frac{\partial h_2}{\partial f} &= -\Delta\epsilon_p + \frac{k_\omega\omega(\boldsymbol{\sigma})}{\widetilde{q}}\left(\widetilde{\boldsymbol{\sigma}}_{\text{dev}} : \Delta\boldsymbol{\epsilon}^P + f\frac{\partial\widetilde{\boldsymbol{\sigma}}_{\text{dev}}}{\partial f}\Delta\boldsymbol{\epsilon}^P - \dots\right. \\
&\quad \left.\dots - f\frac{\widetilde{\boldsymbol{\sigma}}_{\text{dev}} : \Delta\boldsymbol{\epsilon}^P}{\widetilde{q}}\frac{\partial\widetilde{q}}{\partial f}\right) \\
\frac{\partial h_2}{\partial\sigma_Y} &= -\mathcal{A}\frac{\widetilde{\boldsymbol{\sigma}} : \Delta\boldsymbol{\epsilon}^P}{(1-f)\sigma_Y^2}
\end{aligned}$$

where:

$$\begin{aligned}
\frac{\partial\widetilde{\boldsymbol{\sigma}}_{\text{dev}}}{\partial\boldsymbol{\sigma}} &= 1 \qquad \frac{\partial\widetilde{q}}{\partial\boldsymbol{\sigma}} = \boldsymbol{n} \qquad \frac{\partial\widetilde{\boldsymbol{\sigma}}_{\text{dev}}}{\partial\Delta\boldsymbol{\epsilon}^P} = -\frac{\partial\boldsymbol{X}}{\partial\Delta\boldsymbol{\epsilon}^P} \\
\frac{\partial\widetilde{q}}{\partial\Delta\boldsymbol{\epsilon}^P} &= \frac{1}{4\widetilde{q}}\left(\frac{\partial\widetilde{\boldsymbol{\sigma}}}{\partial\Delta\boldsymbol{\epsilon}^P} : \mathbb{H} : \widetilde{\boldsymbol{\sigma}} + \widetilde{\boldsymbol{\sigma}} : \mathbb{H} : \frac{\partial\widetilde{\boldsymbol{\sigma}}}{\partial\Delta\boldsymbol{\epsilon}^P}\right)
\end{aligned}$$

4.6 Numerical validation

The implementation of the extended Gurson model is tested with different results obtained from the literature, while the plasticity part of the model is compared with results obtained using the LAGAMINE subroutine `HILL3D_KI`. An 8-node 3D brick element, called `BWD3D` (Duchêne et al., 2007), with a mixed formulation adapted to large strains and large displacements is selected. It involves a reduced integration scheme (with only one integration point) and an hourglass control technique. Two versions of the Gurson subroutine are included within the results: one using the perturbation method implemented *inside* the material subroutine and an analytically calculated consistent tangent matrix (section 4.4). Nonetheless, for the sake of simplicity, only one curve is shown because there is no noticeable difference between both.

4.6.1 Aravas, (1987)

The original implementation from Aravas, (1987) is tested using an hydrostatic test and a tensile test, in an isotropic material with only isotropic hardening and considering nucleation and growth of cavities (no coalescence neither shear). The material parameters are shown in Table 4.2. The results for the hydrostatic test and tensile test in Fig. 4.3 and Fig. 4.4 are very close to the analytical ones from Aravas, (1987).

Table 4.2: Material parameters from Aravas, (1987).

Elasto-plastic parameters				*GTN parameters*					
E	210 GPa	K	1200 MPa	q_1	1.5	f_N	0.04	f_c	-
ν	0.3	ϵ_0	3.17×10^{-3}	q_2	1.0	ϵ_N	0.30	f_F	-
		n	0.1	q_3	2.25	S_N	0.10		

4.6.2 Xue, (2008)

Xue, (2008) tested the implementation of the shear extension using a tensile and a shear test[7] in an isotropic material without kinematic hardening. The material parameters are shown in Table 4.3. Fig. 4.5 only shows the results from the shear test, however good results are also obtained for the case of the tensile test. One additional curve is included ($k_g = 0.25$) to show the strong influence of the parameter k_g in shear dominated situations.

It must be highlighted that the shear test performed for this extension and the following from Nahshon and Xue, (2009), a sub-interval integration of the stress at each FE step was needed to obtain good results (with the parameter `NINTV`, see section 4.3.3). In this way, a sufficiently small time step can be passed to the law loop without passing through the element loop.

[7] The author used 3 finite elements for the tensile test but only one for the shear test.

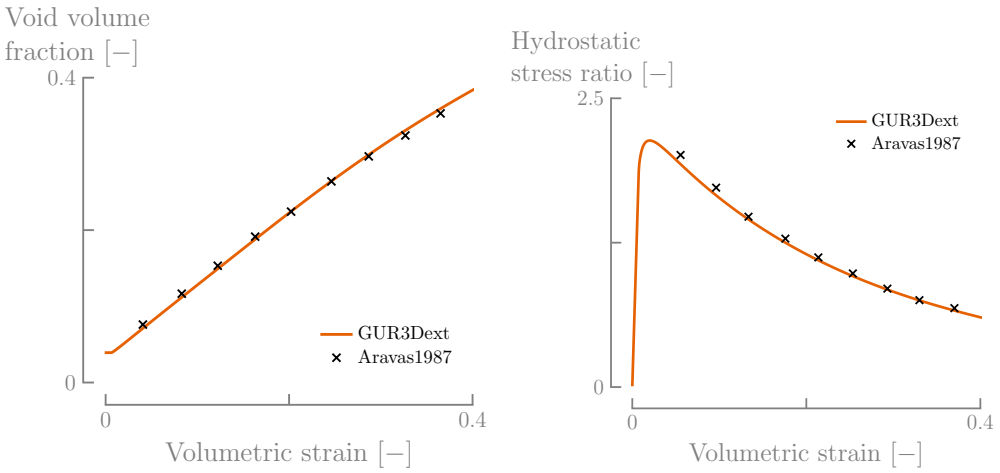

(a) Porosity evolution f vs. ϵ_p.

(b) Stress ratio p/σ_Y vs. volumetric strain ϵ_p.

Figure 4.3: Comparison of the predictions of the extended Gurson model for the hydrostatic test with the ones published in Aravas, (1987) with f_0 =0.04.

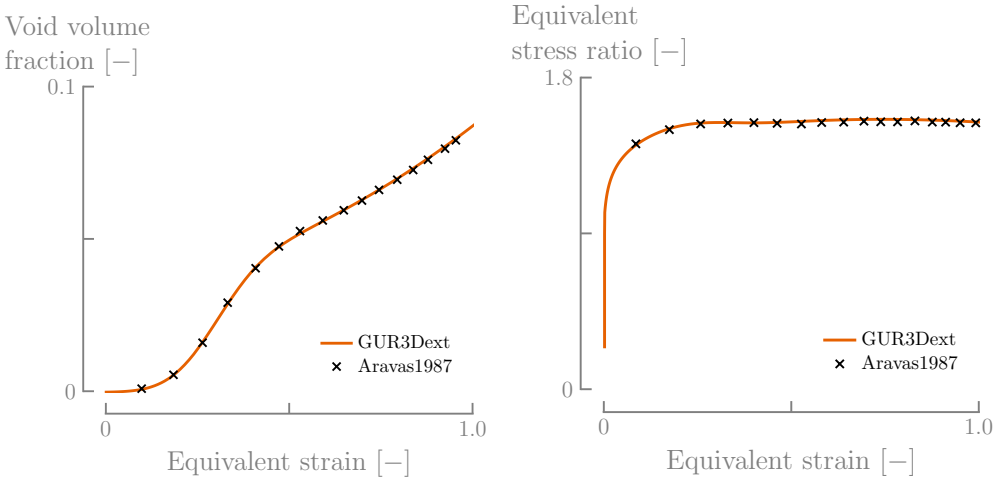

(a) Porosity evolution f vs. ϵ_q.

(b) Stress ratio q/σ_Y vs. volumetric strain ϵ_q.

Figure 4.4: Comparison of the predictions of the extended Gurson model for the tensile test with the ones published in Aravas, (1987) with f_0 =0.0.

Table 4.3: Material parameters from Xue, (2008).

Elasto-plastic parameters				*GTN parameters*					
E	70 GPa	K	409.04 MPa	q_1	1.5	f_N	0.04	f_0	0.00
ν	0.3	ϵ_0	3.3×10^{-3}	q_2	1.0	ϵ_N	0.20	f_c	0.05
		n	0.1	q_3	2.25	S_N	0.10	f_F	0.25

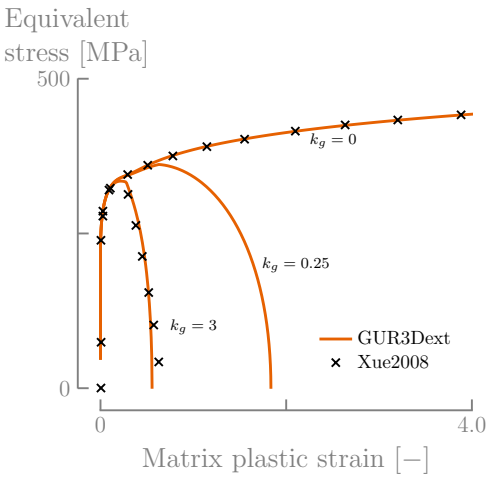

(a) Eq. stress q vs. volumetric strain ϵ_M^P.

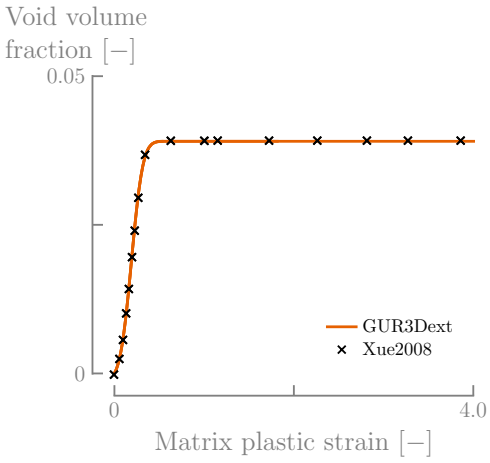

(b) Porosity evolution f vs. ϵ_M^P.

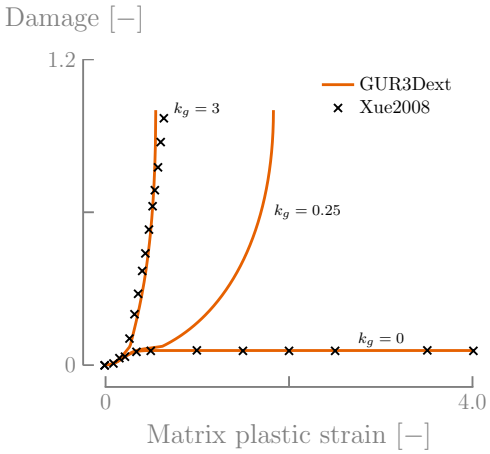

(c) Damage evolution D vs. ϵ_M^P.

Figure 4.5: Comparison of the predictions of the extended Gurson model for the shear test with the ones published in Xue, (2008). Note that a small change in k_g can induce earlier localization.

4.6.3 Nahshon and Xue, (2009)

Nahshon and Xue, (2009) tested the implementation of the shear extension proposed by Nahshon and Hutchinson, (2008) with an hydrostatic test and a shear test, using an isotropic material without kinematic hardening. The material parameters are shown in Table 4.4. In the hydrostatic test a classical GTN model (without shear or $k_\omega = 0$) was considered. For the shear test three different values of k_ω (see Eq. 3.4.5 for k_ω impact) are depicted. In Fig. 4.6 and in Fig. 4.7 it can be seen that the results for both tests are in agreement with those found in the literature.

Table 4.4: Material parameters from Nahshon and Xue, (2009).

Elasto-plastic parameters				*GTN parameters*					
E	200 GPa	K	399.05 MPa	q_1	1.0	f_N	0.04	f_0	0.005
ν	0.3	ϵ_0	1.0×10^{-3}	q_2	1.0	ϵ_N	0.30	f_c	0.15
		n	0.1	q_3	1.0	S_N	0.10	f_F	0.25

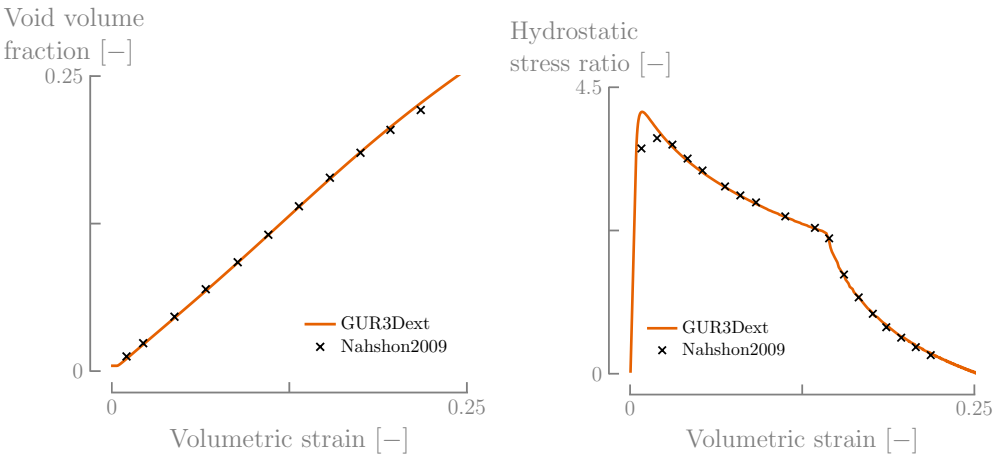

(a) Porosity evolution f vs. ϵ_p.

(b) Stress ratio p/σ_Y vs. volumetric strain ϵ_p.

Figure 4.6: Comparison of the predictions of the extended Gurson model for the hydrostatic test with those published in Nahshon and Xue, (2009).

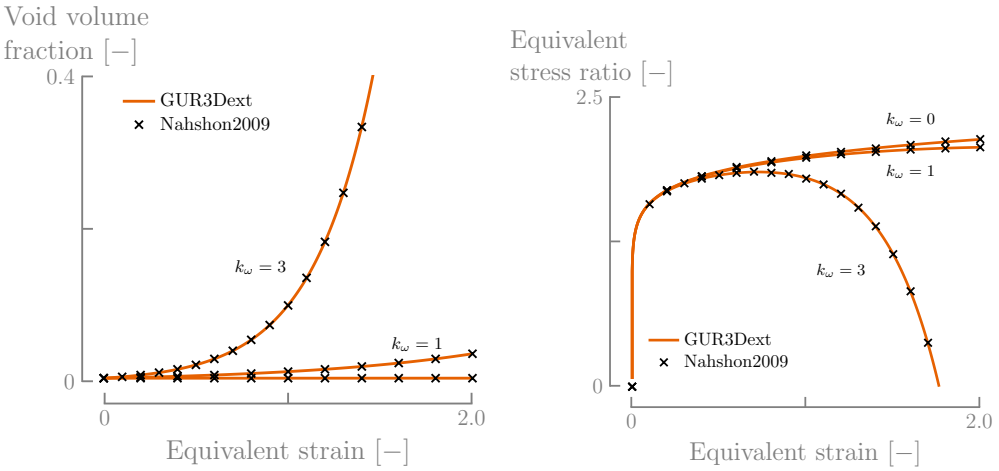

(a) Porosity evolution f vs. ϵ_q.

(b) Stress ratio q/σ_Y vs. eq. strain ϵ_q.

Figure 4.7: Comparison of the predictions of the extended Gurson model for the shear test with those published in Nahshon and Xue, (2009).

4.6.4 Anisotropy

In the article by Benzerga and Besson, (2001), the authors identified two different effects: the *scalar effect* by means of parameter κ and the *directional effect* expressed in the damage anisotropy. Since the numerical validation used in this article is not straightforward, only the effect of the Hill/Lankford coefficients on damage evolution is analyzed. The simulations were performed using a simple tensile test in one single FE element using the material parameters from Ben Bettaieb et al., (2011c). Three different set of anisotropic coefficients were selected and shown in Table 4.5: set 1 has a strong anisotropy (κ =1.69) while set 2 is slightly anisotropic (κ =2.07). In Fig. 4.8 it is clear that for anisotropic κ (set 1), the directionality effect in Fig. 4.8(a) is more important. In the stress strain curve Fig. 4.8(b) the anisotropy effect is harder to observe since in all the three directions the results are almost the same. However, even if κ for the isotropic material and set 2 are similar the porosity evolution is clearly different.

Table 4.5: Lankford coefficients used for the anisotropic simulations.

	Isotropic	*Set 1*	*Set 2*
H	1.0	1.13	0.925
F	1.0	0.69	1.051
G	1.0	0.87	1.076
$L = M = N$	3.0	3.26	3.182
r_0	1.0	1.98	0.86
r_{45}	1.0	2.56	0.99
r_{90}	1.0	1.67	0.88
κ	2.00	1.69	2.07

4.6.5 Strain hardening

The original model from Ben Bettaieb et al., (2011c) includes material anisotropy (expressed in the material parameter κ) and mixed isotropic-kinematic hardening (Swift Eq. 2.2.11 and Armstrong and Fredrick, (1966) Eq. 2.2.14). The previous tests are highly academic cases and represent idealized material properties. In this section the plastic anisotropy and kinematic hardening implementation is validated using material parameters extracted from Flores, (2005) for DC06 steel. Cases with yield anisotropy, isotropic (Swift) and kinematic hardening (Armstrong and Fredrick) but without damage (Table 4.6) are provided. The element tangent matrix is calculated using the perturbation method implemented inside the subroutine `HILL3D_KI`. The implementation proves to be good for both anisotropy and hardening. As seen in Fig. 4.9 no important differences are observed.

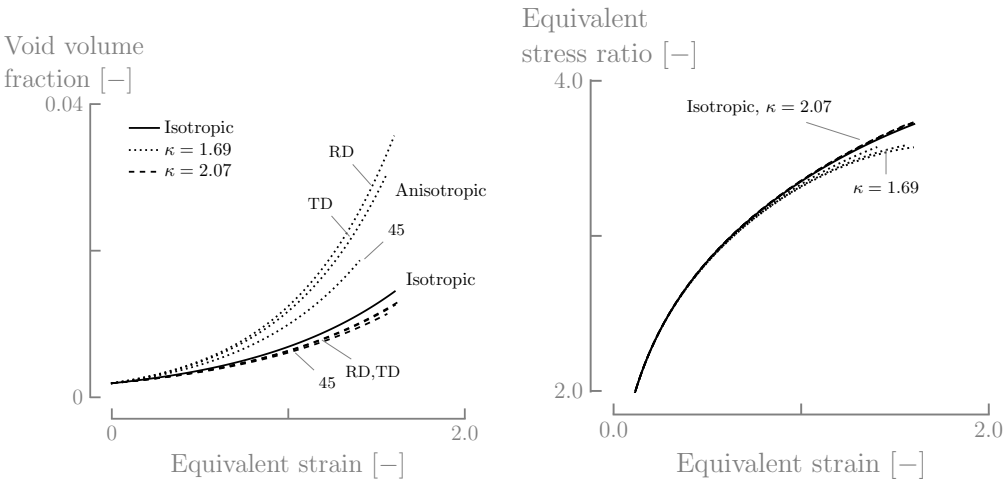

(a) Porosity evolution f vs. ϵ_q.

(b) Stress ratio q/σ_Y vs. eq. strain ϵ_q.

Figure 4.8: Influence of the anisotropic coefficients of Table 4.5 in the porosity evolution and in the stress-strain curve of tensile test performed using a single FE.

Table 4.6: Material parameters from the hardening tests.

Elasto-plastic parameters				*Anisotropy*			
E	183.083 GPa	K	499.9 MPa	F	0.69	L	3.26
ν	0.35	ϵ_0	6.3×10^{-3}	G	0.87	M	3.26
		n	0.25	H	1.13	N	3.26
C_X	12.70			r_0	1.298		
X_{sat}	16.75			r_{45}	1.589		
				r_{90}	1.637		

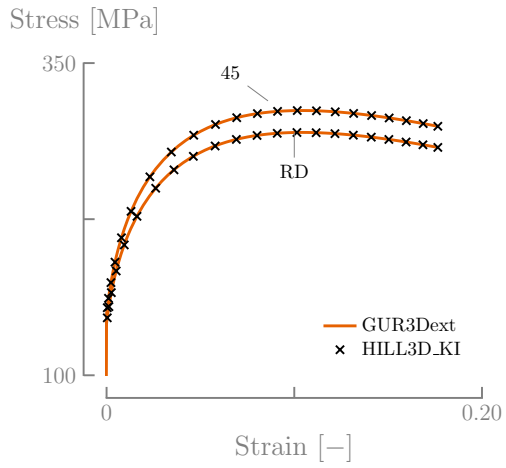

(a) Tensile test performed at the RD and at 45°.

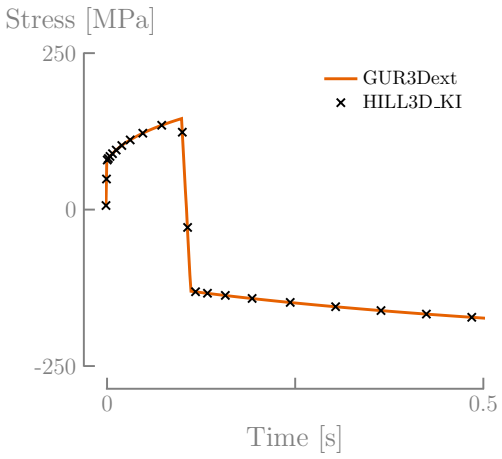

(b) Bauschinger test 10%.

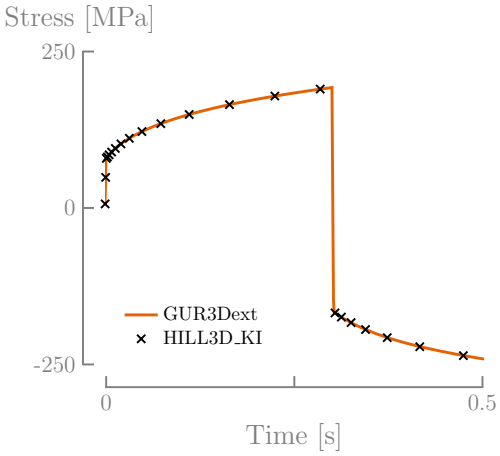

(c) Bauschinger test 30%.

Figure 4.9: Plasticity test performed using the new implementation.

4.7 Conclusions

In this chapter, a detailed implementation of the GTN model plus shear extensions into the FE framework has been presented. The algorithm developed by Ben Bettaieb et al., (2011c) for the integration scheme of this model with anisotropic behavior and kinematic hardening is described and further developed to include new internal variables. The original feature of this scheme is that all variables are integrated in an implicit way based on the projection algorithm, while the consistent tangent matrix is obtained analytically. The efficiency of the implementation is assessed by comparing the numerical results of homogeneous cases found in the literature. Nucleation, coalescence and shear extensions are exactly validated, while anisotropy and kinematic hardening were analyzed. As a general conclusion, the current model (including all the mentioned extensions) can be used in more complex simulations involving heterogeneous strain paths. Because models involving the GTN extensions (shear, anisotropy and mixed hardening) are not widely available, further work could be focused on more academic oriented research such as iso-error maps, localization analysis, etc. on simple loading schemes. However this line was not followed in order to devote more time to identify material parameters and incremental forming applications.

Chapter 5

Material parameter characterization of the GTN model

The Gurson model (and its extensions) includes several parameters of different nature. Some of them have micromechanical roots while others are strictly phenomenological. Since the coupling and relation among the parameters is highly non-linear, it is hard to determine *a priori* the influence of each on the final result with a sensitivity analysis. Hence, a methodology should be developed in order to obtain a robust set of parameters with both numerical and physical meaning. In this chapter, an identification methodology for damage parameters is proposed and briefly detailed, based on results found in the literature and an experimental-numerical approach. This hybrid approach requires microscopic measurements to estimate the void volume fraction near the crack, a test campaign with selected specimen shape and loading, and numerical simulations. The method is applied on a DC01 ferritic steel sheet. An extended version of the Gurson model, incorporating plastic anisotropy, kinematic hardening, void nucleation, growth, coalescence and shear is used. Overall, the described identification methodology leads to satisfactory results when compared to other techniques.

5.1 Introduction

The original version of the Gurson, (1977a) model has only one material parameter outside the elasto-plastic set: the initial void volume fraction of the sound material. The subsequent extensions of the model add specific parameters regarding nucleation, growth, coalescence, void shape, distribution, etc. In the most commonly used extension of the Gurson model, the Gurson-Tvergaard-Needleman (GTN) extension, up to 8 parameters are identified:

- f_0, the initial volume fraction of the Gurson, (1977a) model;
- correction factors q_1 and q_2 (and eventually q_3);
- ϵ_n, S_n and f_n, for the strain based nucleation model;

- f_{cr} and f_F, coalescence parameters.
- k_ω and k_g, material parameters of the shear extension by Xue, (2008) and Nahshon and Hutchinson, (2008) respectively.

Determining these parameters is far for being trivial. Indeed, the actual nature of the damage leading to fracture presents challenges for both the numerical simulation and the experimental characterization. Unlike plasticity, which is usually characterized using homogeneous strain fields at macroscopic scale, damage and fracture frequently present strong localization associated with microscopic voids which eventually coalesce to form a crack.

In the following chapter, a review of experimental and numerical procedures commonly used to identify the material parameters within the literature, are presented and discussed. The GTN model parameters are taken as a reference but the discussion is not only limited to this model. The final goal is to identify the proper methodology for the characterization of the DC01 ferritic steel sheet, the main material used in the current research.

5.2 Identification methodologies

One of the main characteristics of the ductile fracture is the localization phenomenon associated with large plastic strain gradients in zones with crystal defects (like inclusions). For these ductile materials, if the deformation is not large enough to soften the material, the influence of these crystal defects on the macroscopic behavior can safely be neglected. For instance, in a tensile test, it is possible to rely on the beginning of the stress-strain curve for experimental-numerical validation of plasticity models. After a certain level of plastic deformation, the macroscopic response of the specimen is notoriously modified due to microscopic defects. The random distribution of these defects induces an heterogeneous stress-strain field, increasing its gradient and localizing the deformation.

Because the material model has to capture the localization phenomenon, the force vs. displacement curve is commonly used instead of the stress vs. strain curve. When measuring forces (using force cells) and displacements (through axial extensometers or DIC), localization is already included within the *observable* (macroscopic) behavior of the material. Nevertheless, the measured force is also a function of the specimen geometry. Thus the results lack the generality required to identify a constitutive law, which is expressed in terms of stress and strain. As we will see, most of researchers employ a combination of both force-displacement and stress-strain curves using different approaches.

According to Ben Bettaieb, (2008), there are three possible identification methodologies, irrespective of equipment, time and money availability:

1. *Based on microstructure characterization*, in order to obtain parameters such as the initial void volume fraction f_0, initial void shape factor, initial void spacing between close cavities, etc. In theory, damage can be entirely characterized using microscopic measurements so this type of identification is highly recommended.

2. *Based on mechanical tests*, to identify macroscopic measurands like the displacement at the onset of rupture, the force-displacement curve under different values of triaxiality, the evolution of the Lankford coefficient, etc. The use of techniques like DIC allows to obtain the strain field from a particular zone of the specimen.

3. *Calibration by numerical simulations*, to compare the results obtained using FE simulations and experimental tests. With an optimization algorithm, it is possible to fit the parameters for a particular finite element model. Theoretically, all the parameters can be found using this approach, however the strong non-linearity of the equations and the coupling among parameter relations induce several local minima increasing the risk to identify a non-unique set of parameters.

The experimental characterization of damage usually involves specially designed specimens, different from those used for plasticity characterization. Such a development is based on the experimental evidence that strain at fracture exponentially decreases as triaxiality increases (Hancock and Brown, 1983) (see Fig. 5.1) and that the fracture locus is strongly path dependent. In order to validate numerical models, it is necessary to cover a wide range of stress states each of them defined by a single value of triaxiality[1]. This approach is achieved by tensile specimens with varying notch radii, which artificially create a neck, avoid instabilities and generate three dimensional stress states. However, the characterization can also be performed using compression bars (at low stress triaxiality), cracked specimens, Charpy specimens, etc. An important drawback of these tests is that necked regions contain large stress and strain gradients through the cross section, thus making the identification of the stress state extremely difficult. As the damage mechanisms within the nucleation, growth and coalescence of cavities are strongly dependent on the stress state, it is hard to distinguish which one(s) of these damage phases is (are) actually happening. In this respect, it is also im-

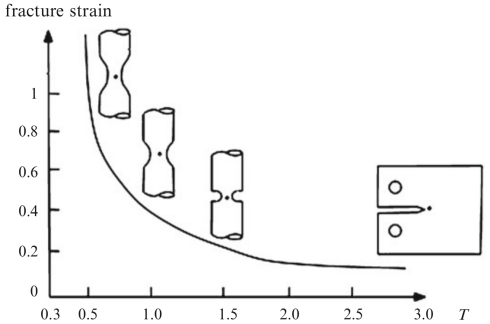

Figure 5.1: The fracture strain exponentially decreases with the triaxiality (decreasing the notch radius of the specimen implies a higher triaxiality), from Pineau and Pardoen, (2007).

portant to understand the role of each parameter in the model and the sensitivity

[1] and eventually a Lode parameter value.

of the results to them. For example, Picart et al., (1997) showed that an accurate characterization of f_0 is not needed for small values of the initial porosity in the base material. In the following section, some identification methodologies are chronologically presented and discussed with a special focus on articles dealing with thin metal sheets.

Besson, (2004) proposed some guidelines to identify material parameters. It is important to mention that whenever it is possible, damage should be measured before and after the tests. In between, different load levels could be applied to determine the damage kinetics. Regarding microscopic image processing and analysis, 3D information can be retrieved from 2D images using stereology relations (like void or inclusion volume fraction, damaged specific surface, integral of the average curvature, number of objects, etc.). Some special algorithms exist in order to enhance the details of raw images of interest, they facilitate the subsequent measurements of observed particles and defects. After processing the images (and as a general rule) the following questions should be asked:

- Is the nucleation of new voids observed?
- Is there any influence of the loading type or of the microstructure on the development of voids?
- Do we observe damage initiation by particle cracking, interface decohesion, matrix cracking around inclusions, etc.?

It is often assumed that during the early stages of damage the shape of the voids most of the time is spherical. Nevertheless, the interdistance and morphology of the voids can have an enormous importance on how the coalescence will occur.

Lievers et al., (2004), instead of relying on tests with heterogeneous deformation used a forming process with a high formability (SPIF) to identify the nucleation parameters of the GTN model. The basic hypothesis adopted in the article is that, since characterization in homogeneous zones is limited by an instability (such as local necking or shear bands), it is thus more efficient to enlarge this homogeneous step phase by delaying localization. In this case, it is claimed that a forming process such as SPIF can suppress necking. The limit of its formability is controlled by the evolution of voids and shear bands. The analyzed materials by Lievers et al., (2004) are three different aluminum alloys: AA5182, AA5754 and AA6111. Several SPIF quadrangular pyramid frustums of 1.0 mm thickness were created with different forming angles thus allowing different strain levels. Circular sections of the frustum were cut and then density measurements based on Archimedes' principle, were taken in the deformed and undeformed material. Using a single finite element simulation, the nucleation parameters were fitted until the porosity evolution versus the major true strain was close enough to the experiments. The authors also claim that a minimum level of void damage is needed to use this technique. More details on the SPIF application of this procedure and the experimental results can be seen in sections 5.4.3 and 6.1.2.

Lassance et al., (2007) introduced an extended version of the Gurson model applied to the extrusion process on AlMgSi alloys. It found that ductility is

affected by several factors such as stress triaxiality, chemical composition, casting homogenization (all related with the microstructure of the billet), strength, strain-hardening and strain rate sensitivity of the matrix around voids. The methodology comprised:

- Characterization by X-ray and electron microscopy (SEM) of the alloys after their homogenization .
- Ductility measurements with uniaxial test on smooth and notched cylindrical rods.
- Characterization of damage using tensile tests and fractographic analysis.

The methodology is shown in Fig. 5.2.

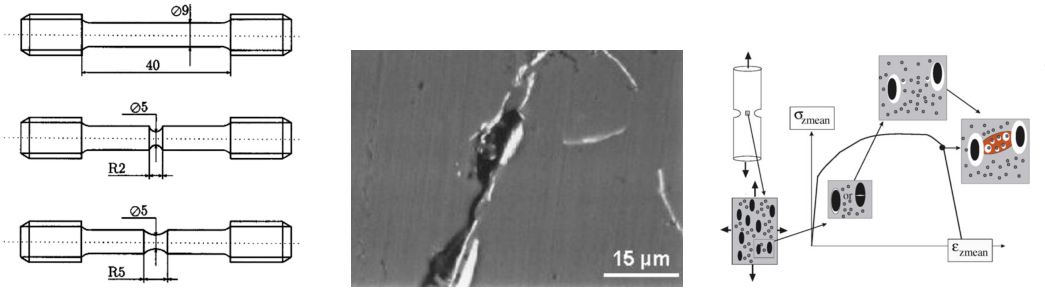

(a) Smooth and notched round bars.

(b) SEM micrographs showing void growth and coalescence.

(c) Micromechanical modeling of fracture through micro- and macro-mechanical tests.

Figure 5.2: General methodology used by Lassance et al., (2007).

Xue et al., (2010) discussed the calibration procedure for a Gurson, (1977a) model extended to coalescence (Tvergaard and Needleman, 1984) and shear (Nahshon and Hutchinson, 2008) without nucleation. Only two damage-related parameters were identified: f_0 and k_ω. Additionally to these parameters, the typical size of the finite elements within the mesh was calibrated. The experimental setup consisted of three different tests:

1. A round bar under tension, to infer the stress-strain behavior of the undamaged material (plasticity).
2. A mode I compact tension specimen, to calibrate the initial void volume fraction f_0 and the element size D.
3. A mode 2 shear off specimen, to determine the shear damage coefficient k_ω.

They are shown in Fig. 5.3. The test 1 (Fig. 5.3(a)) was used to study the post-necking behavior. One important feature of this procedure is the study of the influence of the parameters with each other. The author mentioned that f_0 and k_ω should not affect the identification of the true stress-strain curve. Strain

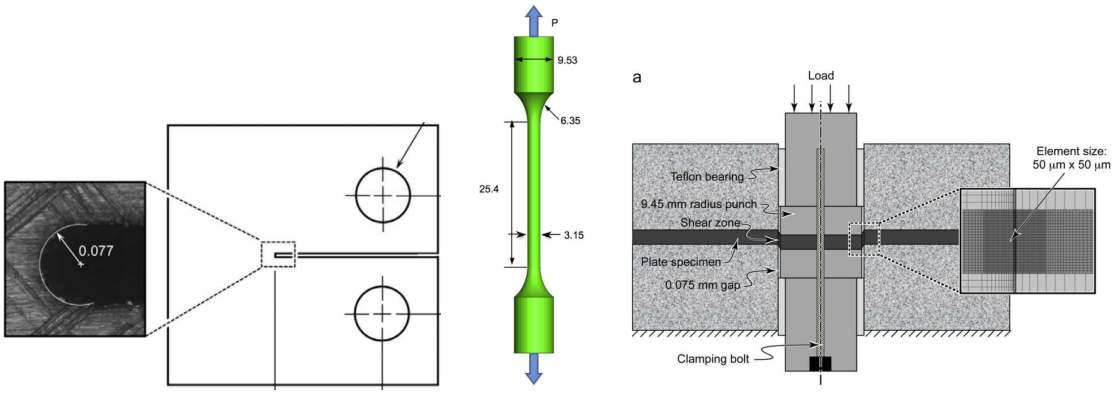

(a) Mode I compact tension specimen. (b) Tensile round bar. (c) Shear off test.

Figure 5.3: Specimens used by Xue et al., (2010).

localization should be accurately captured using a small element size. It was found that the finite element size must be of the order of the spacing between voids.

Dunand and Mohr, (2011a) proposed a methodology to calibrate a shear modified Gurson model for a TRIP steel sheet. Based on an experimental campaign using notched specimens (Dunand and Mohr, 2010) plus a newly developed butterfly specimen (Dunand and Mohr, 2011b). It is highlighted that the tests have loading conditions ranging from pure shear to equibiaxial tension thus covering an important range of triaxiality and Lode parameter values. The approach uses DIC measurements to detect the *instant* (not the location) of the onset of fracture (considered as the first discontinuity in the measured displacement field). Then, FE simulations were performed in order to detect the FE with the highest value of equivalent strain in order to trace the triaxiality and Lode parameter histories for this element. The shear modified Gurson model is calibrated performing a sensitivity analysis within four different tests:

- Uniaxial tension to determine the matrix hardening parameters.
- Biaxial punch test to fit the correction parameters q_1 and q_2, plus the coalescence parameters.
- Notched test $R = 20\,\text{mm}$, to identify the nucleation parameters.
- Shear dominated test with the butterfly specimen, to fit the Gurson shear extension parameter k_ω.

They are shown in Fig. 5.4. The model is then validated comparing prediction and experimental curves of force vs. displacement (from the machine).

From the above review, it is clear that the characterization using microscopic measurements is highly desirable. Nevertheless, even if the setup is not available, it is still possible to calibrate the model relying solely on macroscopic tests. In the

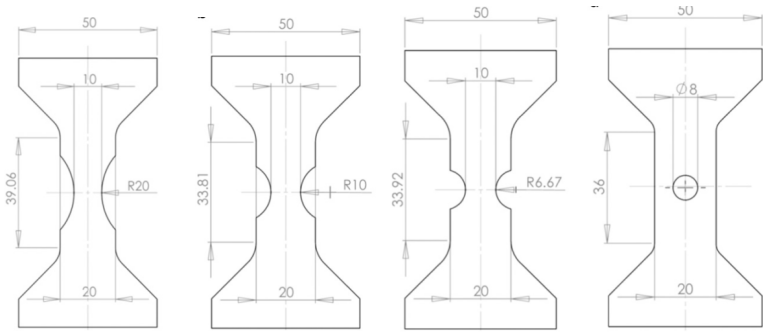

(a) Notched specimens and specimen with a central hole.

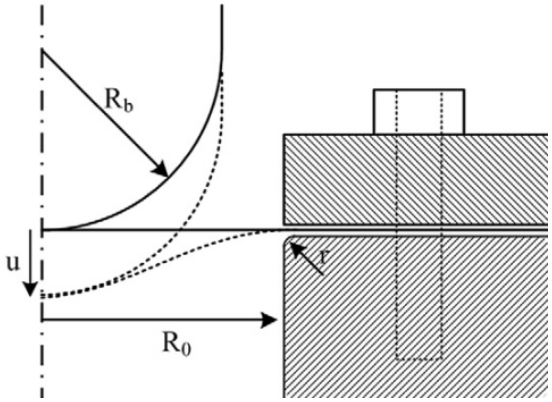

(b) Punch test.

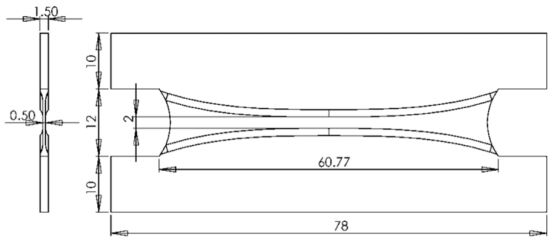

(c) Butterfly specimen.

Figure 5.4: Tests campaign performed by Dunand and Mohr, (2011a).

following sections, a microscopic and macroscopic characterization of the DC01 steel sheet is performed.

5.3 Macroscopic characterization

The fracture specimens should be defined in such way to allow the study of damage and fracture for different loading types in the studied ductile material as to identify and check the reliability of the numerical model. From an experimental standpoint, plasticity can be studied using specially designed tests (e.g., uniaxial tensile test, monotonic and Bauschinger shear tests, orthogonal test, etc.) based on the hypothesis of homogeneous distribution of stress and strain. In general, plasticity models behave well when they rely on these standard test campaigns. A correct description of the yield locus and the hardening law can be obtained when deformations remain under the localization limit i.e., before the appearance of diffuse necking in a tensile test specimen. This classical and well known framework can be naturally extended to model the post-necking behavior. However, damage (and eventually fracture) is a more complex phenomenon involving properties outside the mere description of the yield limit and the hardening law. Therefore, it requires a more rigorous analysis. Damage, localization and fracture depend on the stress state (represented by the stress triaxiality and the Lode angle), internal imperfections (such as the void volume fraction), hardening law, sample geometry, etc. Moreover, the post-necking zone has such a degree of heterogeneous stress and strain fields that an hybrid experimental-numerical approach is often required in order to obtain the histories of the local stresses and the strains leading to fracture.

Considering the above, the specimen selection plays an important role when characterizing the material damage and fracture. In general, the specimen geometry should allow a clear analysis of the three following points:

- Plastic strain level in the specimen as an indicator of the crack appearance;
- Triaxiality near the crack due to its influence in damage development;
- Non-homogeneous localization of plastic deformation in a particular zone.

Based on these points, 4 different specimens are selected:

- Two specimens with different notches of radius R =5 mm and R =10 mm, respectively. The notch acts as a stress concentrator which artificially increases the triaxiality at the center of the specimen. The triaxiality level within the specimen is inversely proportional to the notch radius.
- A specimen with a central hole of diameter ϕ =15 mm. Following the analysis of Dunand and Mohr, (2010), this type of specimen induces a stress concentrator without necking development with a more stable value of the triaxiality throughout the deformation.
- A special shear specimen designed by Peirs et al., (2011). A particularity of this specimen is that failure occurs at very low values of triaxiality thus being hard for the classic Gurson model to capture damage leading to fracture. Hence, this geometry is appropriate to evaluate the reliability of shear extensions of the Gurson model.

These specimens are cut using WEDM and are depicted in Fig. 5.5. The tests are

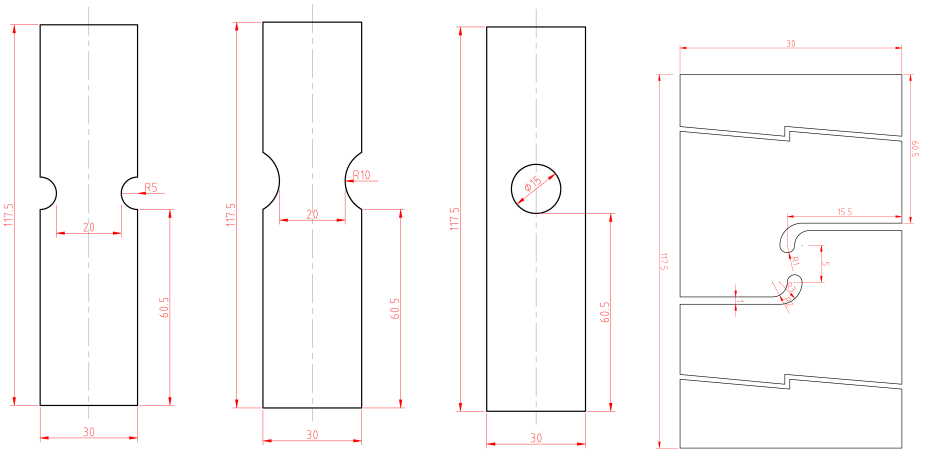

(a) R =5 mm. (b) R =10 mm. (c) Central hole. (d) Shear.

Figure 5.5: Selected specimens for the macroscopic characterization.

performed using a Zwick machine with a load capacity of ±100 kN and the same DIC hardware setup detailed in section 2.3.2, with Istra4D as the correlation software. It is important to highlight that the displacements are taken from a (virtual) displacement gauge draw with the DIC software and not directly from the analog data from the machine. This decision is based on two observations:

- Sliding could be observed between the clamps and the specimen.
- Rigid body motion of the specimen with respect to the machine. Hence, the displacement is overestimated when directly measured by the machine.

The displacement gauges used in the DIC measurements are depicted in 5.6. Strains are measured in the axial (loading) direction and taken from a point located at half-length of the gauge. Another important remark is that the DIC

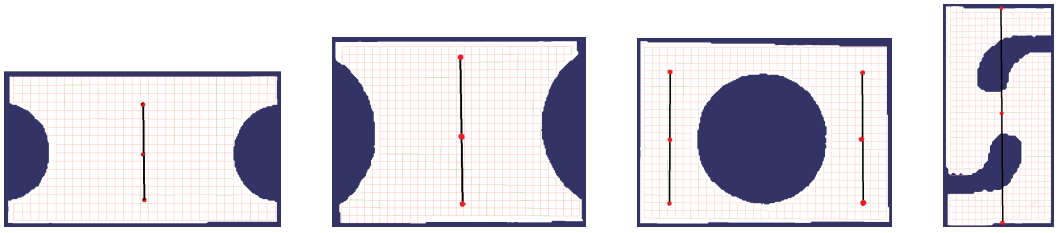

(a) Notch R =5 mm. (b) Notch R =10 mm. (c) Central hole. (d) Shear.

Figure 5.6: Displacement gauges used to obtain the displacement of the specimen relative to the reference position. Strain is taken at half-length of the gauge.

software parameters are slightly different from those used for plasticity characterization in chapter 2. As discussed in section 2.3.2, the subset size should be lower than those used for plasticity characterization in order to capture heterogeneous deformation gradients. The experimental results are gathered in Fig. 5.7. Note that both specimens with notch reached almost the same force level but

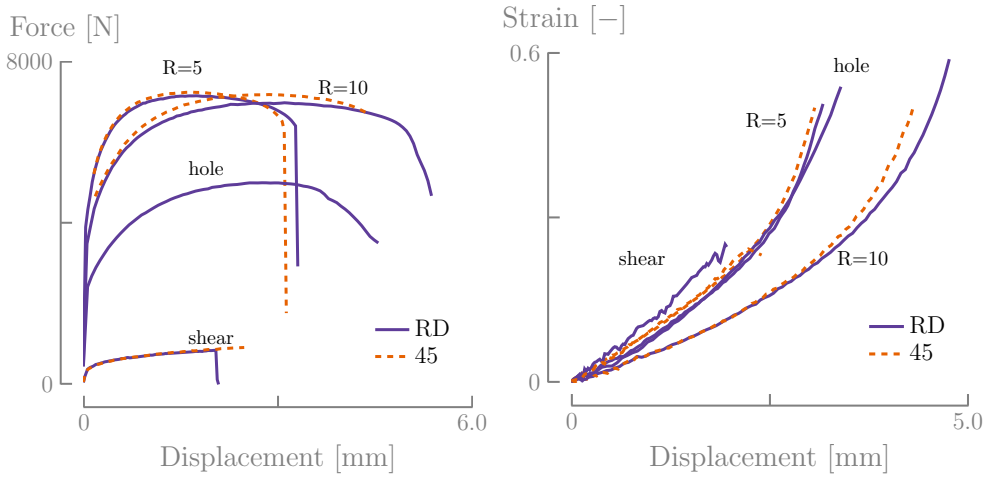

(a) Force vs. displacement.

(b) Axial Strain vs. displacement.

Figure 5.7: Experimental results of the fracture tests performed in different directions. Error bars are omitted for the sake of simplicity.

for different displacement at fracture. For the specimen with central hole, the displacement to fracture is among those identified for the specimens with notch. The shear test has a very low value of force compared to the machine capacity, so it was difficult to remove noise from data. Nevertheless, acceptable results were retrieved from the load cell.

Another important aspect to consider is the fracture strain. Because of the large deformation undergone by the speckle pattern on the specimen surface, experimental data is lost in zones with large plastic deformation (the speckle pattern is destroyed). Some authors (Dunand and Mohr, 2010) used an hybrid numerical-experimental approach to obtain this value, relying on both FE simulations and DIC measurements. In this research, it was observed that the fracture strain is highly dependent on the material model so no reliable value of strain could be identified *a priori* (i.e., before a proper material identification). Dunand and Mohr, (2010) extrapolated the strain-hardening curve of a notched specimen to capture softening behavior but still only relying on a (non damage) plasticity model. In the current work a different approach is followed: interpolation of the strain-displacement experimental curve using different polynomial degrees. It is then possible to extrapolate the fracture strain until the *observed* displacement at fracture of the virtual gauge, as this value (and not its derivative) is less sensitive to the speckle pattern. This approach is shown in Fig. 5.8 and the obtained results are depicted in Table 5.1. Variation between different tests of the fracture

displacements d_f is less than 3.0% for the specimens with notch and hole and around 10.0% for the shear specimens.

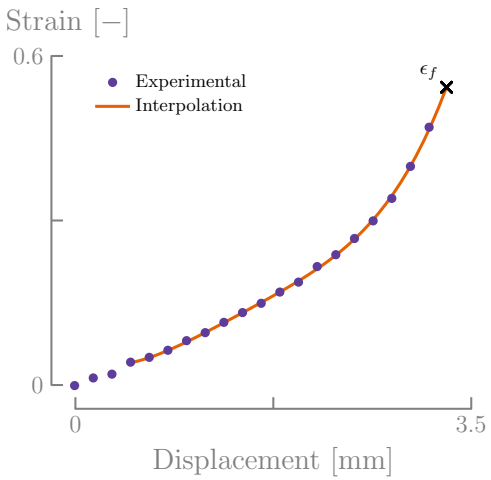

Figure 5.8: Strain-to-fracture extrapolation based on the experimental strain-displacement curve interpolated using a 4th degree polynomial.

Table 5.1: Experimental fracture strain for the fracture specimens.

Specimen	*Direction*	d_f [mm]	ϵ_f
Notch R =5.0 mm	RD	3.377 ± 0.098	0.667 ± 0.113
	45	3.193 ± 0.042	0.594 ± 0.038
Notch R =10.0 mm	RD	5.168 ± 0.032	0.819 ± 0.017
	45	4.498 ± 0.010	0.592 ± 0.057
Central hole	RD	4.068 ± 0.085	0.880 ± 0.076
	TD	4.192 ± 0.042	0.826 ± 0.014
Shear	RD	2.039 ± 0.148	0.246 ± 0.058
	45	2.754 ± 0.346	0.304 ± 0.032

5.4 Microscopic characterization

The macroscopic mechanical test campaign proposed in section 5.3 is supported by microscopic measurements. The main purpose is to give a physical frame of the observed (macroscopic) behavior. The methodology comprises the following points:

1. Early estimation of damage based on empirical equations related to the amount of damage and the chemical composition of the material.

2. Fractography analysis of the broken specimens.

3. Optical microscopy image analysis of selected samples to characterize the damage evolution.

5.4.1 Previous estimations

Void nucleation is frequently found in the presence of inclusions, acting as inhomogeneities (stress concentrators) within the material matrix. It is possible to approximate the initial void volume fraction for steels using a semi-empirical formula proposed by Franklin, (1969), relating the volume of non-metallic inclusions with the chemical composition of the material. In this way, f_0 can be estimated from the amount of chemical composition of sulphide (S), manganese (Mn) and oxygen (O) in the material:

$$f_0 = f_{\text{inc}} \frac{\sqrt{d_x d_y}}{d_z} \tag{5.4.1}$$

where d_x, d_y and d_z are the average dimensions of the inclusions within three orthogonal directions x, y and z. f_{inc} is the void volume fraction of inclusions and is given by:

$$f_{\text{inc}} \approx 0.054 \left(\text{S}(\%) - \frac{0.001}{\text{Mn}(\%)} \right) + 0.005\, \text{O}(\%) \tag{5.4.2}$$

where S(%), Mn(%) and O(%) are the weight percentages of sulphide, manganese and oxygen present in the matrix. If a spherical shape is assumed for inclusions, then Eq. 5.4.2 is simplified to $f_0 = f_{\text{inc}}$. This approach has been suggested by Bauvineau et al., (1996), Maire, (2004), and Yang et al., (2012). Benzerga et al., (2004) used this formula to estimate the amount of MnS inclusions in a low/medium carbon alloy steel. Soyarslan et al., (2012) did not applied the formula in a ferritic-martensitic DP1000 steel, arguing that a modification should be introduced in order to consider the combined effect of inclusions and secondary phases. In the case of the DC01 steel sheet, the initial porosity can be estimated as $f_0 \approx 1.75 \times 10^{-4}$ using the chemical composition presented in Table 2.1.

Parameters of the GTN model, like the initial porosity f_0 and the nucleation parameters f_n and ϵ_n, can robustly be estimated from microscopic measurements. The classical coalescence criterion of Tvergaard and Needleman, (1984) is, however, strictly phenomenological and an estimation of the parameters f_{cr} and f_F has to be empirically identified using load-displacement curves and an inverse modeling approach. Koplik and Needleman, (1988) showed using unit cell calculations that f_{cr} depends more on the initial porosity f_0 than on the triaxiality. Based on these results, Benseddiq and Imad, (2008) and Yang et al., (2012) proposed the following relation for an axisymmetric specimen of a NiCr steel:

$$f_{cr} = 0.0186 \ln f_0 + 0.1508 \tag{5.4.3}$$

Note that if f_0 is negligible, then f_{cr} =0.1508, which is near the value of f_{cr} =0.15 originally proposed by Tvergaard and Needleman, (1984). Zhang et al., (2000) investigated the effect of f_F on the global numerical response using plane strain cell models. The following empirical equation was obtained:

$$f_F = 0.15 + 2 f_0 \tag{5.4.4}$$

Thus f_F can be fixed to f_F =0.15 for low initial porosities. The estimations for the DC01 steel sheet are summarized in Table 5.2. Note that $f_0 \approx 1.75 \times 10^{-4}$ estimated using Eq. 5.4.2 leads to negative values of f_{cr} and f_F. Hence the value $f_0 \approx 8.0 \times 10^{-4}$ (obtained in section 5.4.4) is used to estimate f_{cr} and f_F. It is important to remark that all these empirical coalescence formulas are derived from the observed behavior of asymmetrical specimens or unit cells. In the present research, we use thin metal sheets in which the underlying mechanisms of damage and fracture can be different.

Table 5.2: DC01 steel material parameters estimations based on empirical formulas.

Parameter	*Estimation*	*Reference*
f_0	1.75×10^{-4}	Franklin, (1969)
f_{cr}	0.0181	Yang et al., (2012)
f_F	0.1516	Zhang et al., (2000)

5.4.2 Fracture surfaces

Fractographies of the broken tensile specimens (section 2.4) were taken by Anne Mertens of the A&M department (MMS division) using a field-emission environmental scanning electron microscope (SEM) Philips XL30 at the Center for Applied Technology of Microscopy of the ULg. Different images from specimens at different directions from the RD were analyzed with no observable difference. Fig. 5.9 shows a common trend in all taken SEM microphotographs, in which (for tensile tests) the inner region of the sample has a typical equiaxed dimples (indicating ductile fracture) while the zones near the surface have parabolic dimples (from shear loads). This observation confirms that in a tensile test the material failure is due to the growth and coalescence of voids. Hence, we can conclude that the GTN model approach is appropriate for this type of material.

5.4.3 Measurements based on the Archimedes' principle

Most of the metallic materials deform at constant volume in the absence of damage. When damage occurs the volume of the material increases (Maire, 2004). Hence, it is possible to relate the amount of the void volume fraction with the density of the material through the equation:

$$\frac{\Delta f}{1-f} = -\frac{\Delta \rho}{\rho} \tag{5.4.5}$$

Mertens et al., (2012) assessed the feasibility of using density measurements to characterize damage based on the Archimedes' principle. Using a methodology developed by Lievers et al., (2004) applied to a SPIF formed sample, this method is supposed to lead to quicker results compared to other methods, such as image analysis by optical microscopy, which is quite tedious and time-consuming.

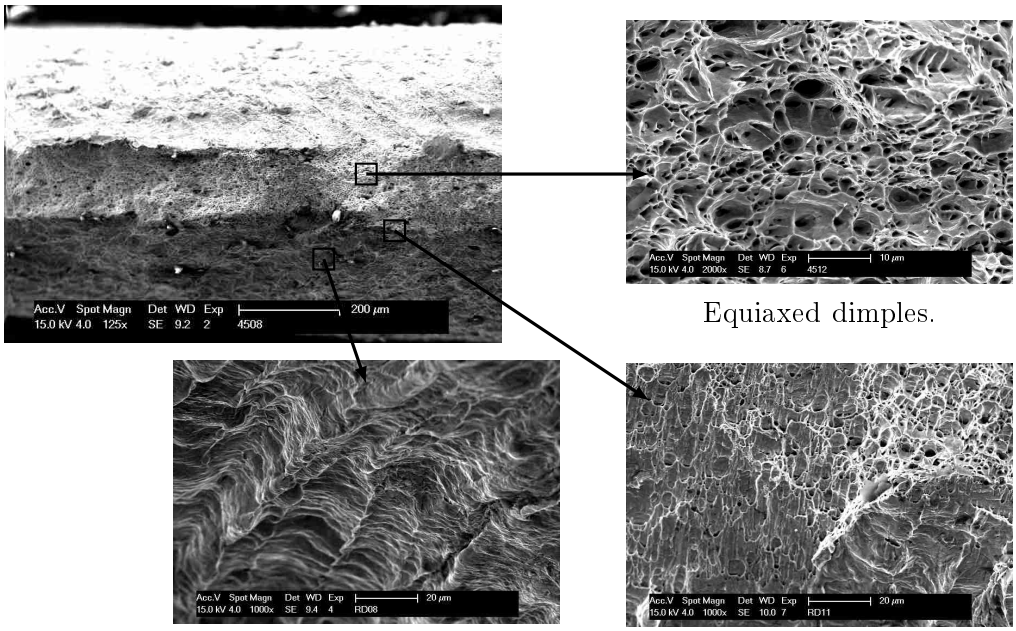

Equiaxed dimples.

Parabolic dimples.

Transition zone.

Figure 5.9: SEM microphotographs showing a ductile behavior in the inner region (equiaxed dimples) of the sheet and shear zones near the surface (parabolic dimples). There is sharp transition between the core and the surface.

The analyzed sample is a 1.0 mm thick pyramid frustum with a 70° wall angle (just above the maximum drawing angle) to induce failure of the material. Samples of ≈1.0 cm × 1.0 cm were cut on both sides of the crack as shown in Fig. 5.10(a). Segment A is right above the crack, segment B is in the pyramid wall, segment D in the curved region of the part and segment E in the undeformed zone that was fixed by the clamping rig. The densities of the samples were measured following a procedure based on the Archimedes' principle (Ratcliffe, 1965). The samples were firstly weighed in air (mass $\mathfrak{A}$) and secondly in a liquid (mass $\mathfrak{B}$) of known density ρ_l (deionised water). The specimen density ρ_0 is then obtained through:

$$\rho_0 = \frac{\mathfrak{A}}{\mathfrak{A} - \mathfrak{B}} \rho_l \tag{5.4.6}$$

The results are shown in Fig. 5.11(a). It can be observed that segment E, which does not undergo any important deformation, has a density similar to the base material (BM). As expected, density is lower in deformed samples, particularly in segment B which is next to the crack. In order to assess this method, densities are converted to void volume fraction through Eq. 5.4.5 and Eq. 5.4.6 and then compared with results from microscopic image analysis (approach detailed in section 5.4.4), as shown in Fig. 5.11(b). There is a big discrepancy between these two methods with a difference of two orders of magnitude. Another difference is that density measurements are not sensitive to local variations of the void volume fraction within the 1.0 cm × 1.0 cm, hence giving an *average value* of porosity.

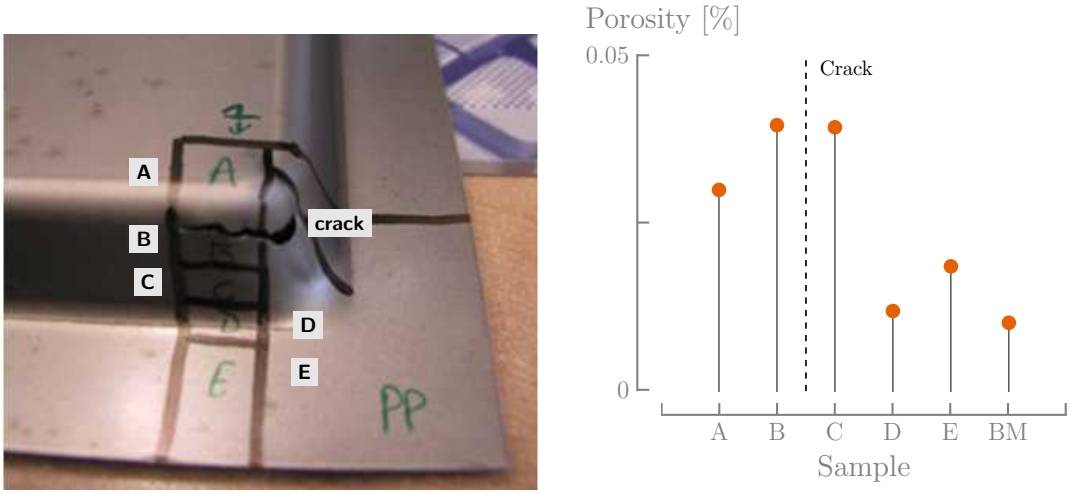

(a) SPIF pyramid samples.

(b) Image analysis results.

Figure 5.10: Porosity distribution over a SPIF pyramid frustum. The image analysis results were obtained following the procedure detailed in section 5.4.4.

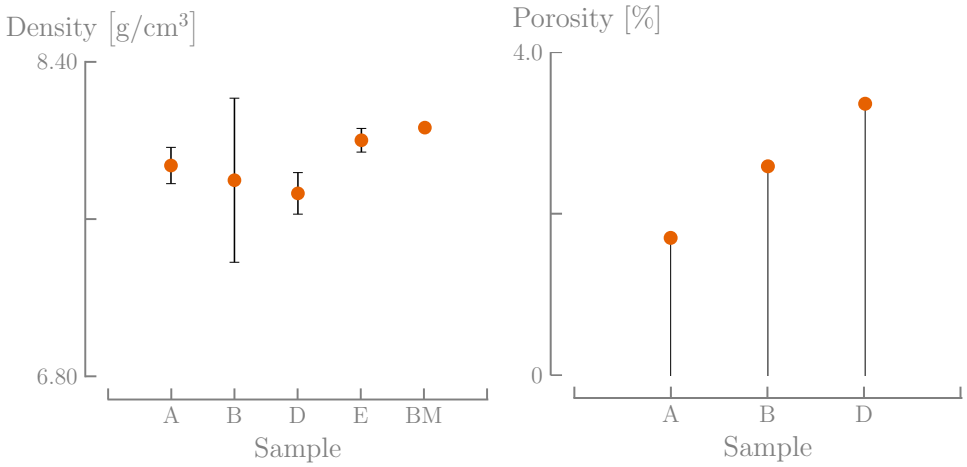

(a) Density measurements.

(b) Void volume fraction.

Figure 5.11: Density measurements and equivalent void volume fraction of the SPIF samples and the base material.

This is clearly seen for segment D in Fig. 5.11, which is overestimated when compared to the image analysis result of Fig. 5.10(b). A normal trend would show a lower porosity in segment D than B, since it is farther from the crack. Mertens et al., (2012) argues that this could be ascribed to different factors, such as the contribution of open porosities on the average volume fraction of voids. These open porosities can be linked to the surface roughness, which is a common feature on sheet forming (e.g. the *orange peel* effect) and expected on this DC01 steel sheet (see section 2.1.2 for the relation between the surface roughness and the grain size). This view is also supported by the fact that segment B, which is part of the wall and the last segment to make contact with the tool, exhibits a great surface roughness as a result of the contouring toolpath and also the greatest dispersion in the density values. It is conclude that density measurements are not appropriate for damage characterization of this DC01 steel sheet.

5.4.4 Microscopic image analysis

An image analysis of broken samples of the mechanical tests (section 5.3) was performed by Hakan Paydas from the A&M department (MMS division) of the ULg. The preparation of the specimen for image analysis involves a special procedure where each specimen is cut using WEDM near the crack zone, coated with a phenolic resin and polished until having a mirror finish near the surface. The sample preparation is shown in Fig. 5.12 and allows to have a clearer view of the porosity. After the preparation, different images were taken for each speci-

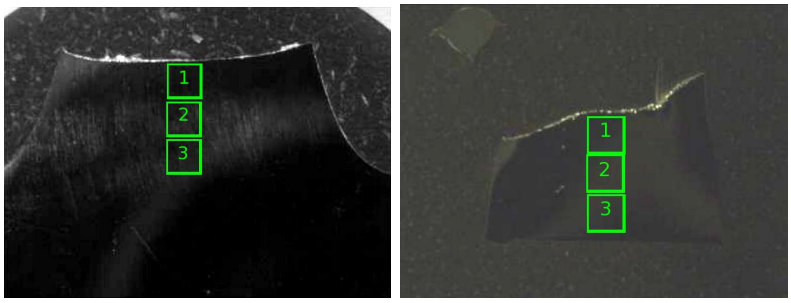

(a) Plane strain specimen. (b) Specimen with notch.

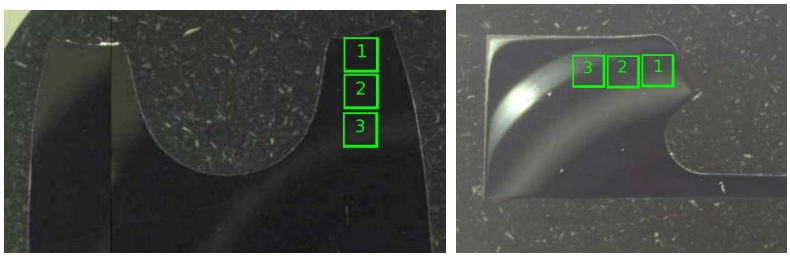

(c) Specimen with a central hole. (d) Shear specimen.

Figure 5.12: Samples preparations of different specimens to measure porosity. Three images are taken (with the same magnification) in the zone indicated with squares.

men (including the base material) using an Olympus BX 60 M optical microscope equipped with a Olympus UC30 digital camera. The fracture surfaces are shown in Fig. 5.13. The fracture surface of the specimens have the typical *bathtub-like*

(a) Notch R =5 mm.

(b) Notch R =10 mm.

(c) Central hole, left side.

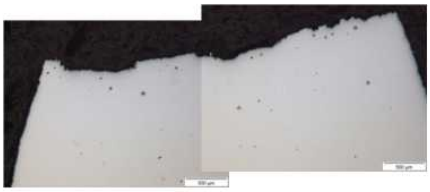

(d) Central hole, left side.

(e) Shear specimen.

Figure 5.13: Image compositions of the fracture zone of fracture specimens prepared for image analysis.

pattern of the flat-type of fracture mode, common in thin metal sheets (Benzerga and Leblond, 2010). Some notched specimens also presented a flat mode in the center and slightly slanted near the edges, as shown in Fig. 5.14. The observed fracture modes are summarized in Table 5.3.

The numerical processing of the images was performed using ImageJ (Abràmoff et al., 2004; Schneider et al., 2012) to quantify the porosity and to measure different granulometric parameters describing the morphology and size of each identified particle. The numerical treatment of the images involves the following steps:

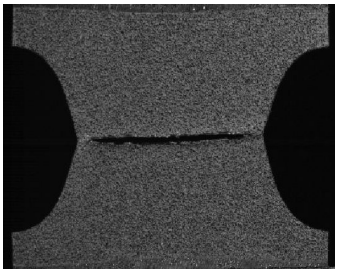

(a) Notch R =5 mm, flat.

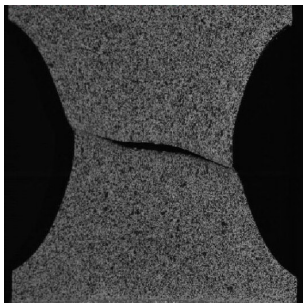

(b) Notch R =10 mm, slanted.

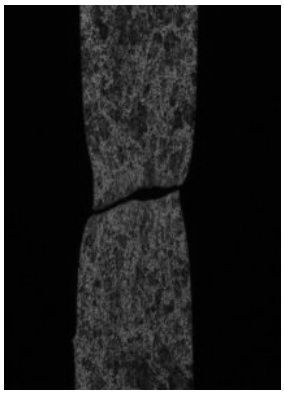

(c) Tensile, slanted.

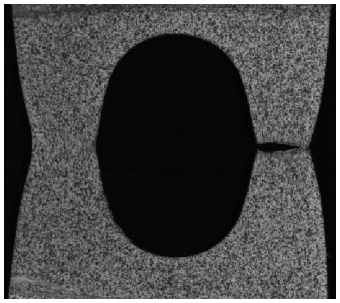

(d) Central hole, flat.

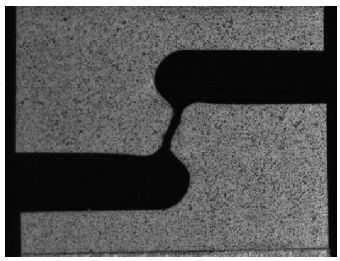

(e) Shear.

Figure 5.14: Fracture modes observed for different specimens.

Table 5.3: Fracture modes observed in the specimens.

Sample	*Fracture mode*
tensile	slanted
Notch R =5 mm	mostly flat
Notch R =10 mm	slanted
Central hole	flat

1. Convert the image from color to greyscale (16-bit).
2. Contrast increment.
3. Automatic thresholding of the image with the six different algorithms implemented in IMAGEJ .
4. From the binary image with the applied algorithm, measure porosity and other parameters like the void shape.

(a) Specimen preparation.

(b) Binary image with Yen's thresholding algorithm.

Figure 5.15: Image preparation and numerical processing of image analysis. Note that the black dots represent the inclusions within the matrix.

In this work, the Yen's thresholding algorithm (Sezgin and Sankur, 2004; Yen et al., 1995) led to the best results in terms of the number and shape of the detected particles within the processed image. Assuming that each particle corresponds to a void, three morphological patterns were obtained using this algorithm: the aspect ratio, circularity and orientation of the detected voids. The aspect ratio is defined as:

$$A_R := \frac{\text{major axis}}{\text{minor axis}} \tag{5.4.7}$$

and is obtained after fitting an ellipse on the detected void. The orientation θ of the void is given by this ellipse, being the angle between the primary (major) axis of the ellipse and a line parallel to the X-axis of the image. The circularity is defined as:

$$C_R := 4\pi \frac{\text{Area}}{\text{perimeter}} \tag{5.4.8}$$

where a value of C_R =1.0 means a perfect circle. Since the value approaches to C_R =0.0, it indicates an increasingly elongated shape.

The first analysis was carried on using the base material i.e., without any type of deformation. Preliminary results on broken tensile specimens showed that some voids can be very small (∼1 µm), so a high magnification had to be used. In the following results, 2.5x corresponds to a scale of 1.361 µm/pixel while 10x to 0.342 µm/pixel. Six different images of the base material were taken and

Table 5.4: Image analysis data obtained from the base material using IMAGEJ (Average values from six samples).

Initial porosity (%) f_0	*Circularity* C_R	*Aspect ratio* A_R	*Orientation* (°) θ
0.0779 ± 0.0290	0.9067 ± 0.0149	1.5667 ± 0.0735	67.8095 ± 8.4907

the results are shown in Table 5.4. Porosity is found to have a high dispersion depending on the image. Since the value identified $f_0 = 8.0 \times 10^{-4}$ is relatively small, the presence of large inclusions has an important influence in analyzed data. Voids tends to be elongated even if circularity is close to 1.0.

The next step is to analyze the fracture specimens following the procedure described above. Images were taken near the crack as in Fig. 5.13. A MATLAB script was developed to obtain the porosity distribution near the crack and the results are shown in Fig. 5.16. The porosity is found to be very low ($\ll 1.0 \times 10^{-3}$)

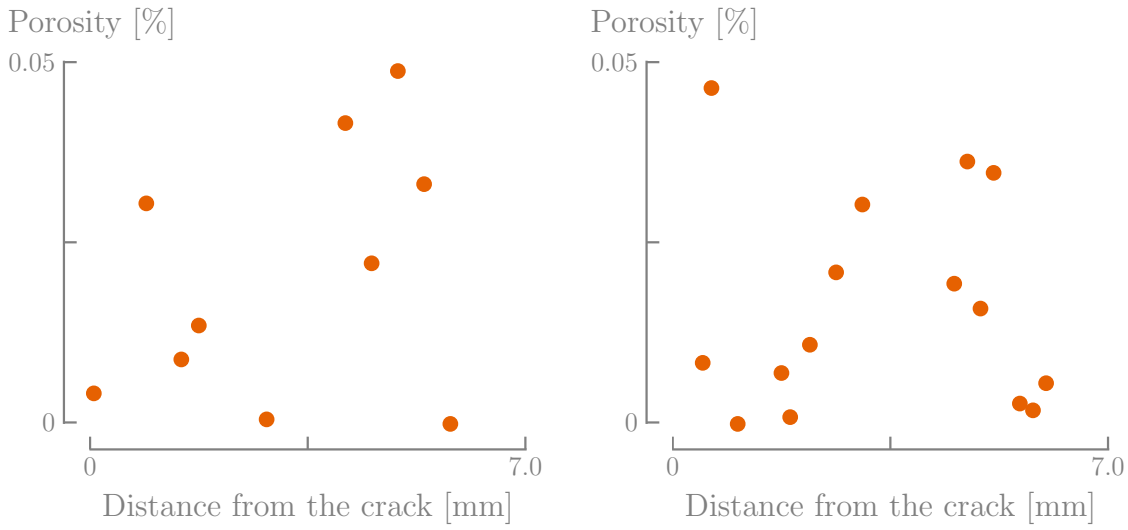

(a) Notch $R = 5$ mm. (b) Notch $R = 10$ mm.

Figure 5.16: Porosity distribution in the notched samples (in percentages).

in all analyzed samples. Moreover, they do not follow any particular trend as an exponential distribution (due to nucleation, growth and coalescence of voids) near the crack as expected. Identical observation is found for other morphological patterns. A possible explanation for these results is that the polishing step was performed too close to the specimen surface and did not reach the core. Near the surface, as analyzed in section 5.4.2, dimples are parabolic with hardly observable voids. So this microscopic section did not provide interesting results for the Gurson model identification, except for f_0 value which will be set to 8.0×10^{-4} from Table 5.4. A more adapted technique could have been tomography as used, for instance, by Maire and coworkers (c.f. Bouaziz et al., 2008; Bouchard et al., 2008; Fansi et al., 2013; Landron et al., 2011; Maire, 2004; Weck et al., 2006).

5.5 Numerical identification

The previous section focused on the experimental characterization of damage based on both microscopic and macroscopic measurements. This current section uses these experimental results to calibrate the Gurson model parameters of nucleation, coalescence and shear. As previously stated, the strong non-linearity of the implemented equations greatly complicates the task. Hence, the following methodology is proposed:

1. Evaluation of the plasticity model through an experimental-numerical comparison of the force-displacement and strain-displacement curve. The goal here is to choose one hardening law for subsequent developments. This first step also evaluates the effect of both mesh and boundary conditions, before their use within the damage model identification.

2. Characterization of the nucleation law, coalescence model and shear extensions using inverse analysis with Optim (described in section 2.7.2).

3. Analysis of the evolution of triaxiality, Lode angle, etc.

All the simulations were performed using the `BWD3D` finite element (see section 6.2 for further details), which only has one integration point. The meshes were generated using Gmsh (Geuzaine and Remacle, 2009) and then exported to Lagamine using a Matlab script. They are shown in Fig. 5.17. A sensitivity was carried to out to determine the influence of the mesh on the results. Three FE meshes were analyzed, two with 3 element layers in the thickness direction and different mesh refinement and one with 10 element layers, as seen in Fig. 5.18. The results of this mesh sensitivity analysis are shown in Fig. 5.20(a). There is no appreciable influence of the mesh on the results, so mesh1 will be used for subsequent simulations.

5.5.1 Plasticity simulations

The plasticity material set of parameters obtained in chapter 2 are applied to simulate the fracture specimens. Here, no damage is simulated since the goal is to check the plastic model predictions. The simulations are stopped at the fracture displacement but no crack prediction is available. Therefore, and depending on the hardening law, four set of parameters are available: pure isotropic hardening using the Swift or Voce law or Mixed hardening using the Swift or Voce law plus Armstrong and Fredrick, (1966) kinematic hardening. Moreover, four sets of parameters are added depending on if they were identified using an isotropic (Von Mises) or anisotropic (Hill, 1948) yield locus. Table 5.5 summarizes all the sets. The displacement is calculated from the nodes matching the DIC virtual gauge shown in Fig. 5.6, while the strain in the loading direction is obtained from an element depicted in Fig. 5.19. A comparison between the yield locus is given in Fig. 5.20(b), using `set 3` and `set 7`. The sets using the VM yield locus are slightly better than the sets using Hill, (1948), but they are not able to correctly predict the force at 45° from the RD, as shown in section 2.7.3.2 (Fig. 2.25). Hence,

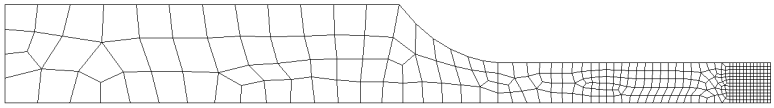

(a) Tensile mesh.

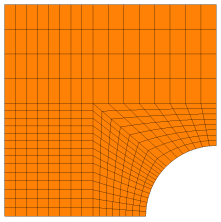

(b) R =5 mm mesh.

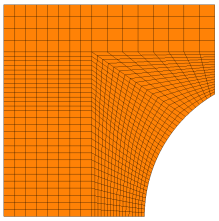

(c) R =10 mm mesh.

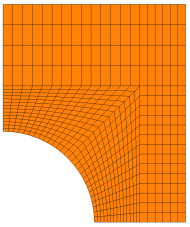

(d) Central hole mesh.

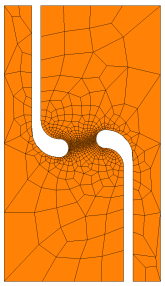

(e) Shear mesh.

Figure 5.17: Meshes used for the identification methodology. For the tensile specimen, specimens with notch and central hole, symmetry conditions are applied so only one quarter of the specimen is simulated.

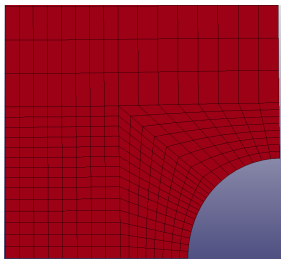

(a) mesh1: 1708 elements, 3 layers.

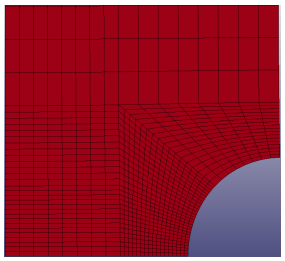

(b) mesh2: 3864 elements, 3 layers.

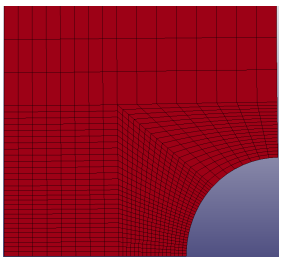

(c) mesh3: 10 626 elements, 10 layers.

Figure 5.18: Meshes used for the sensitivity analysis.

Table 5.5: Set of plastic parameters tested.

	Von Mises	*Hill, (1948)*	*Swift law*	*Voce law*	*A-F model*
`set 1`	√		√		
`set 2`	√			√	
`set 3`	√		√		√
`set 4`	√			√	√
`set 5`		√	√		
`set 6`		√		√	
`set 7`		√	√		√
`set 8`		√		√	√

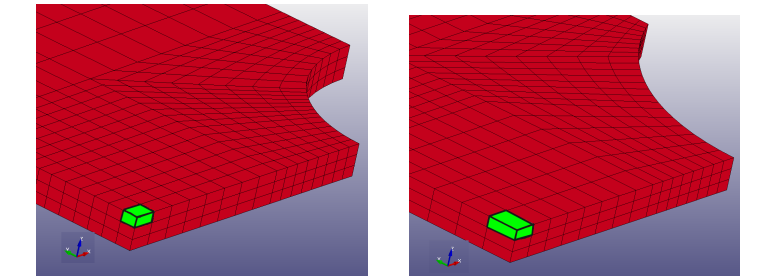

(a) Notch R =5 mm. (b) Notch R =10 mm.

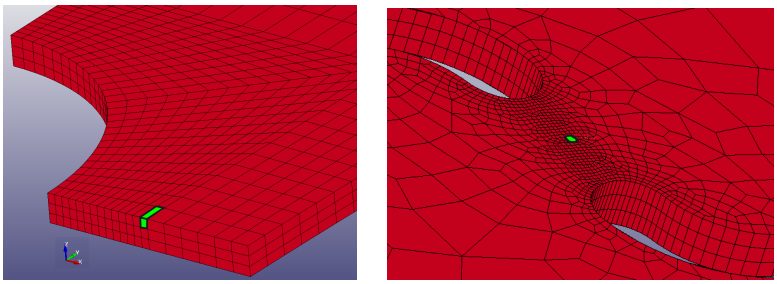

(c) Center hole. (d) Shear.

Figure 5.19: Elements in the FE mesh where the strains (and other state variables) are extracted.

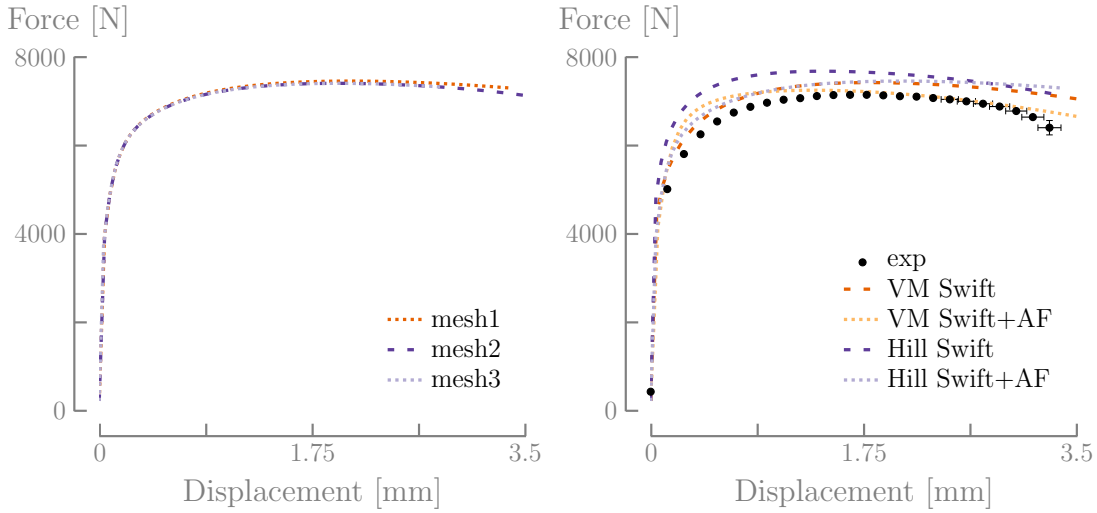

(a) Mesh influence. (b) Von Mises versus Hill, (1948) yield locus.

Figure 5.20: Preliminary results regarding the mesh and yield locus influence on the force vs. displacement curve, in the specimen with a notch R =5 mm.

the results for the Hill, (1948) yield locus (`set 5` to `set 8`) are analyzed, in Fig. 5.21 for the force-displacement curve and in Fig. 5.22 for the strain-displacement curve. In general, the force prediction in Fig. 5.21 tends to overestimate the experimental measurements while fracture displacement and strain predictions in Fig. 5.22 and Fig. 5.23 reasonably match with DIC measurements with no clear trends of under or overestimation. This is a consequence of the plastic identification procedure of chapter 2. As shown in Table 2.15, the optimized set of Hill, (1948) parameters (section 2.7.4.2) are closer to the SMM approach than the SSF approach. Thus, a better prediction of deformation than forces is expected. As damage development is associated with material softening, from a pragmatic point of view a slight overestimation of force is desirable when simulating without damage as subsequent damage development will soften the material.

From the numerical results, it is observed that the pure isotropic Voce hardening law tends to localize the plastic flow before the end of the test. Localization refers to the phenomenon involving the development of strong strain gradients near a particular zone. This strain localization is in the form of a neck developed in the notch test, as observed in Fig. 5.24. This phenomenon starts when the increase on the load bearing capacity (hardening) is not longer balanced with the reduction of the cross section area, as predicted by the Considère, (1885) criterion. Hachez, (2008) observed the same early localization for Al6082 sheets of different thickness. In order to circumvent this localization, Hachez, (2008) proposed to use different linear extrapolations of the Swift law in order to allow the material to harden more than the limit given by the real hardening law. This approach, despite being useful in cases explored by Hachez, (2008), is not needed to be implemented in this work as it was clear from Fig. 5.21 that using a mixed-type of hardening stabilizes the deformation for the pure Voce law thus avoiding localization. The observed localization of the pure Voce law seems to be due to both a *geometric* factor (thin sheet metal) and the constitutive modeling (lack of hardening at the end of the stress-strain curve). To conclude, it is observed that the set of parameters with the mixed Swift-Armstrong and Fredrick, (1966) and Hill, (1948) yield locus is the only that overestimates the force level for the specimen with central hole. This set of parameters will be used hereafter for damage characterization.

5.5.2 Damage characterization

f_0 is fixed to 8.0×10^{-4} based on the results obtained using image analysis from section 5.4.4. This is a very low value and in some cases could be neglected, but preliminary numerical tests showed that f_0 can have an important impact on nucleation and coalescence parameters. Hence, $f_0 = 8.0 \times 10^{-4}$ will be used hereafter. As previously stated, nucleation and coalescence parameters of the Gurson model can be identified through an inverse analysis using OPTIM. Several issues prevent the use of this approach entirely:

- Each simulation can take a considerable amount of CPU time (more than one hour for simulations using the meshes depicted in Fig. 5.17). Single-

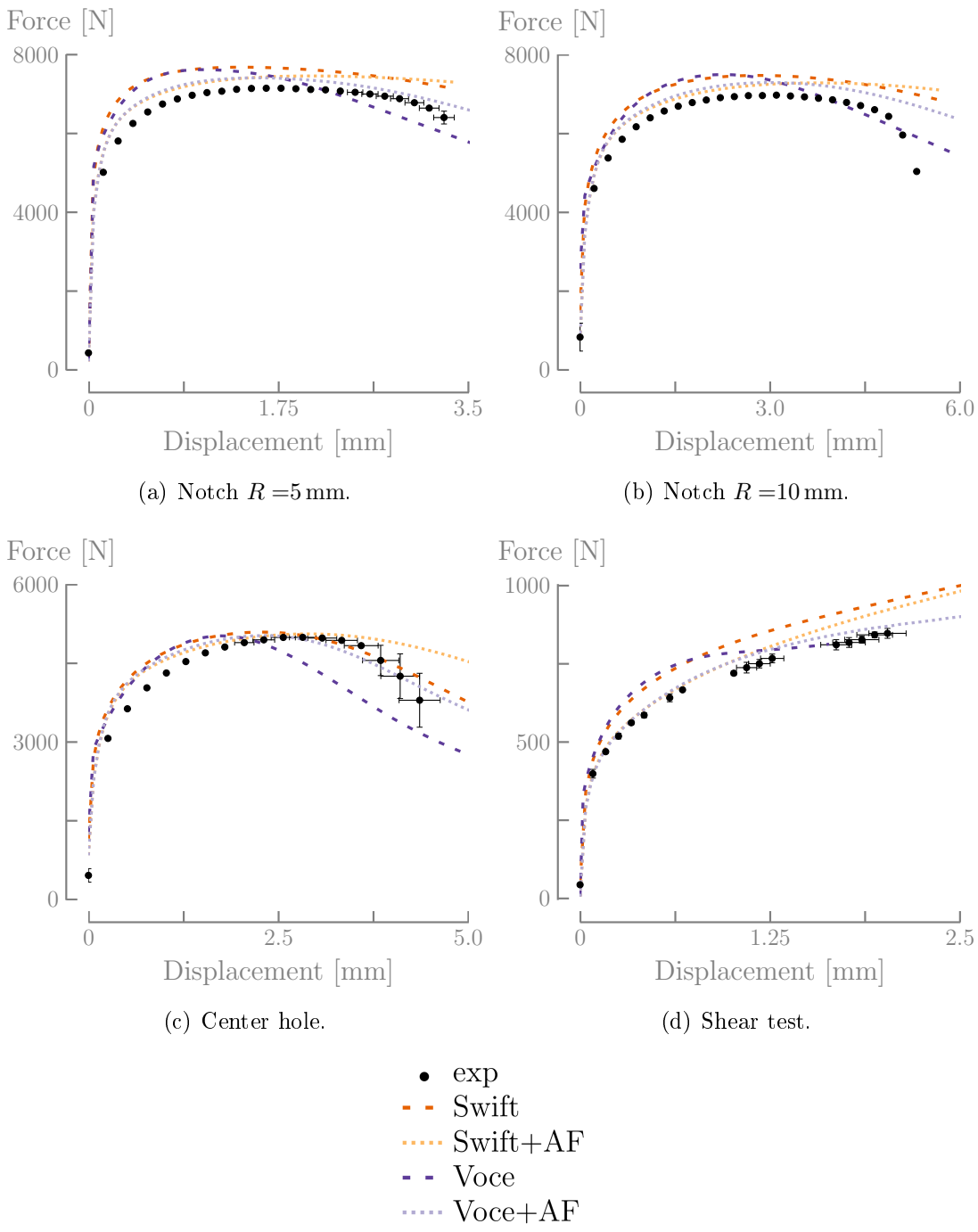

(a) Notch $R = 5\,\text{mm}$.

(b) Notch $R = 10\,\text{mm}$.

(c) Center hole.

(d) Shear test.

(e) Legend.

Figure 5.21: Force vs. displacement using the load cell for experiments and simulations using plasticity parameters (without damage). Using sets with the Hill, (1948) yield locus of Table 5.5.

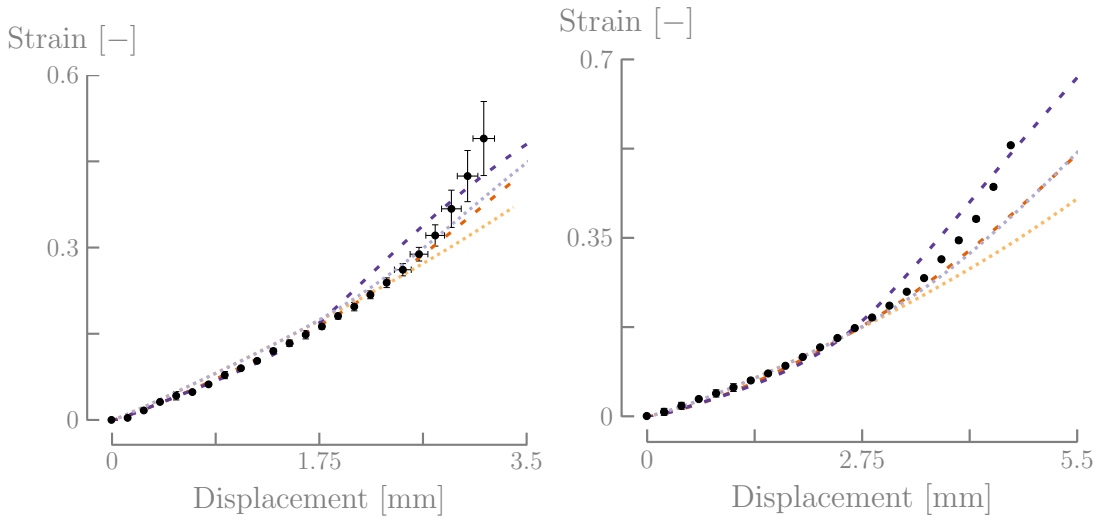

(a) Notch $R = 5\,\text{mm}$.

(b) Notch $R = 10\,\text{mm}$.

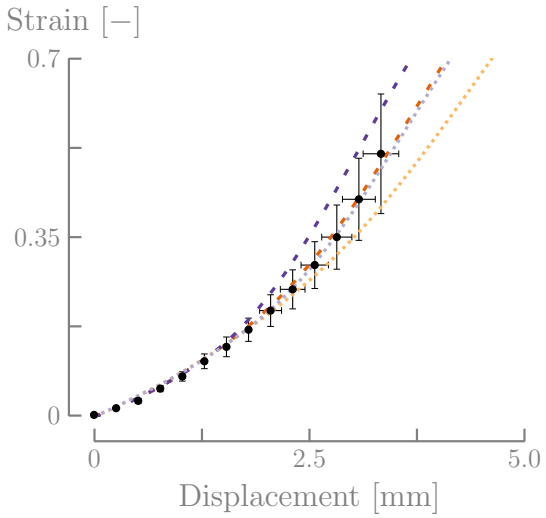

(c) Center hole.

Figure 5.22: Strain vs. displacement using DIC for experiments and simulations using plasticity parameters (without damage). Using sets with the Hill, (1948) yield locus of Table 5.5. Legend in Fig. 5.21(e).

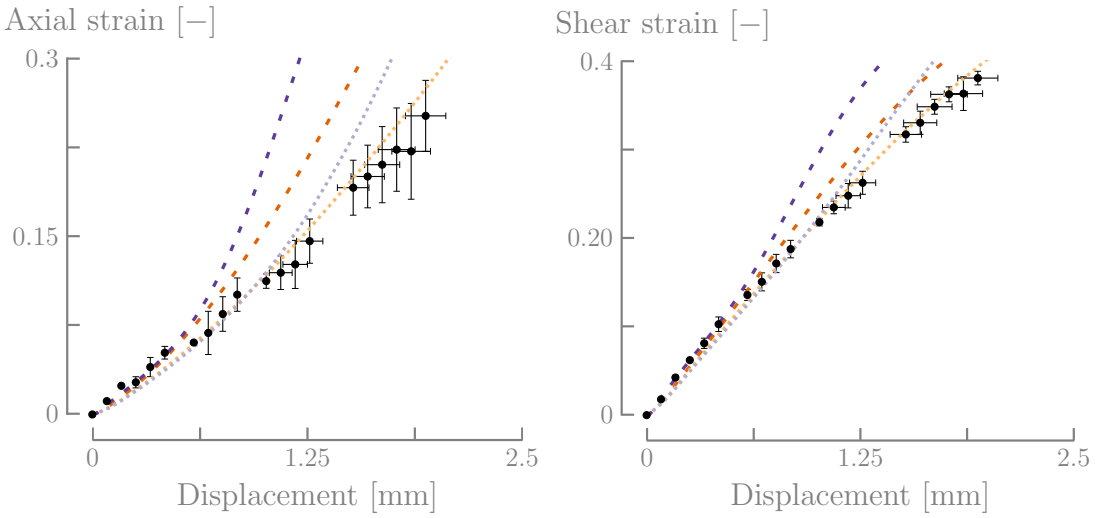

(a) Axial strain. (b) Shear strain.

Figure 5.23: Strain vs. displacement for the shear tests, using DIC for experiments and simulations using plasticity parameters (without damage). Using sets with the Hill, (1948) yield locus of Table 5.5. Legend in Fig. 5.21(e).

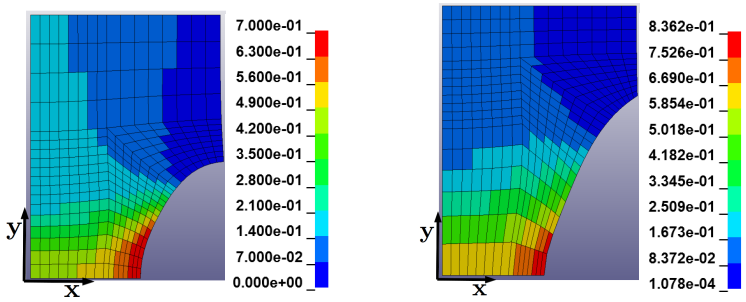

(a) Notch $R = 5\,\text{mm}$. (b) Notch $R = 10\,\text{mm}$.

Figure 5.24: Equivalent plastic strain distribution at the end of the simulation using the (pure isotropic) Voce law.

element simulations, used for plasticity characterization as in chapter 2, can not be used due to the heterogeneous nature of damage simulations and strain distribution.

- OPTIM could require several simulations to be performed in each optimization loop, depending on the selected number of tests to optimize.
- Nucleation parameters are very sensitive to the initial proposed solution. This is a characteristic of the optimization function which has several local minima.
- Nucleation and coalescence are not relevant at the beginning of the simulation, so *weights* should be introduced into Eq. 2.7.2 in order to optimize particular zones of the force-displacement curve.
- In its current state, OPTIM does not have a parallel version and can not be coupled with the existing parallel version of LAGAMINE. Therefore, performing an optimization can take (several) days without any guarantee that the obtained solution will fall within a desired range.

Hence, a different approach is used here. Because each simulation takes a considerable amount of CPU time and performing an optimization requires even more time, LAGAMINE will be used until a certain displacement d_1. This displacement is determined based on the comparison between the results using a set with only initial porosity ($f_0 = 8.0 \times 10^{-4}$, without nucleation neither coalescence) and the experimental curve. The point where both curves separate is defined to be d_1. At this point, the set of results is saved by LAGAMINE. Since nucleation parameters are very sensitive to the initial solution, several preliminary simulations were performed in order to find parameter ranges that will allow a good force prediction. Then, the set of results saved is retrieved by OPTIM to perform an optimization over the nucleation parameters. Indeed, OPTIM is used *to validate* a set of preliminary nucleation parameters by identifying another set which does not significantly differs from the preliminary set. Nucleation parameters are found using this approach applied to the notched specimens. Fig. 5.25 schematize the described approach. This approach has some limitations that are worth mentioning. When the initial damage f_0 is considerable or when nucleation is important, it is sometimes difficult to separate the effect of plasticity and damage. Hence, starting with the saved set of results from LAGAMINE at d_1, the identified set of nucleation parameters do not consider the coupling between damage and plasticity in the beginning of the simulation ($d < d_1$). The numerical tests confirm that for the case of the DC01 steel, the coupling between plasticity and damage at the beginning of the curve is negligible and hence d_1 can be considered as an acceptable start for damage development.

Coalescence parameters were not possible to identify using this methodology, as they are strongly sensitive not only to the initial proposed solution but also to the convergence parameters of the simulation (maximum time step, value of norms telling that convergence is reached, maximum number of iterations, ...). Function weights seem to be necessary to perform an inverse analysis within this

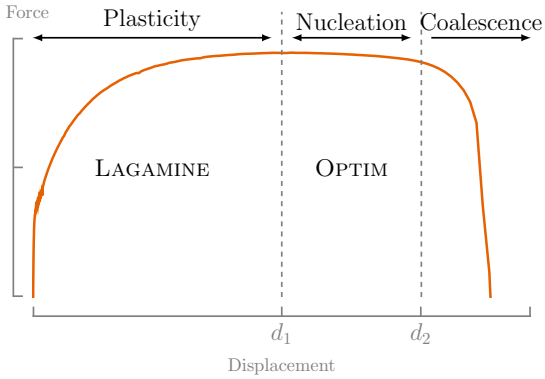

Figure 5.25: Damage parameters identification methodology. LAGAMINE is used until a displacement d_1. Then, OPTIM is used to verify the proposed parameters performing an optimization from d_1 until d_2.

zone of the force vs. displacement curve. For this reason, a sensitivity analysis was used with the physically based values obtained in section 5.4.1. Several simulations were performed using the notched specimens in order to fix the most representative parameters. It must be remarked that for coalescence identification, the calibration of material parameters is highly dependent on the previous set of nucleation parameters. Hence, each calibration step (i.e., nucleation and then coalescence) are iteratively repeated until satisfactory results are obtained.

After obtaining nucleation and coalescence parameters, the shear parameters are obtained relying on the shear tests. Indeed, these parameters are arguably independent of the calibration step performed in the notched specimens because the GTN shear extensions are relevant only when triaxiality is low. However, Nielsen and Tvergaard, (2010) showed that the extension by Nahshon and Hutchinson, (2008) predicts void growth due to shear even for large triaxialities, thus they introduced some corrections factors (detailed in section 3.4.3). Therefore, the calibration of these correction factors should be done in the notched tests.

Another issue involves the integration scheme of the GTN implementation, as the damage material parameters were found to be sensitive to the (user defined) parameter N_{intv}:

$$\delta t = \frac{\Delta t}{N_{\text{intv}}} \tag{5.5.1}$$

which is the subinterval integration parameter of the subroutine `GUR3Dext`, detailed in section 4.3.3. It was observed that this value plays an important role in the results, both in terms of accuracy and convergence. For instance, it is noted that:

- For a damaging model ($f_0 \neq 0.0$), the force and the strain are affected by N_{intv} but not some state variables such as the porosity, the triaxiality or the Lode parameter.
- Convergence is harder to achieve using coalescence parameters than only using nucleation parameters. Higher values of N_{intv} are thus required to simulate coalescence.

- N_{intv} does not have an influence on the global results (in terms of force, displacement, strain, etc.) for a plasticity model without damage (f_0 =0.0). It only affects the convergence of the simulation at the constitutive law level.

The explanation behind these observations is the calculation of the stiffness matrix at the element level (subroutine `ELEMB` in LAGAMINE). When the tangent matrix is analytically calculated, there is a contribution from both element derivatives (large deformations) and the material subroutine. Changing N_{intv} will affect the material contribution and thus the calculation of force and displacement at the element level. In order to overcome this unwanted characteristic of the model, another methodology is proposed:

1. Find preliminary values of N_{intv} that will allow convergence, using a preliminary set of nucleation and coalescence parameters.

2. With these values it is possible to find a $\Delta\boldsymbol{\epsilon}_{\max}$ that will allow convergence of the simulation. It is also possible to estimate the required time interval that will simulate coalescence without convergence issues. To do this, it is necessary to observe the evolution of $\Delta\epsilon_q$ in a simulation [2].

3. With the value of $\Delta\epsilon_{\max}$, define N_{intv} (and N_ϵ eventually) for the next simulations.

4. Redefine or validate the nucleation parameters.

5. Find coalescence and shear parameters.

It is found that a strain increment of $\Delta\epsilon_q$ <0.004 allows to simulate coalescence without convergence issues, needing N_{intv} ≈10 and N_ϵ ≈3000.

Following the above procedure, the obtained parameters are shown in Table 5.6. No important influence of the mesh refinement was observed for the tests simulations neither in terms of accuracy of the results nor convergence characteristics. The meshes of Fig. 5.17 were used. The Xue, (2008) shear extension did

Table 5.6: Set of parameters obtained for the GTN model extended to shear.

		Nucleation			*Coalescence*		*Shear*
Set name	f_0	f_N	S_N	ϵ_N	f_c	f_F	k_ω
`coa1`	0.0008	0.0025	0.175	0.42	0.0055	0.135	-
`coa2`	0.0008	0.0025	0.175	0.42	0.0045	0.145	-
`coa3`	0.0008	0.0025	0.175	0.42	0.0025	0.170	-
`shear1`	0.0008	0.0025	0.175	0.42	0.0055	0.135	0.25
`shear2`	0.0008	0.0025	0.175	0.42	0.0045	0.145	0.25
`shear3`	0.0008	0.0025	0.175	0.42	0.0025	0.170	0.075

not converge for most of the tests simulations and was discarded from the analysis.

[2] $\Delta\epsilon_q$ can be considered as an estimation of the deformation tensor $\Delta\boldsymbol{\epsilon}$. Refer to section 4.3 for the precise definition of $\Delta\epsilon_q$.

Different set of parameters were obtained since it was not possible to retrieve one single set matching all the tests. Comparing the set of coalescence parameters with the physically-based estimation of Table 5.2, f_F has a good agreement but f_{cr} is one order of magnitude lower than the estimation. This confirms the fact that f_F is easier to estimate in ductile metallic materials than f_{cr}, which depends not only on f_0 but on other factors such as the triaxiality.

The results using the parameters from Table 5.6 are shown in Fig. 5.26 for the force vs. displacement curve, in Fig. 5.28 and Fig. 5.29 for the axial and shear strain respectively. Note that in Fig. 5.29 the shear strain is also included, because its magnitude is higher than the axial strain on this test. First, the

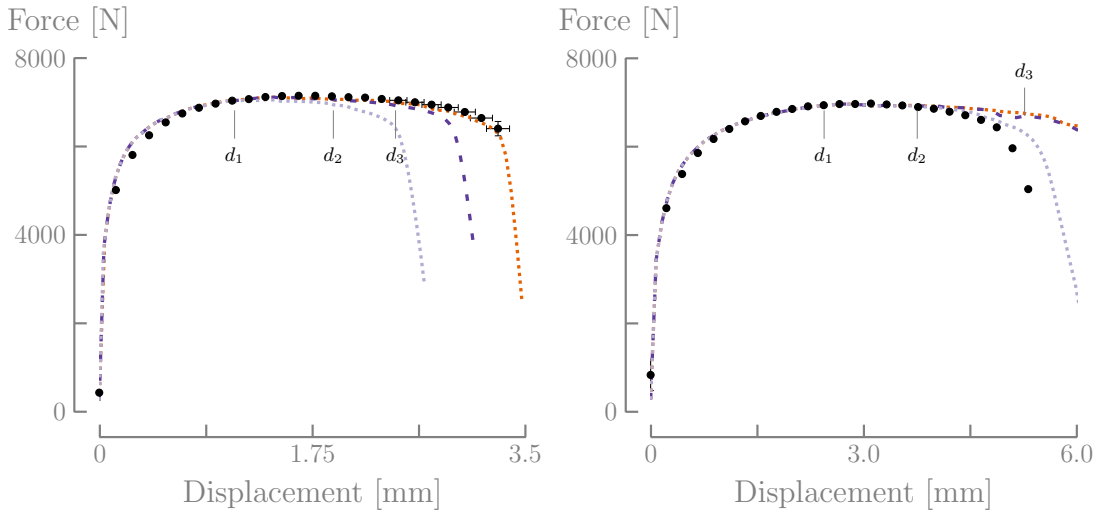

(a) Notch R =5 mm.

(b) Notch R =10 mm.

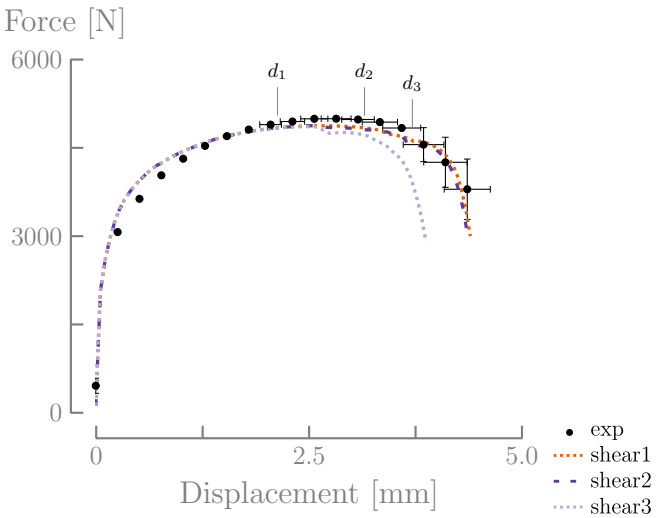

(c) Center hole.

(d) Legend.

Figure 5.26: Force vs. displacement using the load cell for experiments and FE simulations predictions using the GTN model extended to shear.

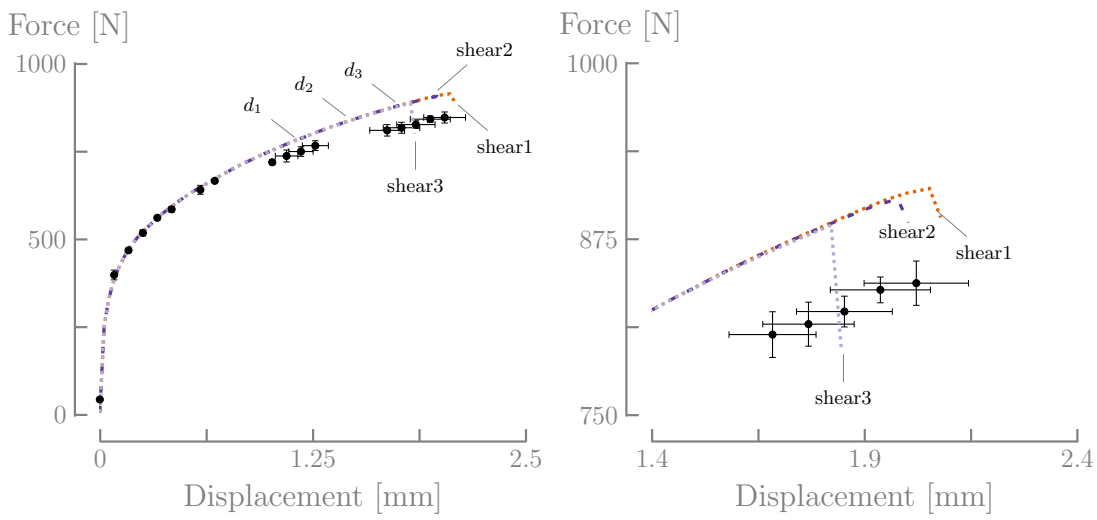

(a) Shear test.

(b) Zoom near the fracture displacement.

Figure 5.27: Force vs. displacement using the load cell for shear specimen experiments and FE simulations predictions using the GTN model extended to shear. A zoom is added to have a clearer view of the near the fracture displacement.

identification was done for the nucleation and coalescence parameters without the shear extension. `coa1` set is optimal for the R =5 mm notch specimen, the shear specimen and specimen with central hole. `coa2` set is optimal for the specimen with central hole and `coa3` set is adapted to the specimen with R =10 mm notch. In general, it was observed that the sets `coa1` and `coa2` match very well the *flat* type of fracture, depicted in Fig. 5.14. The specimen with R =10 mm notch (and the tensile test) presents a *slanted* type of fracture which is not captured by the sets `coa1` and `coa2`. Based on these coalescence parameters, three different sets using the shear extension proposed by Nahshon and Hutchinson, (2008) were obtained: `shear1`, `shear2` and `shear3`. In addition, correction parameters proposed by Nielsen and Tvergaard, (2010) (see Eq. 3.4.8) were identified in order to reduce the influence of the Lode parameter at high triaxialities ie., for the specimens with notch and central hole. It was found that the proposed correction parameters, T_1 =0.35 and T_2 =0.70, leads to good results. The effect of the correction is shown in Fig. 5.30. Independent of the shear set of parameters used, the force in the shear tests is over predicted in less than 8% (see Fig. 5.27). This can be due to the role of the shear anisotropy coefficients L, M and N, which are assumed to be equal for thin sheets.

In general, the model is able to correctly capture the coalescence features of the material. Table 5.7 presents a qualitative summary of the comparison between experimental and numerical results. In theory, an unique set of parameters of GTN parameters should be able to predict coalescence for all analyzed tests. Nevertheless, in this work it was not possible to obtain except if lack of accuracy is agreed on the notch R =10 mm; in this case, the set `shear1` is acceptable. Some

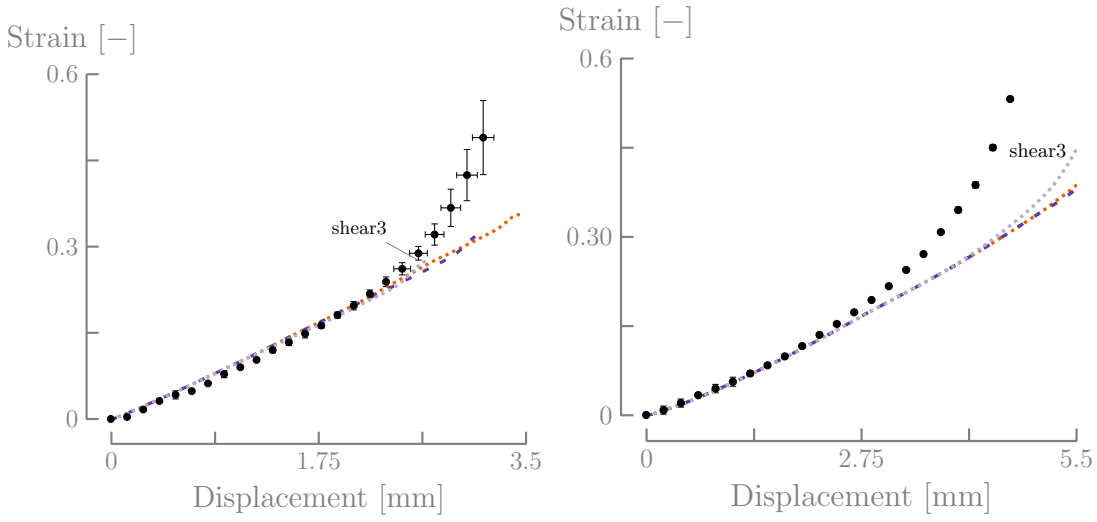

(a) Notch R =5 mm.

(b) Notch R =10 mm.

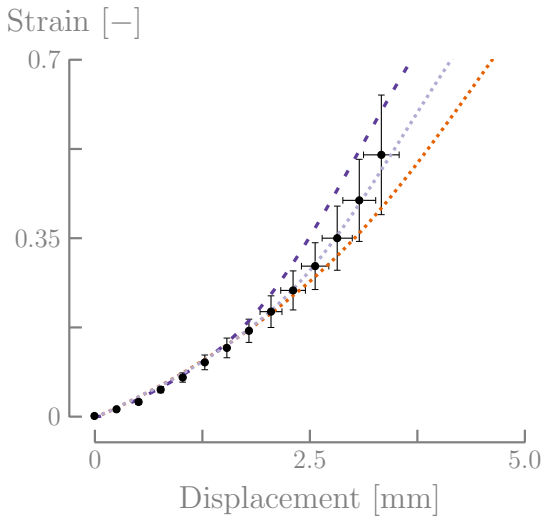

(c) Center hole.

Figure 5.28: Strain vs. displacement using DIC for experiments and FE simulations predictions using the GTN model extended to shear.

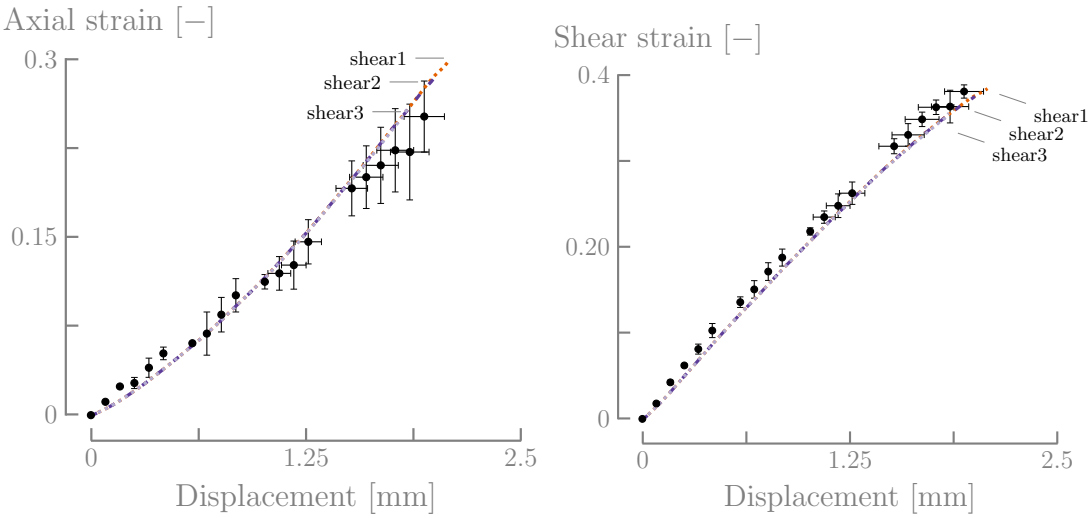

(a) Axial strain. (b) Shear strain.

Figure 5.29: Strain vs. displacement using DIC for the shear test and FE simulations predictions using the GTN model extended to shear.

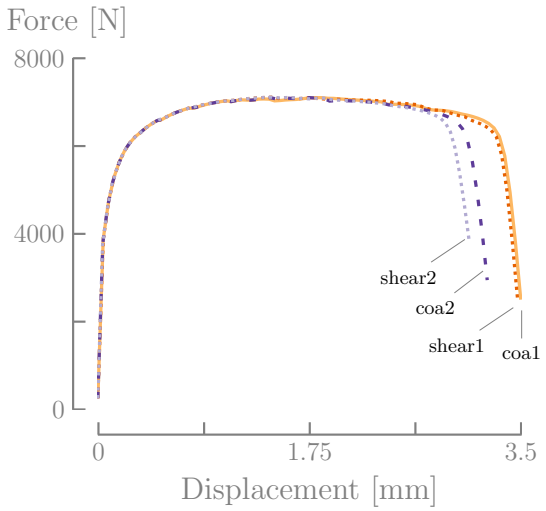

Figure 5.30: Force vs. displacement results on the R =5 mm notch specimen showing the influence of the Nielsen and Tvergaard, (2010) correction. It can be seen that the correction improves the shear extension prediction at high triaxiality.

possible explanations are:

- The GTN yield locus parameters q_1 and q_2 were not calibrated. They can play a role similar to nucleation parameters, as shown by Dunand and Mohr, (2011a).
- It is shown in section 5.5.1 that kinematic hardening can stabilize the deformation. Nevertheless, in chapter 2, it is clearly observed that the A-F model is not adequate for this material because it does not predict hardening stagnation.
- Yield locus anisotropy can play an important role on damage development, here only the Hill, (1948) is taken into account.
- The numerical integration scheme using sub-intervals requires further analysis due to the role that parameter N_{intv} and N_ϵ play in the predictions and convergence of the simulations.
- A different test campaign could lead to different results.

Table 5.7: Qualitative comparison between the FE predictions using the GTN model and experimental results.

	Set	R =5 mm	R =10 mm	Central hole	Shear
Force level	`shear1`	√	√	√	over
	`shear2`	√	√	√	over
	`shear3`	√	√	√	over
Force decrease	`shear1`	√	–	–	√
	`shear2`	–	–	√	√
	`shear3`	–	√	–	√
Strain	`shear1`	too low	too low	too low	√
	`shear2`	too low	too low	too high	√
	`shear3`	too low	better	√	√

In terms of the strain prediction, almost no influence of the set of parameters on the strain level is observed. For the specimens with notch (Fig. 5.28(a) and Fig. 5.28(b)), the FE simulation was not able to predict the sudden increase of strain measured by DIC (localized strain band). As a consequence, the strain at fracture predicted by the Gurson model is severely underestimated on the notched specimens. This increase on the strain was also (experimentally) observed by Dunand and Mohr, (2010, 2011b), due to the development of diffuse and localized necking at the center of the specimen. On the contrary, DIC measurements over the specimen with central hole did not present this behavior. The explanation is the severe distortion of the speckle pattern applied on the surface, which disallowed the observation of the strain evolution near fracture. For this specimen, Table 5.1

predicts a strain at fracture of $\epsilon_f \approx 0.88$ which is far from the last measured point (≈ 0.53 in Fig. 5.28(c)). Forthcoming experiments using this specimen should consider a reduced hole diameter in order to have less distortion at the width. Shear tests in Fig. 5.29 also did not present strain localization as present in the notched specimens. This is highly desirable as this test is designed to identify shear parameters prone to failure of the shear type.

To further explore the reasons behind the fact that a localized strain band observed in notched specimens (see Fig. 5.28(a) and Fig. 5.28(b)) is not predicted, it is necessary to look at the iso-values maps of the strain. Fig. 5.31 to Fig. 5.34 show a comparison between the axial strain measured in the loading direction using DIC and FE predictions for the (shear) set of parameters of Table 5.6 for the four specimens geometries. Fig. 5.35 provides the shear strain within the shear sample.

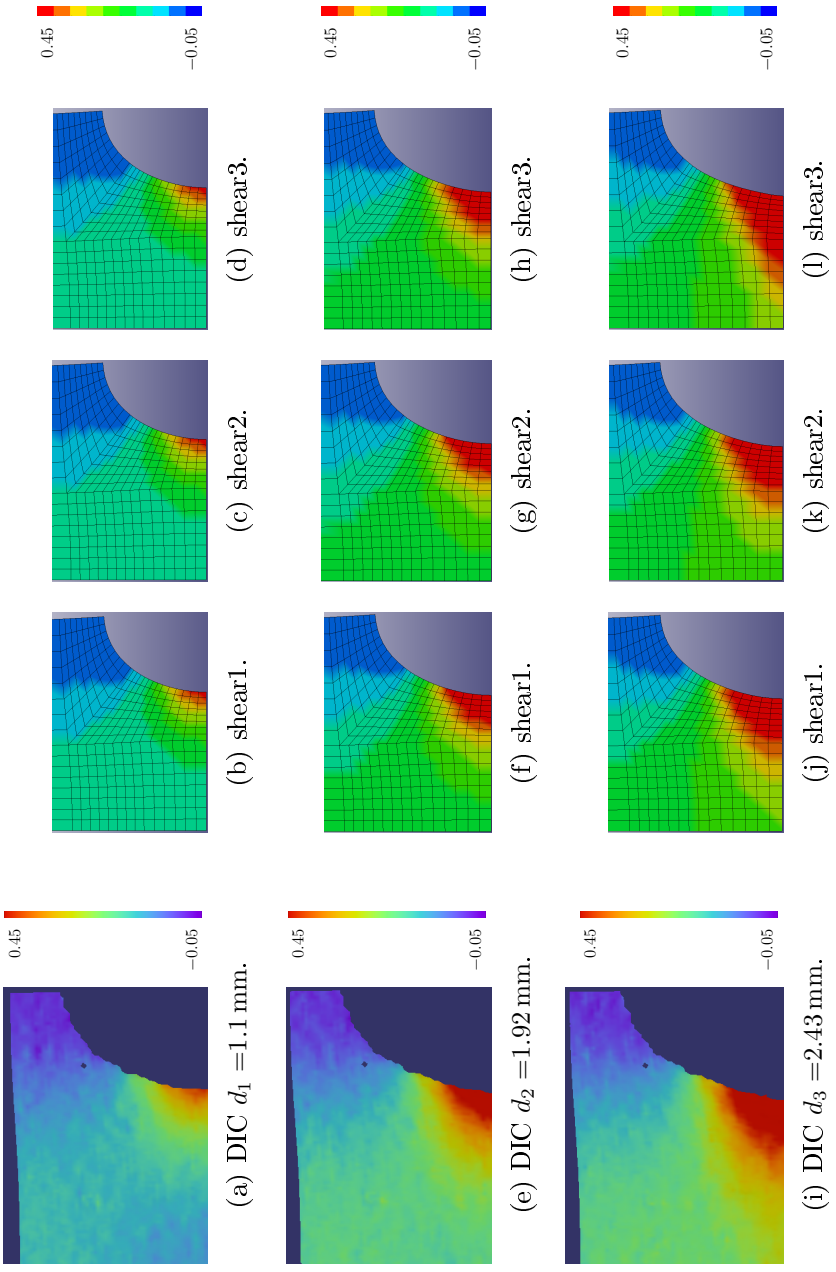

(a) DIC d_1 =1.1 mm. (b) shear1. (c) shear2. (d) shear3.

(e) DIC d_2 =1.92 mm. (f) shear1. (g) shear2. (h) shear3.

(i) DIC d_3 =2.43 mm. (j) shear1. (k) shear2. (l) shear3.

Figure 5.31: Iso-values maps comparison between DIC and FE results of axial strain at different gauge displacements. Results for the specimen with notch R =5 mm. d_1, d_2 and d_3 are the displacements at where the results are obtained, as seen in Fig. 5.26.

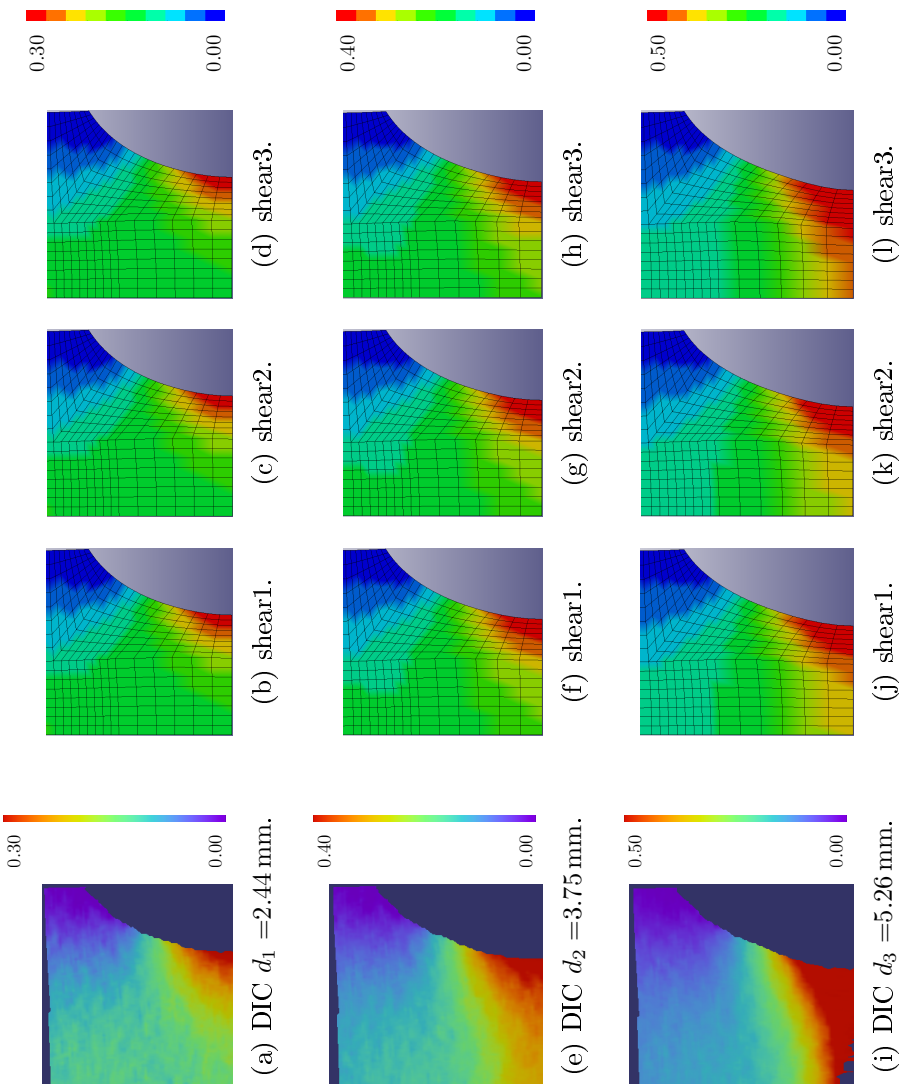

Figure 5.32: Iso-values maps comparison between DIC and FE results of axial strain at different gauge displacements. Results for the specimen with notch R =10 mm. d_1, d_2 and d_3 are the displacements at where the results are obtained, as seen in Fig. 5.26.

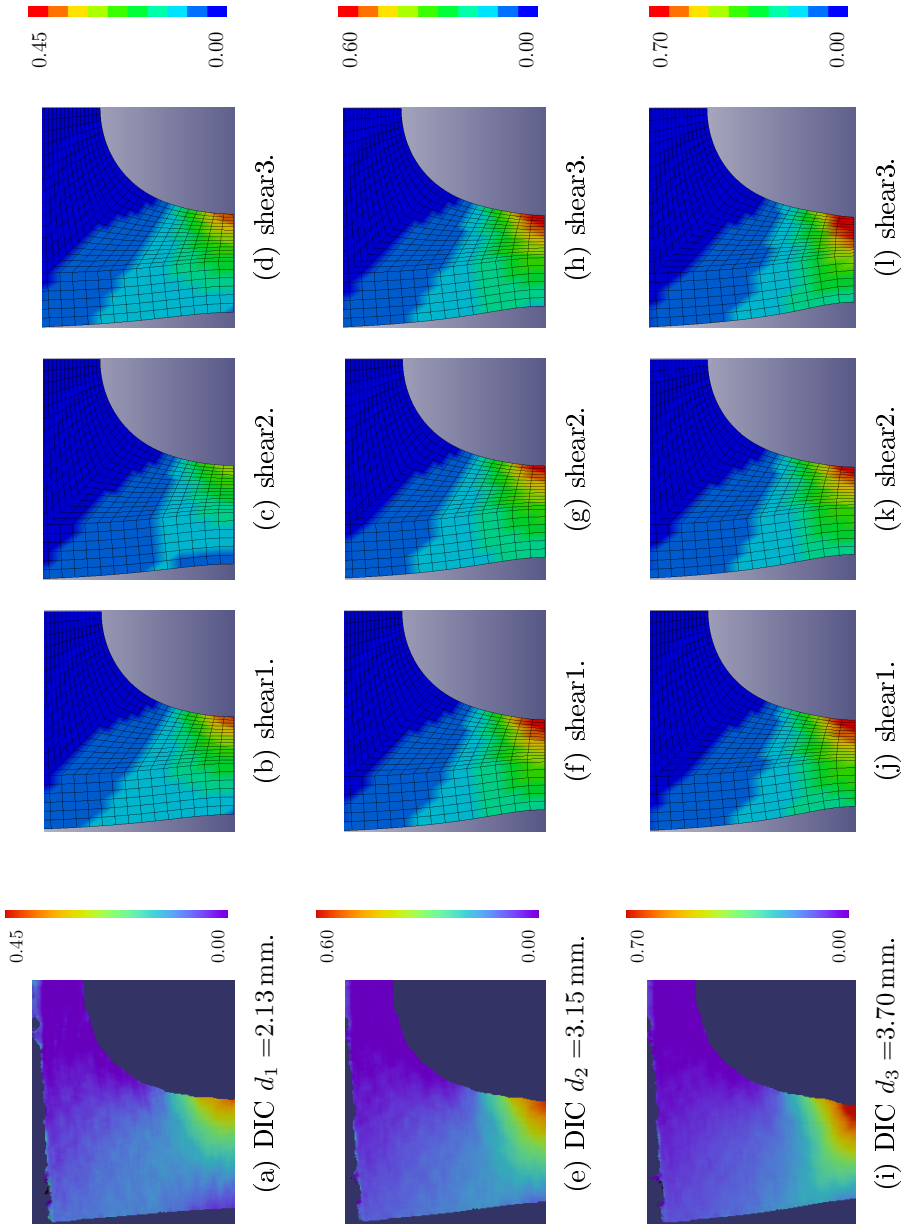

Figure 5.33: Iso-values maps comparison between DIC and FE results of axial strain at different gauge displacements. Results for the specimen with a central hole. d_1, d_2 and d_3 are the displacements at where the results are obtained, as seen in Fig. 5.26.

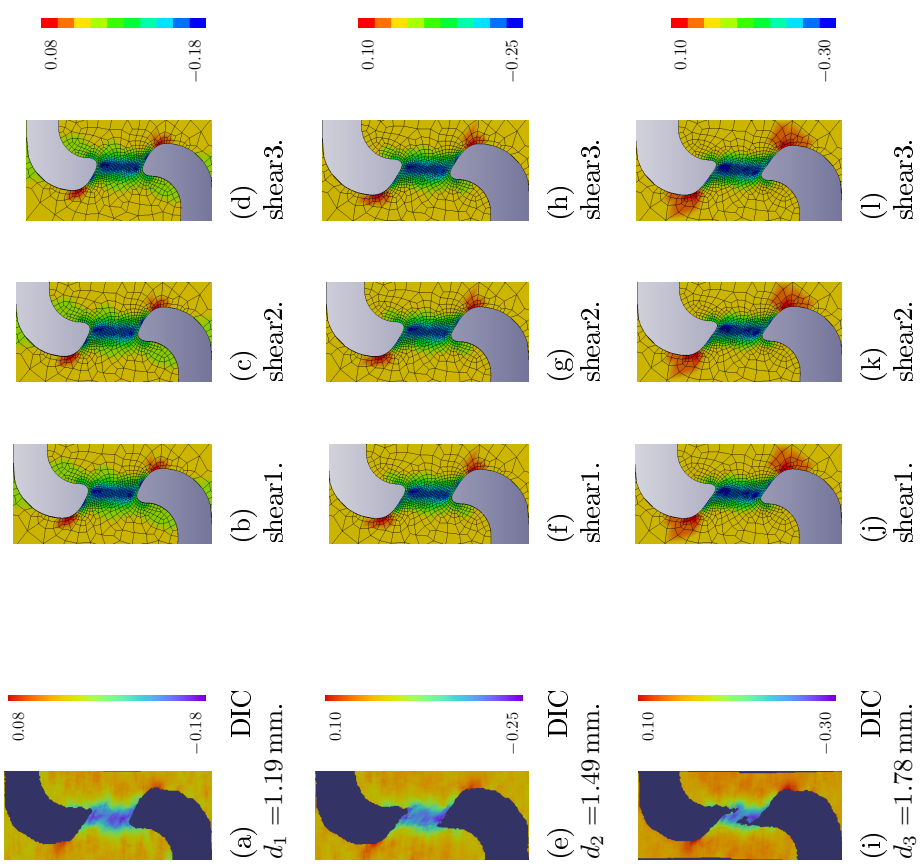

(a) DIC d_1 =1.19 mm. (b) shear1. (c) shear2. (d) shear3.

(e) DIC d_2 =1.49 mm. (f) shear1. (g) shear2. (h) shear3.

(i) DIC d_3 =1.78 mm. (j) shear1. (k) shear2. (l) shear3.

Figure 5.34: Iso-values maps comparison between DIC and FE results of axial strain at different gauge displacements. Results for the shear specimen. d_1, d_2 and d_3 are the displacements at where the results are obtained, as seen in Fig. 5.26.

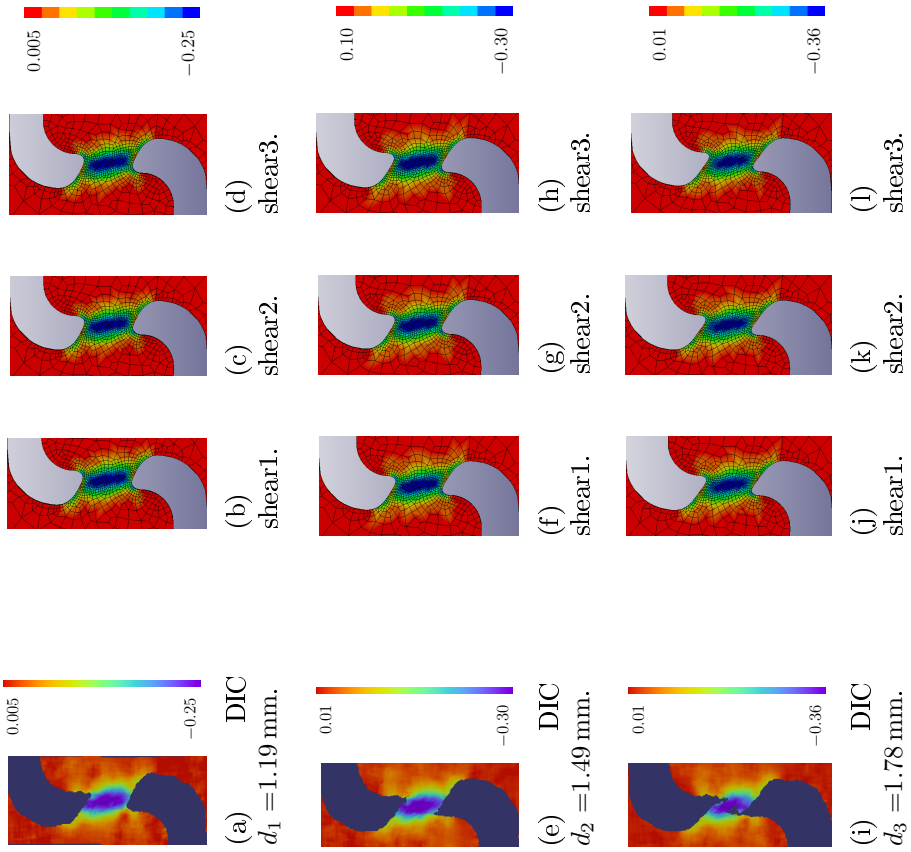

(a) DIC d_1 =1.19 mm. (b) shear1. (c) shear2. (d) shear3.

(e) DIC d_2 =1.49 mm. (f) shear1. (g) shear2. (h) shear3.

(i) DIC d_3 =1.78 mm. (j) shear1. (k) shear2. (l) shear3.

Figure 5.35: Iso-values maps comparison between DIC and FE results of shear strain at different gauge displacements. Results for the shear specimen. d_1, d_2 and d_3 are the displacements at where the results are obtained, as seen in Fig. 5.26.

Note that the same scale is used in DIC measurements and FE predictions to facilitate the analysis. Qualitatively, it is observed that the strain distribution is satisfactorily predicted by the FE simulations. The quantitative differences between both can be caused by different factors, such as DIC software parameters (displacement/strain smoothing, subset size, etc.) or the FE simulation characteristics (material mode, FE size, etc.).

An hypothesis of the inability of the Gurson model to capture the strain localization on notched specimens is given hereafter. As discussed in section 5.5.1, localization can be triggered due to an insufficient increase in hardening. However within the FE results, the Gurson model predicts that the material loses all his load carrying capacity due to void growth and coalescence *before* strain localizes.

On the other hand, the non-damage model used by Dunand and Mohr, (2010) is able to correctly predict this strain localization (cf. Dunand and Mohr, 2011b). These results were obtained using a modified isotropic hardening, which extrapolates the hardening behavior after localization without the need of a any damage model[3] to induce softening, as shown in Fig. 5.36.

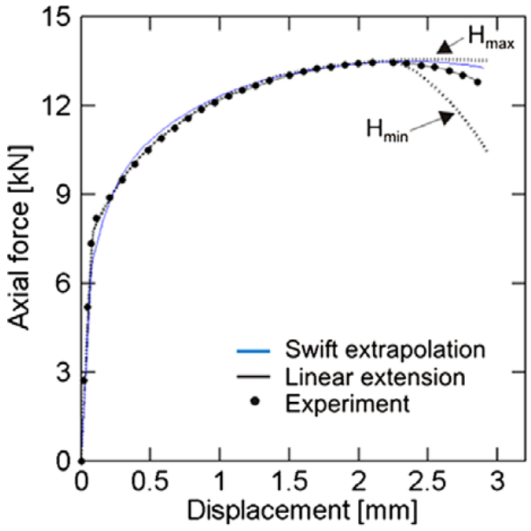

Figure 5.36: Strain hardening extrapolation used by (Dunand and Mohr, 2010) and its influence on the force displacement curve.

In this PhD, the Gurson model is used with a classic isotropic hardening law (Swift), without any type of extrapolation. Therefore, localization is triggered solely by relying on the void evolution. As experimentally demonstrated by Pardoen and Delannay, (1998), damage evolution in metallic materials largely depends on the hardening exponent n. Faleskog et al., (1998) and Kim et al., (2004) confirmed this using unit cell calculations. Hence, there must be a balance between damage increase (expressed by the fast *decrease* of the force) and limited hardening (expressed by fast *increase* of the strain) in the simulations of the notched specimens.

[3]Unfortunately, in other publication by the same authors (cf. Dunand and Mohr, 2011a), they use a shear modified Gurson model but no comparison with the strain predictions is given.

Another evidence regarding the importance of hardening is given by Mansouri, (2014), who evaluated the ability of the GTN model to predict localized necking. A sensitivity analysis was carried out in order to evaluate the influence of damage (f_0, f_N, etc.) and hardening (K, n and ϵ_0) parameters on the prediction of localized necking. Mansouri, (2014) found that the damage parameters have a considerable influence on the deformation levels at the onset of localized necking, whereas hardening parameters have only a minor influence on the localization predictions. The reason behind this numerical observation is that the Gurson model does not take into account the coupling between the evolution of the damage variable and the matrix hardening. As already mentioned, damage is the only mechanism triggering loss of ellipticity and material localization. This decoupling between the damage variable and hardening is due to the way that hardening is introduced into the Gurson model, as noted by Leblond et al., (1995) and Leblond and Perrin, (1996). As shown in section 3.5.2, the strain hardening behavior of the matrix is introduced heuristically into the Gurson model.

Recently, Tekoglu et al., (2015) discussed the mechanisms (failure scenarios) leading ductile fracture. In particular, (macroscopic) localization and void coalescence, which are not easily distinguished under certain values of triaxiality. This article concludes that at high triaxialities both mechanisms are clearly separated, while at low stress triaxialities they occur simultaneously. This could explain why the FE predictions using the Gurson model are better for the shear test. Nevertheless, the competition between these two modes of localization is still a subject of research (viz. Tekoglu et al., 2015).

5.5.3 State variables analysis

Fig. 5.37 shows the evolution of the triaxiality and the Lode parameter (used in the Nahshon and Hutchinson, (2008) shear extension, refer to Appendix A.1.2) versus the equivalent (macroscopic) plastic strain. The state variables are obtained for the elements depicted in Fig. 5.19. They help identifying the stress state acting on each test. The results are obtained using the set `shear1` of Table 5.5. It is observed that triaxiality is high (over $\frac{1}{3}$) in the specimens with notch and hole, and low for the shear tests. As expected, the Lode parameter evolution for the shear test is almost constant during the test, while for the notched tests it remains under 0.5.

Fig. 5.38 to Fig. 5.41 shows iso-values maps of triaxiality and the Lode parameter at different displacements. The results are depicted without a smooth transition between elements, in order to highlight the strong gradients near the fracture zone. The same trends described in Fig. 5.37 are here observed globally. In particular, the zones where the onset of fracture is experimentally observed present high values of triaxiality for notched specimens and the specimen with a central hole. The shear test present a low value of triaxiality (near zero) and a Lode parameter close to 1.0 at the fracture zone. Fig. 5.42 and Fig. 5.43 present the results for the porosity distribution. It is important to note that due to the shear extensions by Nahshon and Hutchinson, (2008), the porosity variable f should be regarded as a damage parameter more than the (strictly) physical

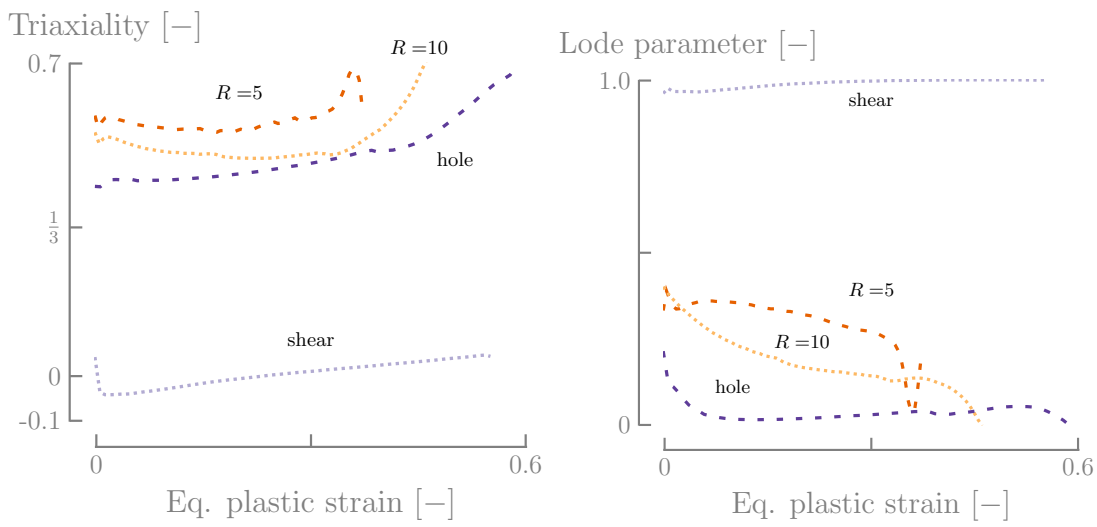

(a) Triaxiality.

(b) Lode parameter $\omega(\boldsymbol{\sigma})$.

Figure 5.37: State variables evolution for different fracture tests.

sense of the void volume fraction of voids. The iso-values scale is modified in order to have f_{cr} =0.0055 as the highest value. Because porosity rapidly increases after f_{cr} due to the coalescence model, using a higher value within the scale will hide the gradients. Porosity rapidly increases in the zone near the edges in the notches specimens, while for the specimen with hole it develops from the inside (hole) to the outside (edge). For the shear tests, it is also observed that porosity quickly develops at the edges.

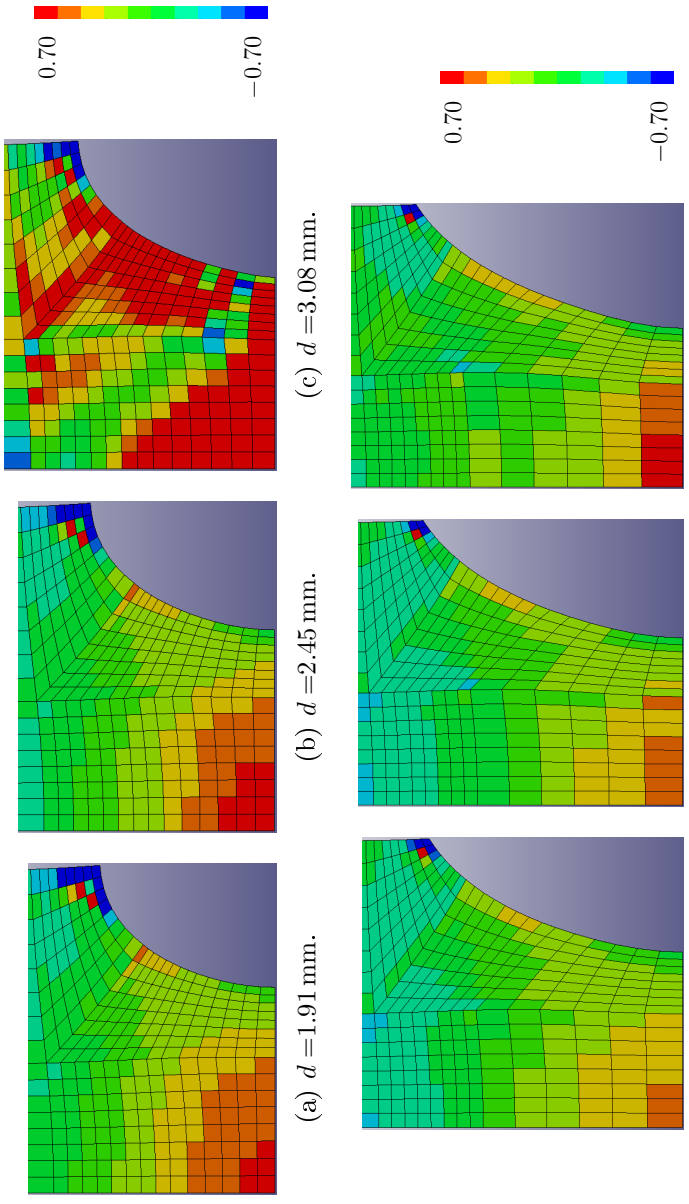

(a) $d = 1.91\,\text{mm}$. (b) $d = 2.45\,\text{mm}$. (c) $d = 3.08\,\text{mm}$.

(d) $d = 4.49\,\text{mm}$. (e) $d = 5.29\,\text{mm}$. (f) $d = 6.18\,\text{mm}$.

Figure 5.38: Iso-values maps of the triaxiality evolution over different displacements. Results for the specimens with $R = 5\,\text{mm}$ ((a), (b) and (c)) and $10\,\text{mm}$ notch ((d), (e) and (f)).

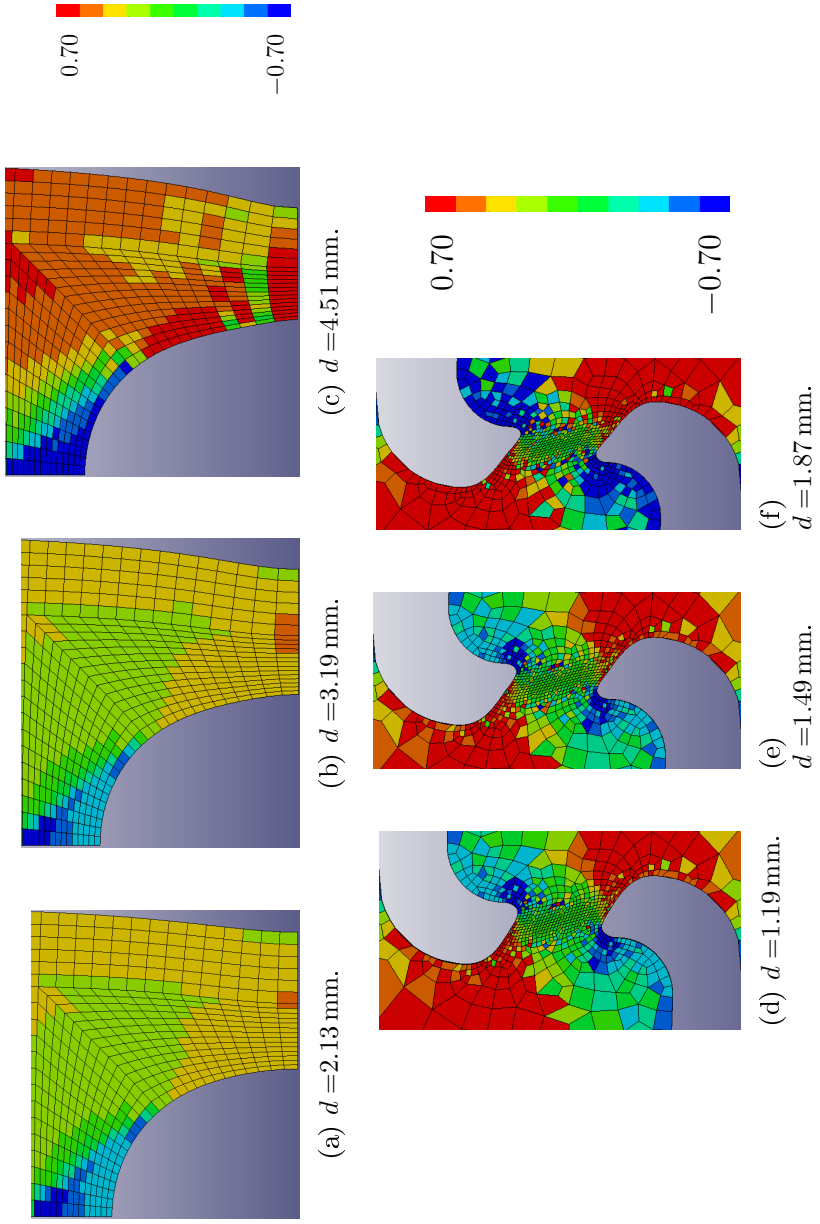

(a) $d = 2.13\,\text{mm}$. (b) $d = 3.19\,\text{mm}$. (c) $d = 4.51\,\text{mm}$.

(d) $d = 1.19\,\text{mm}$. (e) $d = 1.49\,\text{mm}$. (f) $d = 1.87\,\text{mm}$.

Figure 5.39: Iso-values maps of the triaxiality evolution over different displacements. Results for the specimen with central hole ((a), (b) and (c)) and the shear specimen ((d), (e) and (f)).

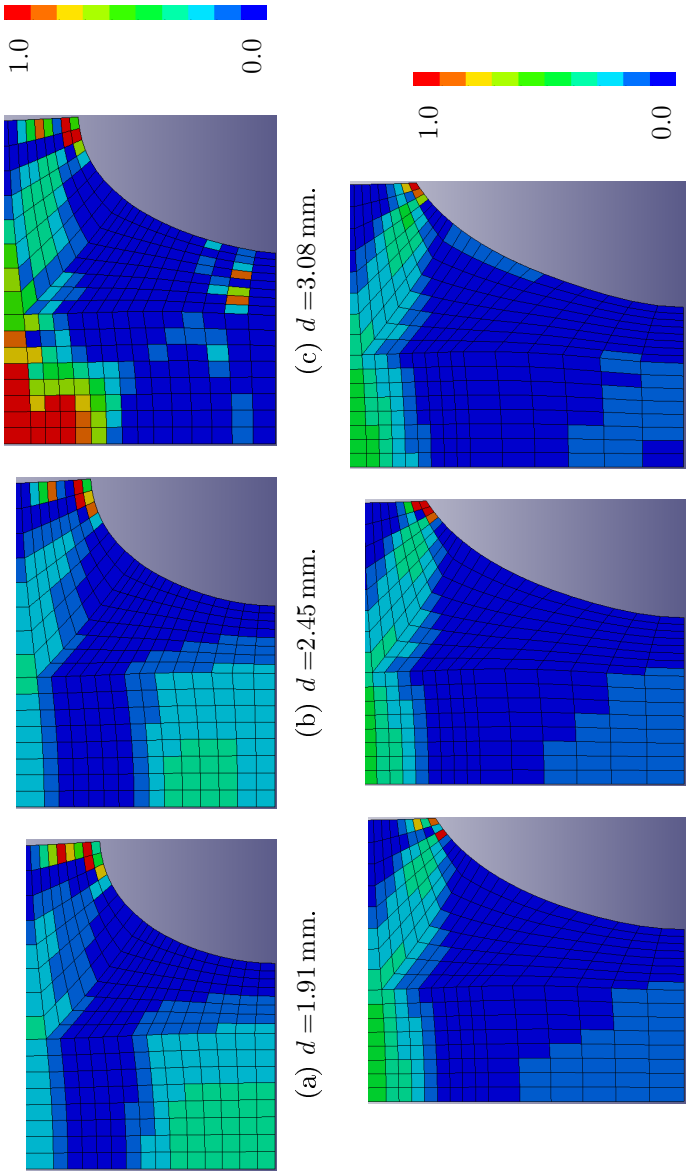

(a) d =1.91 mm. (b) d =2.45 mm. (c) d =3.08 mm.

(d) d =4.49 mm. (e) d =5.29 mm. (f) d =6.18 mm.

Figure 5.40: Iso-values maps of the Lode parameter $\omega(\boldsymbol{\sigma})$ evolution over different displacements. Results for the specimens with R =5 mm ((a), (b) and (c)) and 10 mm notch ((d), (e) and (f)).

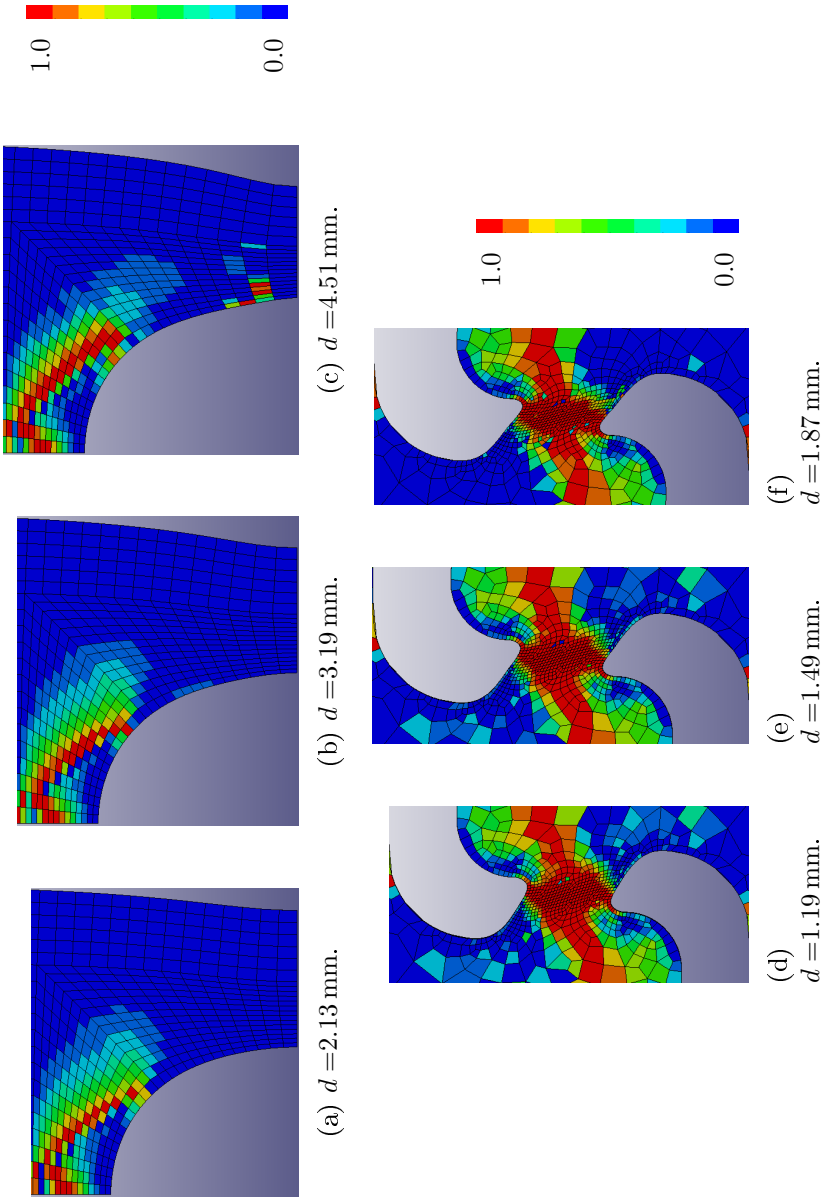

Figure 5.41: Iso-values maps of the Lode parameter $\omega(\boldsymbol{\sigma})$ evolution over different displacements. Results for the specimen with central hole ((a), (b) and (c)) and the shear specimen ((d), (e) and (f)).

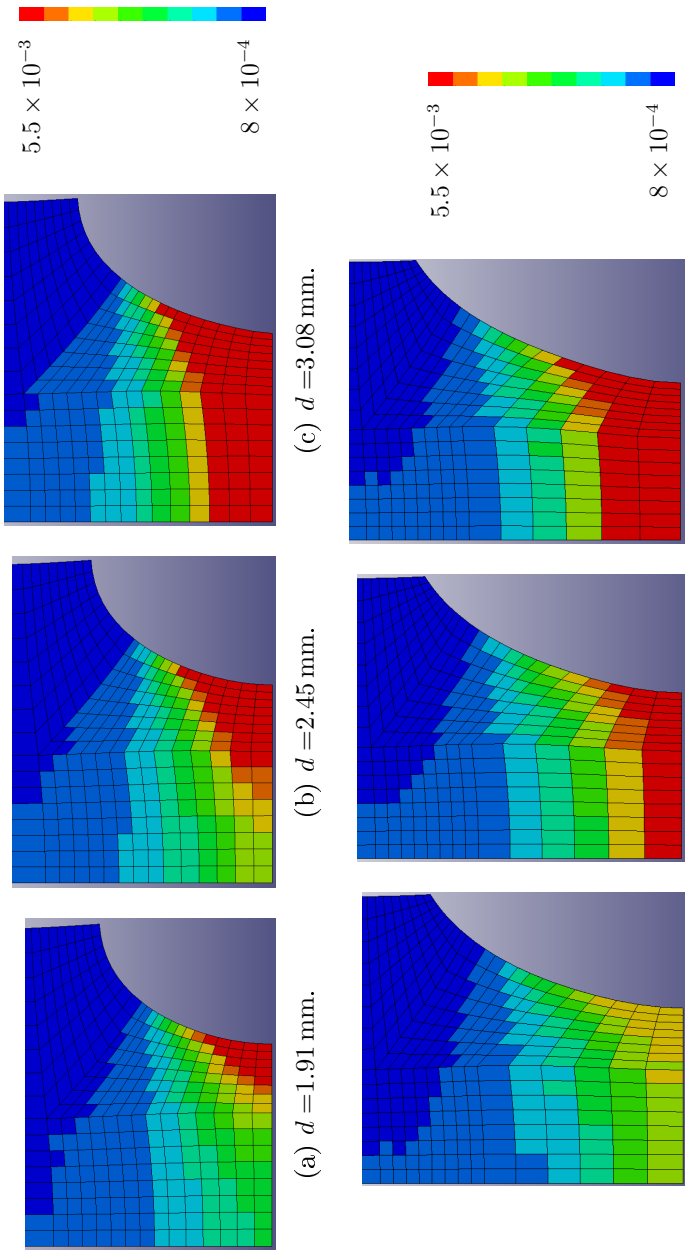

(a) d =1.91 mm. (b) d =2.45 mm. (c) d =3.08 mm.

(d) d =4.49 mm. (e) d =5.29 mm. (f) d =6.18 mm.

Figure 5.42: Iso-values maps of the porosity evolution over different displacements. Results for the specimens with R =5 mm ((a), (b) and (c)) and 10 mm notch ((d), (e) and (f)).

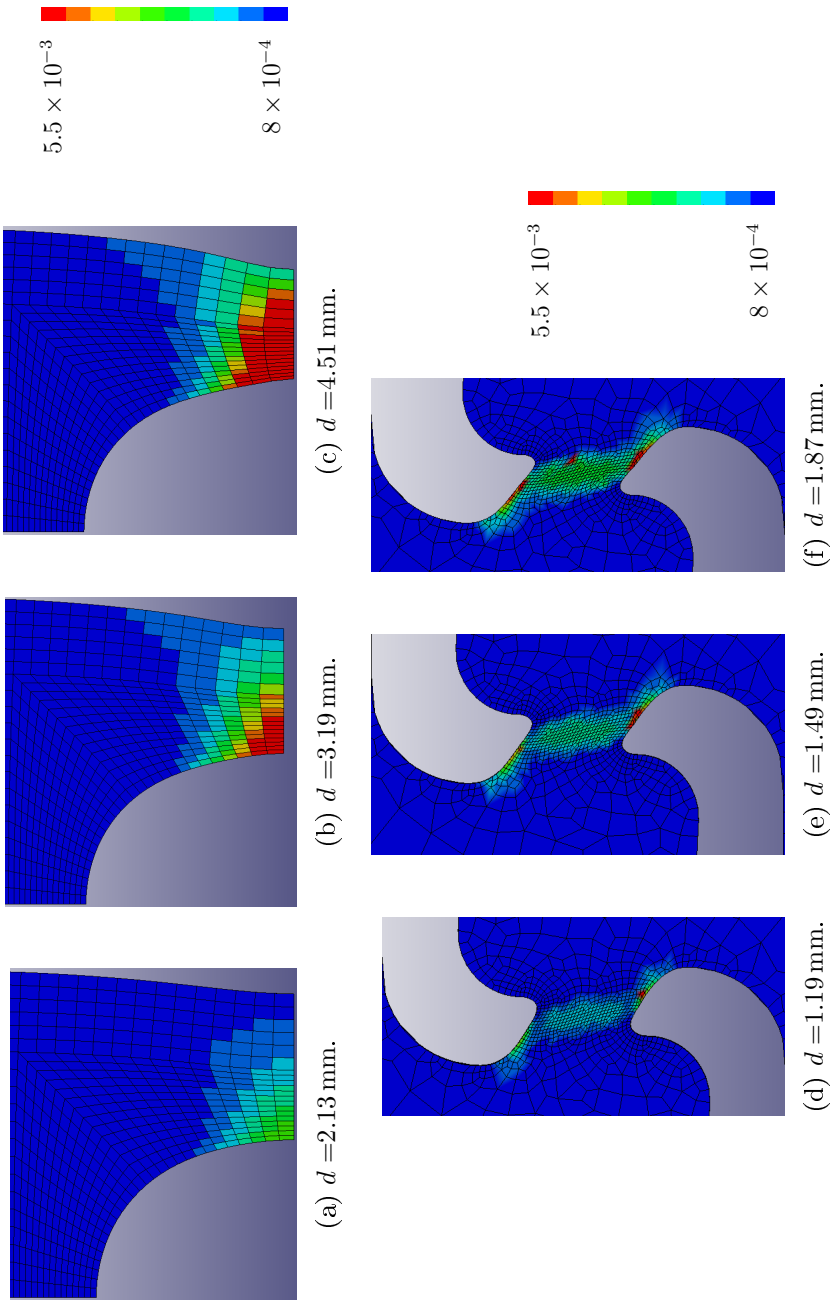

Figure 5.43: Iso-values maps of the porosity evolution over different displacements. Results for the specimen with central hole ((a), (b) and (c)) and the shear specimen ((d), (e) and (f)).

5.6 Conclusions

In this chapter, the methodology behind the material parameters identification of the GTN model for the DC01 steel sheet is presented. The chapter starts by reviewing some identification methodologies found in the literature for sheet metals, reflecting the need of both a microscopic and macroscopic analysis. Then, a microscopic characterization based on fractography and optical microscopy image analysis is detailed. Measurements based on Archimedes' principle are also presented despite not being useful for the current research. An experimental campaign, comprising notched specimens, a specimen with a central hole and a shear specimen, is carried out. The specimens were selected based on the well-known effect of triaxiality and the Lode parameter on damage development and fracture. The results show that the performed microscopic measurements are not representative of the actual damage, but they give a qualitative estimation of the physical mechanism of fracture. For instance, the material exhibits a clear ductile behavior that can be modeled using the GTN model. The initial porosity of the material was determined using optical microscopy measurements on the base material. The macroscopic campaign allowed to identify the rest of the parameters for nucleation, coalescence and shear. An unique set of results matching all experiments was not possible to obtain, so different sets of parameters are retrieved following an approach that included inverse and sensitivity analysis. The set `shear1` will be used hereafter giving overall good results obtained in the majority of tests. A numerical-experimental comparison of strain in the loading direction shows that the model is able to correctly predict the strain distribution except at the end of the test. The model does not to predict strain localization because of the decoupling between the damage variable and hardening. This is an inherent limitation of the GTN model, due to the heuristic approach followed to introduce the strain hardening behavior in the matrix. Globally, the set of parameters are able to capture coalescence in all tests, including the shear test. Further work can be focused to analyze the effect of the kinematic hardening or yield locus anisotropy on damage development. The competition between void coalescence versus strain localization should be considered in future research involving the GTN model.

Chapter 6

Damage modeling in SPIF

Single Point Incremental Forming has several advantages over traditional forming, such as the high formability attainable by the material. Different hypothesis have been proposed to explain this behavior, but there is still not a clear understanding of the relation between the particular stress and strain state induced in the material during forming and the material degradation leading to localization or fracture. In this chapter, the scope is to validate the GTN damage model extended to shear for SPIF FE simulations. A complete state of the art about SPIF, covering geometrical accuracy, deformation mechanism, formability and damage is also presented. Three types of SPIF test, namely the line test, cone test and the pyramid test, are simulated using the LAGAMINE FE code. The line test is used to validate the simulations by comparing force and shape prediction with experimental results. Then, a two-slope pyramid is simulated to evaluate the performance of the solid-shell formulation. In general, the results of the shape prediction are in good agreement with the experimental results, both for the line and pyramid test. The force FE predictions are higher than the experimental values, probably because of the boundary conditions. For the pyramid test, the GTN model predicts a premature onset of material failure compared with the experimental failure angle for the same material and geometry. To further analyze the failure prediction, several simulations of SPIF cones at different wall angles are performed. It is concluded that the GTN model underestimates the failure angle on SPIF. This is due to a bad coalescence modeling and inherent limitations of the GTN model.

6.1 State of the art

This SPIF state of the art considers four topics:

- SPIF FE simulations, in section 6.1.1.
- Deformation mechanisms of the sheet during the forming process, in section 6.1.2.
- Deviations of the intended geometry, in section 6.1.3.

- Material formability, in section 6.1.4.
- Damage and fracture, in section 6.1.5.

These topics were chosen based on the thesis scope (damage prediction can be readily linked to the formability and the deformation mechanisms) but also on the wide experimental evidence regarding shape inaccuracies, which present an interesting challenge for numerical simulations.

SPIF and his variants has been covered by several authors. One of the first review articles of the process was due to Jeswiet et al., (2005), a classical work covering almost every aspect of the SPIF process, from the experimental setup to FE analysis. Despite the date of publication, it is interesting to find that many questions and issues remain unsolved. Emmens and van den Boogaard, (2010) performed a review of technical developments on incremental forming through the years, digging into patents (from USA and Europe, but also from Japan) mainly issued from the automotive industry. It is important to note that the review from Emmens and van den Boogaard, (2010) is more focused on ISF than SPIF. Recently, Reddy et al., (2015) reviewed SPIF concentrating their efforts in the shape inaccuracy and formability.

6.1.1 SPIF FE simulations

FE simulations of SPIF have been a subject of extensive research in the last years. In the beginning, it became clear that simulating SPIF was challenging for the following reasons:

- The small contact zone implies small time steps in order to guarantee convergence. Moreover, an accurate constitutive modeling of the contact phenomenon is needed.
- The incremental nature of the process requires huge number of stages (time steps) to model the entire process, implying large simulation times.
- High levels of deformation are usually attained, so FE can be severely distorted being prone to locking or hourglass modes.
- Several mechanical phenomena, like springback and bending, act during the process thus requiring adequate constitutive models and FE formulations.

Several approaches have been proposed to meet these drawbacks looking for an acceptable compromise between CPU time and accuracy. They will be described hereafter, together with a compilation of works involving SPIF FE simulations in the LAGAMINE FE code.

6.1.1.1 SPIF FE simulations in LAGAMINE

Henrard thesis (Henrard, 2008) is a comprehensive work on SPIF FE simulations, gathering information about different meshes, element types and other related publications (e.g. Bouffioux et al., 2007; Eyckens et al., 2010; Henrard et al.,

2005a,b, 2010). An explicit scheme was also implemented in Lagamine (cf. Henrard et al., 2007). In general, the Lagamine shell element COQJ4 (Henrard, 2008; Jetteur and Frey, 1986; Li, 1995) was found to have the best compromise between accuracy and CPU time, even in the case of a two-slope pyramid (Guzmán et al., 2012b). However, the element was not able to simulate a 90° angle cone failing to predict the shape correctly (Henrard, 2008, chapter 8). Bouffioux et al. (Bouffioux et al., 2007, 2008a,b, 2010, 2011; Henrard et al., 2010) addressed the force prediction on SPIF, demonstrating the importance of the identification method of the material model on the predicted forces and the limitations of the COQJ4 shell element to represent the through-thickness gradients. Lequesne et al., (2008) later implemented an adaptive remeshing method for the COQJ4 element, based on the tool movement and deformation level of the elements (cf. Bouffioux et al., 2011). The above mentioned limitations of the shell elements motivated the use of solid elements; in particular, the solid-shell element formulation. The SSH3D solid-shell element (Ben Bettaieb et al., 2011a; Duchêne et al., 2011) was used to simulate the line test (Guzmán et al., 2012a), the two-slope pyramid (Duchêne et al., 2013) and a 70° angle SPIF cone (Guzmán, 2013; Guzmán and Habraken, 2013). Later, the solid shell element RESS (Alves de Sousa et al., 2007) was used as well as an extension of the adaptive remeshing of Lequesne et al., (2008) to solid-shell elements by Sena et al., (2013, 2015). These FE elements will be later described in section 6.2.

6.1.1.2 Explicit vs. implicit

There exists two possible schemes for both the formulation and the numerical solution of the (discretized) equilibrium equations: *explicit* and *implicit*. In implicit schemes, the equilibrium equation is satisfied at each time step so iterations are needed for every step. If there are convergence problems, the time step can be automatically reduced until a convergence criterion is attained. This method is unconditionally stable, meaning that the stability of the error propagation does not depend on the time step and the finite element size. To avoid convergence problems related with implicit schemes, explicit schemes compute the equilibrium at the beginning of the time step but it is never fully satisfied. Calculation of the tangent matrix at the end of the time step is not required. Nevertheless, the time step must fulfill some requirements in order to guarantee stability, which depends on the mesh size, material model, mass and time (Henrard, 2008, chapter 7). Usually more time steps are needed for an explicit approach but each one is considerable faster than in an implicit scheme.

When applied to the SPIF process, implicit schemes can mean large simulations times (Bambach et al., 2005; Henrard, 2008; Jeswiet et al., 2005). Nevertheless, they usually provide a better geometrical accuracy than explicit schemes, but with higher simulation times. Bambach, (2004) performed a benchmark using both explicit and implicit schemes, using Abaqus *Standard* and Abaqus *Explicit* with 2304 shell elements. Fig. 6.1 shows that the implicit scheme gives good predictions compared to experimental results, but the simulation time is 14 times higher than using the explicit scheme. In general, the CPU time for

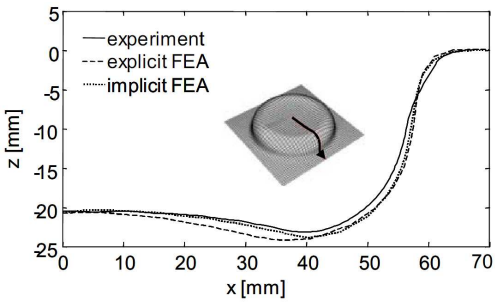

Figure 6.1: Transveral cut comparison between the experimental results and numerical simulations using explicit and implicit schemes (Bambach, 2004).

explicit schemes can be reduced using numerical techniques such as *mass scaling* or *time scaling*. Nevertheless, adjusting a critical time step to avoid numerical instabilities and finding the right compromise between speed and accuracy is far for being trivial, as demonstrated by Henrard et al., (2007) and Henrard, (2008, chapter 7). Table 6.1 lists some representative publications since 2006 where no particular trend is observed in terms of which scheme is preferred. The time re-

Table 6.1: Authors using either explicit or implicit scheme for SPIF FE simulations.

Explicit	*Implicit*
Azaouzi and Lebaal, (2012), Bambach, (2014), Cerro et al., (2006), Dejardin et al., (2010), Kurra and Regalla, (2014), Malhotra et al., (2012), Mohammadi et al., (2014), Ndip-Agbor et al., (2015), Robert et al., (2012), Shanmuganatan and Senthil Kumar, (2012), and Yamashita et al., (2008)	Aerens et al., (2009), Arfa et al., (2013), Essa and Hartley, (2010), Flores et al., (2007), Guzmán et al., (2012b), Hadoush and van den Boogaard, (2009, 2011), Li et al., (2012), and Sena et al., (2015)

duction related to either the explicit or the implicit scheme seems to be greatly related with the FE code used. Indeed, Henrard et al., (2007) concludes that the LAGAMINE FE code is not adapted for explicit simulations, observing higher CPU times for an explicit simulation than an implicit simulation. Similarly, in the NUMISHEET SPIF benchmark (Elford et al., 2013) the team from ESI group, using PAM-STAMP 2G, presented larger simulations times with an explicit scheme than an implicit scheme.

6.1.1.3 FE element type

The choice of the FE is an important decision when simulating SPIF. Bambach and Hirt, (2005) assessed different elements formulation from the Abaqus library, concluding that the element formulation plays a significant role on the shape prediction. For instance, the best performance (both in terms of CPU time and accuracy) was achieved using plane-stress shell elements because solid elements (with two element layers through the thickness) were prone to locking. As shown in Table 6.2, many researches involving FE simulations have been carried on using shell elements due to the good compromise between accuracy and CPU time.

It has been proved that the stress/strain gradients can play an important role both in the deformation mechanism (Jackson and Allwood, 2009) and in the formability (Eyckens et al., 2009). Due to the Kirchhoff-Love or Mindlin-Reissner hypothesis, shell elements do not allow computing full 3D stress and strain fields. An exhaustive study of SPIF requires the use of 3D solid elements but the simulation time can be too high (several days or weeks) even for simple geometries (Eyckens et al., 2010; Henrard, 2008). Nevertheless, the results from Kim and Yang, (2000) and Bambach et al., (2003) show that 3D elements are necessary when the local stresses under the tool are important. However, in order to simulate bending several elements layers in the thickness direction are needed. Henrard et al., (2010) obtained acceptable results in Lagamine in terms of accuracy, using a reduced integration `BWD3D` element (Duchêne et al., 2007) but 3 layers of elements were needed increasing the computation time considerably (Henrard, 2008).

New FE technology has allowed a new family of elements to model sheet metal forming processes. This family falls between the classical shell and brick formulation and it will be referred to as solid-shell elements (also known as thick-shell). Solid-shells allow to model very thin sheets using only one element layer without locking issues. An improvement can be achieved in terms of accuracy prediction when comparing the results generated by the solid-shell or the shell element. For instance, the results from Duchêne et al., (2013) compared to Guzmán et al., (2012b) for a two-slope SPIF pyramid. The `COQJ4` shell element from Guzmán et al., (2012b) is based on the shallow shell theory (Carnoy, 1981; Debongnie, 1979; Marguerre, 1938), which assumes that the mid-plane coincides with the neutral plane. In Duchêne et al., (2013), a 3D solid shell-formulation allows considering through thickness shear, normal stresses and membrane stresses. New publications about SPIF FE simulations using solid-shell elements (Sena et al., 2015; Seong et al., 2014) have shown promising results. It is thus probable that in a near future, classical shells and bricks will be replaced by solid-shells as the standard FE for SPIF simulations.

6.1.1.4 Towards quicker SPIF FE simulation

Globally, improving FE simulations in terms of CPU time involves two different approaches. One approach is to simulate a simplified representation of a physical phenomenon happening in the SPIF process and another approach is the use of numerical techniques.

Table 6.2: Authors using either shell or solid type of FE for SPIF simulations.

Shell	*Solid*	*Solid-Shell*
Arfa et al., (2013), Azaouzi and Lebaal, (2012), Bambach, (2014), Bouffioux et al., (2011), Cerro et al., (2006), Cui et al., (2013), Dejardin et al., (2010), Eyckens et al., (2010), Guzmán et al., (2012b), Hadoush and van den Boogaard, (2009, 2011), Henrard et al., (2010), Kurra and Regalla, (2014), Li et al., (2012), Robert et al., (2012), Shanmuganatan and Senthil Kumar, (2012), and Yamashita et al., (2008)	Aerens et al., (2009), Duflou et al., (2010), Essa and Hartley, (2010), Eyckens et al., (2010), Flores et al., (2007), Henrard et al., (2010), Malhotra et al., (2012), Mohammadi et al., (2014), and Ndip-Agbor et al., (2015)	Meier et al., (2013), Sena et al., (2015), and Seong et al., (2014)

Within the first approach, Kim and Yang, (2000) simplified the deformation mechanism by assuming that SPIF is dominated by pure shear. Lievers et al., (2004) performed a single-element single-step simulation using the same hypothesis as Kim and Yang, (2000) (These results are further discussed in section 6.1.5). The contact modeling between the tool and the sheet has also been object of simplifications, because of the limitations of the classical penalty approach for simulating contact[1]. Hence, Henrard, (2005) and Henrard et al., (2007) proposed a modified contact approach in a dynamic explicit scheme, which it was not successful on reducing the CPU time. Better results were obtained by Delamézière et al., (2011) and Robert et al., (2010) and later improved by Ben Ayed et al., (2014), based on the imposition of the displacement on the nodes in contact with the tool. Robert et al., (2012) proposed a new algorithm based on the Hencky incremental plastic deformation theory instead of the classical flow rules, but the time saving is negligible in the SPIF case.

Numerical techniques on the other hand, are more general since they were formulated for processes other than SPIF. Among them we can mention:

- *Sub-modeling* technique implemented in ABAQUS, which allow using a very fine (sub-millimitre) mesh in a small part of the original mesh (Aerens et al., 2009; Eyckens et al., 2008, 2010; Henrard et al., 2010).

- *Domain decomposition* methods, in which the finite element mesh is *split* in a first zone concentrating strong non-linearities (as under the tool) and in a second zone which observes almost elastic behavior (Brunssen and Wohlmuth, 2009; Hadoush and van den Boogaard, 2009, 2011; Sebastiani et al., 2007).

[1] In particular, the penalty coefficient should be adjusted as a result of a compromise between accuracy and convergence.

- *Subcycling* in which coarse elements are integrated with larger time steps than fine elements near the deformation zone (Bambach, 2014; Hadoush and van den Boogaard, 2011).

- *Remeshing methods* (Dejardin et al., 2010; Hadoush and van den Boogaard, 2011; Lequesne et al., 2008). Given the localized plastic deformation in SPIF, there is a strong non linearity around the tool contact zone (neighborhood) while the rest of the mesh keeps a slight geometrical non linearity.

6.1.1.5 Constitutive laws

The choice of material model for materials not sensitive to strain rates should be regarded in terms of two components: the shape of the yield surface (yield criterion) and its evolution with respect to the deformation (hardening). In general, simple criteria such as von Mises and Hill, (1948) have been extensively used because of their simplicity, the overall good results obtained and the fact that both the CPU time and the material parameter identification complexity is low compared to more advanced models. Considering the choice of the von Mises and the Hill, (1948) yield criterion, the influence on the results is small when predicting shape (Bambach and Hirt, 2005; Flores et al., 2007; He et al., 2005a), strains (Eyckens et al., 2010) and forces (Flores et al., 2007; Henrard et al., 2010). According to Eyckens et al., (2010), this can be explained because ISF simulations are displacement controlled and that strains are independent of the yield surface. In the Numisheet benchmark (Elford et al., 2013), the available material data allowed the different participant teams to use more specific models for aluminum. Yield criteria such as the one proposed by Barlat and Lian, (1989) and Barlat et al., (1991, 2003), Vegter et al., (2009) and Banabic et al., (2005) were possible to use. Nonetheless, the difference among these models and the von Mises or the Hill, (1948) yield criteria in term of shape and strain predictions is small.

Nevertheless, the hardening law can greatly affect the force prediction, as shown by Bouffioux et al., (2011) for an AlMgSc alloy, and Henrard et al., (2010) for an aluminum alloy. In both articles, the predicted vertical forces were higher than the experimental measurements. Overestimation of the force prediction seems to be a common issue in SPIF FE simulations, as it has been widely observed in the literature (e.g., the results from the Numisheet benchmark in Elford et al., (2013)). In these articles, it was hypothesized that the over prediction of the force was due to the inability of the shell elements to capture through-thickness gradients. An identification method was proposed which, instead of relying solely in the classical in-plane tests (tensile test, plane strain test, simple shear test, etc.), uses an indent step of incremental forming to fit new material parameters. Using a mixed isotropic-kinematic hardening with the new identification method leads to good force predictions.

The importance of the isotropic hardening parameters was also discussed by Jeswiet et al., (2002), which performed tensile tests on aluminum specimens taken from SPIF pyramids of different wall angles. It is observed that the strain hardening parameter of the Swift law is inversely proportional to the wall angle, meaning

that the use of a hardening extrapolation (as it is the case in SPIF FE simulations, where large strains are reached) could lead to wrong predictions. The same procedure was used by Eyckens et al., (2011b) to investigate the effect of the tool directionality and sheet anisotropy on an aluminum alloy and a low carbon steel. It is observed that the Swift law overestimates the strength of the aluminum specimens. It is also mentioned that this behavior is not observed for the low carbon steel, contrary to Emmens and van den Boogaard, (2009b) which observed the same trend for another low carbon steel, suggesting that the forming operation *softens* the material. The Voce law, which saturates after certain deformation level, can improve the force prediction as showed by Henrard et al., (2010) and Bouffioux et al., (2011). Belchior et al., (2013) analyzed the influence of the through thickness shear (TTS), isotropic hardening law and clamping system on the predicted FE forces. The best results are obtained using a brick element, Voce isotropic hardening law and a model incorporating the clamping pressure. However, more details are not given. The Voce law was also used by Lievers et al., (2004) and Seong et al., (2014).

6.1.2 Deformation mechanisms

Research during the last decade has focused on the development of new applications and a better characterization of the forming limits in SPIF. Even so, a wide consensus has not yet been reached about the deformation mechanism because the inherent SPIF complexity (localized contact stresses, incremental deformation, etc.) and limitations of the available numerical tools. However, measuring and predicting the deformations is a key point to go towards greater accuracy (Henrard, 2008). Likewise, Jackson and Allwood, (2009) confirms that the knowledge of the deformation mechanism is important not only for the development of more accurate numerical models, but also for the design and control of the toolpath and the study of the forming limits.

Previous investigations have contemplated three different perspectives:

- *Experimental measurements* of displacements and deformations: circular or rectangular grids can be glued to the sheet surface (Duflou et al., 2010; Emmens and van den Boogaard, 2007; Filice et al., 2002; Jackson et al., 2008; Ji and Park, 2008; Kim and Park, 2002; Martins et al., 2009), electrochemically etched circle grids (Silva et al., 2011), through the thickness measurements (Eyckens, 2010; Jackson and Allwood, 2009) or DIC (Duflou et al., 2010; Eyckens et al., 2010; Vasilakos et al., 2011).

- *Theoretical models*, like the sine law (explained below) or membrane assumed deformation (Silva et al., 2008).

- *FE simulations* (Duflou et al., 2008b, 2010; Eyckens, 2010; Eyckens et al., 2010; Guzmán et al., 2012b; He et al., 2005b; Henrard, 2008; Ji and Park, 2008; Sena et al., 2015; Vasilakos et al., 2011).

SPIF is characterized by a sheet thickness reduction when forming the sheet. In this regard, there exists a simple analytical tool to estimate the thickness at the

end of the process, given the wall angle and the initial sheet thickness. This rule is called the *sine law* and assumes that the deformation is solely based on shear mechanisms (Fig 6.3(a)), allowing to estimate the final thickness. The sine law is given by:

$$t_f = t_i \sin \alpha \tag{6.1.1}$$

where t_i is the initial thickness, t_f is the final thickness and α is the angle shown in Fig. 6.2. Nevertheless, the simplicity of this relation does not allows the prediction

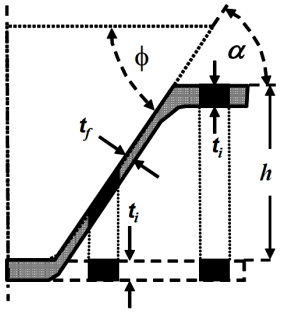

Figure 6.2: Sine law for shear forming (Jeswiet et al., 2005; Kobayashi et al., 1961).

of the observed effects of stretching or bending. Bambach, (2010) points out three cases where the sine law is not valid:

1. In the transition zone between the deformed and undeformed parts (bending zone).

2. Under overspinning, leading to overprediction of the final thickness (cf. Li et al., 2012).

3. In large wall angles where a *thinning band* appears (necking zone).

In addition, Duflou et al., (2008b) compared the multi-step forming and thickness distribution achieved in a conical shape, testing the sine rule and showing that the law is no longer valid after the first stage, when tangential deformations become more important. Hence, Bambach, (2010) proposed an improvement of the sine law by considering curved trajectories. Likewise, different analytical methods had been proposed to predict thickness (Cao et al., 2014; Mirnia et al., 2013), covering more general types of deformations.

In the beginning of the SPIF research, researchers believed that incremental forming was mainly governed by shear instead of stretching (Fig. 6.3). This assumption was mostly motivated by the SPIF origins and the relatively good results obtained using the sine law (Emmens and van den Boogaard, 2007). With the intention to improve formability, Kim and Yang, (2000) proposed a double pass forming technique[2] assuming pure shear. Nevertheless, this argument is not robust as the sine law can also be applied to alternative mechanisms like pure bending or

[2]Initially proposed to remedy thinning, it means forming first a pre-form before the final shape.

stretching in the plane of the sheet, which have only minor relative displacement between the upper and lower surfaces (Emmens and van den Boogaard, 2007). More recent analysis have found that the mechanism seems to be pure shear in

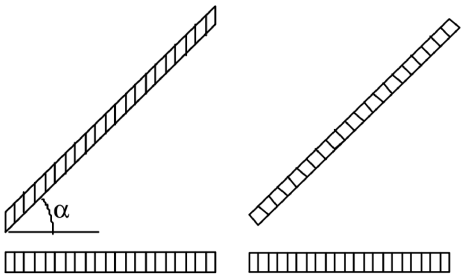

(a) Shear. (b) Stretching.

Figure 6.3: Schematic representation of sheet metal forming by shear and stretching (Emmens and van den Boogaard, 2007).

the thickness with plane deformation in the direction parallel to the initial undeformed sheet. Measurements and numerical simulations on SPIF and two point incremental forming (TPIF) have shown that for a spiral trajectory, in straight or slightly curved faces, the material does not move significatively in the plane of the initial undeformed sheet. In this manner, the deformations on the sheet surface are nearly zero, negligible in direction parallel to the tool direction and positive in the perpendicular direction to the tool direction. Kim and Park, (2002) analyzed the deformation pattern and the formability claiming that the formability is higher when the deformation is stretching under plane deformation. To demonstrate this, they used the so-called straight groove test[3] recommended by Kim and Park, (2002) to assess formability. Lievers et al., (2004) experimentally verified in a quadrangular SPIF pyramid that the average major true strain, measured using DIC, correspond to pure shear mechanism as suggested by Kim and Yang, (2000). Higher deformation is achieved in the surface perpendicular to the tool direction and in larger wall angles, as represented by the sine law. Emmens and van den Boogaard, (2007) indicates that if the deformation is shear dominated, the principal deformations cannot be measured using glued meshes patterns on the surface because the surface strains are not the principal ones. In addition, assuming a shear dominated deformation means that the principal deformations are higher that those assumed by pure stretching. This affirmation is easier to understand using the Mohr's circle (Fig. 6.5). Martins et al., (2008) derived the state of deformation starting from a membrane analysis concluding that there are plane deformations in both smooth and curved surfaces and equibiaxial stretching states in the corners, without considering any effect of shear due to the tool contact. Jackson and Allwood, (2009) performed a wide study of the deformation mechanism using copper sheets. The sheets were thicker than usual (3.1 mm) in order to measure the TTS. An interesting state-of-art review is included, which can be resumed in the following quote:

[3]Similar to the line test, later described in section 6.3.

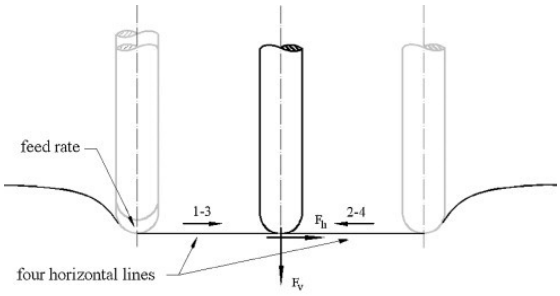

(a) Straight groove test toolpath, where tool alternates between a stroke, back and forth twice along an straight line (Durante et al., 2009).

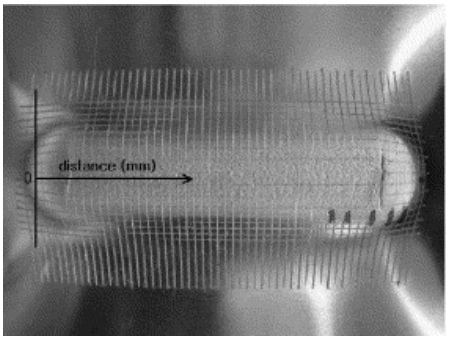

(b) Coordinate system and deformed grids from the straight groove test (Kim and Park, 2002).

Figure 6.4: Straight groove test.

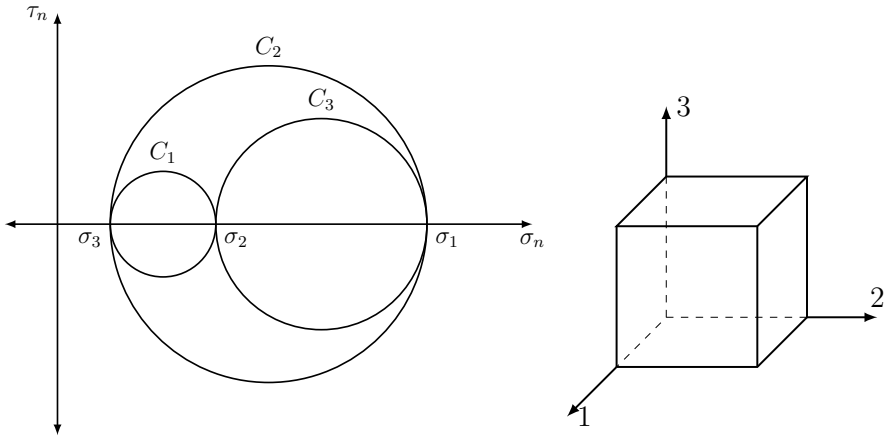

(a) (b)

Figure 6.5: Mohr's circles for a (general) three-dimensional state of stress. σ_n and τ_n give the normal and shear stress acting on a particular cut plane with a fixed normal direction. Each circle, C_1, C_2 and C_3, represent the state of stress in the plane normal to direction 1, 2 and 3 respectively.

> [...] for a conventional spiral tool path along straight or gently curved sides, material does not move significantly in the original plane of the undeformed sheet, but moves mainly normal to this plane. Hence, strains on the surface of the sheet are zero or negligible parallel to the tool direction and positive perpendicular to the tool direction, and these directions correspond to the minor and major directions of surface strain, respectively.

6.1.3 Geometrical accuracy

One of the most important disadvantages of the SPIF process is its poor geometrical accuracy (Ambrogio et al., 2010; Micari et al., 2007) preventing a massive industrial acceptance (Allwood et al., 2005), where accuracies around $\pm 0.5\,\text{mm}$ (Jeswiet et al., 2005) or even $\pm 0.2\,\text{mm}$ (Allwood et al., 2010) are needed.

6.1.3.1 Classification

Geometrical errors arise from several sources and likewise can be classified in different ways. For instance, Essa and Hartley, (2010) identified some geometrical *effects* leading to inaccuracies. Among them, it is mentioned the sheet bending in the initial contact zone, the pillow effect on the base (Ambrogio et al., 2007), springback, etc. as shown in Fig. 6.6(a). Other inaccuracy categorization can be seen in Fig. 6.6(b). The source and severity of these deviations depend on both the process parameters and the material behavior. For instance, it is known that steel exhibits larger geometrical deviation compared to aluminum because of its larger elastic modulus. The tool trajectory strategy also plays an important role, like in the tent effect identified by Behera et al., (2013b) as a typical example of feature interaction and analyzed by Guzmán et al., (2012b) using FE simulations (Fig. 6.7). The achievable accuracy is also dependent on the machine stiffness (Meier et al., 2013), with milling machines being stiffer than industrial robots and hence obtaining higher accuracy (Behera, 2013; Verbert, 2010).

6.1.3.2 Optimization techniques for accuracy improvement

Several techniques have been proposed to determine which is the best way to employ SPIF in order to obtain a certain shape. According to Ambrogio et al., (2007) and Micari et al., (2007), the best way to reduce the inaccuracies is using a toolpath different from the target CAD geometry. When the tool is removed, the elastic deformations in the sheet will give the desired shape. For example, as some shape inaccuracies are caused by the absence of a die (Ambrogio et al., 2004), adding a backing plate can help to reduce sheet bending while using another tool (TSPIF) can reduce springback (Essa and Hartley, 2010). Nevertheless, some solutions can severely alter SPIF main advantages and neither they can achieve accuracies at industrial levels. Following this point, several accuracy enhancements have been proposed keeping SPIF most important features. They can be classified in two groups: those requiring toolpath modifications and those involving new hardware. Within the first group it is identified:

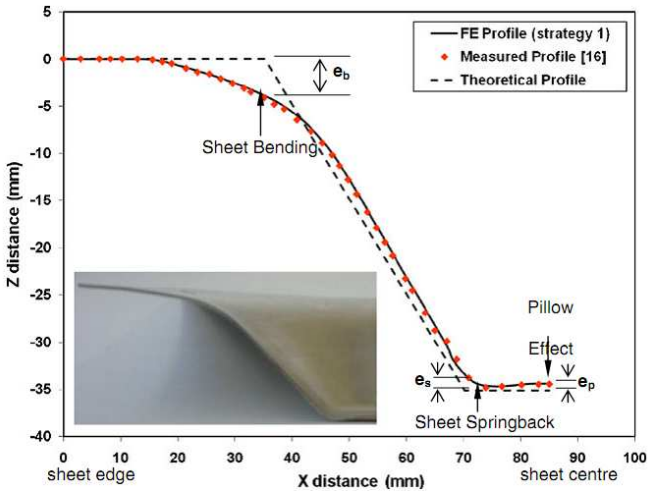

(a) Deformation effects on geometrical innacuracy observed in a SPIF cone (Essa and Hartley, 2010).

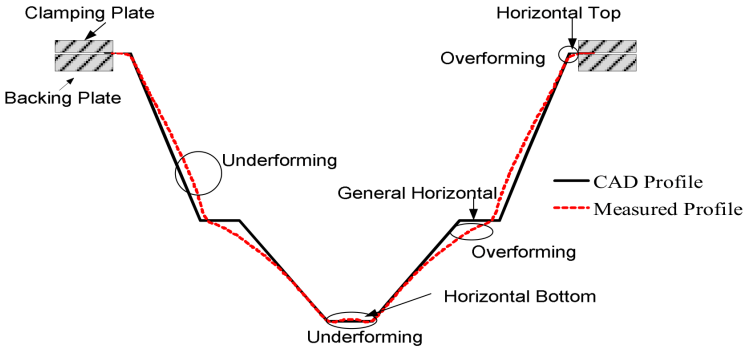

(b) Terminology used to describe the different types of geometrical innacuracies on ISF (Behera, 2013; Behera et al., 2011). This particular example shows the intended and obtained geometry when using horizontal planar features.

Figure 6.6: Schematic figures representing observed shape inaccuracies in SPIF process.

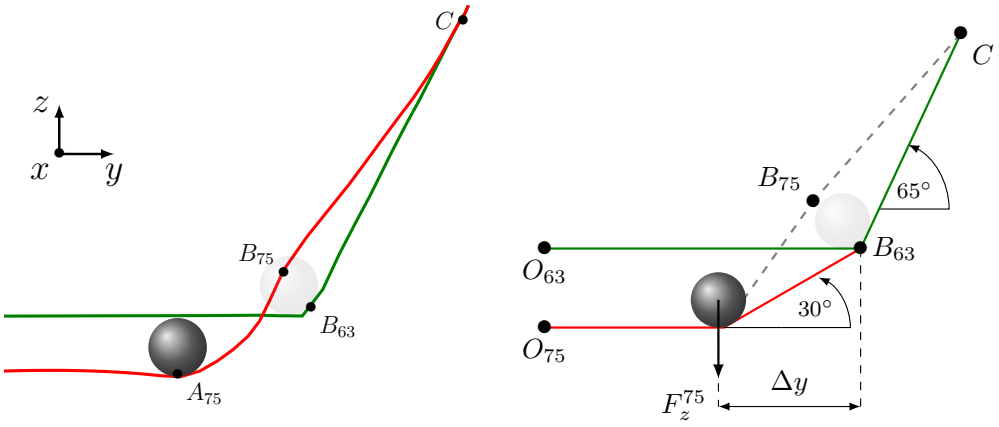

(a) Tent effect.

(b) Scheme of the displacement of point B at two different tool contours.

Figure 6.7: The tent effect reflecting an undesired movement of the wall when forming a second wall angle (Guzmán et al., 2012b).

- *Real time toolpath optimization*, where process data is evaluated by CNC controllers and a new toolpath is generated (Meier et al., 2009; Rauch et al., 2009).
- *Iterative toolpath correction* (Fu et al., 2013; Hirt et al., 2004; Ndip-Agbor et al., 2015).
- *Automatic toolpath generation methods*, which can be based on the behavior of individual features (known as feature assisted SPIF, FSPIF) (Verbert, 2010) and their interactions (Behera et al., 2013a).

Within the second group:

- *Compensation strategy*, considering the robot kinematics and stiffness (Belchior et al., 2013; Verbert et al., 2009).
- *Shape modifications* after forming by reprocessing the workpiece (Allwood et al., 2010; Duflou et al., 2005; Verbert et al., 2007).
- *Stress-relief annealing* after forming (Bambach et al., 2009) or *local heating through laser beam* during forming, also known as laser assisted SPIF (LASPIF) (Duflou et al., 2007, 2008a; Mohammadi et al., 2014).

It is worth to mention that toolpath plays a significant role not only in the accuracy, but also in the thickness distribution and forming limits. Some tool strategies, like spiral (Filice et al., 2002) and conical (Bambach et al., 2005) toolpaths, have positive impacts on formability and thinning. Kopač and Kampus, (2005) showed that a toolpath starting in the center of the sheet and moving to the exterior has better formability. Nevertheless, accuracy improvement techniques do not necessarily imply higher formability, as shown by Azaouzi and Lebaal, (2012) using an optimized spiral toolpath. Eyckens et al., (2011b) also found that using

a bidirectional toolpath (Jeswiet et al., 2005) has higher forming limit than a unidirectional toolpath.

6.1.4 Formability

Formability can be understood as the ability of a material to undergo a certain plastic deformation without damage and/or fracture. SPIF can reach very large levels of deformation before fracture, even larger than conventional process like the hemispherical dome (punch) test (Filice et al., 2002) or deep drawing (Jeswiet et al., 2005). These observations have prompted the characterization and study of the SPIF forming limits for different materials and geometries. In general, the approach towards the understanding of the increased formability has followed two main perspectives:

- Based on the observed deformations mechanisms acting on SPIF, the application of formability characterization methodologies used in other sheet metal forming operations, like forming limit diagrams (FLD).

- Study of particular SPIF process parameters on the material formability, expressed on the maximum wall angle achievable without fracture.

Within the literature, sometimes it is not easy to distinguish between both approaches but, for sake of understanding, an effort will be undertaken on describing each one separately.

6.1.4.1 General formability analysis

Most of the formability studies about sheet metal are rigorously embodied using a FLD, which are based on detecting a (diffuse or localized) necking condition followed by a rupture phase. FLDs were initially introduced by Keeler and Backofen, (1963) and given an analytical basis by Marciniak and Kuczynski, (1967) (herein referred indistinctly as MK approach/analysis), mainly for deep drawing. This commonly used framework has been widely adopted in literature but suffers from important drawbacks when applied to SPIF (Emmens and van den Boogaard, 2009a). For instance, the presence of TTS implies that the principal axes are not in the sheet plane, so FLDs based on surface strains can lead to wrong conclusions (Allwood et al., 2007; Emmens and van den Boogaard, 2007). Hence, FLDs should be regarded only as an useful tool that provides important insights on the material formability but not as the definitive tool to characterize it.

One of the first studies applying FLDs to SPIF was due to Filice et al., (2002). The methodology considered the determination of critical strains at fracture for different straining conditions, using circular grids on the sheet surface. Different types of strains, ranging from pure uni-axial stretching to bi-axial stretching, can be achieved changing the tool trajectory:

1. Pure uni-axial stretching occurs along straight edges.

2. Bi-axial stretching in the center of a cross consisting of two perpendicular straight lines.

3. Strains between pure uni-axial and bi-axial when changing the corner radius in a spiral toolpath. The ratio between the major and minor strain is directly proportional to the spiral loop diameter.

Another interesting observation is that the ratio between the punch depth (vertical step) and the horizontal displacement is directly proportional to the measured strains. One of the main conclusions driven from Filice's article is that the form-

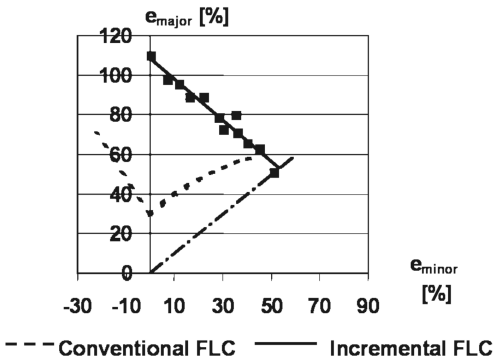

(a) Experimental FLC of AA1050 (Filice et al., 2002).

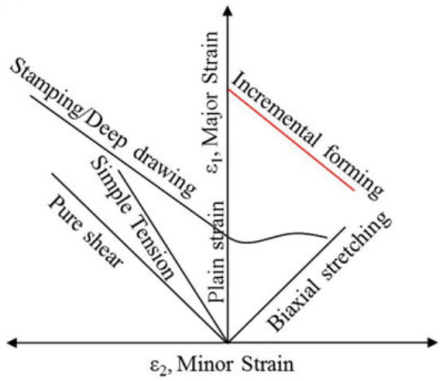

(b) FLC of SPIF and other forming processes (Reddy et al., 2015).

Figure 6.8: FLC of SPIF is higher than conventional forming.

ing limit curve (FLC) has a negative slope equal to -1.0 (Fig. 6.8(a)), somewhat confirming the results obtained previously by Iseki et al., (1993), who identified a slope of -0.7 for an aluminum alloy. Later, the use of circular grids was questioned by Emmens and van den Boogaard, (2007). Basically, the shear mechanism acting in SPIF prevents considering the surface strains as the principal strains. Hence it is not correct to say that the mechanism is pure uniaxial stretch neither biaxial stretch. Nevertheless, the observed high formability of SPIF was later confirmed using different methodologies. A short review of the mechanisms claimed to enhance formability are listed by Emmens and van den Boogaard, (2009a) and further detailed in Emmens, (2011a). An overview of some of them is given hereafter:

Through Thickness Shear (TTS). In theory, under simple shear necking is not developed because there is no thinning. But in stretch forming, shear brings a stabilization effect by reducing the yield stress in tension[4], as shown by Emmens and van den Boogaard, (2009a). This stabilization effect is clearer in Fig. 6.9(a), where the introduction of shear loads delay the neck formation. Shear can also increase the formability, as shown analytically by Allwood et al., (2007) and Eyckens et al., (2009). For instance, Allwood et al., (2007) used a

[4]Also experimentally observed in a combined test by Flores, (2005, chapter 4).

modified MK approach assuming that all six components of the strain tensor are linearly proportional, to integrate TTS into the MK analysis. It is concluded that TTS significantly changes the perceived forming limit measured by surface strains. The approach used by Allwood et al., (2007) was quite unusual, because instead of simulating SPIF, a process called *paddle forming* (Allwood and Shouler, 2007) was analyzed because of numerical difficulties observed in SPIF FE simulations. Eyckens et al., (2009) generalized the MK approach to incorporate TTS. Then, it was applied to isotropic materials subjected to monotonic loads. It is found that formability is increased by the presence of shear for all in-plane strain modes, except equibiaxial stretching, however each one in a different degree. The highest increase in formability is found when TTS acts on the plane perpendicular to the major in-plane strain direction, as shown in Fig. 6.9(b). The authors also

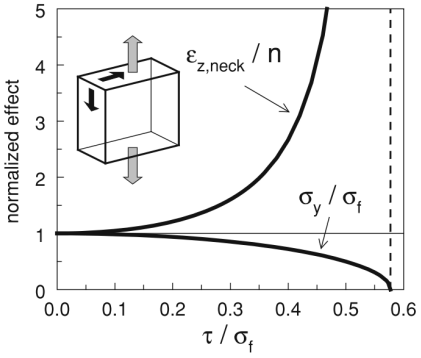

(a) Necking can be delayed by applying some shear loading (Emmens, 2011b; Emmens and van den Boogaard, 2009a). σ_y is the yield stress in tension, σ_f is the initial yield stress, $\epsilon_{z,\text{neck}}$ is the axial strain in the necking zone and n the strain hardening coefficient.

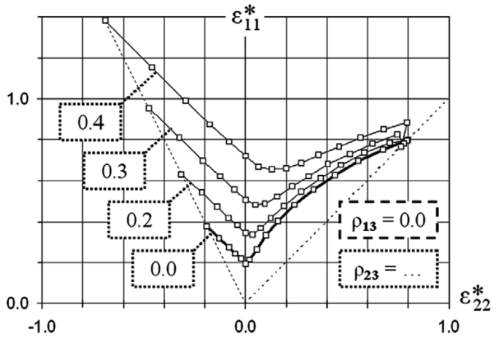

(b) Effect of the shear strain mode ρ_{23}, acting on the plane perpendicular to the major in-plane direction, in the FLC (Eyckens et al., 2009). The thicker line represents the traditional MK model without TTS.

Figure 6.9: Effect of shear on the forming limits.

concluded that a correct representation of the yield locus is crucial. Hence, in Eyckens et al., (2011a) the generalized approach of Eyckens et al., (2009) was extended to anisotropic yield locus. Other extended versions of the MK approach integrating TTS have shown that formability is directly proportional to TTS (Allwood and Shouler, 2009; Eyckens et al., 2011a).

Bending-Under-Tension (BUT). Also referred to as stretch bending, BUT is another mechanism claimed to improve formability (Emmens and van den Boogaard, 2008) since the combined effects of stretching and bending are known to improve formability. For instance, according to Ghosh and Hecker, (1974) the presence of strain gradients across the thickness (due to the sheet curvature) modifies the instability condition retarding the formation of a local neck. Then, Charpentier, (1975) investigated the effect of the punch radius and thickness on the forming limits of a stretch bend test (cf. Banabic et al., 2000, chapter 5).

It is concluded that the limit strain (the maximum measured strain before localized necking) increases with the punch curvature at constant thickness i.e., increasing the punch curvature leads to an increase of the strain gradients (Fig. 6.10). Kitting et al., (2011) confirms that ductility is inversely proportional to the tool radius. Moreover, the effect on formability is more pronounced under plane strain than in uniaxial or biaxial stretch bending. In any case, there is a considerable increase on formability compared to cases without bending. An interesting observation is that due to the stabilizing effect of bending, the conventional FLC may underestimate the forming potential. One way to overcome this drawback is to formulate the FLC in the principal stress space, instead of using (the traditional) strain-based FLC. Stoughton and Yoon, (2011) used a stress-based approach differentiating between necking and fracture limit. This difference can vary in different degrees dependent on the material, with some material exhibiting a substantial post-necking behavior (e.g. AA2024-T 351). It is found that due to the variation of stress through-thickness, a material with a large gap between necking and fracture will be easier to bend due to suppression of necking by the stress gradients.

BUT was first related to ISF by Sawada et al., (2001) and later considered as a stabilization mechanism by Emmens and van den Boogaard, (2008, 2009a,c). Emmens and van den Boogaard, (2008) analyzed tensile tests with simultaneous bending, confirming that the maximum attainable level of uniform strain is directly proportional to the bending angle. Emmens and van den Boogaard, (2009a) emphasized on the localized nature[5] of BUT which acts only when sheet is being bent. More relevant is that BUT creates a small regime of stable deformation at every pass of the tool. When relating the ISF process parameters and the conclusions obtained previously, it is safe to assume that BUT is directly proportional to sheet thickness and inversely proportional to the tool radius (Fig. 6.10).

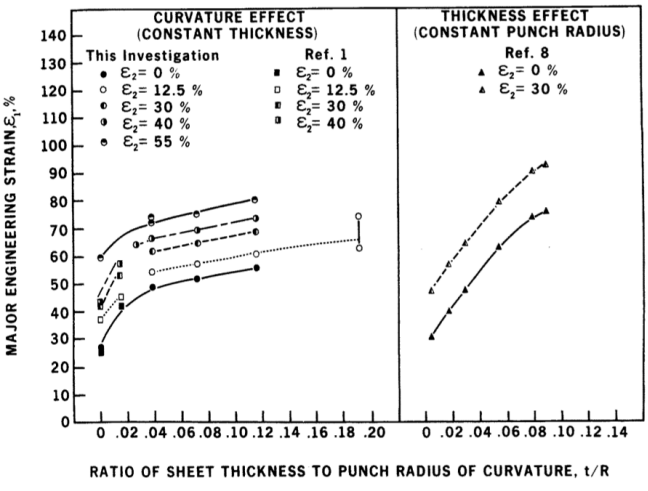

Figure 6.10: Effect of curvature and thickness on the stretching limits (Charpentier, 1975).

[5]Cf. Malhotra et al., (2012) on the effect of the localized deformation.

Cyclic effects. It must be noted that during SPIF the strain history is not proportional because of bending and unbending around the tool. Cyclic loading, generated in serrated strain paths, has been widely observed in FE simulations within the ISF literature (Emmens and van den Boogaard, 2011; Eyckens et al., 2007; Flores et al., 2007; Henrard, 2008; Seong et al., 2014) but also experimentally through DIC measurements (Eyckens et al., 2010), as depicted in Fig. 6.11. Conventional FLCs can be modified to incorporate non-linear strain paths, as

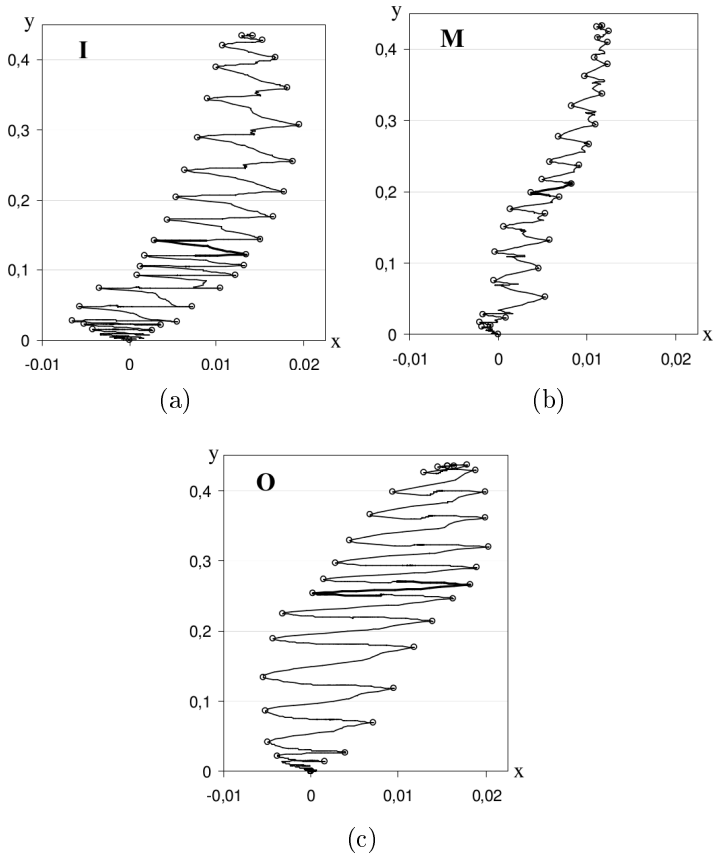

Figure 6.11: Different serrated strain paths observed in a SPIF FE simulation (Eyckens et al., 2007).

proved by Yao and Cao, (2002). The evolution of the yield surface can be expressed in terms of changes of its center (backstress) and curvature. This cyclic effect can have a great influence on formability, as demonstrated by Eyckens et al., (2007). Using a modified version of the MK approach adapted to strain path changes, different types of serrated strain paths (Fig. 6.11) at plane strain loading were analyzed and later compared to a monotonic FLD (van Bael et al., 2007a). The forming limits values can change drastically depending on the strain path, as shown in Table 6.3. It is mentioned by Emmens and van den Boogaard, (2009a) that BUT can be confused with cyclic effects, because it involves repetitive bending but not necessarily cyclic (with an inhomogeneous stress distribution over the thickness), while the cyclic loading involves cyclic straining but not necessarily bending (and maybe with homogeneous stress distribution over the thickness).

Table 6.3: Strain values under plane strain loading. The serrated strain path value is obtained from a MK analysis on the strain paths shown in Fig. 6.11. The monotonic forming limit strain is obtained from van Bael et al., (2007a).

Strain path	*Strain* (%)
Monotonic	19.3
Serrated (**I**)	17.4
Serrated (**M**)	26.6
Serrated (**O**)	40.0

van Bael et al., (2007b) used a modified MK approach to investigate at which extent the non-monotonic strain path may be responsible of the high formability. The predicted forming limits are considerably higher than those predicted using monotonic loadings, but still lower than those observed experimentally.

Normal-compressive-stress. The localized normal stresses induced by the tool contact has also been argued as a mechanism to improve formability. Gotoh et al., (1995) presented three different ways to evaluate the effect of the normal compressive forces over formability, using sheets subjected to in-plane stress plus out-of-plane compressive forces. The first one was using the theoretical framework of the Swift, (1952) and Hill, (1952) criterion for plastic instability condition (both for localized and diffuse necking). The second approach considered an extension of the criterion proposed by Stören and Rice, (1975) (Bifurcation approach), including a positive ratio between the minor and major strain (cf. Filice et al., 2002). The first two criteria were purely analytical, i.e. no numerical calculations nor MK analysis involved. The last approach was using a FE simulations with a modified version of J_2-plasticity model. It is found that the localization of strain is delayed because of the normal stress (Fig. 6.12(b)) and that in the tensile test both the force level and the peak force are affected by the compressive force (Fig. 6.12(c)). These three different approaches yield the same conclusion: out-of-plane stress may notably raise the forming limit diagram, as can be seen when comparing Fig. 6.12(a) and Fig. 6.12(b).

6.1.4.2 SPIF process parameters linked to formability

In a SPIF hardware setup, several parameters can be changed in order to obtain the desired shape and surface finish. These parameters can be linked to:

- The *sheet metal geometry*, such as the thickness or the desired wall angle.
- The *hardware setup*, like the tool size, spindle angular speed or lubrication.

From all listed parameters, the wall angle and sheet thickness seem to be the most relevant in terms of formability. The tool diameter and step-down play a minor role on the forming angle (Ham and Jeswiet, 2007). As mentioned by Behera,

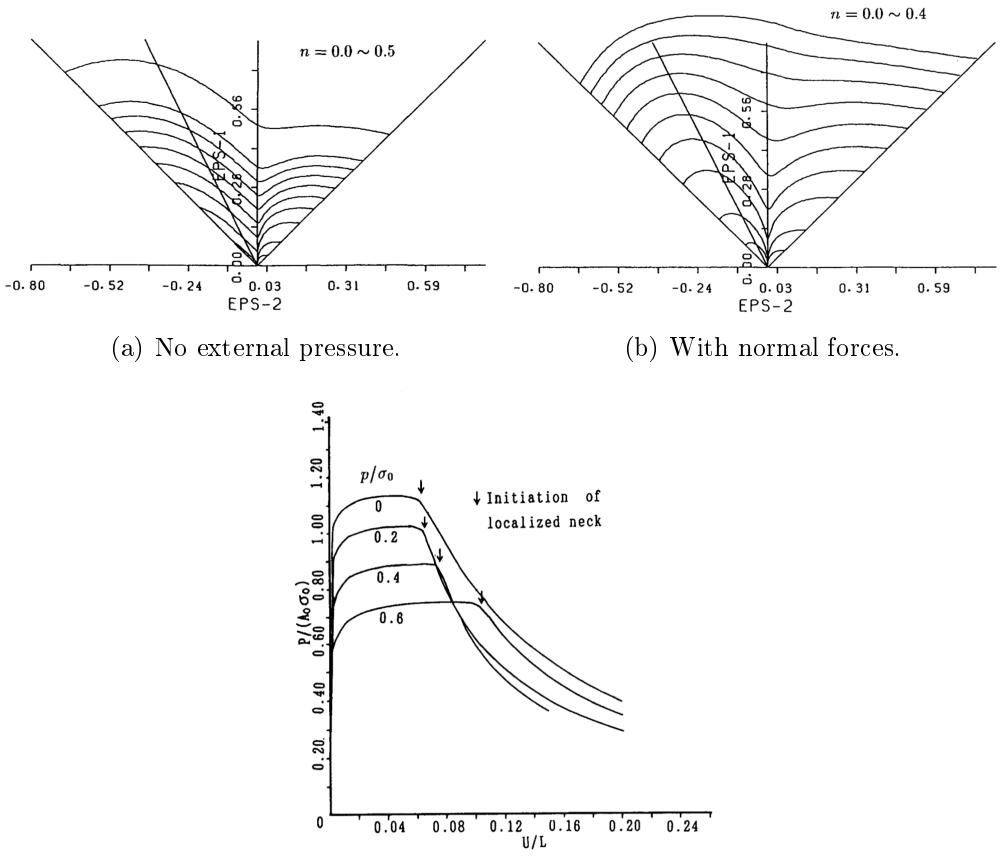

(a) No external pressure.

(b) With normal forces.

(c) Tensile test.

Figure 6.12: Influence of an external compressive load (p) in the ductile rupture of thin sheets (Gotoh et al., 1995).

(2013), incremental forming is characterized by well defined forming limits for a specific material thickness and process parameters. Hence, the maximum draw angle can be used as a formability indicator. It is useful to note that failure does not take place immediately in a part with a wall angle above the failure limit; it takes place at a certain depth. For example, Table 6.4 lists critical wall angles for some materials and thickness. This methodology can be linked to the sine

Table 6.4: Experimental critical wall angles for some materials and thickness. Taken from Behera, (2013) and Verbert, (2010). Also referred in Reddy et al., (2015).

Material	*Thickness* [mm]	*Max. achievable wall angle*
65Cr2	0.5	57°
DC01	1.0	67°
DC04	1.0	64°

law, where it is possible to establish a limit for thinning based on the wall angle and the initial thickness. Thus, it is straightforward to hypothesize that in order

to increase the maximum wall angle one could also increase the initial thickness. However, this strategy has its practical limitations like the maximum machine load and thickness specifications of the material batch.

Obtaining the formability limits in terms of the wall angle, as depicted in Table 6.4, requires a large amount of experimental trial and errors. Therefore, Hussain and Gao, (2007) proposed to use a curved-line-generatrix to generate a revolved surface whose wall angle varies. The formed axisymmetrical conical surface has a varying wall angle which is capable to determine the formability at low cost and reduced processing time. Later, Hussain et al., (2007) tested this varying angle geometry with three different shapes derived from three analytical generatrix: elliptical, exponential and parabolic. The authors proposed a new methodology, where the limiting fracture is determined in a iterative way: taking the varying angle specimen as the first value and then performing the test in a cone in a classical way, by decreasing the wall angle until it does not break. Tisza, (2012) confirmed the suitability of this method in aluminum AA1050A for different thickness, using the geometry generated through a circular generatrix (instead of elliptical, exponential or parabolic). Small differences arose between the constant slope approach and varying wall angle approach allowing to skip the two step approach by Hussain et al., (2007).

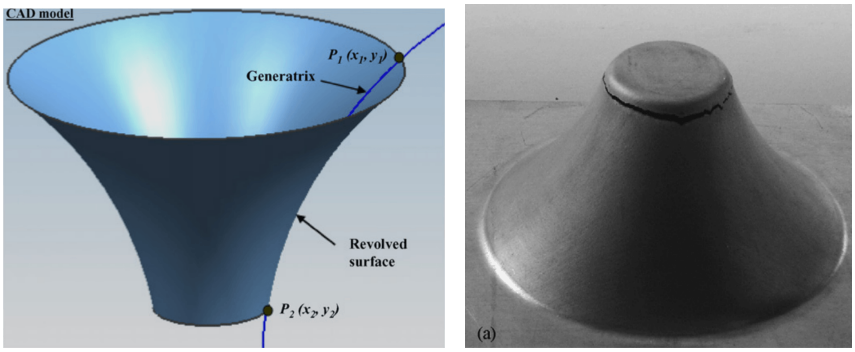

(a) CAD geometry. (b) Formed SPIF geometry.

Figure 6.13: Varying wall angle cone formed (Hussain et al., 2007).

6.1.5 Damage and fracture in the SPIF process

In the previous sections, some concepts relating formability, fracture and the mechanisms of incremental forming were revised. Formability analysis has been for long time the traditional way to optimize the sheet metal forming operation. However, here the damage model focuses on a different aspect: the mechanisms of degradation/softening leading to final fracture[6]. Within this section, the scope is the understanding of the phenomena that lead to crack formation and not the way to avoid fracture or instability. Of course, formability and damage prediction can easily be linked, but they are essentially different. Formability can be regarded as

[6]Also known as local approach to fracture (Berdin et al., 2004)

a more practical (engineering) concept, involving material and process parameters analyzed through FLDs. While the material damage, on the other hand, results from a particular stress or strain field acting in a material continuum. Thus, damage concerns continuum mechanical models where a specific damage variable evolves until a limit is reached at the onset of crack formation. Another fundamental difference between these approaches is that during damage development, the microscopic scale is not negligible, so the analysis should permanently be regarded as material dependent and needs a modeling of the microstructure evolution. The literature review shows a relatively scarce amount of SPIF researches related to damage. One possible explanation is that damage analysis does not often provides simplified solutions in terms of the forming process parameters. Moreover, complex damage models also require complex characterization methodologies, which are not always feasible.

Porosity within SPIF process has been studied, for instance, by Lievers et al., (2004) and Hirt et al., (2004). Lievers et al., (2004) presented a novel method to fit void nucleation parameters using SPIF. This approach is sustained under the hypothesis that in some forming processes, like stretching and stretch flanging and SPIF, necking is suppressed[7] and formability is controlled by void damage and shear band instability. Quadrangular SPIF pyramids for different aluminum alloys and wall angles were formed by Lievers et al., (2004). Density measurements were taken following the procedure described in section 5.4.3. Some interesting results are shown in Fig. 6.14(a) for different deformation levels and wall angles. Planar isotropy is observed thus density is similar between RD and TD.

Hirt et al., (2004) performed a simulation of a truncated pyramid formed using multi-stage forming, using a partial die. To study the stress state, the GTN model was used together with shell elements. Despite the limitations of the shell elements (already mentioned in section 6.1.1), the predictions shows a clear trend that higher forming limits can be achieved with smaller forming heads and larger values for the vertical pitch, as shown in Fig. 6.14(b).

Silva et al., (2008) proposed a theoretical model for a rotational symmetric SPIF shape, based on a membrane analysis. Sheet stretching is considered but bending and shear are neglected. It is observed that the opening mode of cracks in symmetric SPIF is similar to that in conventional stamping (mode I in fracture mechanics) and the cracks open through a meridional tensile stress as shown in Fig. 6.15(a). The analysis is done in the transition zone between the inclined wall angle and the corner of a (rotational symmetric) conical shape, because the onset of cracking was observed in that area. The characterization of the stress state within the cone shape is given assuming plane strain condition (Filice et al., 2002; Jeswiet and Young, 2005; Jeswiet et al., 2005). In terms of damage evolution, the decrease of the sheet thickness (or increase of the tool radius) will shift the Mohr circle (Fig. 6.5) to the tensile region, thus increasing the hydrostatic stress and the accumulated damage. This results is consistent with the findings of Hirt et al., (2004). The higher formability of SPIF process, compared to conventional

[7] Necking generally involves large stress/strain gradients concentrated in a small region, being difficult to characterize.

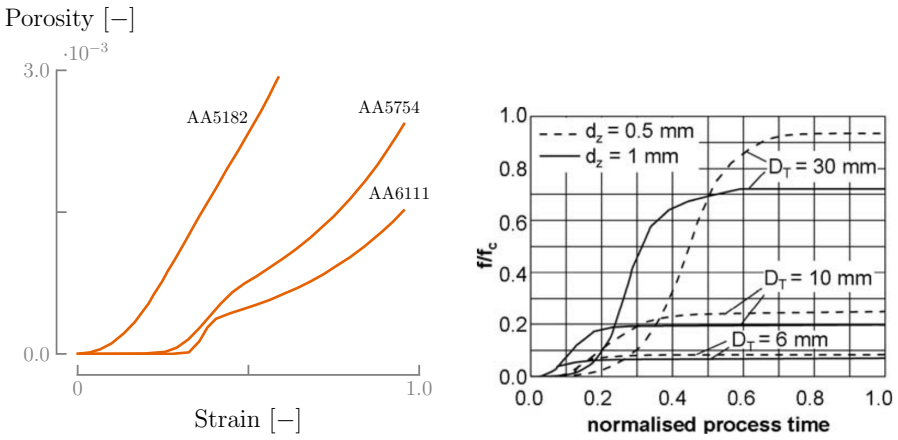

(a) Porosity evolution in different materials within SPIF pyramids. Adapted from Lievers et al., (2004).

(b) Simulation of the SPIF pyramids (Hirt et al., 2004), where D_T is the tool diameter, d_z is the vertical pitch and f_c is the critical void volume fraction.

Figure 6.14: Evolution of the porosity.

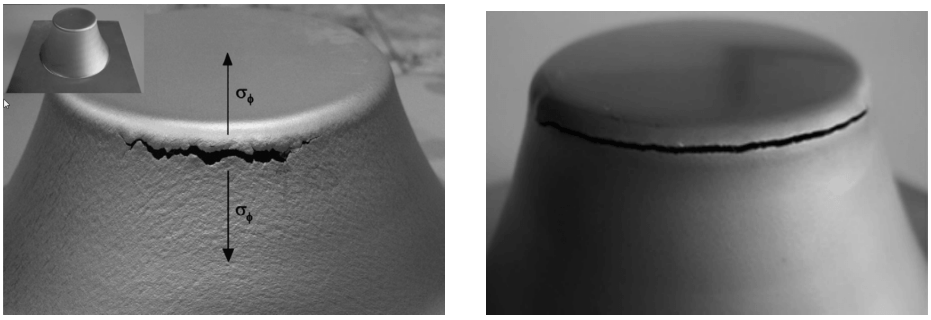

(a) Zigzag crack on a conventional deep drawing steel due to the meridional stress σ_ϕ.

(b) Straight crack on a deep drawing stainless steel.

Figure 6.15: Different types of crack propagation observed in a SPIF axisymmetrical cone for different materials (Silva et al., 2008).

stamping, is then explained in terms of the meriodional stress. In stamping, the level of hydrostatic stress in biaxial stretching is higher than in plane strain (and in the SPIF process), so damage grows faster.

Silva et al., (2011) groups the literature review in two families:

- *Necking view*, where formability is limited by necking and the raise of formability is due to stabilization mechanisms. This view was examined in section 6.1.4.

- *Fracture view*, where formability is limited by fracture. High levels of formability come as a results of suppression of necking or low damage growth.

Each view has its advantages and disadvantages. Against the necking view, it is known that forming limits in SPIF are well above conventional FLC and closer to the fracture forming limits (FFL). In the other hand, a puristic view of the fracture requires that all possible strains located on a specific line to be dependent on the material properties. Nevertheless, it is shown that the FFL can be sensible to the tool size. Moreover, crack appearances seems to be dependent on the formed shape. Within the article from Silva et al., (2011), the effect of the tool radius on the maximum draw angle was analyzed in two SPIF geometries: a truncated conical shape and a truncated pyramid both with varying wall angle (as in Hussain et al., (2007) and Malhotra et al., (2012)). The results are depicted in Fig. 6.16(a) where three different zones are clear: zone A shows an effect of the tool radius but not from the shape, zone B shows an effect of the shape but not from force and in zone C neither parameter affects the maximum draw angle. Thinning is

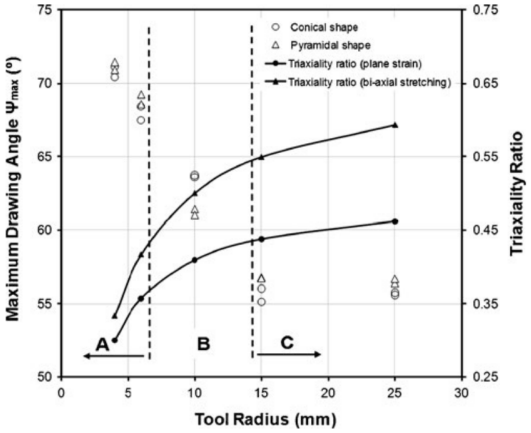

(a) Maximum drawing angle and triaxiality ratio as a function of the tool radius for the truncated cone and pyramid.

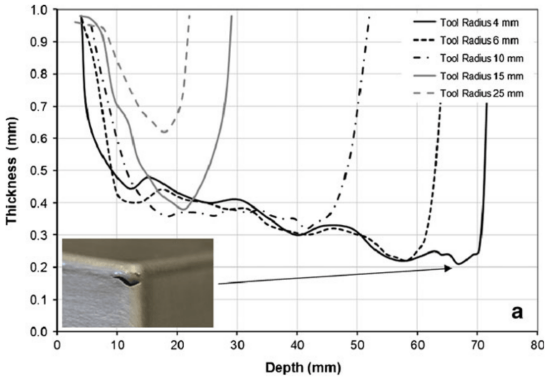

(b) Thickness distribution for the truncated pyramid for different tool radius.

Figure 6.16: Effect of the tool radius on formability and thinning (Silva et al., 2011).

more evenly distributed for small tools compared to larger tools, where thinning is localized. Results for larger radius are consistent with those observed by stamping (fracture with necking). The authors proposed a threshold where, depending on the tool radius, there is a transition between SPIF and stamping. This is proposed in terms of necking/suppression of necking. It will be seen afterwards that this view is not clear because localization can be a characteristic of SPIF.

Malhotra et al., (2012) used the Xue, (2007) damage model to predict the mechanics of fracture on SPIF through FE simulations. The model was validated in terms of thickness, forming forces and fracture depth using a 70° cone and varying angle cone (cf. Hussain et al., 2007) (refer to as a *funnel*). The Xue, (2007) model is a coupled damage model (see section 3.1) which combines plastic strain, hydrostatic pressure and shear on fracture. One of the main features of this model

is that not only damage[8] accumulation and fracture can be predicted, but also the occurrence of diffused and localized necking (Xue and Belytschko, 2010). The simulations involved the explicit LS-DYNA code with a deletion element technique and 8 layers of solid 3D elements. The crack occurs at a location where all elements through the thickness are removed. The authors presented several results concerning the evolution of damage variable, (equivalent) plastic strain, hydrostatic pressure, TTS and reference fracture strain[9]. Between the observations, we can point out:

- The outer side of the sheet exhibits higher damage accumulation than the inner side.
- In the funnel, the initial damage is low due to the low initial angle, it increases dramatically until reaching a higher angle than 70°.
- The shear strain is higher in the element from the inner side of the sheet, delaying damage accumulation.
- Shear along the toolpath is greater than the shear perpendicular to the toolpath.
- Local bending implies higher damage in the outside part because of the higher equivalent plastic strain.

These results confirm findings by previous SPIF researches, like the effect of the localized deformation of BUT. Nevertheless, the most important observation is that shear solely cannot explain the higher formability. Even if it is shown that shear can delay damage accumulation, when comparing SPIF to punch forming (which does not have shear and the deformation mechanism is predominantly by stretching), damage accumulation is faster in SPIF. Damage triggers localization and the simulation results depicted in Table 6.5 clearly show that the SPIF localized at a lower depth that punch forming, but failure is greatly delayed. In order

Table 6.5: Predicted localizations and fracture depth using the Xue, (2007) model (Malhotra et al., 2012). Note that SPIF localized before punch forming, but fracture is greatly delayed.

Type of localization	*Punch forming* [mm]	*SPIF* [mm]
Diffuse	8.0	5.4
Localized	11.0	8.4
Fracture	12.8	14.8

to explain this, the *noodle theory* is proposed (Fig. 6.17). Conventional forming

[8] In the Xue, (2007) model, damage is a phenomenological variable with no relation with the void volume fraction of the GTN model.

[9] A variable from the Xue, (2007) model which is inversely proportional to damage accumulation.

can be represented as pulling the free end of the string (Fig. 6.17(a)) until localization of deformation (Fig. 6.17(c)) and fracture (Fig. 6.17(e)), similarly as in a tensile test. For SPIF, the noodle theory can be represented as locally pulling near the clamped end (Fig. 6.17(b)), which imposes a stretch which localizes a deformation sufficiently small to not break the string. Then the pulling forces moves to another extension and pulls the string in subsequent section (BB', CC' and DD, as in Fig. 6.17(d)), thus the string can be stretched longer than conventional forming. Two observations can be regarded at this point. One is that from the observed thinning, plastic deformation is evenly distributed so the first localization (section AA') has to still undergone neck growth when the pulling force is far (section DD'). This is explained in noodle theory as the ability of the shear band to *share* some subsequent deformation. The second observation is that if section AA' is still undergoing deformation after localization, it should break in this point instead of the contact zone (as is experimentally observed). It is proposed that since the distance from the neck to the load application increases, the ability of this neck (section AA') to share deformation decreases (Fig. 6.17(f)).

Here, the localized effect of SPIF implies that the plastic strain is distributed more evenly than stamping. The already formed zone is still undergoing plastic deformation. This can explain that the inability of conventional FLC to predict failure in SPIF, comes from the observed slow transition between material localization and actual fracture.

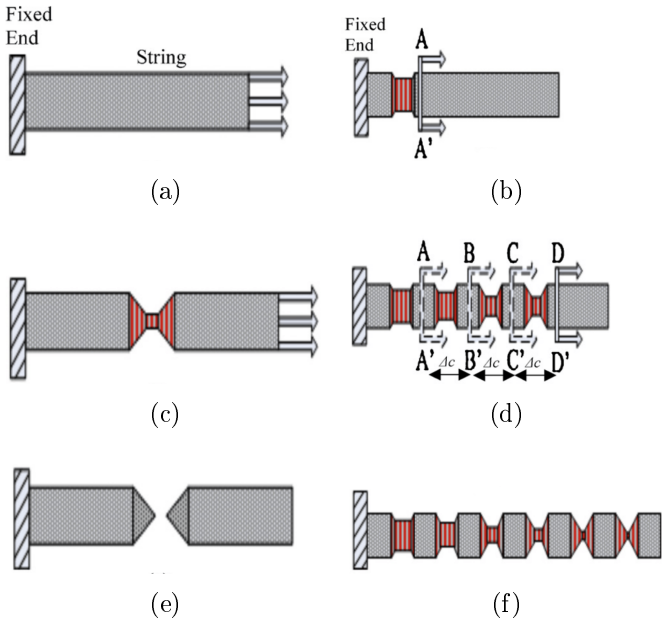

Figure 6.17: Noodle theory (Malhotra et al., 2012).

Summarizing, the classical way to analyze the high formability on FLC can help to understand the effect of the process parameters. However, the complexity of process seems to goes beyond the scope of this approach. For instance, the results obtained using FLCs suggest that TTS is an important stabilization mech-

anism. Malhotra et al., (2012) showed that TSS by itself cannot explain the high formability. Comparing with the formability review of section 6.1.4, the localized effect of BUT seems to be more important than TTS. Moreover, Silva et al., (2011) shows that the geometry and the tool can have a coupled effect on formability. The effect of the thickness distribution prior to necking or failure without necking are also hard to capture by a classical formability analysis. Damage models, on the other hand, can allow a more comprehensive understanding of the material behavior leading to fracture. It is not hard to observe that both approaches can be complemented. Experimental results from the FLC can be used to validate damage models.

6.2 Finite element type

The finite element type, as mentioned in section 6.1.1.3, plays an important role in SPIF FE simulations. The LAGAMINE FE code element library allows using several different FE types, ranging from a 4-node shell element to a 8-node solid elements. Due to the important stress and strain gradients found in the sheet during SPIF and the use of a 3D material model (`GUR3Dext` from section 4.5), the focus will be on three different 8-node mechanical solid elements available in LAGAMINE: `BWD3D`, `SSH3D` and `RESS`. The `COQJ4` shell element, despite being used for SPIF FE simulations in previous publications by the author (viz., Guzmán et al., 2012b), is not described here because it is out of the scope of the thesis. For this element and other type of shell elements used for SPIF FE simulation, refer to Henrard, (2008) thesis. The `BWD3D` element is a *classic* 8-node solid element while

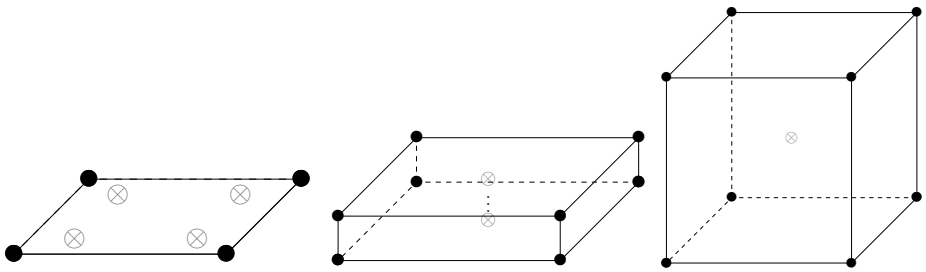

(a) COQJ4. (b) RESS. (c) BWD3D.

Figure 6.18: Finite elements used in LAGAMINE for SPIF FE simulations.

`SSH3D` and `RESS` are based on the *solid shell* element concept, which is basically a mix between a 4-node shell element and a 8-node solid element. These elements are depicted in Fig. 6.18 and will be described in the following paragraphs.

BWD3D. It is a 8-node 3D brick element with a mixed formulation adapted to large strains and large displacements. It can be considered as an updated version of the `BLZ3D` element (Zhu, 1992; Zhu and Cescotto, 1994) but with a different type of locking treatment based on a corotational reference system.

This element is based on the non-linear three-field (stress, strain and displacement) Fraeijs de Veubeke-Hu-Washizu (FHW) variational principle[10] (Fraeijs de Veubeke, 1951; Hu, 1955; Washizu, 1955) with the *assumed strain* method (Belytschko and Bindeman, 1991; Simo and Hughes, 1986). It is formulated using an hourglass control technique and reduced integration with only one integration point through the thickness. The shear locking treatment is based on the Wang and Wagoner, (2004) method, which identifies the hourglass modes responsible for the shear locking and removes them. This feature is a key improvement over the `BLZ3D` element which uses the Zhu and Cescotto, (1994) shear locking treatment. The volumetric locking treatment is also based on the elimination of inconvenient hourglass modes. As shown by Duchêne et al., (2007), the `BWD3D` element gives better results than the `BLZ3D` element in deep drawing simulations proving that shear locking treatment plays an important rule on the accuracy (see also Alves de Sousa et al., 2007). For more information about the `BWD3D` element see Duchêne et al., (2007) and Henrard, (2008).

SSH3D. This element is based on the Enhanced Assumed Strain (EAS) technique and the Assumed Natural Strain (ANS) technique. These techniques avoid locking problems even in very bad conditions (nearly incompressible materials, very thin elements conducting to large aspect ratios, distorted element geometry, etc.).

The EAS technique artificially introduces additional degrees of freedom (DOFs) to the element. Contrarily to the nodal displacements, these additional DOFs are not linked between adjacent elements so they can be eliminated at the element level during the computation of the solution, before the assembling procedure. Hence, the calculation of element strain at the IP level is given by:

$$\boldsymbol{\epsilon} = \boldsymbol{\epsilon}^{\text{com}} + \boldsymbol{\epsilon}^{\text{EAS}} \tag{6.2.1}$$

where $\boldsymbol{\epsilon}^{\text{com}}$ is the strain contribution at the integration point calculated from the nodal displacements and $\boldsymbol{\epsilon}^{\text{EAS}}$ is the additional strain calculated based on the introduced EAS modes. This technique increases the flexibility of the element and is very efficient to solve several locking issues. In the current configuration of the `SSH3D` element, up to 30 independent DOFs can be added to the 24 classical displacement DOFs (corresponding to the 3 displacements of the 8 element nodes).

On the other hand, the ANS technique modifies the interpolation scheme for particular strain components. Again, the strain can be calculated from the nodal displacement and evaluated at the integration points using the transformation matrix $\boldsymbol{B}$. For some particular cases, this approach yields inadequate strain values for some components depending on the IP location. Originally proposed by Dvorkin and Bathe, (1984) for shell elements, the ANS technique proposes to compute the problematic strain components in two steps. First, these strain components are evaluated by the classical interpolation method at the so-called *sampling points*

[10] Commonly referred to as the Hu-Washizu variational principle, this name neglects early contributions by Prof. Fraeijs de Veubeke (see for instance Fraeijs de Veubeke, 1965) from ULg as later revealed by Felippa, (2000).

(SP), where the erroneous values are not likely to be encountered. In a second step, these strain components are interpolated linearly from the sampling points to the integration points (or any location in the element) using a $\boldsymbol{B}^{\text{ANS}}$ transformation matrix, as represented in Fig. 6.19. The sampling points vary according to

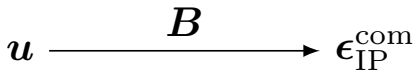

(a) Classical one step interpolation.

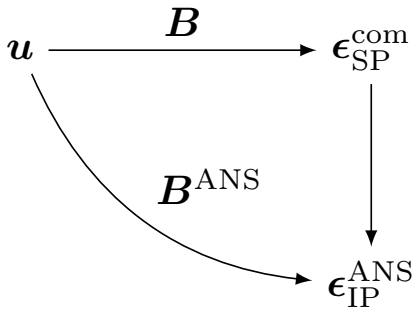

(b) ANS two step interpolation.

Figure 6.19: Strain interpolations, where u is the nodal stretch tensor.

different authors. Fig. 6.20 shows a couple of sampling points used in two versions of the ANS scheme implemented in the `SSH3D` element. This technique is useful

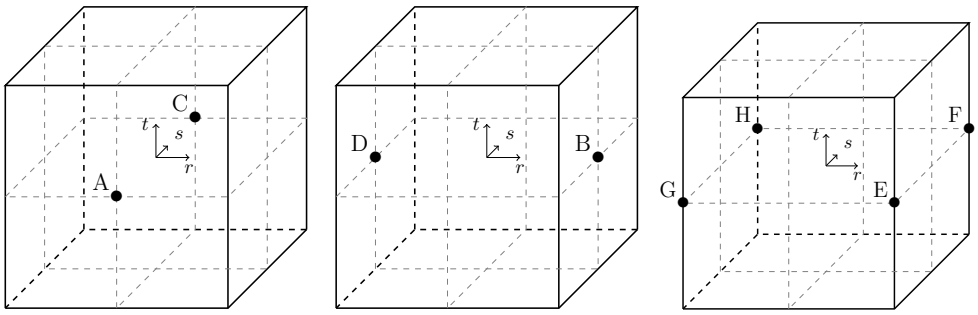

(a) Version 1. (b) Version 2.

Figure 6.20: Sampling points in different ANS versions.

when shear and curvature locking problems are encountered. It allows eliminating the transverse shear locking from the element in bending dominated situations. In the current configuration of the `SSH3D` element, four different versions of the ANS technique are implemented.

Besides these techniques, the number and the location of the Gauss points inside the element can have a significant influence on its mechanical behavior. For instance, the reduced integration or the selective reduced integration schemes are often used to avoid volumetric locking issues for hexahedral elements with an

isochoric or nearly isochoric material behavior. In the development of a solid-shell element dedicated to the modeling of thin-walled structures, an integration scheme with a large number of integration points along the thickness direction is considered. It is indeed expected that a high gradient of stress and strain along the thickness direction is present during the deformation of thin materials (e.g. within a bending deformation mode). The classical full integration of a 8-node brick element (with two integration points along each direction) is not able to accurately capture such large gradients. In this respect, in the `SSH3D` element the stress is computed along a user-defined number (ranging from 2 to 10) of integration points along the thickness direction. For more information about the `SSH3D` element, see Ben Bettaieb et al., (2011a, 2015) and Duchêne et al., (2011).

RESS. The Reduced Enhanced Solid Shell (`RESS`) element is a 8-node element developed by prof. R. de Souza (Alves de Sousa, 2006; Alves de Sousa et al., 2007) and his team (Sena, 2015). It uses only one EAS mode and a reduced integration scheme in the plane. The element allows an arbitrary number of integration points in the thickness direction. To eliminate the hourglass effect due the reduced integration in plane, the stabilization technique proposed by Li and Cescotto, (1997) is used at the element center. To eliminate the volumetric locking, the B-bar method is applied (Alves de Sousa et al., 2005). In this case, only the deviatoric hourglass strain-displacement matrices are used in the finite element stabilization part.

The `BWD3D` element has only one integration point in the thickness direction, so it is the fastest solid element of those presented here. However, it has a limited aspect ratio (the ratio between the width and the thickness of the FE) leading to unwanted locking when simulating sheet metal bending, so usually three or more layers of elements are needed. On the contrary, the `SSH3D` and `RESS` elements can be safely used with only one FE layer. Moreover, the number of integration point through the thickness can be selected by the user while the `BWD3D` is limited to only one IP. According to these features, each element is applied to different cases:

- The `BWD3D` element is used for material parameter identification (both for plasticity and fracture), like in chapters 2 and 5. Through-thickness gradients are not important in these simulated tests. Standalone, `BWD3D` is faster than the `SSH3D` and the `RESS` element, but it needs several FE layers through-thickness when simulating bending in sheet metal forming processes. A very refined mesh is also needed, reducing its performance (cf. Guzmán et al., 2012a).

- The `SSH3D` element is useful for academic purposes, to test the influence of the EAS modes and the ANS version in particular applications (eg. Guzmán et al., 2012a). Having a more complete formulation has also its drawbacks, as it the slowest of all the three elements presented.

- The `RESS` element is used for practical sheet metal applications, because its good compromise between accuracy and CPU time. It does not need several

layers of elements (as the `BWD3D` element) or selecting the EAS modes (as the `SSH3D` element).

In all the LAGAMINE simulations presented hereafter, the contact element used is the `CFI3D` element based on a penalty approach and Coulomb's friction law (Cescotto and Charlier, 1993; Habraken and Cescotto, 1998). This approach is the same as the one used previously for the shell element `COQJ4` (e.g. Guzmán et al., 2012b; Henrard, 2008).

6.3 Line test

The line test is the simplest form of SPIF and the large size of the step-down even induces larger stress gradients than in classical SPIF problems. It allows verifying the accuracy of the identified material parameters and to study SPIF deformation mechanisms. The stress and strain histories during the test are similar to the ones found in SPIF test of a simple geometry. In this research, the target material is a DC01 squared sheet of 182 mm × 182 mm and 1.0 mm thickness, clamped along its edges as shown in Fig. 6.21(a). A non-rotating spindle tool of diameter 10 mm, feedrate of 300 mm/min and with lubrication (Nuto 46 at constant stream), is used. The toolpath consists of five different stages: at the test beginning, the tool is located above the sheet at $X = -50$ mm. Then, the tool moves down until touching the sheet followed by a vertical indent step of $Z = 3$ mm (step 1). A linear horizontal displacement is applied along the X axis until $X = 50$ mm (step 2) and then a second indent of $Z = 3$ mm depth (step 3). Keeping the same depth, the tool returns to $X = -50$ mm (step 4) and finally it is lifted (step 5). The toolpath is schematically represented in Fig. 6.22. The test was experimentally performed

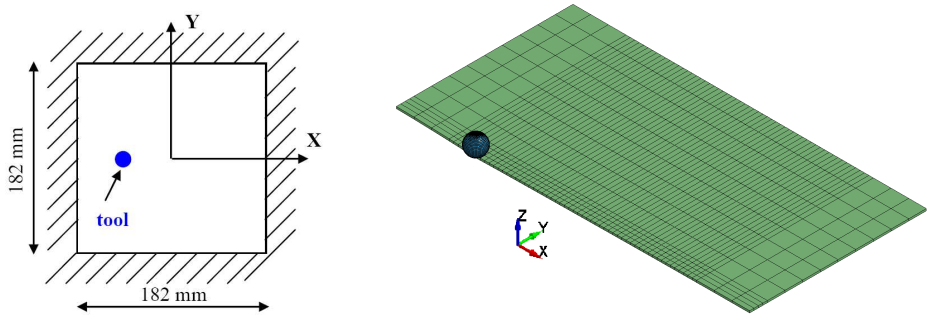

(a) Top view of the squared sheet showing the clamped edges.

(b) Perspective view of the line test FE mesh.

Figure 6.21: Geometry and mesh of the line test.

by Hans Vanhove from KULeuven. In order to ensure the reproducibility of the results, the whole line test was performed three times and the bolts of the frame were tightened using the same torque.

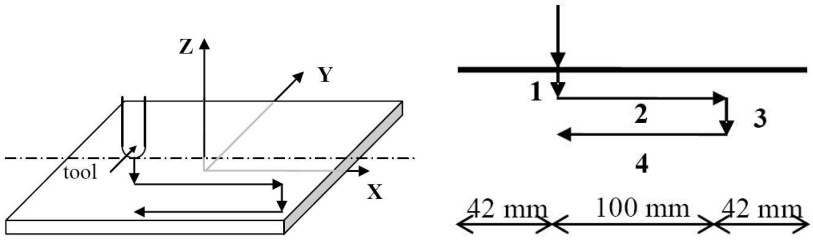

(a) Toolpath perspective. (b) Steps scheme.

Figure 6.22: Line test toolpath.

6.3.1 FE simulation

The FE mesh is depicted in Fig. 6.21(b). It consists of 806 `RESS` solid shell elements with 3 IP through the thickness[11] and 806 `CFI3D` elements with 4 IP. Symmetry boundary conditions are used along the X axis (Y =0) so only half of sheet is simulated. Numerical tests performed by Henrard, (2008, chapter 7), shows that a penalty coefficient of K_p =1000 N mm^{-3} leads to the best compromise between accuracy and convergence. The tool force is computed by a static implicit strategy. No friction is applied between the tool and the sheet. The mesh is adjusted to limit the number of elements while keeping accuracy.

Following the procedure described in section 5.5, different material parameters have been evaluated. The plasticity set of parameters (f_0 =0) obtained in chapter 2 are used to validate the plastic model predictions. Another set of parameters with damage is also analyzed to check the influence of different damage phases (nucleation, coalescence and shear) on the results. The validation is carried out comparing experimental measurements of shape and force.

The set of plastic parameters is reminded in Table 6.6. Taken the `Swift+AF` set as the reference plastic parameters, Table 6.7 presents the GTN model parameters identified in chapter 5.

Table 6.6: Plasticity parameters using the Hill, (1948) yield locus for the line test simulation. See Table 2.16.

		Isotropic		*Kinematic (AF)*	
Set name	K	ϵ_0/ σ_0	n	C_X	X_{sat}
`Swift`	601.88	9.48×10^{-6}	0.2127	-	-
`Swift+AF`	542.49	1.78×10^{-2}	0.4328	113.63	81.96
`Voce`	255.03	182.84	14.28	-	-
`Voce+AF`	264.36	87.02	5.69	119.04	92.94

[11] Convergence issues were observed using more IPs.

Table 6.7: GTN model parameters used in the line test simulations. See Table 5.6.

		Nucleation			*Coalescence*		*Shear*
Set name	f_0	f_N	ϵ_N	S_N	f_c	f_F	k_ω
`nuc`	0.0008	0.0025	0.175	0.42	-	-	-
`coa`	0.0008	0.0025	0.175	0.42	0.0055	0.135	-
`shear`	0.0008	0.0025	0.175	0.42	0.0055	0.135	0.25

6.3.2 Shape prediction

An experimental-numerical comparison for different material parameters is given in Fig. 6.23. The scale of the Z axis is not equal to the X axis in order to get a better view of the cut. In both cases, the curves are defined by the nodal position of the nodes located in the top and bottom layer of the `RESS` element. The experimental results of the shape are obtained through a laser line scanner mounted on the machine. Fig. 6.23(a) shows the results for the set of parameters without damage and Fig. 6.23(b) the comparison using sets considering damage. Globally,

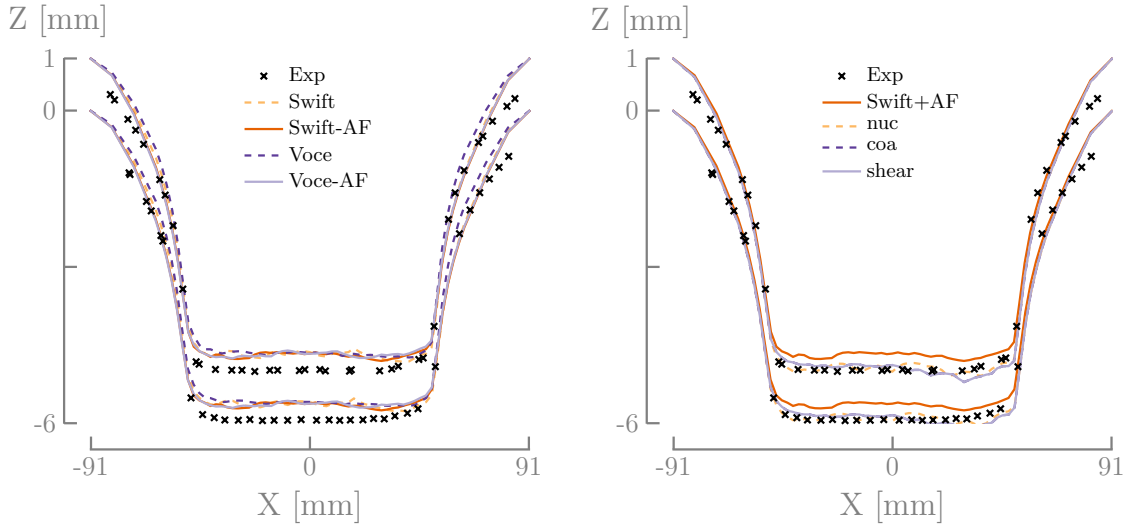

(a) Shape comparison between simulations using plasticity (Hill, (1948) yield locus) parameters (without damage) and experiments.

(b) Shape comparison between simulations using the GTN model extended to shear and experiments.

Figure 6.23: Shape prediction for the line test.

the predicted shapes are in good agreement with the experimental results. The predictions using the GTN model are better than those using only plastic parameters. Nevertheless, the differences between the predicted shape by Hill, (1948) or by the GTN model and the experimental measurements are less than 0.3 mm near X =0 mm, which is small compared to the shape depth. The difference between sets considering damage or not is due to the softening effect induced by damage, allowing the material to deform more than using the set without damage. In the

simulations using the GTN model, no noticeable difference is observed between `nuc`, `coa` and `shear`.

6.3.3 Force prediction

Fig. 6.24 shows the tool reaction in the Z (axial) direction during the process. The experimental force is measured using a load cell mounted on the machine. As no time-dependent law is considered, each step of the line test has a simulation time that is not proportional to the experimental time. Hence, the experimental time is modified in order to match the simulation (reference) time. From Fig. 6.24(a),

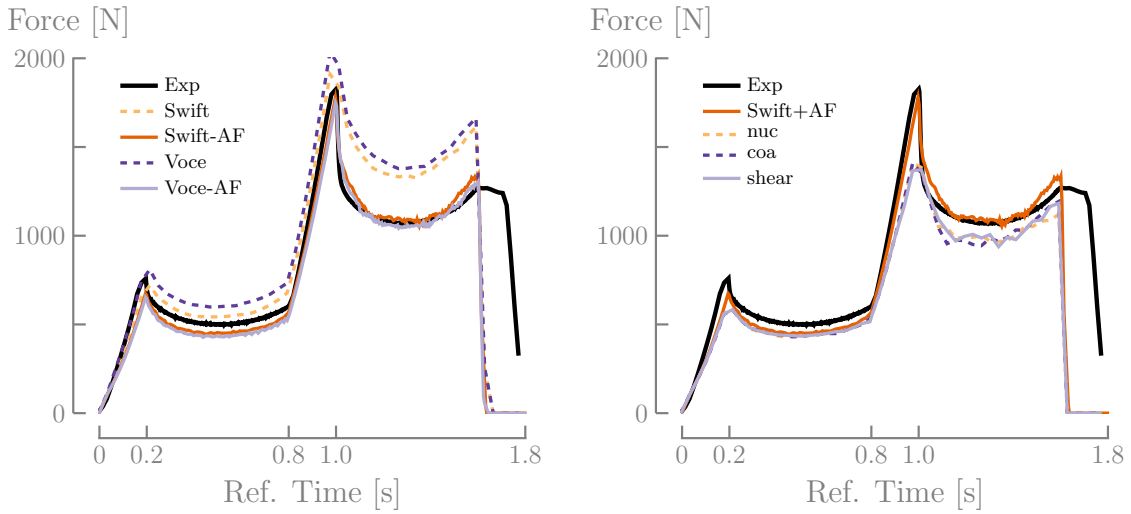

(a) Axial force comparison between simulations using plasticity (Hill, (1948) yield locus) parameters (without damage) and load cell measurements.

(b) Axial force comparison between simulations using using the GTN model extended to shear parameters and load cell measurements.

Figure 6.24: Axial force predictions and measurements for the line test.

it can be observed that a mixed isotropic-kinematic hardening law leads to better predictions than using a pure isotropic hardening model. The predictions based on the set of parameters of the damage model are slightly lower (less than 10%) than the ones associated with the plastic model using mixed hardening. Again, there is no important difference among the force predictions of damage activating nucleation and coalescence steps or taking into account a shear extension.

6.3.4 Analysis of state variables

The material state variables are analyzed from the simulations using the most complete GTN model (`shear` set). The variables are retrieved from three different solid-shell elements: 118, 404 and 690, shown in Fig. 6.25. Elements 118 and 690 are located under the tool at the first (step 1) and second indent (step 3), respectively. Element 404 is located between these two elements. The first integration point (closer to the outer surface, not making contact with the tool) is

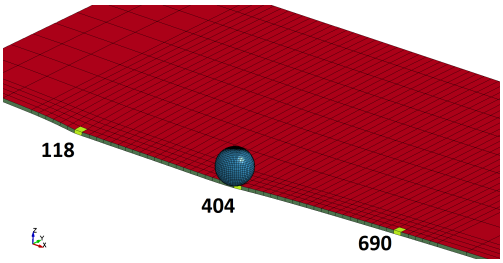

Figure 6.25: Line test FE mesh showing elements 118, 404 and 690 selected to display state variables evolution.

found to give the highest equivalent plastic strain of the three integration points. This is expected, as the local stretching and bending of the sheet around the tool causes the zone in the outer side of the sheet to stretch more than zones in the inner side. Therefore, the state variables are analyzed at this integration point. From Fig. 6.26(a) showing the porosity evolution, it is clear that the indent steps play a major role in the porosity history for the elements under the tool indentation (118 and 690). Element 404 is not affected by the tool indentation as it is too far. Nevertheless, there is a porosity increment due to the tool contact. It is also clear that the major contribution to porosity comes from the growth phase (Fig. 6.26(b)). Nucleation (Fig. 6.26(c)) only plays a minor role while the shear contribution (Fig. 6.26(d)) can be neglected. These features are linked with the fact that ϵ_M^P (and ϵ_q) is low and nucleation is function of this value. The same happens with the shear contribution, indirectly related to the Lode angle which is low except for some peaks. However, it can be hypothesized that triaxiality (and the hydrostatic stress) will play an important role on damage evolution, which is studied in Fig. 6.27. The porosity increment after each indent can be related with a triaxiality *peak* (marked with an arrow in Fig. 6.27(a) when the tool approaches to the element. It can be observed that triaxiality increases when the tool approaches to the element, and decreases when the tool moves away from the (plastically deformed) element. It must be noted that even if the triaxiality is high for element 404 and 690 during the first indent, there is no increment of the porosity as these elements do not deform plastically (see Fig. 6.27(c)) at this moment.

Triaxiality explains why there is a porosity increment, but does not explain why element 690 reaches a higher porosity than element 118, as both present the same level of deformation (Fig. 6.27(c)). The reason of this higher value is based on the mean (volumetric) plastic strain evolution shown in Fig. 6.27(d). It can be easily linked with the porosity evolution in Fig. 6.26(a). Therefore, the porosity mechanism during the line test is mainly governed by the triaxiality and the volumetric parts of the plastic strain. As expected, the simulation does not predict material failure as no crack appeared within the experiment. Note that the coalescence stage is not activated within this line test, as the porosity is still far from the critical value f_{cr} =0.055.

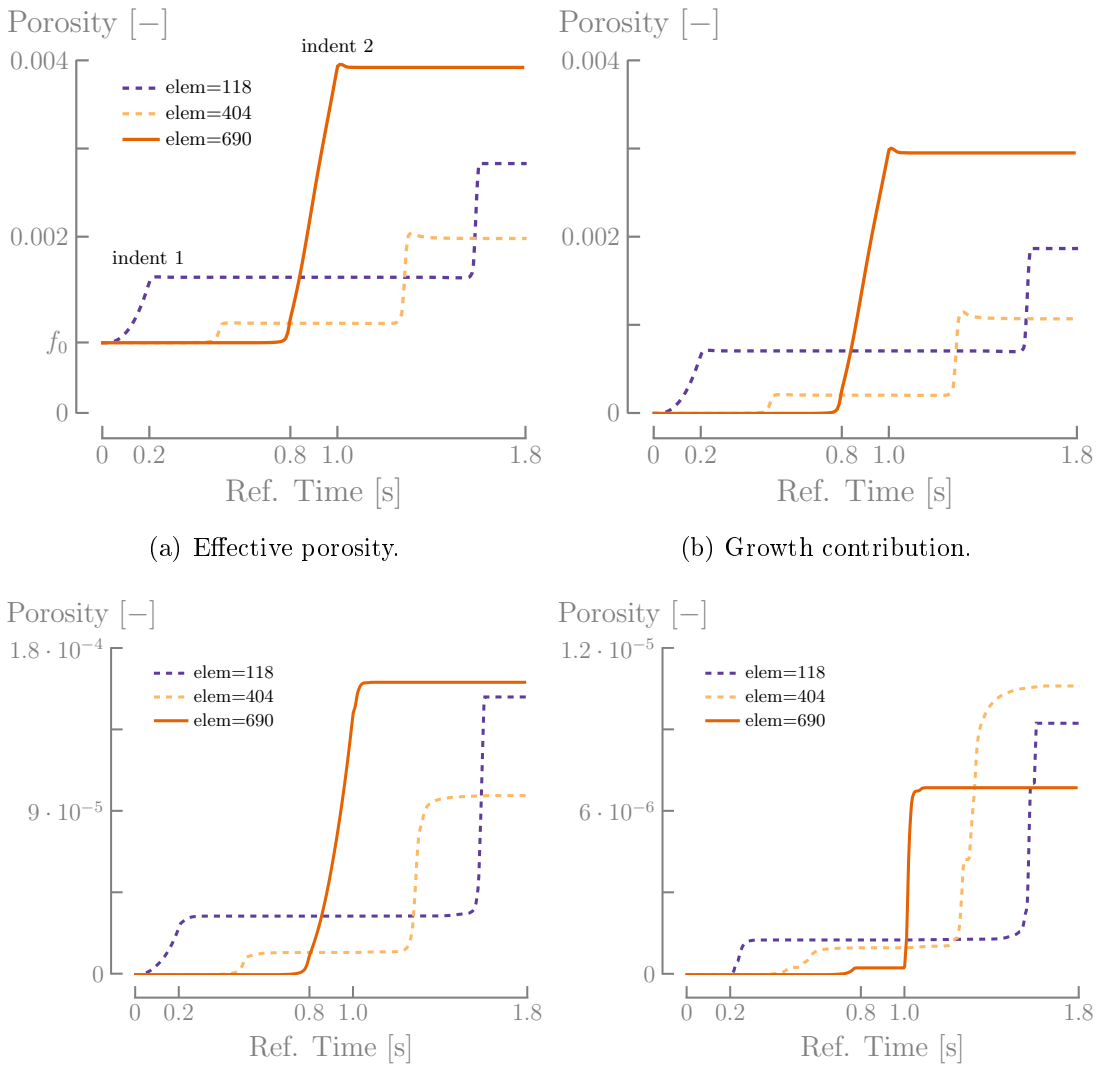

(a) Effective porosity.

(b) Growth contribution.

(c) Nucleation contribution.

(d) Shear contribution.

Figure 6.26: Effective porosity evolution and the contribution from the different phases (nucleation, growth and shear) for elements 118, 404 and 690

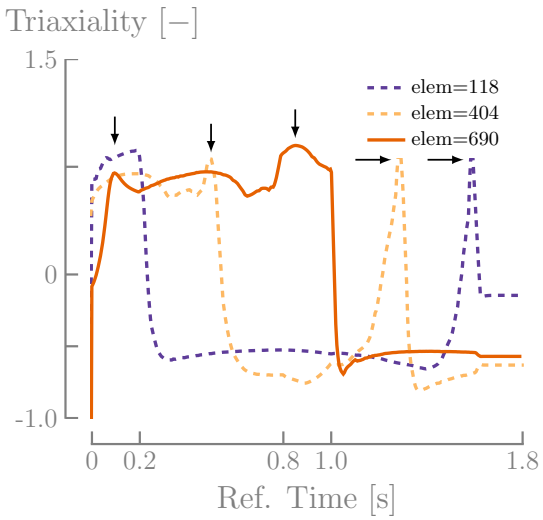

(a) Triaxiality.

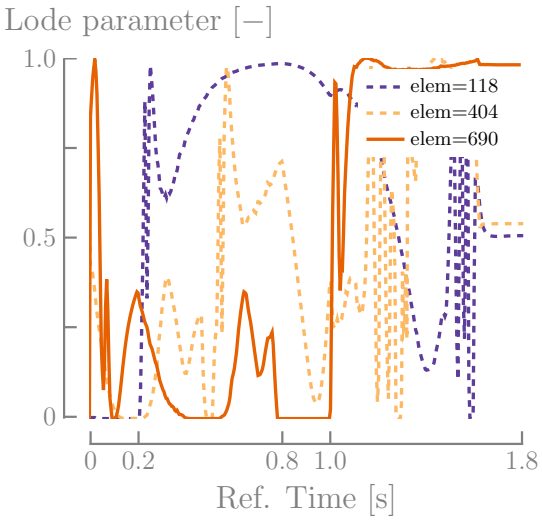

(b) Lode parameter (corrected).

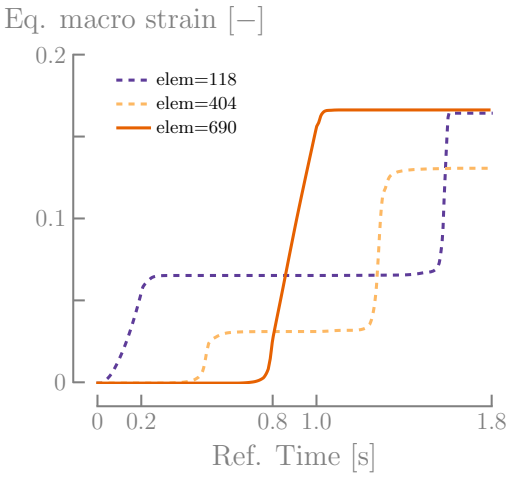

(c) Equivalent (macroscopic) plastic strain.

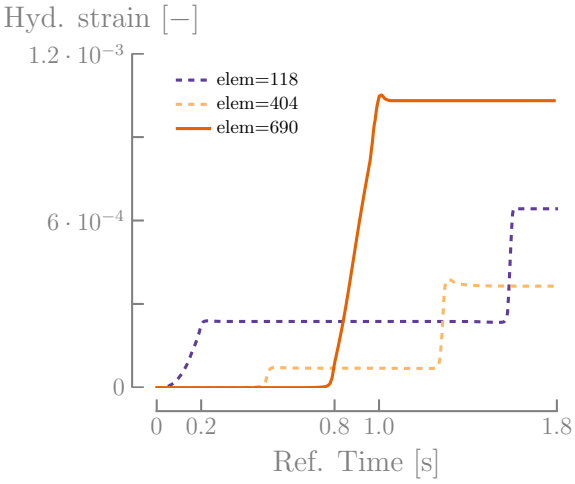

(d) Mean plastic strain.

Figure 6.27: State variables evolution in th line test for elements 118, 404 and 690. The arrows mark triaxiality *peaks*.

6.4 Pyramid test

In this section, FE simulations are carried out to model the forming of a two truncated two-slope pyramid, studied previously as a solar cooker application by Duflou et al., (2005). This geometry suffers from large geometric deviations when comparing the intended and final shapes, so it is ideal to tests the accuracy of the FE type. The blank used in the SPIF process is a DC01 steel sheet with in plane initial dimensions 225 mm × 225 mm and 1.0 mm thickness. It is clamped on its four edges with a 182 mm × 182 mm backing plate in such a way that only the material located inside the orifice of the backing plate could be deformed by the tool. The nominal geometry is depicted in Fig. 6.28. A three-axis MAHO CNC milling machine was used as the platform for the SPIF process. The forming tool was a cylindrical stylus with a 10 mm diameter spherical head mounted on the horizontal axis of the machine, so that the blank was perpendicular to the stylus (Henrard et al., 2010). After traveling an entire path of one contour, the tool moves deeper with a 1 mm step-down to perform the next contour until the desired depth is reached. The number of contours for the first slope of the pyramid is 60 and it is 30 for the second slope. The shape of the pyramid is measured using

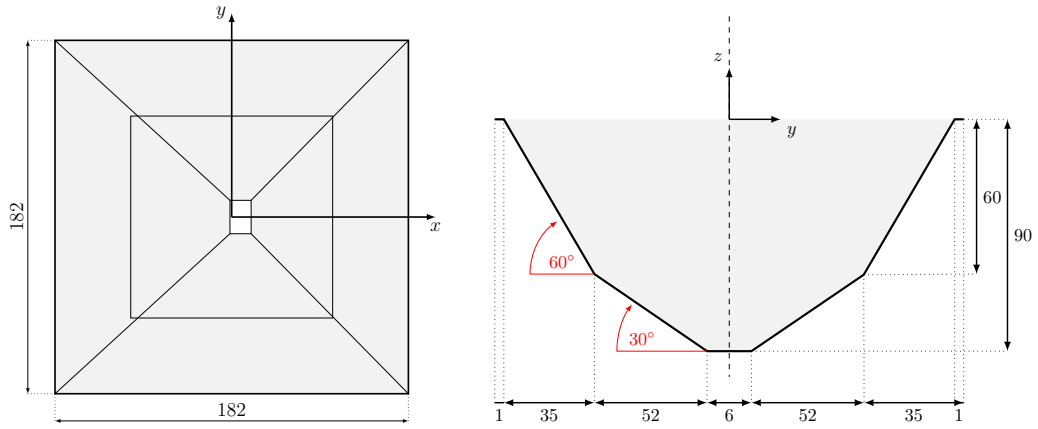

(a) Top view. (b) Side view.

Figure 6.28: Target geometry.

DIC. The tool travels with a feed rate of 500 mm/min, which is slower than usual in order to allow the DIC cameras to capture more images. More details about the DIC technique applied to the SPIF process can be found in Vasilakos et al., (2009) and Eyckens et al., (2010).

6.4.1 FE simulations

The initial undeformed FE mesh for this pyramid simulation is shown in Fig. 6.29. 1058 `RESS` elements are used to model the blank. Due to the symmetry of the shape, only half of the sheet is meshed. Rotational boundary conditions (Fig. 6.30(b)) are imposed[12]. Hence, any node O or P identified in Fig. 6.30(a) follows

[12] In Lagamine this is done using the BINDS elements.

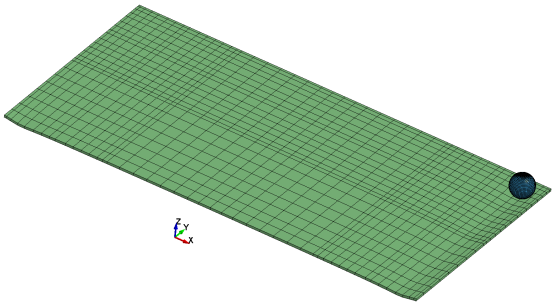

Figure 6.29: FE mesh considered for the simulation of the pyramid test.

Eq. 6.4.1 for its displacements.

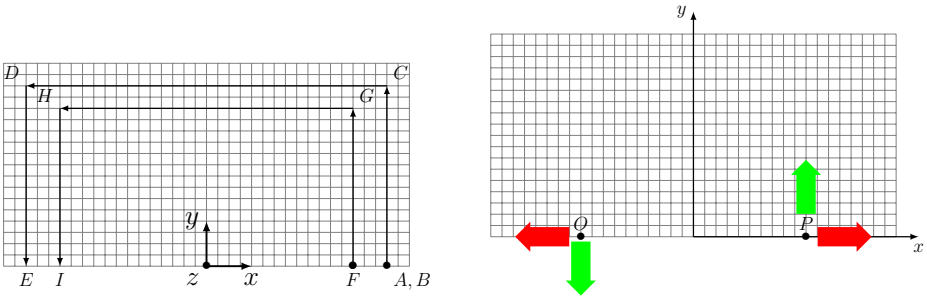

(a) Toolpath scheme. The letters are referenced in Table 6.8.

(b) Rotational boundary conditions.

Figure 6.30: Scheme of the toolpath for two contours and the rotational boundary conditions for the pyramid simulation. The first contour is defined by: A,B indent, then B-C, C-D and D-E (edges of the pyramid). The second contour: F indent, then F-G, G-H and H-I (edges).

The definition of the toolpath for the simulation should be as close as possible to the experiments, but some simplifications are introduced. For instance, the forming tool is modeled as a rigid sphere and no friction is applied between the tool and the sheet. Like for the line test, no time-dependent law is considered so the simulation time can be different compared to the real process to decrease the CPU time. Fig. 6.30(a) depicts the toolpath seen from the top, with each tool position defined in Table 6.8. The tool center at the beginning of the first contours are specified in Table 6.9. This is avoided by defining a non linear path. In the pyramids, the change of angle from 60° to 30° occurs after contour 60 (at 600 s, because every contour lasts 10 s). The simulation is completed after the tool removal (unloading step) at 901 s.

As the experimental pyramid is clamped, the nodes along the outer part of the mesh are completely fixed (in all three translations). Along the symmetry axis a link between the displacements is imposed, also known as rotational boundary conditions (Bouffioux et al., 2010; Guzmán et al., 2012b; Henrard et al., 2010). Hence, the displacements of the nodes O and P of Fig. 6.37(b) are related through

Table 6.8: Tool position during the simulation of the pyramid. The depth depends on the step-down being different for pyramid A and B. The coordinates are defined in Table 6.9.

	Time (s)	Position	Depth	X [mm]	Y [mm]
Contour 1	0	A	0	X1	0
	1	B	Δz	X1	0
	3.25	C	Δz	X1	X1
	7.75	D	Δz	-X1	X1
	10	E	Δz	-X1	0
	10.01	B	Δz-1	X1	0
	10.02	B	Δz	X1	0
Contour 2	11	F	2*Δz	X2	0
	13.25	G	2*Δz	X2	X2
	17.75	H	2*Δz	-X2	X2
	20	I	2*Δz	-X2	0
	20.01	F	2*Δz-2	X2	0
	20.02	F	2*Δz	X2	0
	⋮	⋮	⋮	⋮	
	900	...	90*Δz	-X90	0
	901	...	90*Δz-90	-X90	0

Table 6.9: X coordinate of the tool center during the simulation of the SPIF pyramid.

	Coordinate [mm]
X1	84.5
X2	83.5
X3	82.881
X4	82.304
X5	81.727
⋮	⋮
X59	49.972
X60	49.395
X61	48.426
X62	46.998
X63	45.570
⋮	⋮
X90	8.449

the following equations:

$$\begin{aligned}(u_x)_O &= -(u_x)_P \\ (u_y)_O &= -(u_y)_P \\ (u_z)_O &= (u_z)_P\end{aligned} \tag{6.4.1}$$

where $\boldsymbol{u}$ is the vector of nodal displacements.

6.4.2 Shape and force predictions

Material points in a cut of the sheet in the X-Z plane in the undeformed sheet (see Fig. 6.28(b)), starting from X =10 mm and ending in X =80 mm, are selected and their Z positions measured. They are extracted at the end of three different contours, just before the tool is lifted to move to another contour (point E and I in Fig. 6.30(a)). The experimental and numerical comparison is depicted in Fig. 6.31(a). It should be noted that the numerical and experimental curves are intentionally shifted to coincide at $X \approx$80 mm and $Z \approx -10$ mm. The reason is that near the backing plate it is very difficult to extract data, and there is no accurate information about the shape between $X \approx$80 mm and $Y \approx$90 mm. This *transition zone* between the clamped part and the pyramid wall has been previously considered by Eyckens et al., 2010. The DIC also cannot retrieve information about the point near $X \approx$0 mm at the end of the process.

The predictions up to the 60th contours are in very good agreement with the experimental results. The deviation between the deformed sheet and the nominal shape is correctly reproduced by the model, showing that the deformation mechanisms (springback, through thickness shear,...) are adequately captured during the simulations.

From the 60th to the 90th contours, i.e. corresponding to the second slope of the pyramid, a very small discrepancy from the experimental results can be noticed on the upper part of the deformed pyramid. Overall, the prediction of the FEM is quite satisfactory. It appears that, due to the change in the slope of the tool path, the deviation from the nominal shape is larger after the sixtieth contour because of two effects: a usual *springback* (sheet displacement after tool removal) as well as a *tent effect* due to the force applied on the already formed shape of the first angle pyramid, during the forming process of the second angle pyramid. The tent effect can imply only elastic or both elastic and plastic strains. In the present case, plastic strain is involved. The interested reader is referred to Behera et al., (2011), Guzmán et al., (2012b), and Sena et al., (2015) for more information about this geometry inaccuracy. These phenomena are well captured by the model.

Force prediction is shown in Fig. 6.31(b) for four different material models. To simplify the visualization of the results, an average value of the numerical force evolution is considered in each contour (Bouffioux et al., 2010), calculated between points C and D in Fig. 6.30(a) for the first contour, points G and H for the second contour, etc.. The results are presented in Fig. 6.31(b), showing a clear difference between the forces when forming the 60° pyramid and the 30° pyramid. Guzmán

et al., (2012b) showed that the Aerens et al., (2009) formula (initially proposed for cones) works also for pyramids. Aerens et al., (2009) formula is further discussed in section 6.5.2. This formula predicts a (steady) force of Fz_s =1158.01 N for this DC01 steel for the 60° pyramid, which is clearly below the forces obtained from the FE simulation. This is a well known limitation of the current FE simulations, as documented in section 6.1.1.5.

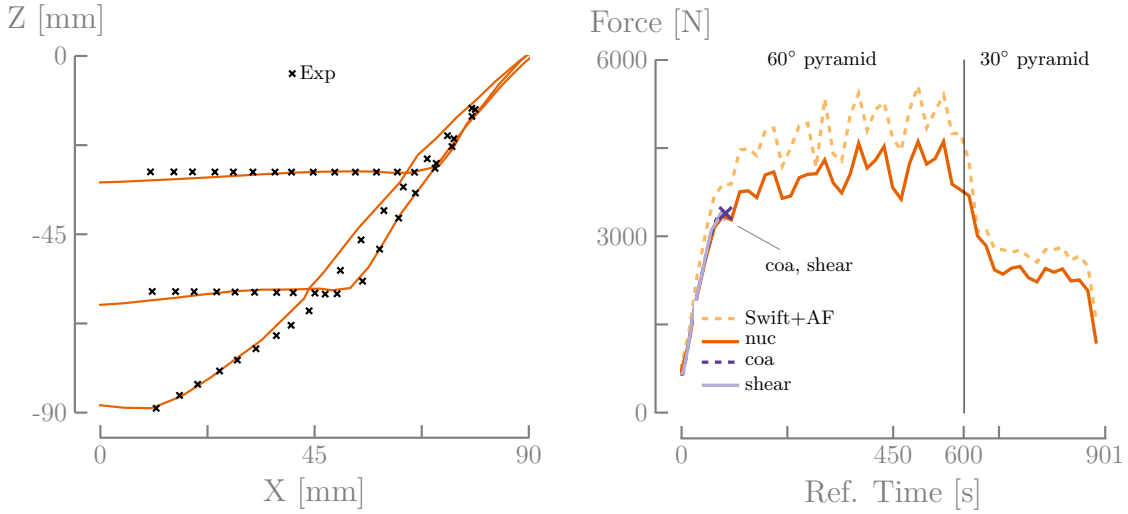

(a) Comparison between experimental and numerical curves in different contours. The selected experimental points and mesh nodes corresponds to a cut along $Y = 0$ in the undeformed mesh.

(b) Force predictions using four different material models.

Figure 6.31: FE predictions for the shape and force.

The most interesting observation of these simulation from the damage point of view is that the set of parameters using coalescence (`coa` and `shear`) stopped before the implicit simulations were completed. The reason is that porosity in one IP reaches $f = f_u$, in a small zone in the corners, as shown in Fig. 6.34(a). The material stiffness then abruptly decreases leading to the final failure. Fig. 6.32(a) to Fig. 6.33(a) shows the porosity distribution at different coalescence stages. f_{cr} is reached in a early stage of the simulation (t =33 s). Then, Fig. 6.33(a) confirms that porosity localizes near the corners which is expected due to the high degree of deformation. Fig. 6.34(a), retrieved at the last stages of coalescence, shows an abrupt increase of the porosity in one particular element in the right corner. It is interesting to compare this porosity distribution with the equivalent (macroscopic) plastic strain ϵ_q distribution, shown in Fig. 6.32(b) to Fig. 6.34(b). ϵ_q is more evenly distributed, with higher deformation in the corners but without strong gradients as it is the case for the porosity. In overall, the FE model wrongly predicts material failure for this material and geometry. The reasons will be further explored in the next section for different cone angles.

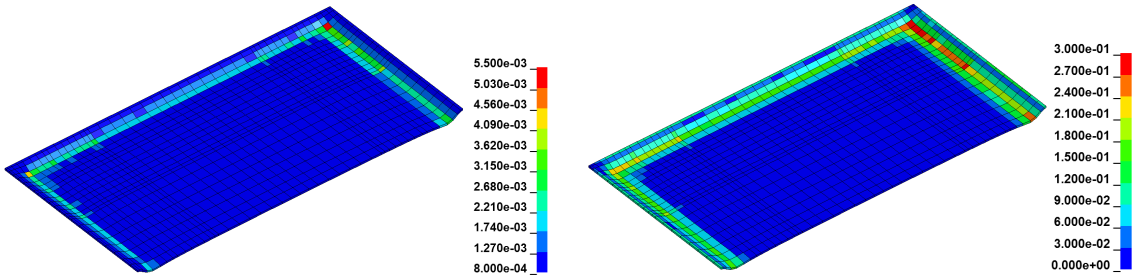

(a) Porosity. (b) Equivalent plastic strain.

Figure 6.32: Porosity and equivalent (macroscopic) plastic strain distribution at t =33 s, when one IP reaches $f_{\max} = f_{cr}$ =0.0055.

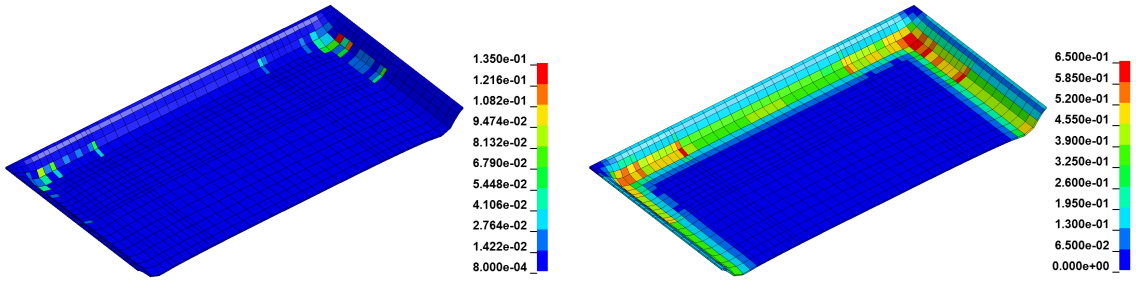

(a) Porosity. (b) Equivalent plastic strain.

Figure 6.33: Porosity and equivalent (macroscopic) plastic strain distribution at t =83 s, when one IP reaches $f_{\max} = f_F$ =0.135.

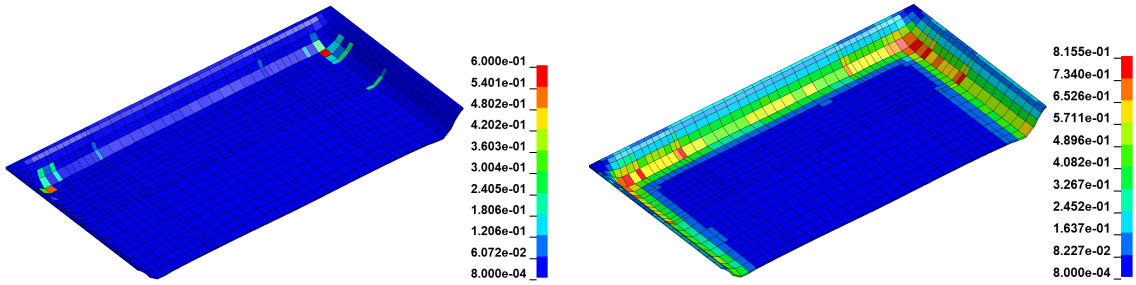

(a) Porosity. (b) Equivalent plastic strain.

Figure 6.34: Porosity and equivalent (macroscopic) plastic strain distribution at t =103 s, when one IP reaches $f_{\max} = f_u$ =0.6.

6.5 Cone test

Fig. 6.35 shows a schematic view of a cone of wall angle α and 30 mm depth. As mentioned in the literature review, the wall angle is used as a measurement of the formability limits of SPIF for a determined material. For the DC01 steel of 1.0 mm thickness, 67° is the (experimental) maximum achievable wall angle without failure. It was identified by the KULeuven team (Behera, 2013; Verbert, 2010) by forming successive cones to accurately identify this angle, after a first set of experiments where α is systematically increased. In this section, SPIF cones with different wall angles are simulated and the porosity field is analyzed. The experimental measurements (forces and shapes) are not available for these cones, but here the goal is to study the influence of the wall angle on the damage development.

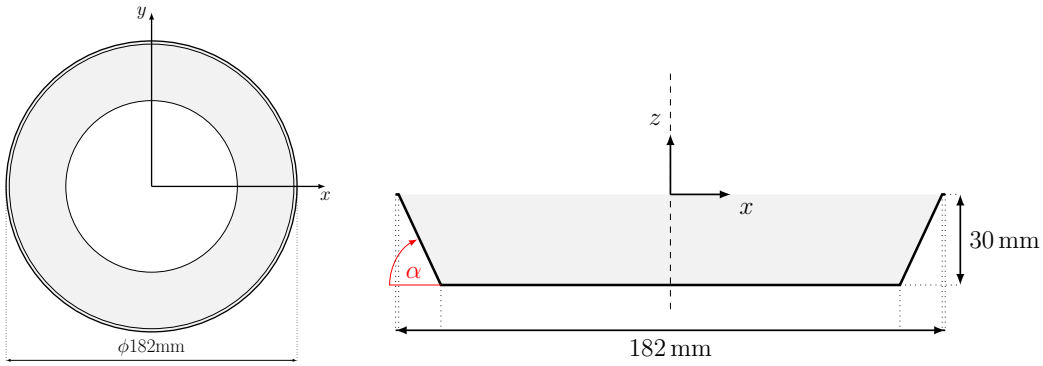

(a) Top view. (b) Front view.

Figure 6.35: Target cone geometry.

6.5.1 FE simulation

Due to the complexity of the material model and the SPIF FE simulation itself, different FE meshes were analyzed in order to reduce CPU time while keeping accuracy. Fig. 6.36 shows a 90° angle pie with 1492 `RESS` elements which lead to the best results. The 45° angle pie presented border effects while the simulation time for 180° angle pie was too large (several days).

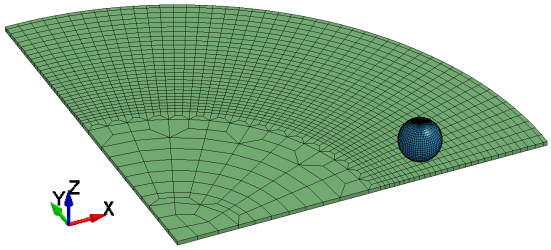

Figure 6.36: FE mesh considered for the simulation of the cone test.

The toolpath is composed of 60 contours with a step down of 0.5 mm between two successive contours. Fig. 6.37(a) depicts the toolpath seen from the top for two contours. Each tool position is defined in Table 6.10. The tool center positions at the beginning of the first contours are specified in Table 6.11.

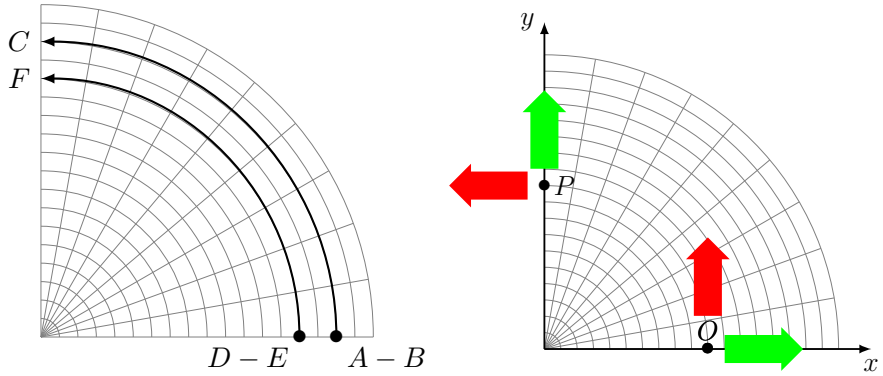

(a) Toolpath scheme. The letters are references in table 6.10.

(b) Rotational boundary conditions.

Figure 6.37: Scheme of the toolpath and the rotational boundary conditions for the cone simulation.

Table 6.10: Tool position during the simulation of the cone. The X coordinate is defined in Table 6.11 for a 67° cone.

	Time [s]	Position	Depth	X [mm]	Y [mm]
Cont. 1	0	A	0	X1	0
	1	B	Δz	X1	0
	10	C	Δz	0	X1
	10.001	B	Δz	X1	0
Cont. 2	11	D	2*Δz	X2	0
	20	E	2*Δz	0	X2
	20.001	D	2*Δz	X2	0
Cont. 3	21	F	3*Δz	X3	0
	30	G	3*Δz	0	X3
	30.001	F	3*Δz	X3	0
	⋮	⋮	⋮	⋮	⋮
	600	...	60*Δz	0	X60
	601	...	60*Δz-10	0	X60

As the experimental cone is clamped, the nodes along the outer circumferential part of the 90° pie mesh are completely fixed (in the three translations). In the other edges, rotational boundary conditions are imposed. Hence, the displacements of the nodes O and P in Fig. 6.37(b) are related following Eq. 6.4.1.

Table 6.11: X coordinate of the tool center during the SPIF 67° cone simulation.

	Coordinate [mm]
X1	85.642
X2	84
X3	82.786
X4	82.3197
X5	81.8535
X6	81.3872
⋮	⋮
X60	56.2093

6.5.2 Force prediction

As experimental measurements are not available for this geometry, the predicted force is assessed using Aerens et al., (2009) formula. The axial *steady*[13] force in the axis of the tool in a general material is calculated using the following equation:

$$Fz\_s = 0.0716 R_m t^{1.57} {d_t}^{0.41} \Delta h^{0.09} (\alpha - d\alpha) \cos(\alpha - d\alpha) \tag{6.5.1}$$

where R_m is the tensile strength, t is the sheet thickness, d_t is the tool diameter and α is the wall angle in degrees. This is a corrected version of the original formula proposed by Aerens et al., (2009), using an empirical correction of $d\alpha$ =2.86 introduced later by the article's author [14]. Δh is the scallop height, related to the depth increment Δz through the following equation:

$$\Delta h = \frac{1}{d_t} \left(\frac{\Delta z}{2 \sin \alpha} \right)^2 \tag{6.5.2}$$

For the particular case of the DC01 steel, Aerens et al., (2009) proposed the following equation relation for the *peak* force:

$$Fz\_p = 40.7 t^{1.42} d_t^{0.48} \Delta h^{0.12} (\alpha - d\alpha)^{0.73} \tag{6.5.3}$$

and for the steady force:

$$Fz\_s = 16.26 t^{1.35} d_t^{0.48} \Delta h^{0.12} (\alpha - d\alpha)^{1.11} \cos(\alpha - d\alpha) \tag{6.5.4}$$

Eq. 6.5.3 and Eq. 6.5.4 assumes that for the DC01 steel the (reference) tensile strength is equal to R_m =357 MPa. In the batch analyzed in this thesis, the measured tensile strength is R_m =312.26 MPa as shown in chapter 2. The results obtained for different wall angles are shown in Table 6.12, considering both tensile strengths. The difference between the first and third row of Table 6.12 (or between Eq. 6.5.1 and Eq. 6.5.4) is around 15%, which is close to the same difference

[13] Aerens et al., (2009) observed that the force evolution during the cone test has a *peak* during the first contours and then decrease to a *steady* level until the end.

[14] Email from Aerens, Friday 19 October 2012.

Table 6.12: Steady and peak force for the DC01 steel cone predicted using the Aerens et al., (2009) formula at different wall angles.

Equation	R_m [MPa]	α =30° [N]	α =47° [N]	α =48° [N]	α =60° [N]	α =67° [N]
Fz_s (Eq. 6.5.1)	312.26	995.85	1219.70	1222.49	1158.01	1033.53
Fz_p (Eq. 6.5.3)	357	-	-	-	1326.35	1422.13
Fz_s (Eq. 6.5.4)	357	1095.26	1383.27	1388.52	1337.49	1204.57

between the reference tensile strength Aerens et al., (2009) and the one measured in this work. This proves that the general Eq. 6.5.1 is adequate for the DC01 steel batch used in the current thesis.

In order to explain the premature prediction of material failure found for simulation of the pyramid test, several FE simulations were carried out on SPIF cones with different wall angles. The FE predictions of the force are shown in Fig. 6.38 for four selected angles, two of them predicting material failure. The GTN

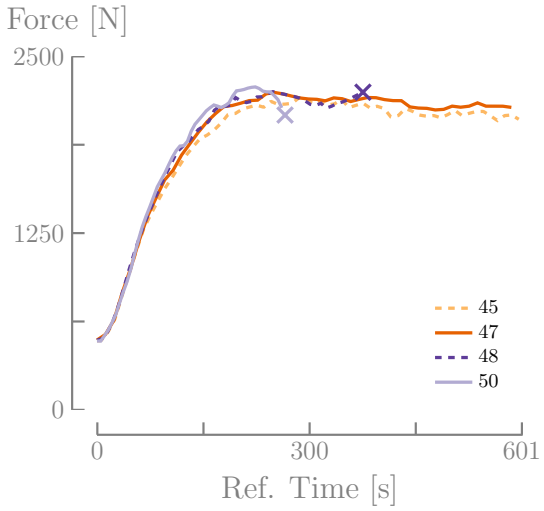

Figure 6.38: Axial force predictions for the cone test for different wall angles. The cross denotes the moment where $f = f_u$ in one FE.

model predicts a failure for a 48° cone. The model underestimates the failure angle, since for this material and thickness the (experimental) critical wall angle is 67°. This issue will be analyzed in the next section. Compared to the results of Table 6.12, the simulations results of Fig. 6.38 overpredict the force in more than 100%.

The issue of the force prediction overestimation was already discussed in section 6.1.1.5. In the previous section, only the force of the line test (section 6.3.3) was well predicted compared to experimental results. Both the pyramid and the cone FE prediction overestimate the reference force predicted by the Aerens et al., (2009) formula. The only difference in terms of the FE simulation among these geometries is the mesh configuration, with the cone and the pyramid using rota-

tional boundary conditions. Nevertheless, the force evolution in both the pyramid and the cone have different characteristics than those from the line test because of the toolpath. The finite element formulation can also play a role on the force prediction. Guzmán et al., (2012a) showed using the `SSH3D` solid-shell element for a line test simulation, that the element flexibility modified with EAS modes can severely decrease the force level. This was later confirmed for a pyramid test simulation by Duchêne et al., (2013). Sena et al., (2013) and Sena, (2015, chapter 5) showed using the `RESS` finite element that the hardening law has an important effect on the force level. The results using the Voce law are better the Swift law, overpredicting the force in only 30% for an AA7075-O aluminum alloy. In this case, the FE force prediction for aluminum alloys is better compared to the prediction for the steel using the `RESS` FE.

6.5.3 Analysis of fracture prediction

It is clear in Fig. 6.38 that the GTN model predicts fracture on a early stage. This wrong prediction of fracture could be due to different factors:

1. The attained force level (100% higher than the Aerens et al., (2009)).
2. Bad modeling of the deformation mechanisms. Localization and thinning play an important role.
3. Limitations of the GTN model.

In this section, each point will be analyzed separately.

1. Regarding the force, a bad force prediction does not necessarily mean a bad damage prediction. Indeed, the predicted force is much higher than the experimental force predicted by the Aerens et al., (2009) formula. If the reaction force predicted by the FE simulations was the reason why damage increases too quickly, then the 47° cone should have failed too. Therefore, the bad force prediction of the FE is not the reason of the premature failure.
2. Localization and thinning are a crucial aspect of material formability (see section 6.1.4). The shape (and thickness) distribution is correctly predicted by the solid shell, as shown in Fig. 6.23(b). This fact is also supported by previous simulations using the solid-shell element formulation eg. Duchêne et al., 2013; Sena et al., 2013. Localization is nonetheless a different aspect of the deformation. The limitations for strain localization and fracture strain prediction using the GTN model were discussed in section 5.5.2. Despite these limitations, it is not straightforward to say that a good prediction of the strain evolution will allow a good prediction of the onset of failure. Malcher et al., (2012) showed that (in general) the GTN model do not predicts the fracture strain accurately, but it behaves relatively well under high and low triaxialities for the prediction of the force level and the displacement at fracture. Fig. 6.39 presents the equivalent plastic strain distribution for the 47° and 48° angle cones. The 47° is the limit case predicted by the

model that does not fail. In the figure it is clear that strain does not localize and the plastic strain is evenly distributed, while for the 48° cone the strain localization is clear before failure. The maximum value of plastic strain in Fig. 6.39(b) is around 0.8, which is below the usual values found on SPIF which are easily over 1.0. It is possible to observe a similar trend in the porosity distribution shown in Fig. 6.40. For the 48° cone, failure is precede by localization of the equivalent plastic strain and porosity. The 47° cone does not fail because $f < f_F$ =0.135, so strain localization is triggered by the coalescence criterion of the GTN model.

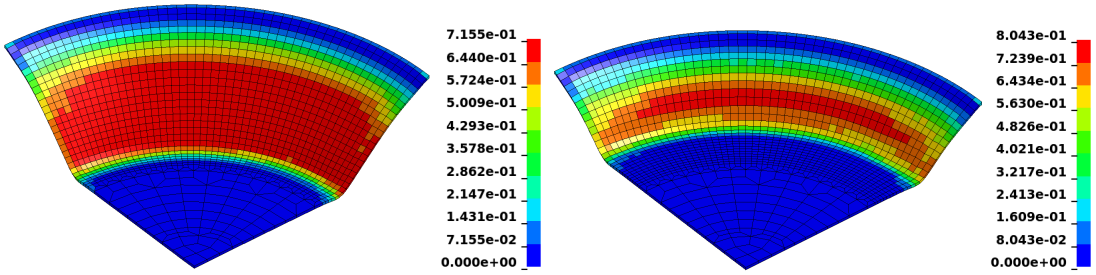

(a) 47° cone at the end of the simulation. (b) 48° cone at fracture.

Figure 6.39: Equivalent plastic strain distribution for the cone test simulation.

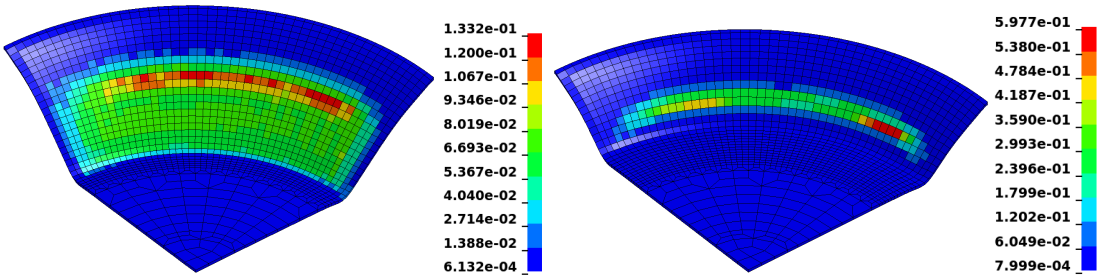

(a) 47° cone at the end of the simulation. (b) 48° cone at fracture.

Figure 6.40: Effective porosity distribution for the cone test simulation.

3. To further analyze the fracture prediction of the GTN model, a comparison will be given with the article by Malhotra et al., (2012) which predicts fracture for a SPIF cone and funnel quite well. Malhotra et al., (2012) used a fracture model developed by Xue, (2007). This model leads to good results when predicting the force and the depth at which fracture happens. As shown in the previous section, the GTN model extended to shear fails to predict the force level and the onset of fracture. Despite both models have two similar internal variables (the equivalent plastic strain and the damage parameter), in the Xue, (2007) model the damage evolution is function of the ratio of plastic strain and the fracture strain (the *self-similarity* hypothesis). This represents a strong coupling between damage and the plastic

strain. As discussed in section 5.5.2, in the GTN model localization is only triggered by the damage variable and there is no coupling with material hardening. Another difference is that both models were developed with different purposes. For instance, the Gurson, (1977a) model was originally developed to represent the deterioration of a porous material (see chapter 3), based on unit-cells calculations. On the contrary, the Xue, (2007) model is based on a theory where the plastic damage incorporates all the three stress invariants. Here the scope is not only the material deterioration but also the determination of the fracture envelope.

Summarizing, the most probable reason of the premature prediction of material failure by the GTN model is an inadequate coalescence criterion. Indeed, it has often been discussed that f_{cr} is not a sufficient criterion to describe the initiation of fracture (eg. Malcher et al., 2014). Triggering failure based only in the damage parameter (effective porosity) could be risky considering the complexity of the stress and strain path found on SPIF. The inherent limitations of the GTN model to represent strain hardening can also play a role.

6.6 Conclusions

In this chapter, an evaluation of the GTN model extended to shear is performed. A review of the state-of-the-art about SPIF, covering geometrical accuracy, deformation mechanism, formability and damage is also presented. The line test is used to validate the simulations by comparing force and shape prediction with experimental results. Then, a two-slope pyramid is simulated to evaluate the performance of the solid-shell formulation. In general, the results of the shape prediction are in good agreement with the experimental results, both for the line and pyramid test. The good results obtained for the line tests are, unfortunately, not replied on more complex shapes like the cone and the pyramid. For example, the force prediction is too high compared to experimental values, probably because of the boundary conditions. This is an issue that requires more research, as the deformation mechanism is highly dependent on the process parameters so conclusions derived from some geometries are not necessarily repeatable in other shapes. On the other hand, the GTN model is capable to detect failure in a pyramid and cone, but the prediction is too premature compared to the experimental failure angle for the same material and geometry. After performing several SPIF cones FE simulations at different wall angles, it is concluded that the GTN model underestimates the reference failure angle. The most probable reason for bad failure modeling is the coalescence model, which depends only on the damage parameter (porosity). Moreover, the GTN model uncouples this damage parameter with hardening. Other models like the one proposed by Xue, (2007), which predicts failure in the SPIF process quite well, couples the damage evolution and failure with the plastic strain. This research indicates that the current failure mode happening cannot be predicted by the classical assumptions of the GTN model. Even if the damage model is capable to predict the loss of the loading

capacity for notched specimens, the stress and strain path found on SPIF are different and certainly more complex.

Chapter 7

Conclusions and perspectives

7.1 General conclusions

In this thesis, a damage model has been developed and implemented in the FE code LAGAMINE. It was experimentally characterized and then applied to predict failure in the SPIF process. Formability of SPIF has been extensively studied before but little has been done regarding the damage evolution leading to final fracture. This dissertation reports the developments and results in detail through a series of chapters, each one covering different contributions to the fields of damage modeling and sheet metal forming analysis.

Chapter 2 describes the selection of the material and the characterization of the plastic behavior through mechanical tests and FE simulations. Since the elasto-plastic behavior precedes the damage behavior, a correct identification of plasticity is important for the modeling of damage. The criterion of the material selection is primarily based on the ISF application. The chosen material, a DC01 ferritic steel sheet, was characterized using different mechanical tests. Material parameters for plastic model considering the anisotropic behavior and hardening were identified using optimization algorithms. The results show that the material exhibits an anisotropic behavior at 45° of the RD during the tensile test, but it is mainly isotropic during the plane strain tests. The Hill, (1948) yield locus is able to capture this anisotropic behavior quite well despite its limitations. Moreover, the simplicity of this model is desirable considering further theoretical developments (viz. extensions of the GTN model) and CPU time (viz. sheet metal forming simulations). The Swift, (1952) law satisfactorily describes the isotropic hardening behavior. The kinematic hardening presents a clear work-hardening *stagnation*, which is a phenomenon that cannot be represented using the classical Armstrong and Fredrick, (1966) model. Nonetheless, for sake of simplicity the A-F model will be chosen because describing the stagnation would required a more complex model not compatible with implicit simulations of SPIF. In general, the methodology used in this chapter can be considered as an application of the one developed by Flores, (2005) and Gilles, (2015) for plastic characterization. Hence, based on the presented results, the methodology can be considered acceptable for the DC01 steel sheet characterization.

Chapter 3 explores the historial developments and physical roots of the Gurson model. The importance of this chapter is that contextualizes extensions of the Gurson model that will be used throughout the thesis. Among them, the Gurson-Tvergaard-Needleman (GTN) which includes the three stages of damage evolution leading to fracture: void nucleation, growth and coalescence. Another review is presented regarding the limitations of the GTN model to simulate shear dominated cases i.e., in low stress triaxialities. Improvements of the GTN model to incorporate shear-type softening are thus presented. Extension based on microscopic observations are also briefly presented, directed towards specific materials. As described in chapter 2, an important part of the plastic behavior description goes into the anisotropic and hardening modeling. In the case of the GTN model, extensions including matrix anisotropy and mixed hardening are also considered. Despite the numerous extensions proposed previously, models considering all the mentioned extensions are not widely available throughout the literature. Hence, the next challenge is to implement this advanced model within a FE code.

Chapter 4 details the implementation of the extensions of the Gurson model presented in chapter 3. It covers in great detail the required mathematical developments (also covered in **Appendix B**) and the general framework of the implementation algorithms. The classical return-mapping and the implicit backward Euler algorithms, which are the adopted scheme, are described. The original feature of this scheme is that all the variables are integrated in an implicit way based on the projection algorithm, while the consistent tangent matrix is calculated analytically. The implementation is validated by numerical results of homogeneous cases found in the literature. Nucleation, coalescence and shear extensions are accurately validated, as well as plastic anisotropy and kinematic hardening. The good results of the validation allow concluding that the model can be used in more complex simulations. Moreover, due to the range of extensions several phenomena can be explored and their results brings other point of view than unit-cell calculations, the Lemaitre, (1985) damage model, fracture criteria, etc.

Chapter 5 proposes a methodology for damage characterization of the DC01 steel sheet. This methodology includes microscopic and macroscopic measurements, based on a test campaign with specially designed specimens e.g., notched specimens, a specimen with a central hole and special shear specimen designed by Peirs et al., (2011). The experimental microscopic measurements show results that are not representative of the actual damage, but they give a qualitative estimation of the physical mechanism of fracture. The studies conducted in previous chapters allow performing the required simulations for the identification of the material parameters of the GTN model extended to shear. The results of the experimental mechanical tests are used to find the material parameters for nucleation, coalescence and shear. Because of the strong nonlinearity of the equations plus the inherent experimental errors, a single set of results able to match all the performed tests was not possible to obtain. The limitations linked to the model formulation are discussed. In particular, it is found that the GTN model is not

able to predict the strain localization (measured by DIC) due to the heuristic way used to introduce hardening into the matrix behavior. Even with these limitations, the GTN model captures coalescence and failure within an acceptable range. Indeed, the material also relatively works well for materials like a bulk Ti-6AL-4V alloy, as presented in the **Appendix D**.

Chapter 6 presents the final evaluation of the GTN model. Using the material parameters identified in chapter 5, several SPIF FE simulations are performed and their results discussed. Here the scope is to evaluate if the GTN model extended to shear is able to predict failure. A review of the state-of-the-art about SPIF, covering geometrical accuracy, deformation mechanism, formability and damage is also presented. The first simulation is the SPIF line test. The numerical simulation is validated thanks to experimental results provided by the KULeuven team. A deep analysis of the state variables show that each vertical indent step increases the strain and triaxiality in a way that the major contribution to damage development comes from the void growth. The next validation is performed using a two-slope pyramid test, where the shape is not easily captured by FEs in the zone near the angle transition. If coalescence is not considered in the simulations, the shape is well predicted but the force is overestimated compared to the force calculated using the Aerens et al., (2009) formula. This discrepancy is explained due the (rotational) boundary conditions of the mesh or the (solid-shell) FE formulation. The simulations using the GTN model plus coalescence predict failure for this pyramid, which is not experimentally observed. To further analyze this anomaly, SPIF cone FE simulations are performed at different wall angles. The GTN model predicts failure at 48°, which underestimates the failure angle for this geometry and thickness, which is experimentally measured as 68°. It is concluded that the GTN model fails to predict failure on SPIF due to limitations of the GTN model. Notably, in the coalescence model the porosity is the only parameter triggering the onset of localization. Other publications (cf. Malhotra et al., 2012) have shown the importance of strain localization and thinning. Moreover, as shown in chapter 5, the GTN model does not correctly predict strain localization.

Summarizing, the final goal of predicting failure for the SPIF process was not possible to achieve. The GTN model extended to shear presents inherent flaws that prevent an accurate prediction of the failure angle for a SPIF cone. Hence, an extensive research on the damage mechanisms leading to fracture for SPIF cannot rely (only) on the GTN model. Nevertheless, during the development of this thesis a robust implementation of the GTN model into the FE code Lagamine was done. The parallelization of the Lagamine code was successfully updated for new Walloon clusters (covered in **Appendix E**). An extensive experimental database of microscopic and macroscopic measurements for the DC01 steel sheet is also available for further research. At last but not least, the solid-shell elements are consolidated as an useful tool to simulate the SPIF process (viz. Sena, 2015).

7.2 Perspectives for future work

The main challenge is to predict failure in the SPIF process using simulations relying on the GTN model. Despite other limitations of the GTN model, coalescence is the hardest stage to be captured by the model. The classical coalescence model of Tvergaard and Needleman, (1984) is insufficient to correctly predict material failure, probably because it lacks a coupling between damage (porosity) and hardening. Instead, coalescence in the GTN model is triggered based solely on the porosity evolution. Hence, it is recommended that further analysis concentrates on the description of this particular stage of damage evolution (see for instance, Benzerga and Leblond, 2010). Another damage model (viz., Xue, 2007) can also help to predict failure better in the SPIF process.

SPIF FE simulations can also be improved. Recently, the remeshing method implemented in the LAGAMINE code was successfully validated for solid-shell elements and plasticity models in Sena, (2015) PhD thesis. The damage model implemented in LAGAMINE has different state variables than the plasticity models, hence the data transfer method between old and new elements must be carefully studied. Specifically, the coalescence stage is sensitive to the mesh size presenting a strong challenge to remeshing techniques. Other SPIF optimization techniques, such as the sub-domain decomposition and subcycling, are interesting to study in the context of damage modeling. Both techniques differentiate between the non-linearities in the tool neighborhood and the rest of the mesh. In particular, sub-cycling use larger times steps in coarse elements. In this thesis, it is demonstrated through the parameter `NINTV` that the time step can have important consequences on the results.

The solid-shell element formulation can also be improved for SPIF FE simulations. The effect of the EAS modes on the force evolution is known and a similar analysis can be done for damage modeling using the `SSH3D` FE. In this thesis, SPIF simulations were performed using the `RESS`. The study of the effect of the FE formulation (EAS modes and number of integration points through-thickness) on damage evolution during the SPIF process seems attractive. Recently, Ben Bettaieb et al., (2015) compared both elements concluding that `SSH3D` is more versatile in terms of the EAS modes choice and integration scheme. On the contrary, `RESS` is more efficient than `SSH3D` is terms of CPU time.

In the field of material modeling, there is still relevant work to be done. An accurate simulation of work-hardening *stagnation*, observed in cyclic tests of the DC01 steel was not achieved because it requires a more complex model than the classical from Armstrong and Fredrick, (1966). The effect of this phenomenon on the plastic behavior was analyzed by Flores et al., (2007) for a similar material (DC06 steel). However, the effect of stagnation on damage evolution is unknown. Using DIC measurements, strain localization is observed at the center of the notched specimens. This behavior is not well captured by the GTN model. It is hypothesized that this limitation is due to the heuristic way that hardening is

introduced into the matrix behavior. Further extensions of the GTN model can cover this topic and use the identified material parameters for validation.

In terms of the algorithm used to integrate the GTN model into the Lagamine FE code, further work can be focused on more academic oriented research. For instance, study the effect of the sub-intervals on the accuracy of the algorithm using iso-error maps or performance assessment in terms of the CPU time (see Ben Bettaieb et al., 2011c). Since models incorporating all the presented extensions (shear, anisotropy and mixed hardening) are not widely available, a sensitivity analysis can help to check the ability of the model to predict localization under different loading cases. Then, the results can be compared to unit-cell calculations found in the literature (viz., Tvergaard and Nielsen, 2010).

Appendix A

Stress measures and invariants

A.1 Stress measures

For an isotropic material, plastic yielding is dependent on the principal stresses and not on their magnitudes. In addition, the *representation theorem* (Salençon, 2005) establishes:

> Every (isotropic) function F of a symmetric tensor is expressed as a function of the tensor's invariant of the principal stresses.

In other words, the stress state of an isotropic material can be expressed in terms of the principal components of the stress tensor or the invariants.

$$F(I_1, I_2, I_3) = 0 \Rightarrow F(\sigma_1, \sigma_2, \sigma_3) = 0 \tag{A.1.1}$$

Note the direction of the implication, given the lack of generality in the opposite direction. Using the stress invariants instead of the stress tensor components is useful in the study of yielding or fracture. They are dimensionless scalar values which can have different physical interpretations. For example, the first stress invariant I_1 defines the hydrostatic (spherical) stress while the second invariant of the deviatoric stress J_2 represents the distortional energy defining yielding in isotropic materials (von Mises criterion). Other scalar metrics can also be related to invariants, such as the triaxiality and the Lode, (1926) parameter. In this section, we define the triaxiality and the Lode angle both in the stress invariants sense and as a vector in the stress space.

A.1.1 Triaxiality

Triaxiality has traditionally been used as a metric to characterize the stress state. It can be defined as the ratio between the hydrostatic (first stress invariant) and deviatoric (second deviatoric stress invariant) part on the stress state. If the second deviatoric stress invariant is defined as:

$$J_2 := \frac{1}{3}\sigma_{eq}^2 \tag{A.1.2}$$

then triaxiality can be expressed as:

$$T(I_1, J_2) = \frac{\sigma_m}{\sigma_{eq}} = \frac{1}{3}\frac{\sigma_{ii}}{\sigma_{eq}} \tag{A.1.3}$$

A.1.2 Stress tensor in the stress space and Lode angle

A stress tensor can be graphically represented in the principal stress space[1] as a position vector $\overrightarrow{OP}$, as depicted in Fig. A.1. A stress state can be split in a

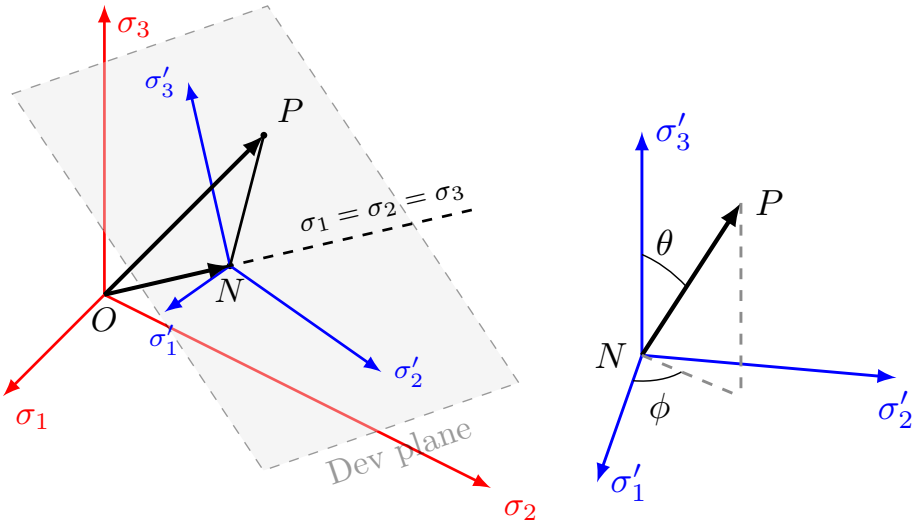

(a) Principal stress plane. (b) Deviatoric plane.

Figure A.1: Stress state represented in the Haigh-Westergaard space.

deviatioric and hydrostatic part:

$$\overrightarrow{OP} = \underbrace{\overrightarrow{ON}}_{\text{Hydrostatic}} + \underbrace{\overrightarrow{NP}}_{\text{Deviatoric}} \tag{A.1.4}$$

where $\overrightarrow{ON} \perp \overrightarrow{NP}$ and $\overrightarrow{NP}$ lies on the deviatoric plane, defined as:

$$\sigma_1 + \sigma_1 + \sigma_1 = \sqrt{3}C \tag{A.1.5}$$

where C is a constant, with C =0 representing the so-called π-plane. $\overrightarrow{ON}$ lies on the hydrostatic axis, whose normal is given by the following basis:

$$\boldsymbol{n} = \left(\frac{1}{\sqrt{3}}, \frac{1}{\sqrt{3}}, \frac{1}{\sqrt{3}}\right) \tag{A.1.6}$$

Hence, $|\overrightarrow{ON}| = \overrightarrow{OP} \cdot \boldsymbol{n}$ is the projection of $\overrightarrow{OP}$ in the hydrostatic axis .

[1] Also known as the *Haigh-Westergaard* space, as proposed simultaneously by Haigh, (1920a,b) and Westergaard, (1920).

Experimental evidence shows that plastic yielding is independent of the hydrostatic stress (Bridgman, 1952), thus a yield criterion for metals can be conveniently represented in terms of the magnitude and the orientation of $\overrightarrow{NP}$. It can be shown that the magnitude of $\overrightarrow{NP}$ is $\sqrt{2J_2}$ and the orientation with respect to the deviatoric plane is called *Lode angle*, ξ_L:

$$\|\overrightarrow{NP}\|_2 = \|\boldsymbol{\sigma}_{\text{dev}}\|_2 = \sqrt{\boldsymbol{\sigma}_{\text{dev}} : \boldsymbol{\sigma}_{\text{dev}}} = \sqrt{2J_2} \tag{A.1.7}$$

As the Lode angle is defined between one axis and the $\overrightarrow{NP}$ vector, it can be necessary to get its projection on a determined axis of the principal stresses. For convenience, the following definition is taken about this projection on the first principal stress (with $\sigma_1 > \sigma_2 > \sigma_3$). This leads to (Khan and Huang, 1995; Voyiadjis et al., 2012):

$$\cos 3\xi_L = \frac{3\sqrt{3}}{2}\frac{J_3}{J_2^{\frac{3}{2}}} \qquad 0° \leq \xi_L \leq 60° \tag{A.1.8}$$

where ξ_L is the Lode angle in degrees. So, any stress state could be represented for the next equation (Khan and Huang, 1995):

$$\begin{pmatrix} \sigma_1 \\ \sigma_2 \\ \sigma_3 \end{pmatrix} = \frac{I_1}{3}\begin{pmatrix} 1 \\ 1 \\ 1 \end{pmatrix} + \frac{2}{\sqrt{3}}\sqrt{J_2}\begin{pmatrix} \cos\xi_L \\ \cos\left(120 - \xi_L\right) \\ \cos\left(120 + \xi_L\right) \end{pmatrix} \tag{A.1.9}$$

Eq. A.1.9 can also be written in terms of the equivalent von Mises stress and the triaxiality (Danas and Ponte Castañeda, 2012)[2]:

$$\frac{3}{2\sigma_{eq}}\begin{pmatrix} \sigma_1 \\ \sigma_2 \\ \sigma_3 \end{pmatrix} = \frac{3}{2}T\begin{pmatrix} 1 \\ 1 \\ 1 \end{pmatrix} + \frac{2}{\sqrt{3}}\sqrt{J_2}\begin{pmatrix} -\cos\left(\xi_L + 60\right) \\ -\cos\left(\xi_L - 60\right) \\ \cos\xi_L \end{pmatrix} \tag{A.1.10}$$

The stress components of the left side of the equation are called *normalized principal stress components*.

A.1.3 Other definitions of the Lode angle

In terms of the principal stresses space, the *Lode's parameter* is defined as:

$$\mu_\sigma(\boldsymbol{\sigma}) = \frac{2\sigma_2 - \sigma_1 - \sigma_3}{\sigma_1 - \sigma_3} \qquad -1 \leq \mu_\sigma \leq 1 \tag{A.1.11}$$

with $\sigma_1 > \sigma_2 > \sigma_3$. This was the original proposal by Lode, (1926) and is usually used by Civil engineers (Zhang et al., 2001). The relation between the Lode parameter and the Lode angle of Eq. A.1.8 is given by:

$$\mu_\sigma(\boldsymbol{\sigma}) = -\sqrt{3}\tan\xi_L \tag{A.1.12}$$

[2]Note the slightly difference due to the choice principal directions, using $\sigma_3 > \sigma_1 > \sigma_2$ instead.

Other authors (Coppola et al., 2009; Danas and Ponte Castañeda, 2012; Gao et al., 2009; Wierzbicki et al., 2005) prefer to use the parameter:

$$\xi = \cos 3\xi_L = \pm \frac{27}{2} \frac{J_3}{\sigma_{eq}^3} \qquad -1 \leq \xi \leq 1 \tag{A.1.13}$$

which is the same as Eq. A.1.8 using Eq. A.1.2. The $\pm$ sign depends on the author. Dunand and Mohr, (2011a) introduced the parameter ξ as the *normalized third invariant*. Danas and Ponte Castañeda, (2012) also used Eq. A.1.13 but multiplies it by -1. Li et al., (2011) in Eq. 4 wrongly defines ξ using σ_h instead of σ_{eq}. Another modification was introduced by Bai and Wierzbicki, (2008) and later used by Bai and Wierzbicki, (2009), Beese and Mohr, (2012), Dunand and Mohr, (2011a), and Malcher et al., (2012):

$$\overline{\theta} = 1 - \frac{6\xi_L}{\pi} = 1 - \frac{2}{\pi} \arccos \xi \qquad -1 \leq \overline{\theta} \leq 1 \tag{A.1.14}$$

This parameter is called *normalized Lode angle*. Nahshon and Hutchinson, (2008) slightly modified Eq. A.1.13 to be in the positive range, in order to incorporate it into their shear modified version of the GTN model:

$$\omega = 1 - \xi^2 = 1 - \left(\frac{27}{2} \frac{J_3}{\sigma_{eq}} \right)^2 \qquad 0 \leq \omega \leq 1 \tag{A.1.15}$$

with $\omega = 0$ for all axisymmetric stress states and $\omega = 1$ for pure shear plus a hydrostatic contribution. Voyiadjis et al., (2012) proposed:

$$\overline{\theta}_V = \sin 3\xi_L = \sqrt{1 - \frac{27}{4} \frac{J_3^2}{J_2^3}} \qquad 0 \leq \overline{\theta}_V \leq 1 \tag{A.1.16}$$

which is obtained by applying a Pythagorean identity to Eq. A.1.8.

Table A.1 shows the different definitions presented here and their references.

Table A.1: Table summarizing the Lode angle definitions that can be found in the current literature.

Definition	*Range*	*Reference*	*Name*
$\mu_\sigma = \frac{2\sigma_2 - \sigma_1 - \sigma_3}{\sigma_1 - \sigma_3}$	$-1 \leq \mu_\sigma \leq 1$	Lode, (1926)	Lode parameter
$\cos 3\xi_L = \frac{3\sqrt{3}}{2}\frac{J_3}{J_2^{\frac{3}{2}}}$	$0° \leq \xi \leq 60°$		Lode angle
$\xi = \frac{27}{2}\frac{J_3}{\sigma_{eq}^3}$	$-1 \leq \xi \leq 1$	Wierzbicki et al., 2005	Normalized third invariant
$\overline{\theta} = 1 - \frac{2}{\pi}\arccos\xi$	$-1 \leq \overline{\theta} \leq 1$	Bai and Wierzbicki, (2008)	Normalized Lode angle
$\omega = 1 - \xi^2$	$0 \leq \omega \leq 1$	Nahshon and Hutchinson, (2008)	
$\overline{\theta}_V = \sqrt{1 - \frac{27}{4}\frac{J_3^2}{J_2^3}}$	$0 \leq \overline{\theta}_V \leq 1$	Voyiadjis et al., (2012)	

A.2 Scalar tensor functions and their derivatives

A.2.1 Invariants

Given the characteristic polynomial of σ_{ij}:

$$\lambda_{1,2,3}{}^3 - I_1\lambda_{1,2,3}{}^2 + I_2\lambda_{1,2,3} - I_3 = 0 \tag{A.2.1}$$

Where $\lambda_{1,2,3}$ is a Lagrange multiplier (principal stresses) and $I_{1,2,3}$ are the invariants of the stress tensor, defined as:

$$I_1(\boldsymbol{\sigma}) = \mathrm{tr}\,(\sigma_{ij}) = \sigma_{xx} + \sigma_{yy} + \sigma_{zz} \tag{A.2.2}$$

$$I_2(\boldsymbol{\sigma}) = \frac{1}{2}\sigma_{ij}\sigma_{ij} = \sigma_{xx}\sigma_{yy} + \sigma_{xx}\sigma_{zz} + \sigma_{yy}\sigma_{zz} - \sigma_{xy}{}^2 - \sigma_{xz}{}^2 - \sigma_{yz}{}^2 \tag{A.2.3}$$

$$I_3(\boldsymbol{\sigma}) = \det\,(\sigma_{ij}) \tag{A.2.4}$$

In terms of the principal stresses:

$$I_1(\boldsymbol{\sigma}) = \sigma_1 + \sigma_2 + \sigma_3 \tag{A.2.5}$$

$$I_2(\boldsymbol{\sigma}) = \sigma_1\sigma_2 + \sigma_2\sigma_3 + \sigma_1\sigma_3 \tag{A.2.6}$$

$$I_3(\boldsymbol{\sigma}) = \sigma_1\sigma_2\sigma_3 \tag{A.2.7}$$

The deviatoric stress invariants are:

$$J_1(\boldsymbol{\sigma}) = 0 \tag{A.2.8}$$

$$J_2(\boldsymbol{\sigma}) = \frac{1}{3}\left(I_1^2 - 3I_2\right) \tag{A.2.9}$$

$$J_3(\boldsymbol{\sigma}) = \frac{1}{27}\left(2I_1^3 - 9I_1I_2 + 27I_3\right) \tag{A.2.10}$$

With the derivatives:

$$\begin{aligned}
\frac{\partial I_1}{\partial \boldsymbol{\sigma}} =& \boldsymbol{I} \\
\frac{\partial I_2}{\partial \boldsymbol{\sigma}} =& I_1 \boldsymbol{I} - \boldsymbol{\sigma}^T \\
\frac{\partial I_3}{\partial \boldsymbol{\sigma}} =& \det \boldsymbol{\sigma} \boldsymbol{\sigma}^{-T} \\
\frac{\partial J_2}{\partial \boldsymbol{\sigma}} =& \frac{2}{3} I_1 \frac{\partial I_1}{\partial \boldsymbol{\sigma}} - 3 \frac{\partial I_2}{\partial \boldsymbol{\sigma}} \\
\frac{\partial J_3}{\partial \boldsymbol{\sigma}} =& \frac{2}{9} I_1^2 \frac{\partial I_1}{\partial \boldsymbol{\sigma}} - 9 I_2 \frac{\partial I_1}{\partial \boldsymbol{\sigma}} - 9 I_1 \frac{\partial I_2}{\partial \boldsymbol{\sigma}} + 27 \frac{\partial I_3}{\partial \boldsymbol{\sigma}}
\end{aligned}$$

A.2.2 Lode angle definitions

Several definitions of the Lode angle can be found in the literature. Here we only present two, which were used in the shear extensions.

$$\omega(\boldsymbol{\sigma}) = 1 - \chi^2, \qquad g_\theta(\boldsymbol{\sigma}) = 1 - \frac{2}{\pi} \arccos \chi(\boldsymbol{\sigma})$$

Where:

$$\chi(\boldsymbol{\sigma}) = \frac{27}{2} \frac{J_3}{q^3}$$

With the derivatives:

$$\begin{aligned}
\frac{\partial \chi(\boldsymbol{\sigma})}{\partial \boldsymbol{\sigma}} &= \frac{27}{2q^3} \left(\frac{\partial J_3}{\partial \boldsymbol{\sigma}} - \frac{3 J_3}{q} \frac{\partial q}{\boldsymbol{\sigma}} \right) \\
\frac{\partial \omega(\boldsymbol{\sigma})}{\partial \boldsymbol{\sigma}} &= 1 - 2\chi(\boldsymbol{\sigma}) \frac{\partial \chi(\boldsymbol{\sigma})}{\partial \boldsymbol{\sigma}} \\
\frac{\partial g_\theta(\boldsymbol{\sigma})}{\partial \boldsymbol{\sigma}} &= 1 + \frac{2}{\pi \sqrt{1 - \chi^2}} \frac{\partial \chi(\boldsymbol{\sigma})}{\partial \boldsymbol{\sigma}}
\end{aligned}$$

Appendix B

GUR3Dext derivatives

Within the subroutine `GUR3DEXT`, the following nomenclature is used:

$$\alpha_1 = -3\frac{q_2\widetilde{p}}{\kappa\sigma_Y} \qquad \alpha_2 = \frac{2\widetilde{q}}{{\sigma_Y}^2}$$
$$\alpha_3 = 6\frac{q_1 q_2}{\kappa\sigma_Y} f^* \sinh\alpha_1 \qquad \alpha_5 = \frac{\mathbb{H} : \widetilde{\boldsymbol{\sigma}}_{\mathrm{dev}}}{2\widetilde{q}}$$

σ_m is used instead of p, so attention should be given to the minus signs in some equations. The jacobian matrix derivatives are complex to evaluate so an external software capable of symbolic derivation was needed. But before, the dependencies of the variables must be identified.

$$\widetilde{\sigma} = \widetilde{\sigma}(q, p, \boldsymbol{n}, \boldsymbol{X}), \qquad \Delta\boldsymbol{\epsilon}^P = \Delta\boldsymbol{\epsilon}^P(\Delta\epsilon_p, \Delta\epsilon_q, \boldsymbol{n})$$

$$\widetilde{p} = \widetilde{p}(p, \boldsymbol{X}), \qquad \widetilde{q} = \widetilde{q}(q, \boldsymbol{X})$$

$$\sigma_Y = \sigma_Y(\epsilon_M^P)$$

$$\boldsymbol{X} = \boldsymbol{X}(\Delta\boldsymbol{\epsilon}^P, f)$$

B.1 Basic derivatives

$$\frac{\partial \boldsymbol{X}}{\partial \Delta\epsilon_p} = \frac{1 - q_1 f}{3}\frac{C_X X_{\mathrm{sat}}}{1 + C_x\Delta\epsilon_q}\boldsymbol{I}$$
$$\frac{\partial \boldsymbol{X}}{\partial \Delta\epsilon_q} = -(1 - q_1 f)\frac{3C_X\boldsymbol{X}^t + {C_X}^2 X_{\mathrm{sat}}\Delta\epsilon_p\boldsymbol{I} - 3C_X X_{\mathrm{sat}}\boldsymbol{n}}{3\left(1 + C_X\Delta\epsilon_q\right)^2}$$
$$\frac{\partial \boldsymbol{X}}{\partial n_i} = (1 - q_1 f)\,\frac{C_X X_{\mathrm{sat}}\Delta\epsilon_q}{1 + C_X\Delta\epsilon_q}\frac{\partial \boldsymbol{n}}{\partial n_i}; \qquad i = 1, \ldots, 5$$
$$\frac{\partial \boldsymbol{X}}{\partial \Delta\epsilon_M^P} = 0$$
$$\frac{\partial \boldsymbol{X}}{\partial f} = -q_1\frac{\boldsymbol{X}^t + C_X X_{\mathrm{sat}}\left(1/3\Delta\epsilon_p\boldsymbol{I} + \Delta\epsilon_q\boldsymbol{n}\right)}{1 + C_x\Delta\epsilon_q}$$

$$
\begin{aligned}
\frac{\partial \widetilde{p}}{\partial \Delta\epsilon_p} &= \frac{\partial p}{\partial \Delta\epsilon_p} - \frac{\partial X_m}{\partial \Delta\epsilon_p} = K - \frac{\partial X_m}{\partial \Delta\epsilon_p} \\
\frac{\partial \widetilde{p}}{\partial \Delta\epsilon_q} &= \frac{\partial p}{\partial \Delta\epsilon_q} - \frac{\partial X_m}{\partial \Delta\epsilon_q} = -\frac{\partial X_m}{\partial \Delta\epsilon_q} \\
\frac{\partial \widetilde{p}}{\partial n_i} &= \frac{\partial p}{\partial n_i} - \frac{\partial X_m}{\partial n_i} = -\frac{\partial X_m}{\partial n_i}; \qquad i = 1, \ldots, 5 \\
\frac{\partial \widetilde{p}}{\partial \Delta\epsilon_M^P} &= 0 \\
\frac{\partial \widetilde{p}}{\partial f} &= \frac{\partial p}{\partial f} - \frac{\partial X_m}{\partial f} = -\frac{\partial X_m}{\partial f}
\end{aligned}
$$

$$
\begin{aligned}
\frac{\partial \widetilde{q}}{\partial \Delta\epsilon_p} &= \frac{1}{4\widetilde{q}} \left(2 \frac{\partial \boldsymbol{\beta}}{\partial \Delta\epsilon_p} : \mathbb{H} : \boldsymbol{\beta} \right) = \frac{1}{2\widetilde{q}} \left(-\frac{\partial \boldsymbol{X}}{\partial \Delta\epsilon_p} : \mathbb{H} : \boldsymbol{\beta} \right) \\
\frac{\partial \widetilde{q}}{\partial \Delta\epsilon_q} &= \frac{1}{4\widetilde{q}} \left(2 \frac{\partial \boldsymbol{\beta}}{\partial \Delta\epsilon_q} : \mathbb{H} : \boldsymbol{\beta} \right) = \frac{1}{2\widetilde{q}} \left[\left(-2G\boldsymbol{n} - \frac{\partial \boldsymbol{X}}{\partial \Delta\epsilon_p} \right) : \mathbb{H} : \boldsymbol{\beta} \right] \\
\frac{\partial \widetilde{q}}{\partial n_i} &= \frac{1}{4\widetilde{q}} \left(2 \frac{\partial \boldsymbol{\beta}}{\partial n_i} : \mathbb{H} : \boldsymbol{\beta} \right) = \frac{1}{2\widetilde{q}} \left[\left(-2G\Delta\epsilon_q \frac{\partial \boldsymbol{n}}{\partial n_i} - \frac{\partial \boldsymbol{X}}{\partial n_i} \right) : \mathbb{H} : \boldsymbol{\beta} \right]; \quad i = 1, ..., 5 \\
\frac{\partial \widetilde{q}}{\partial \Delta\epsilon_M^P} &= 0 \\
\frac{\partial \widetilde{q}}{\partial f} &= \frac{1}{4\widetilde{q}} \left(2 \frac{\partial \boldsymbol{\beta}}{\partial f} : \mathbb{H} : \boldsymbol{\beta} \right) = \frac{1}{2\widetilde{q}} \left(-\frac{\partial \boldsymbol{X}}{\partial f} : \mathbb{H} : \boldsymbol{\beta} \right)
\end{aligned}
$$

$$
\begin{aligned}
\frac{\partial \alpha_1}{\partial \Delta\epsilon_p} &= \frac{3q_2}{\kappa\sigma_Y} \frac{\partial \widetilde{p}}{\partial \Delta\epsilon_p} \\
\frac{\partial \alpha_1}{\partial \Delta\epsilon_q} &= \frac{3q_2}{\kappa\sigma_Y} \frac{\partial \widetilde{p}}{\partial \Delta\epsilon_q} \\
\frac{\partial \alpha_1}{\partial n_i} &= \frac{3q_2}{\kappa\sigma_Y} \frac{\partial \widetilde{p}}{\partial n_i}; \qquad i = 1, \ldots, 5 \\
\frac{\partial \alpha_1}{\partial \Delta\epsilon_M^P} &= \frac{3q_2\widetilde{p}}{\kappa\sigma_Y^2} \frac{\partial \sigma_Y}{\partial \Delta\epsilon_M^P} \\
\frac{\partial \alpha_1}{\partial f} &= \frac{3q_2}{\kappa\sigma_Y} \frac{\partial \widetilde{p}}{\partial f}
\end{aligned}
$$

$$
\begin{aligned}
\frac{\partial \alpha_2}{\partial \Delta\epsilon_p} &= \frac{2}{\sigma_Y^2} \frac{\partial \widetilde{q}}{\partial \Delta\epsilon_p} \\
\frac{\partial \alpha_2}{\partial \Delta\epsilon_q} &= \frac{2}{\sigma_Y^2} \frac{\partial \widetilde{q}}{\partial \Delta\epsilon_q} \\
\frac{\partial \alpha_2}{\partial n_i} &= \frac{2}{\sigma_Y^2} \frac{\partial \widetilde{q}}{\partial n_i}; \qquad i = 1, \ldots, 5 \\
\frac{\partial \alpha_2}{\partial \Delta\epsilon_M^P} &= \frac{4\widetilde{q}}{\sigma_Y^3} \frac{\partial \sigma_Y}{\Delta\epsilon_M^P} \\
\frac{\partial \alpha_2}{\partial f} &= \frac{2}{\sigma_Y^2} \frac{\partial \widetilde{q}}{\partial f}
\end{aligned}
$$

$$
\begin{aligned}
\frac{\partial \alpha_3}{\partial \Delta\epsilon_p} &= 6\frac{q_1 q_2}{\kappa\sigma_Y} f^* \cosh(\alpha_1)\frac{\partial \alpha_1}{\partial \Delta\epsilon_p} \\
\frac{\partial \alpha_3}{\partial \Delta\epsilon_q} &= 6\frac{q_1 q_2}{\kappa\sigma_Y} f^* \cosh(\alpha_1)\frac{\partial \alpha_1}{\partial \Delta\epsilon_q} \\
\frac{\partial \alpha_3}{\partial n_i} &= 6\frac{q_1 q_2}{\kappa\sigma_Y} f^* \cosh(\alpha_1)\frac{\partial \alpha_1}{\partial n_i}; \qquad i = 1,\ldots,5 \\
\frac{\partial \alpha_3}{\partial \Delta\epsilon_M^P} &= 6\frac{q_1 q_2}{\kappa\sigma_Y^2} f^* \left[\sigma_Y \cosh(\alpha_1)\frac{\partial \alpha_1}{\partial \Delta\epsilon_M^P} + \sinh(\alpha_1)\frac{\partial \sigma_Y}{\partial \epsilon_M^P}\right] \\
\frac{\partial \alpha_3}{\partial f} &= 6\frac{q_1 q_2}{\kappa\sigma_Y} \left[f^* \cosh(\alpha_1)\frac{\partial \alpha_1}{\partial f} + K_f \sinh(\alpha_1)\right]
\end{aligned}
$$

B.2 Jacobian matrix derivatives

$$
\begin{aligned}
\text{fjac(1,1):} \quad \frac{\partial \Gamma_1}{\partial \Delta\epsilon_p} &= \frac{2\widetilde{q}}{\sigma_Y^2}\frac{\partial \widetilde{q}}{\partial \Delta\epsilon_p} + 2q_1 f^* \frac{\partial \alpha_1}{\partial \Delta\epsilon_p}\sinh\alpha_1 \\
\text{fjac(1,2):} \quad \frac{\partial \Gamma_1}{\partial \Delta\epsilon_q} &= \frac{2\widetilde{q}}{\sigma_Y^2}\frac{\partial \widetilde{q}}{\partial \Delta\epsilon_q} + 2q_1 f^* \frac{\partial \alpha_1}{\partial \Delta\epsilon_q}\sinh\alpha_1 \\
\text{fjac(1,j(i)):} \quad \frac{\partial \Gamma_1}{\partial n_i} &= \frac{2\widetilde{q}}{\sigma_Y^2}\frac{\partial \widetilde{q}}{\partial n_i} + 2q_1 f^* \frac{\partial \alpha_1}{\partial n_i}\sinh\alpha_1; \qquad j = \{3,4,5,6,7\}, \quad i = 1,\ldots,5 \\
\text{fjac(1,8):} \quad \frac{\partial \Gamma_1}{\partial \Delta\epsilon_M^P} &= -\frac{2\widetilde{q}^2}{\sigma_Y^3}\frac{\partial \sigma_Y}{\partial \epsilon_M^P} - 2q_1 f^* \frac{\partial \alpha_1}{\partial \Delta\epsilon_M^P}\sinh\alpha_1 \\
\text{fjac(1,9):} \quad \frac{\partial \Gamma_1}{\partial f} &= \frac{2\widetilde{q}}{\sigma_Y^2}\frac{\partial \widetilde{q}}{\partial f} + 2q_1 K_f \cosh\alpha_1 + 2q_1 f^* \sinh\alpha_1 \frac{\partial \alpha_1}{\partial f} - 2q_3 f^* K_f
\end{aligned}
$$

$$
\begin{aligned}
\text{fjac(2,1):} \quad \frac{\partial \Gamma_2}{\partial \Delta\epsilon_p} &= \alpha_2 + \Delta\epsilon_p \frac{\partial \alpha_2}{\partial \Delta\epsilon_p} - \Delta\epsilon_q \frac{\partial \alpha_3}{\partial \Delta\epsilon_p} \\
\text{fjac(2,2):} \quad \frac{\partial \Gamma_2}{\partial \Delta\epsilon_p} &= -\alpha_3 + \Delta\epsilon_p \frac{\partial \alpha_2}{\partial \Delta\epsilon_q} - \Delta\epsilon_q \frac{\partial \alpha_3}{\partial \Delta\epsilon_q} \\
\text{fjac(2,j(i)):} \quad \frac{\partial \Gamma_2}{\partial n_i} &= \Delta\epsilon_p \frac{\partial \alpha_2}{\partial n_i} - \Delta\epsilon_q \frac{\partial \alpha_3}{\partial n_i}; \qquad j = \{3,4,5,6,7\}, \quad i = 1,\ldots,5 \\
\text{fjac(2,8):} \quad \frac{\partial \Gamma_2}{\partial \Delta\epsilon_M^P} &= \Delta\epsilon_p \frac{\partial \alpha_2}{\partial \Delta\epsilon_M^P} - \Delta\epsilon_q \frac{\partial \alpha_3}{\partial \Delta\epsilon_M^P} \\
\text{fjac(2,9):} \quad \frac{\partial \Gamma_2}{\partial f} &= \Delta\epsilon_p \frac{\partial \alpha_2}{\partial f} - \Delta\epsilon_q \frac{\partial \alpha_3}{\partial f}
\end{aligned}
$$

$$
\begin{aligned}
\text{fjac(j(i),1):} \quad \left(\frac{\partial \Gamma_{j(i)}}{\partial \Delta\epsilon_p}\right)_i &= -\frac{1}{2\widetilde{q}}\left(\mathbb{H} : \frac{\partial \widetilde{\boldsymbol{\sigma}}_{\text{dev}}}{\partial \Delta\epsilon_p} - \frac{\mathbb{H} : \widetilde{\boldsymbol{\sigma}}_{\text{dev}}}{\widetilde{q}}\frac{\partial \widetilde{q}}{\partial \Delta\epsilon_p}\right); && i = 1,\ldots,5 \\
\text{fjac(j(i),2):} \quad \left(\frac{\partial \Gamma_{j(i)}}{\partial \Delta\epsilon_q}\right)_i &= -\frac{1}{2\widetilde{q}}\left(\mathbb{H} : \frac{\partial \widetilde{\boldsymbol{\sigma}}_{\text{dev}}}{\partial \Delta\epsilon_q} - \frac{\mathbb{H} : \widetilde{\boldsymbol{\sigma}}_{\text{dev}}}{\widetilde{q}}\frac{\partial \widetilde{q}}{\partial \Delta\epsilon_q}\right); && i = 1,\ldots,5 \\
\text{fjac(j(i),j(i)):} \quad \left(\frac{\partial \Gamma_{j(i)}}{\partial n_i}\right)_i &= \frac{\partial \boldsymbol{n}}{\partial n_i} - \frac{1}{2\widetilde{q}}\left(\mathbb{H} : \frac{\partial \widetilde{\boldsymbol{\sigma}}_{\text{dev}}}{\partial n_i} - \frac{\mathbb{H} : \widetilde{\boldsymbol{\sigma}}_{\text{dev}}}{\widetilde{q}}\frac{\partial \widetilde{q}}{\partial n_i}\right); && j = \{3,4,5,6,7\}, \quad i = 1,\ldots,5 \\
\text{fjac(j(i),8):} \quad \left(\frac{\partial \Gamma_{j(i)}}{\partial \Delta\epsilon_M^P}\right)_i &= 0; && i = 1,\ldots,5 \\
\text{fjac(j(i),9):} \quad \left(\frac{\partial \Gamma_{j(i)}}{\partial f}\right)_i &= -\frac{1}{2\widetilde{q}}\left(\mathbb{H} : \frac{\partial \widetilde{\boldsymbol{\sigma}}_{\text{dev}}}{\partial f} - \frac{\mathbb{H} : \widetilde{\boldsymbol{\sigma}}_{\text{dev}}}{\widetilde{q}}\frac{\partial \widetilde{q}}{\partial f}\right); && i = 1,\ldots,5
\end{aligned}
$$

$$
\begin{aligned}
\text{fjac(8,1):} \quad & \frac{\partial \Gamma_8}{\partial \Delta\epsilon_p} && = \frac{\partial \widetilde{p}}{\partial \Delta\epsilon_p}\Delta\epsilon_p - \frac{\partial \widetilde{q}}{\partial \Delta\epsilon_p}\Delta\epsilon_q - \widetilde{p} \\
\text{fjac(8,2):} \quad & \frac{\partial \Gamma_8}{\partial \Delta\epsilon_q} && = \frac{\partial \widetilde{p}}{\partial \Delta\epsilon_q}\Delta\epsilon_p - \frac{\partial \widetilde{q}}{\partial \Delta\epsilon_q}\Delta\epsilon_q - \widetilde{q} \\
\text{fjac(8,j(i)):} \quad & \frac{\partial \Gamma_8}{\partial n_i} && = \frac{\partial \widetilde{p}}{\partial n_i}\Delta\epsilon_p - \frac{\partial \widetilde{q}}{\partial n_i}\Delta\epsilon_q; \qquad j = \{3,4,5,6,7\}, \quad i = 1,\ldots,5 \\
\text{fjac(8,8):} \quad & \frac{\partial \Gamma_8}{\partial \Delta\epsilon_M^P} && = (1-f)\left(\sigma_Y + \Delta\epsilon_M^P \frac{\partial \sigma_Y}{\partial \epsilon_M^P}\right) \\
\text{fjac(8,9):} \quad & \frac{\partial \Gamma_8}{\partial f} && = -\Delta\epsilon_M^P \sigma_Y + \Delta\epsilon_p \frac{\partial \widetilde{p}}{\partial f} - \Delta\epsilon_q \frac{\partial \widetilde{q}}{\partial f}
\end{aligned}
$$

$$
\begin{aligned}
\text{fjac(9,1):} \quad & \frac{\partial \Gamma_9}{\partial \Delta\epsilon_p} = -\frac{1-f^t}{(1+\Delta\epsilon_p)^2} \\
\text{fjac(9,2):} \quad & \frac{\partial \Gamma_9}{\partial \Delta\epsilon_q} = 0 \\
\text{fjac(9,j(i)):} \quad & \frac{\partial \Gamma_9}{\partial n_i} = 0; \qquad j = \{3,4,5,6,7\}, \quad i = 1,\ldots,5 \\
\text{fjac(9,8):} \quad & \frac{\partial \Gamma_9}{\partial \Delta\epsilon_M^P} = 0 \\
\text{fjac(9,9):} \quad & \frac{\partial \Gamma_9}{\partial f} = 1
\end{aligned}
$$

B.3 Tangent matrix derivatives

Defining:

$$
\begin{aligned}
h_1 &:= (1-f)\Delta\epsilon_p \\
h_2 &:= h\frac{\widetilde{\boldsymbol{\sigma}} : \Delta\boldsymbol{\epsilon}^P}{(1-f)\sigma_Y}
\end{aligned}
$$

where:

$$
h = \frac{\partial \sigma_Y\left(\epsilon_M^P\right)}{\partial \epsilon_M^P}
$$

$$
\begin{aligned}
\frac{\partial F_p}{\partial \boldsymbol{\sigma}} &= \frac{\mathbb{H} : \widetilde{\boldsymbol{\sigma}}}{\sigma_Y^2} + 2q_1 f^* \sinh(\alpha_1)\frac{\partial \alpha_1}{\partial \boldsymbol{\sigma}} \\
\frac{\partial F_p}{\partial \Delta\boldsymbol{\epsilon}^P} &= \left(-\frac{\mathbb{H} : \widetilde{\boldsymbol{\sigma}}}{\sigma_Y^2} + 2q_1 f^* \sinh(\alpha_1)\frac{\partial \alpha_1}{\partial \boldsymbol{X}}\right)\frac{\partial \boldsymbol{X}}{\partial \Delta\boldsymbol{\epsilon}^P} \\
\frac{\partial F_p}{\partial f} &= \frac{2\widetilde{q}}{\sigma_Y^2}\frac{\partial \widetilde{q}}{\partial f} + 2q_1 K_f \cosh\alpha_1 + 2q_1 f^* \sinh\alpha_1 \frac{\partial \alpha_1}{\partial f} - 2q_3 f^* K_f \\
\frac{\partial F_p}{\partial \sigma_Y} &= -\frac{2\widetilde{q}^2}{\sigma_Y^3} + 2q_1 f^* \sinh(\alpha_1)\frac{\partial \alpha_1}{\partial \sigma_Y}
\end{aligned}
$$

$$
\begin{aligned}
\frac{\partial^2 F_p}{\partial \boldsymbol{\sigma}^2} =& \frac{\mathbb{H}}{\sigma_Y^2} + 2q_1 f^* \cosh(\alpha_1) \left(\frac{\partial \alpha_1}{\partial \boldsymbol{\sigma}}\right)^2 \\
\frac{\partial^2 F_p}{\partial \boldsymbol{\sigma} \partial \Delta\boldsymbol{\epsilon}^P} =& 2q_1 \cosh(\alpha_1) \frac{\partial \alpha_1}{\partial \boldsymbol{\sigma}} \frac{\partial \alpha_1}{\partial \Delta\boldsymbol{\epsilon}^P} - \frac{1}{\sigma_Y^2} \mathbb{H} : \frac{\partial \boldsymbol{X}}{\partial \Delta\boldsymbol{\epsilon}^P} \\
\frac{\partial^2 F_p}{\partial \boldsymbol{\sigma} \partial f} =& -\frac{1}{\sigma_Y^2} \mathbb{H} : \frac{\partial \boldsymbol{X}}{\partial f} + 2q_1 \sinh(\alpha_1) \frac{\partial \alpha_1}{\partial \boldsymbol{\sigma}} + 2q_1 f^* \cosh(\alpha_1) \frac{\partial \alpha_1}{\partial \boldsymbol{\sigma}} \frac{\partial \alpha_1}{\partial f} \\
\frac{\partial^2 F_p}{\partial \boldsymbol{\sigma} \partial \sigma_Y} =& -\frac{\mathbb{H} : \boldsymbol{X}}{\sigma_Y^3} + 2q_1 f^* \left(\sinh(\alpha_1) \frac{\partial^2 \alpha_1}{\partial \boldsymbol{\sigma} \partial \sigma_Y} + \cosh(\alpha_1) \frac{\partial \alpha_1}{\partial \boldsymbol{\sigma}} \frac{\partial \alpha_1}{\partial \sigma_Y}\right)
\end{aligned}
$$

$$
\begin{aligned}
\frac{\partial \alpha_1}{\partial \boldsymbol{\sigma}} =& \frac{q_2}{\kappa \sigma_Y} \boldsymbol{I} \\
\frac{\partial \alpha_1}{\partial \boldsymbol{\epsilon}^P} =& \frac{\partial \alpha_1}{\partial \boldsymbol{X}} \frac{\partial \boldsymbol{X}}{\partial \boldsymbol{\epsilon}^P} \\
\frac{\partial \alpha_1}{\partial \sigma_Y} =& -\frac{q_2}{\kappa \sigma_Y} \boldsymbol{\sigma} \\
\frac{\partial \alpha_1}{\partial f} =& -\frac{q_2}{\kappa \sigma_Y} \frac{\partial \boldsymbol{X}}{\partial f}
\end{aligned}
$$

$$
\begin{aligned}
\frac{\partial h_1}{\partial \boldsymbol{\sigma}} &= 0 & \frac{\partial h_2}{\partial \boldsymbol{\sigma}} &= \frac{h \Delta\boldsymbol{\epsilon}^P}{(1-f)\sigma_Y} \\
\frac{\partial h_1}{\partial \Delta\boldsymbol{\epsilon}^P} &= (1-f)\boldsymbol{I} & \frac{\partial h_2}{\partial \Delta\boldsymbol{\epsilon}^P} &= \frac{1}{(1-f)\sigma_Y} \left(h\widetilde{\boldsymbol{\sigma}} - h\Delta\boldsymbol{\epsilon}^P \frac{\partial \boldsymbol{X}}{\partial \Delta\boldsymbol{\epsilon}^P}\right) \\
\frac{\partial h_1}{\partial f} &= -\Delta\epsilon_p & \frac{\partial h_2}{\partial f} &= \frac{h\widetilde{\boldsymbol{\sigma}} : \Delta\boldsymbol{\epsilon}^P}{(1-f)^2 \sigma_Y} \\
\frac{\partial h_1}{\partial \sigma_Y} &= 0 & \frac{\partial h_2}{\partial \sigma_Y} &= -\frac{h\widetilde{\boldsymbol{\sigma}} : \Delta\boldsymbol{\epsilon}^P}{(1-f)\sigma_Y^2}
\end{aligned}
$$

$$
\begin{aligned}
\frac{\boldsymbol{X}}{\partial \Delta\boldsymbol{\epsilon}^P} &= \frac{1 - q_1 f}{(1 + C_X \Delta\epsilon_q)^2} \left[C_X X_{\text{sat}} (1 + C_X \Delta\epsilon_q) \boldsymbol{I} - \left(X^t + C_X X_{\text{sat}} \Delta\boldsymbol{\epsilon}^P\right) \frac{\partial \Delta\epsilon_q}{\partial \Delta\boldsymbol{\epsilon}^P}\right] \\
\frac{\partial \Delta\epsilon_q}{\partial \Delta\boldsymbol{\epsilon}^P} &= \frac{2\mathbb{H}^{-1} : \Delta\boldsymbol{\epsilon}}{\Delta\epsilon_q} \\
\frac{\Delta \boldsymbol{X}}{\partial f} &= -\frac{X^t + C_X X_{\text{sat}} \boldsymbol{\epsilon}^P}{1 + C_X \epsilon_q}
\end{aligned}
$$

Appendix C

Texture characteristics of the DC01 steel sheet

The general methodology considers:

1. The measurement of pole figures using X-ray diffraction (XRD) at half of the sheet thickness.
2. The assesment of the orientation distribution function (ODF) using the MTM-FHM software (Van Houtte, 2004).
3. The use of ODF to get the r-values and yield loci using a full constraint Taylor, (1938) model.

A previous research in the DC01 steel was conducted in the frame of the SeMPeR project. The DC01 steel batch used at this moment was different and new measurements were taken.

C.1 SeMPeR results

The Sheet Metal Oriented Prototyping and Rapid Manufacturing (SeMPeR) project gave a qualitative representation of texture to characterize the DC01 sheet anisotropy. Here we present results taken from Eyckens and van Bael, (2006). Eyckens et al., (2011a) can also be checked for the same DC01 steel sheet. To determine the initial texture of each sheet four incomplete pole figures, namely (1 1 0), (2 0 0), (2 1 1) and (3 1 0), were measured by means of XRD. The texture is composed of a full γ-fiber and a partial α-fiber as can be seen in Fig. C.1. The results of the anisotropic coefficients are shown in Table C.1. A comparison of the predicted r-values by crystal plasticity model with the experimental results was later performed (Eyckens and van Bael, 2007). A reasonable agreement can be found between the r-values obtained from the tensile tests and those calculated from the texture with the Taylor model.

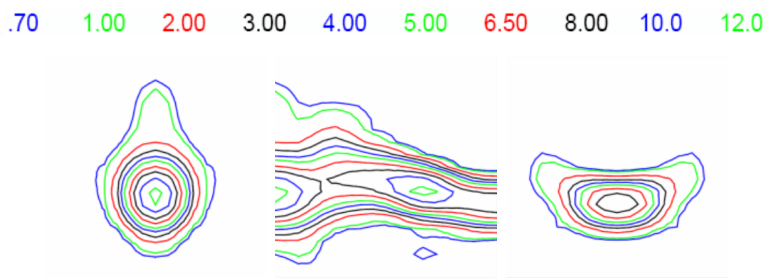

(a) Φ_1=0° (b) Φ_2=45° (c) Φ_1=90°

Figure C.1: Section of the ODF for the DC01 carbon steel used in the SeMPeR project. As expected for a BBC material, at Φ_2=45° clear α-fiber and γ-fiber can be observed.

C.2 New results

Three 1 mm × 1 mm squared samples were used for XRD measurements with the ODF section shown in Fig. C.2. The results are shown in Table C.1 and plotted in Fig. C.3 together with the SeMPeR results. These new values are lower

Table C.1: Anisotropic coefficients predicted by the Taylor, (1938) model using texture measurements from SeMPeR and from the new batch.

Angle from RD	*SeMPeR*	*New*
0°	2.78	2.237 ± 0.054
15°	2.50	2.023 ± 0.064
30°	2.03	1.597 ± 0.023
45°	1.95	1.478 ± 0.028
60°	2.20	1.648 ± 0.040
75°	2.54	2.023 ± 0.063
90°	2.61	2.166 ± 0.074
$\overline{r}$	2.32	1.840 ± 0.046
Δr	0.74	0.724 ± 0.036

compared to SeMPeR results but the overall shape of coefficients versus the angle to the RD is the same.

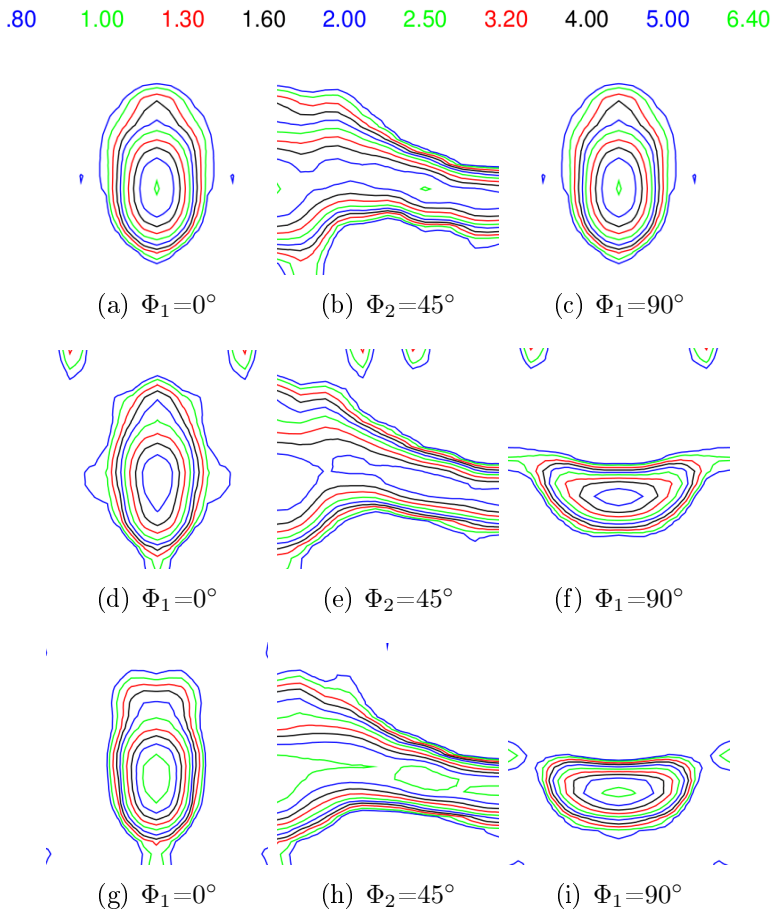

Figure C.2: New ODF sections obtained for the 3 analyzed samples of the DC01 steel sheet. Qualitatively, the results are similar to those in the SeMPeR project but the iso-values scale is lower.

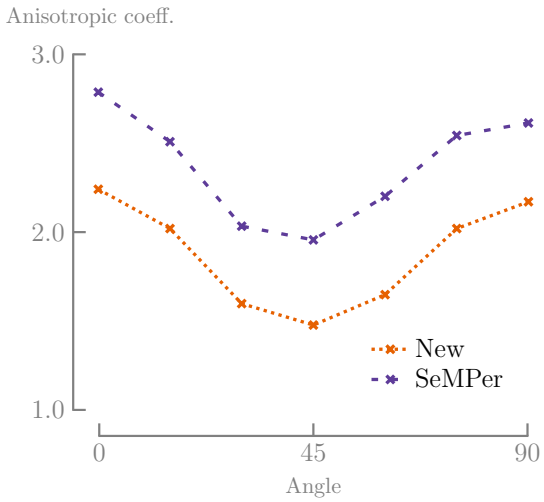

Figure C.3: Anisotropic coefficients from Table C.1. Despite the difference on the value both follow the same distribution.

Appendix D

Assessment of damage and anisotropic plasticity models to predict Ti-6Al-4V behavior

The plastic behavior of the Ti-6Al-4V alloy includes several features as strength differential effect, anisotropy and yield strength sensitivity to temperature and strain rate. Monotonic tensions in the three orthogonal directions of the material are performed to identify the Hill, (1948) yield criterion. Monotonic compression and plane strain tensile tests are also included in the experimental campaign to identify the orthotropic yield criterion of CPB06. An assessment of the two models is done by comparing the yield loci and the experimental data points for different levels of plastic work. A first approach of the damage modeling of the Ti-6AL-4V alloy is investigated with an extended Gurson-Tvergaard-Needleman damage model based on Hill, (1948) yield criterion. Finite element simulations of the experiments are performed and numerical results allows checking force-displacement curves until rupture and local information like displacement and strain fields. The prediction ability of the Hill '48, CPB and extended Gurson models are assessed on simple shear and notched tensile tests until fracture[1].

D.1 Introduction

Aerospace and manufacturing industries have a strong interest in numerically assessment of the ductile fracture of Ti-6Al-4V in real components. Indeed the formability and crashworthiness of Ti-6AL-4V are frequent limitations due to the material ductile fracture. As for most metals and alloys, Ti-6AL-4V shows a process of material degradation including three successive stages of damage mechanism: nucleation, growth and coalescence of voids. Note that the first two mechanisms may occur simultaneously. After nucleation, the voids resulting from interface decohesion of inclusions or particle fracture grow within the surrounding

[1]This chapter was originally published in Guzmán et al., (2015)

matrix and affect its plastic deformation. The first stage of void growth by relatively homogeneous plastic deformation of the surrounding matrix is interrupted by the localization of the plastic flow in the ligament between the voids. This localization corresponds to the onset of coalescence. There are currently several damage models avaible in the literature in order to describe the material degradation. Two categories can be distinguished: the phenomenological (e.g. Lemaitre, 1985)) and the micromechanical approaches. The most popular micromechanical model for ductile damage is the Gurson-Tvergaard-Needleman (GTN). Gurson, (1977a) first proposed a porous plasticity model with the void volume fraction as internal variable. The model was further improved to account the loss of load carrying capacity associated with void nucleation and coalescence (Tvergaard, 1989), hence considering the three stages of damage: void nucleation, growth and coalescence. Since then, the GTN model has been extended to cover different applications. For instance, Benzerga and Besson, (2001) performed the same analysis as Gurson, (1977a) but considering an anisotropic matrix of the Hill, (1948) type. A fully-implicit integration scheme was proposed by Ben Bettaieb et al., (2011c) for this *anisotropic* GTN model, also including the effect of the kinematic hardening. The main goal of this present paper is to calibrate the GTN model on bulk Ti-6AL-4V alloy at room temperature and a quasi-static strain rate and to check its ability to predict fracture. In addition, the load predictions of three different models applied on notched round bars and holed specimens are assessed. The first model is based on the Hill, (1948) yield criteria, which takes into account the anisotropic behavior of Ti-6AL-4V alloy. The second model is defined by the orthotropic yield criterion CPB06 that accounts for both the anisotropy and the strength differential effect of the alloy (Tuninetti et al., 2015). The third one predicts damage by the extended version of the GTN model.

D.2 Material models

Three different material models are used in the article. In the case of the Hill '48 and the GTN model, the used a Voce type of isotropic hardening law.

$$\sigma_Y = \sigma_0 + K\left(1 - \exp\left(-n\epsilon_{eq}^P\right)\right) \tag{D.2.1}$$

where σ_Y is the flow stress, ϵ_{eq}^P is the equivalent plastic strain and K, n, σ_0 are material constants computed from a tensile curve in a reference direction. The CPB06 model uses also the Voce law as a reference hardening curve (Tuninetti et al., 2015).

D.2.1 Hill '48 model.

In the yield criteria introduced by Hill, (1948) the material has three orthogonal symmetry planes and three principal axes of anisotropy: x, y and z. In terms of

the anisotropic axis:

$$F_p(\sigma_{ij}) = \frac{1}{2}\left[F(\sigma_{yy}-\sigma_{zz})^2 + G(\sigma_{zz}-\sigma_{xx})^2 + H(\sigma_{xx}-\sigma_{yy})^2 + 2L{\sigma_{yz}}^2 + 2M{\sigma_{zx}}^2 + 2N{\sigma_{xy}}^2\right] - {\sigma_Y}^2 = 0 \tag{D.2.2}$$

where F, G, H, L, M, N are material parameters. Note that if $F = G = H = 1.0$ and $L = M = N = 3.0$, the Hill '48 yield locus recovers the isotropic von Mises yield locus.

D.2.2 The CPB06 model.

The orthotropic yield criterion CPB06 was developed by Cazacu et al., (2006). The criterion is defined by:

$$F_p(\sigma_{ij}) = (|\Sigma_1| - k\Sigma_1)^a + (|\Sigma_2| - k\Sigma_2)^a + (|\Sigma_3| - k\Sigma_3)^a \tag{D.2.3}$$

where k is a parameter which takes into account the strength differential (SD) effect and a is the degree of homogeneity. Σ_1, Σ_2, Σ_3 are the principal values of the second-order tensor $\Sigma_{ij} = C_{ijkl} : S_{kl}$, where C_{ijkl} is a fourth-order orthotropic tensor that accounts for the plastic anisotropy of the material and S_{ij} is the deviatoric part of the Cauchy stress tensor.

D.2.3 The GTN yield surface.

The classical GTN yield surface is defined by:

$$F_p(\sigma_{ij}, f, \sigma_Y) = \frac{\sigma_{eq}^2}{\sigma_Y^2} - 1 + 2q_1 f\cosh\left(-\frac{3q_2}{2}\frac{\sigma_m}{\sigma_Y}\right) - (q_1 f)^2 = 0 \tag{D.2.4}$$

where σ_{eq} is the (macroscopic) equivalent stress related to Hill '48 yield criterion, σ_Y the yield stress of the matrix material, σ_m the macroscopic mean stress and f is the void volume fraction (also called porosity), defined as the average ratio of the void volume to the total volume of the material. The damage parameters q_1 and q_2, originally equal to 1.0 in the initial Gurson model, are usually set to q_1 =1.5 and q_2 =1.0 allowing the continuum model to be in good agreement with the localization strain for cell analysis (Tvergaard, 1989). The extended Gurson model used for the simulations has been implemented by Guzmán, (2014), featuring Hill '48 type anisotropy of the matrix coupled with a mixed hardening law (Ben Bettaieb et al., 2011c) and classical nucleation and coalescence laws proposed in the GTN model. The evolution of voids is additevely decomposed in the nucleation (f_n) and growth part (f_g), hence:

$$\dot{f} = \dot{f}_n + \dot{f}_g = \frac{f_N}{S_N\sqrt{2\pi}}\exp\left[-\frac{1}{2}\left(\frac{\epsilon_M^P - \epsilon_N}{S_N}\right)^2\right]\dot{\epsilon}_M^P + (1-f)\,\mathrm{tr}\dot{\epsilon_{ij}}^p \tag{D.2.5}$$

with ϵ_M^P as the equivalent plastic strain in the matrix and f_N, S_N, ϵ_N as material parameters. Coalescence is determined by the effective porosity f^* function:

$$f^* = \begin{cases} f & \text{if } f < f_{cr} \\ f_{cr} + \dfrac{\frac{1}{q_1} - f_{cr}}{f_F - f_{cr}}(f - f_{cr}) & \text{if } f > f_{cr} \end{cases} \tag{D.2.6}$$

where f_{cr} and f_F are material parameters.

D.3 Identification of material parameters

The experiments are performed on a bulk Ti-6AL-4V alloy, depicted in Fig. D.1(a). The elasto-visco-plastic behavior of this bulk alloy has been previously characterized by Tuninetti and Habraken, (2014) and Tuninetti et al., (2015).

D.3.1 Plasticity characterization.

The tensile tests were performed in LD direction until fracture using universal testing machine and a three 3D optical strain measuring systems (DIC Limess), allowing obtaining the local strain within the localized zone of the specimens and, consequently, the true stress-true strain curves even after the onset of necking. These data have been used in order to obtain a new set of parameters of the Voce hardening law for the reference direction LD of the CPB06 model (Table D.1). The former hardening parameters used in Tuninetti and Habraken, (2014) and Tuninetti et al., (2015) were identified using stress-strain curves until 0.1 axial strain leading to lower values of the axial tensile stress after the onset of necking compared with the experimental data, and therefore lower values of the load in specimen subjected to axial load. Fig. D.1(b) shows the results using the old set of parameters (Voce 0.1) and the new ones (Voce 0.2).

Table D.1: New Voce-type of hardening material parameters for the Ti-6AL-4V.

K	n	σ_0
918.0	5.8	290.0

The anisotropy of the material is described by measuring the flow stress under different stress states and work hardening levels. The anisotropy parameters for the Hill '48 model are shown in Table D.2, while for CPB06 they have been reported previously (Tuninetti and Habraken, 2014). Evaluating these two models by looking at their analytical prediction in the stress space (Fig. D.2), clear differences appear for the plane stress biaxial and compression states.

D.3.2 GTN identification.

The identification of the GTN model parameters does not follow the same methodology of the previous plasticity models. The nature of the model, mixing macroscopic and microscopic variable, implies that the search of parameters does not

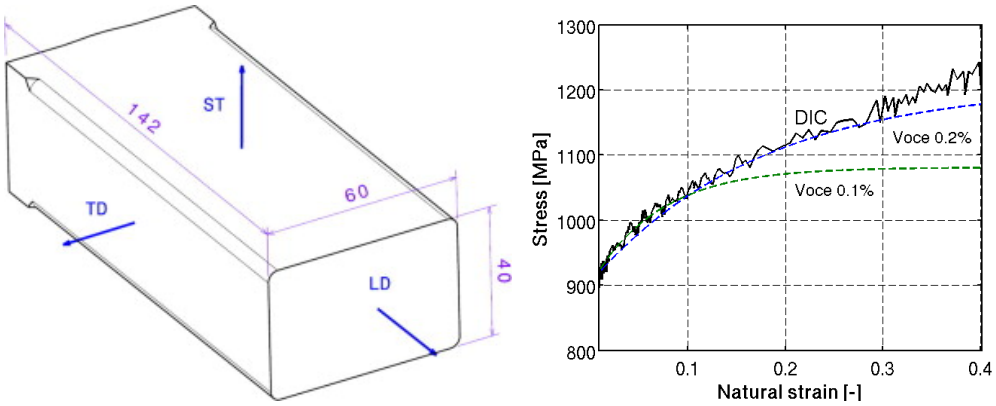

(a) (b)

Figure D.1: (a) Material directions of the TI-6AL-4V ingot (dimensions in [mm]). Longitudinal (LD), Transverse (TD) and Short Transverse (ST) directions. (b) Hardening curve for the TI-6AL-4V, showing the newly identified Voce law until 0.2 axial strain using the DIC curve.

Table D.2: Anisotropic parameter of the initial Hill '48 yield locus for W_p =1.857 [J cm^{-3}], identified from tensile data in the three orthogonal material directions (LD, TD and ST) and the simple shear in LD-ST plane.

H	F	G	N	L	M
1.017	0.958	0.983	3.278	3.278	3.278

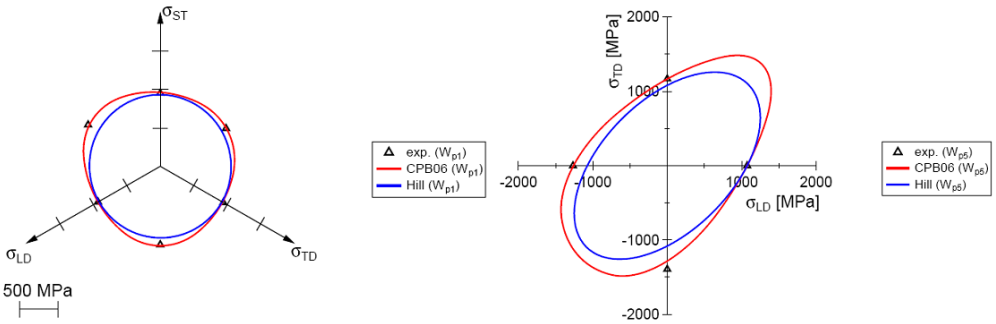

(a) π-plane at W_{p1}. (b) LD-TD plane at W_{p5}.

Figure D.2: Comparison between initial (W_{p1}=1.857 [J cm^{-3}]) and final yield surfaces (W_{p5}=1.857 [J cm^{-3}]) defined by Hill '48 and CPB06 at different planes in the stress space.

rely in a single approach. Moreover, the use of a optimization algorithm could be an ineffective tool due to the appearance of several local roots. As first step towards a correct identification of the model based on notched tensile tests, the set of parameters of Table D.3 was found to be in good agreement with the experimental results. Different microscopic measurements by optical microscopy and tomography confirm that initial porosity is very low ($f_0 < 1.0 \times 10^{-6}$).

Table D.3: Set of parameters used for the GTN model.

	f_0	f_N	S_N	ϵ_N	f_{cr}	f_F
coa1	0.0	0.04	0.10	0.30	0.03	0.04
coa2	0.0	0.04	0.10	0.30	0.04	0.06

D.4 Simulations

Finite element (FE) simulations are performed using the updated Lagrangian FE code Lagamine developed by the ArGEnCo Department of the University of Liège. The 8-node 3D brick element, called BWD3D (Duchêne et al., 2007), with a mixed formulation adapted to large strains and large displacements is selected. It involves a reduced integration scheme (with only one integration point) and an hourglass control technique. The three models are compared on three different tests: tensile test on notched specimens with radius R =1.5 [mm] and R =5.0 [mm] (Tuninetti et al., 2015), plus a tensile test in a specimen with a central hole of R =2.0 [mm] (Tuninetti and Habraken, 2014). The results are shown in Fig. D.3.

Broadly, the three models gives acceptable predictions, with the CPB06 model slightly overpredicting the force. As underlined in Tuninetti et al., (2015), the FE prediction with CPB06 is quite sensitive to its identification methodology. The data set used here (CPB06 identification 4 in Tuninetti et al., (2015)) provides optimal notch results but is less adapted for the case of the specimen with the central hole, where more shear is present. Hill '48 predictions are better, reaching force values which are in close agreement with experiments. Looking at the damage set of parameters coa1 and coa2, the force reduction is more affected in the notched specimens, in particular R =5.0 [mm]. In the other side, the specimen with a hole is less affected by the damage development giving almost the same results as Hill '48. In the latter, and even if the damage development is not noticeable, coa2 data set gives a good prediction of the onset of coalescence. This data set is able to predict correctly the onset of coalescence for the notched specimen, but for an underestimated force. Coa1 data set is more accurate predicting the onset of coalescence for the notched specimen R =1.5 [mm], but also for an underestimated force.

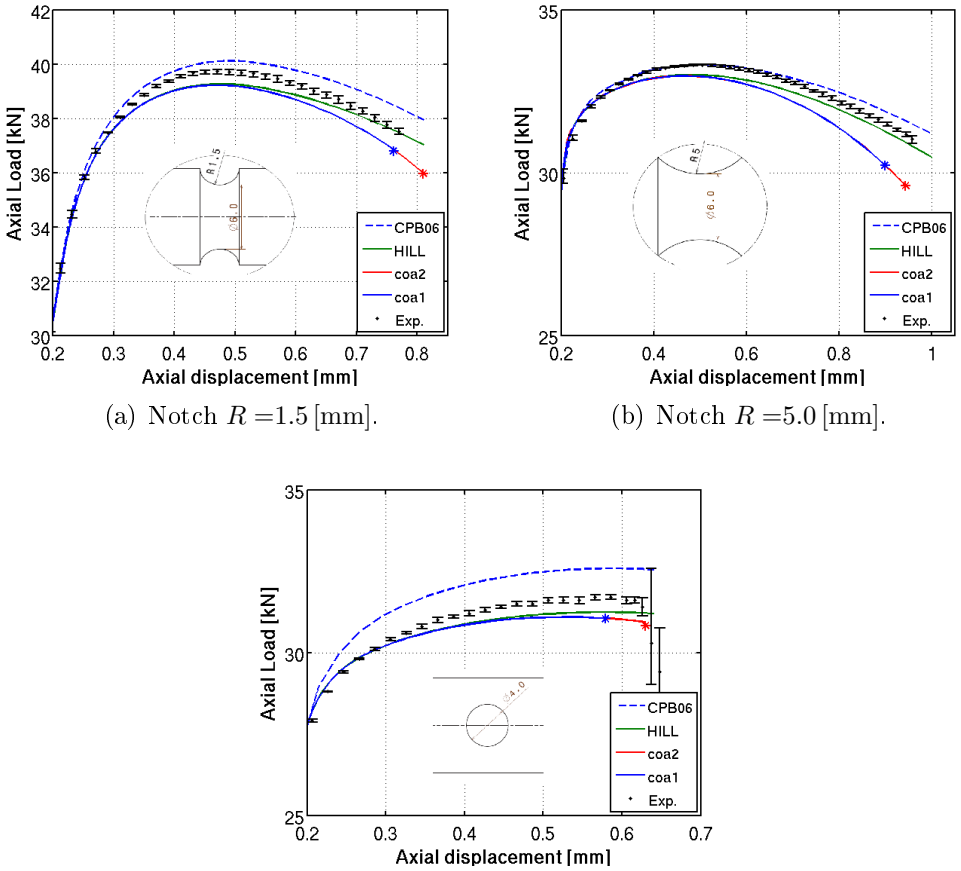

(a) Notch R =1.5 [mm].

(b) Notch R =5.0 [mm].

(c) Specimen with a hole.

Figure D.3: Comparison of the three different models with experimental results, for three different geometries. The stars at the end of the curves indicate the onset of coalescence and experimental scattering is expressed by error bars.

D.5 Conclusions

In this article, a comparison between two plasticity models (Hill '48 and CPB06) and the GTN damage model has been done. From the analyzed specimens, it is clear that a certain amount of damage is being accumulated leading to ductile fracture. The fracture prediction, despite not being perfect, gives a hint of the importance of void nucleation mechanism leading to a ductile fracture. Despite that a single set of parameters matching all the experiments was not possible to obtain, material parameter variation is not severe and the sets should be regarded within a confidence interval. Future work in this topic will be focused in a deeper micromechanical review of the material, plus a more precise characterization of the damage parameters of the GTN model. This also involves damage characterization at low triaxialities or shear-type loads, which is a trending topic in recent years.

Appendix E

Parallelization of the LAGAMINE code

E.1 Introduction

Some type of simulations, like the ones involved in single point incremental forming (SPIF), can take several hours even using coarse meshes and simple constitutive laws. Research on more complex geometries and material models can take large amount of CPUT time in normal computers, preventing to perform more complex analysis. Nonetheless, current computers make extensive use of parallelism, i.e. at least two threads are executed simultaneously to solve a problem, allowing to concentrate computational resources in demanding parts of the code. Hence, it seems straightforward to take advantage of the current low cost computer with parallel processing. Moreover, calculation speed can be greatly boosted using computer clusters.

The question now is how to use this parallel computer capabilities. This greatly depends on the architecture of the computer, for instance:

- *Distributed memory architecture*, where each processor has its own private memory and information is interchanged between processor through messages.

- *Shared memory architecture*, where each processor has access to a globally shared memory.

For distributed memory, message passing interface (MPI) can be used as a protocol to program parallel computers. Basically, it creates a fixed number of identical tasks at program startup and do not allow tasks to be created or destroyed during program execution. For shared memory architectures, open multi-processing (OpenMP) offers a simple and flexible interface for developing parallel applications. By default, each thread executes the parallelized section of the code independently. Compared to MPI, OpenMP is easier to implement but understanding and managing (variable) locality is more difficult.

In this report the LAGAMINE FE code parallelization using and OpenMP and implementation into a cluster is discussed. The scope is to review the already implemented parallelization and extensions to computer clusters.

E.2 LAGAMINE parallelization

The LAGAMINE parallelization is described in a series of works by Montleau et al., (2002), Moto Mpong and Montleau, (2002), and Moto Mpong et al., (2002). OpenMP was selected as the parallelization protocol based on the hardware available (shared memory computers) and the relatively easy implementation process compared to other protocols, like MPI. According to Montleau et al., (2002), 98% of the CPU time is consumed between the element loop and linear system solver. LAGAMINE is a code developed essentially following the old Fortran 77 standard, having a sequential structure as shown in Fig. E.1.

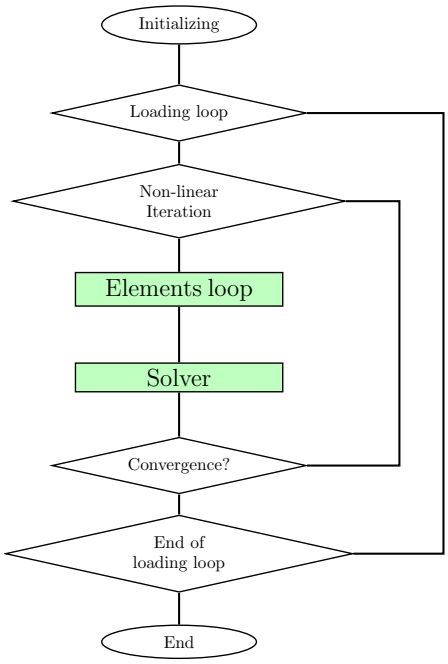

Figure E.1: Structure of the LAGAMINE FE code. The green blocks indicate the parallelized zones. Adapted from Montleau et al., (2002).

The parallelization using OpenMP is carried out at the element loop level (subroutine `ELEMB`). The loop is parallelized using a `PARALLEL DO` construct and shared among threads using `SCHEDULE(DYNAMIC,5)`, where `DYNAMIC` stands for a dynamic repartition of tasks and `5` is the number of threads packs which was found to give the best results. Within the subroutine `ELEMB`, several variables are assigned with the OpenMP attributes `PRIVATE` or `SHARED`. By default, all variables are `SHARED` between threads but in some loops this may lead to several threads trying to access to the same memory location, giving unexpected results. Hence, `PRIVATE` attribute should be employed in order to reserve a variable for the thread. This authorize only a single thread to update the memory location.

The solver can also be parallelized. Within the Lagamine FE code, there are two different methods of banded matrix storage: Morse and Skyline. In the original article by Montleau et al., (2002), a parallel direct solver called CAESAR was available. This solver used a Morse type of storage, METIS programs (Karypis and Kumar, 1998) for fill reducing orderings of sparse matrices and parallelized LU factorisation. Unfortunately, this solver is no longer available so by default the skyline storage plus Cholesky decomposition (`KTYPE`=4) is used instead.

E.3 Implementation

The parallelized version is implemented in different CÉCI clusters (acronym of *Consortium des Équipements de Calcul Intensif*). In its current status, 7 different clusters are available, each one with different characteristics. Among them, Vega (ULB) and HMEM (UCL) are chosen based on their capabilities for shared memory computing.

In this section, the procedure to implement both Lagamine and Prepro into CÉCI clusters is explained. This implies getting the sources from the Obelix server, compilation in the CECI cluster, launching simulations and debugging. A set of bash scripts were developed to carry on these tasks, which are organized within a folder as shown in Fig. E.2.

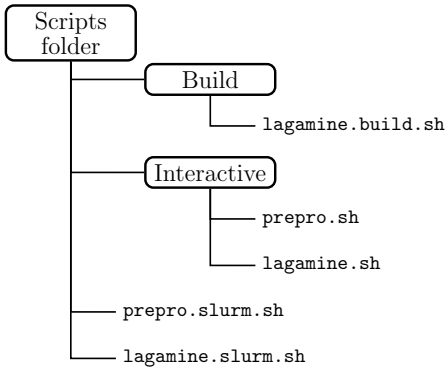

Figure E.2: Structure of the scripts folder.

E.3.1 Updating the sources

1. Open Alacarte, which is available in Obelix. This program allows to convert the minor differences between the Linux and Windows version of Lagamine.

2. After opening Alacarte, select the location of the Lagamine sources into the Obelix server (which is a Windows server). They are located in:

   `\obelix\sources\Lagamine\`

Then you must select `UNIX_NIC`, with *Suppresion des commentaires Ccpp* option marked.

3. The `ALACARTE_Lagamine` folder is generally created in:

   `C:\Documents and Settings\[username]\Local Settings\Temp\`

   This is an hidden folder, so probably you will need to change your folder visualization options in order to see it.

4. You need to transfer the files from Windows to a Linux server. From Windows, one (easy) way to do that is using FileZilla, which is simple FTP server.

E.3.2 Compilation

Depending on the clusters, different compilers are available. In general, the most popular and commonly used are: the GNU Fortran compiler, the Intel compiler and the Portland Group (PGI) compiler. Is always is a good idea to compile with different compilers because it allows to evaluate the robustness of the code and the syntax. In this section the focus is on the Intel compiler.

1. Connect to a CÉCI cluster from your computer. This is widely documented within the CÉCI website so no details will be given here.

2. Copy and paste the Fortran files.

3. To compile, use the `lagamine.build.sh` script located in the `/scripts/build` folder:

   ```
   > ./lagamine_build.sh [compiler_name]
   ```

   The following options are available, all of them using the available intel compiler:

   - `intel_seq` for sequential version.
   - `intel_par` for parallel version (`-openmp`).
   - `intel_deb` for debugging version (`-openmp -g -traceback`).

   All the compilations have the `-O2` optimization flag. The file `lagamine.build.sh` is only an interface for calling the `makefile` contained in the sources folder.

4. For PREPRO there is no script. You need first to add the module:

   ```
   > module add [compiler_module]
   ```

   where `[compiler_module]` could be `intel/compiler/64/11.0/074` depending on the selected cluster. Then compile:

   ```
   > make
   ```

Note. If using Intel MKL subroutines, it is mandatory to use the following environmental variables:

```
export MKL_NUM_THREADS=$nbr_cpu
export MKL_DYNAMIC=true
```

which are defined in all the files within the `scripts/interactive/` folder.

E.3.3 Launching simulations

Since the clusters are operated under GNU/Linux environments, you can compile and launch simulations directly from the GNU/Linux terminal of your machine. Nevertheless, for Windows users who only want to launch simulations there is another way to access to the clusters through the *SSH Secure Shell Client*. Both the software and the documentation can be found in CÉCI website.

To launch simulations, the procedure (both for Windows and GNU/Linux) is the following:

1. Log in into the CÉCI cluster.

2. Locate the execution scripts `prepro.slurm.sh` and `lagamine.slurm.sh`.

3. Go to the location where the simulations are located and then launch the proper scripts:

   ```
   > $HOME/scripts/prepro.slurm.sh [lag_file]
   ```

   Note: You should be careful when naming your simulations files. Linux is case sensitive, so `simu.lag` is not the same as `SIMU.lag`. As a general rule, name your files as follows:

   ```
   simu.lag
   simuex.dat
   simu.dep
   simu.pri
   ```

4. If everything is OK with PREPRO (you can read `NORMAL TERMINATION OF PREPRO` in the `output.prepro` file), proceed with LAGAMINE:

   ```
   > $HOME/scripts/lagamine.slurm.sh [execution_file] [lag_file]
   [number_of_processors] [compiler_name] [compiler_type] [user_email]
   ```

   An example of the last one can be:

   ```
   > $HOME/scripts/lagamine.slurm.sh simuex simu 8 intel parallel foo@ulg.ac.be
   ```

5. You will receive an email confirming that the simulation started in a node. The simulation is performed in a temporary folder (environmental variable `$TMPSCRATCH`), which is specially defined by the cluster to be faster than other directories. If you simulation crashes, the launching script will not be able to retrieve the files from the temporary folder so you will have to manually copy and paste the files into your personal folder.

After a submitting a job, `squeue` gives you the `JOBID` of your running jobs and the node on which they run. For instance:

```
$> squeue -u [user_name]
```

Troubleshooting. Sometimes, it is possible to find segmentation errors (faults) in the LAGAMINE output file. It can appear before the element loop or after a couple the iterations, in the form of a `SIGSEGV` fault. In both cases, the most possible cause is the lack of stack memory[1] given to each OpenMP thread. This can be easily modified augmenting the value of the environmental variable:

```
> export OMP_STACKSIZE=16m
```

where the size is increased to 16 MB per thread. Another option is increase in the size of the initial (master) thread:

```
> ulimit -s unlimited
```

Even if the last option only affects one thread, for some clusters both `OMP_STACKSIZE` and `ulimit` must be defined.

[1]Stack memory, contrary to heap memory, has a limit on the size of variables that can be store.

Bibliography

Abràmoff, M. D., P. J. Magalhães, and S. J. Ram (2004). "Image processing with imageJ." In: *Biophotonics International* 11.7, pp. 36–41. ISSN: 10818693. DOI: 10.1117/1.3589100. arXiv: 1081-8693.

Achouri, M., G. Germain, P. Dal Santo, and D. Saidane (2013). "Experimental characterization and numerical modeling of micromechanical damage under different stress states." In: *Mater. Des.* 50, pp. 207–222. ISSN: 02613069. DOI: 10.1016/j.matdes.2013.02.075.

Aerens, R., P. Eyckens, A. van Bael, and J. Duflou (2009). "Force prediction for single point incremental forming deduced from experimental and FEM observations." In: *The International Journal of Advanced Manufacturing Technology* 46.9-12, pp. 969–982. ISSN: 0268-3768. DOI: 10.1007/s00170-009-2160-2.

Allwood, J. M. and D. R. Shouler (2007). "Paddle forming: a novel class of sheet metal forming processes." In: *CIRP Annals - Manufacturing Technology* 56, pp. 257–260. ISSN: 00078506. DOI: 10.1016/j.cirp.2007.05.060.

Allwood, J. M. and D. R. Shouler (2009). "Generalised forming limit diagrams showing increased forming limits with non-planar stress states." In: *International Journal of Plasticity* 25.7, pp. 1207–1230. ISSN: 07496419. DOI: 10.1016/j.ijplas.2008.11.001.

Allwood, J. M., G. P. F. King, and J. Duflou (2005). "A structured search for applications of the incremental sheet-forming process by product segmentation." In: *Proceedings of the Institution of Mechanical Engineers, Part B: Journal of Engineering Manufacture* 219.2, pp. 239–244. ISSN: 0954-4054. DOI: 10.1243/095440505X8145.

Allwood, J. M., D. R. Shouler, and A. Tekkaya (2007). "The Increased Forming Limits of Incremental Sheet Forming Processes." In: *Key Engineering Materials*. Ed. by M. Geiger, J. Duflou, B. Shirvani, R. Clarke, R. Di Lorenzo, and L. Fratini. Vol. 344. Palermo, Italy: Trans Tech Publications, pp. 621–628. DOI: 10.4028/www.scientific.net/KEM.344.621.

Allwood, J. M., D. Braun, and O. Music (2010). "The effect of partially cut-out blanks on geometric accuracy in incremental sheet forming." In: *Journal of Materials Processing Technology* 210, pp. 1501–1510. ISSN: 09240136. DOI: 10.1016/j.jmatprotec.2010.04.008.

Alves de Sousa, R. J. (2006). "Development of a General Purpose Nonlinear Solid- Shell Element and its Application to Anisotropic Sheet Forming Simulation." PhD Thesis. Universidade de Aveiro.

Alves de Sousa, R. J., R. P. Cardoso, R. A. Fontes Valente, J. W. Yoon, J. J. Grácio, and R. M. Natal Jorge (2005). "A new one-point quadrature enhanced assumed strain (EAS) solid-shell element with multiple integration points along thickness - Part I: geometrically linear applications." In: *International Journal for Numerical Methods in Engineering* 62.7, pp. 952–977. ISSN: 0029-5981. DOI: 10.1002/nme.1226.

Alves de Sousa, R. J., J. W. Yoon, R. P. Cardoso, R. A. Fontes Valente, and J. J. Grácio (2007). "On the use of a reduced enhanced solid-shell (RESS) element for sheet forming simulations." In: *International Journal of Plasticity* 23.3, pp. 490–515. ISSN: 07496419. DOI: 10.1016/j.ijplas.2006.06.004.

Ambrogio, G., I. Costantino, L. De Napoli, L. Filice, L. Fratini, and M. Muzzupappa (2004). "Influence of some relevant process parameters on the dimensional accuracy in incremental forming: a numerical and experimental investigation." In: *Journal of Materials Processing Technology* 153-154, pp. 501–507. ISSN: 09240136. DOI: 10.1016/j.jmatprotec.2004.04.139.

Ambrogio, G., V Cozza, L. Filice, and F. Micari (2007). "An analytical model for improving precision in single point incremental forming." In: *Journal of Materials Processing Technology* 191.1-3, pp. 92–95. ISSN: 09240136. DOI: 10.1016/j.jmatprotec.2007.03.079.

Ambrogio, G., L. Filice, and G. L. Manco (2010). "Improving process performance in incremental sheet forming (ISF)." In: *AIP Conference Proceedings*. Ed. by F. Chinesta, Y. Chastel, and M. El Mansori. Vol. 1315. Paris, France: American Institute of Physics, pp. 613–618. ISBN: 9780735408715. DOI: 10.1063/1.3552515.

Aravas, N. (1987). "On the numerical integration of a class of pressure-dependent plasticity models." In: *International Journal for Numerical Methods in Engineering* 24.7, pp. 1395–1416. ISSN: 0029-5981. DOI: 10.1002/nme.1620240713.

Arfa, H., R. Bahloul, and H. BelHadjSalah (2013). "Finite element modelling and experimental investigation of single point incremental forming process of aluminum sheets: Influence of process parameters

on punch force monitoring and on mechanical and geometrical quality of parts." In: *International Journal of Material Forming* 6.4, pp. 483–510. ISSN: 19606206. DOI: 10.1007/s12289-012-1101-z.

Armstrong, P. and C. Fredrick (1966). *A Mathematical Representation of the Multiaxial Bauschinger Effect*. Technical report. Central Electricity Generating Board.

Arndt, S., B. Svendsen, and D. Klingbeil (1997). "Modellierung der Eigenspannungen an der Rissspitze mit einem Schädigungsmodell." In: *Tech. Mech.* 17.4, pp. 323–332.

Azaouzi, M. and N. Lebaal (2012). "Tool path optimization for single point incremental sheet forming using response surface method." In: *Simulation Modelling Practice and Theory* 24, pp. 49–58. ISSN: 1569190X. DOI: 10.1016/j.simpat.2012.01.008.

Bai, Y. and T. Wierzbicki (2008). "A new model of metal plasticity and fracture with pressure and Lode dependence." In: *Int. J. Plast.* 24.6, pp. 1071–1096. ISSN: 07496419. DOI: 10.1016/j.ijplas.2007.09.004.

Bai, Y. and T. Wierzbicki (2009). "Application of extended Mohr-Coulomb criterion to ductile fracture." In: *Int. J. Fract.* 161.1, pp. 1–20. ISSN: 0376-9429. DOI: 10.1007/s10704-009-9422-8.

Bambach, M. (2004). "Modeling of Optimization Strategies in the Incremental CNC Sheet Metal Forming Process." In: *NUMIFORM*. AIP, pp. 1969–1974. DOI: 10.1063/1.1766822.

Bambach, M. (2010). "A geometrical model of the kinematics of incremental sheet forming for the prediction of membrane strains and sheet thickness." In: *Journal of Materials Processing Technology* 210.12, pp. 1562–1573. ISSN: 09240136. DOI: 10.1016/j.jmatprotec.2010.05.003.

Bambach, M. (2014). "Fast simulation of asymmetric incremental sheet metal forming." In: *International Journal of Material Forming*, pp. 1–8. ISSN: 1960-6206. DOI: 10.1007/s12289-014-1204-9.

Bambach, M. and G. Hirt (2005). "Performance Assessment of Element Formulations and Constitutive Laws for the Simulation of Incremental Sheet Forming (ISF)." In: *COMPLAS*. Ed. by E. Oñate and D. Owen. Barcelona: CIMNE, pp. 1–4.

Bambach, M., G. Hirt, and S. Junk (2003). "Modelling and experimental evaluation of the incremental CNC sheet metal forming process." In: *7th International Conference on Computational Plasticity*. Barcelona, pp. 447–455.

Bambach, M., J. Ames, M. Azaouzi, L. Campagne, G. Hirt, and J. Batoz (2005). "Initial experimental and numerical investigations into a class of new strategies for single point incremental forming simulations." In: *Proceedings of the 8th ESAFORM Conference on Material Forming*. Ed. by D. Banabic. Cluj-Napoca, Romania, pp. 671–674.

Bambach, M., B. Taleb Araghi, and G. Hirt (2009). "Strategies to improve the geometric accuracy in asymmetric single point incremental forming." In: *Production Engineering* 3.2, pp. 145–156. ISSN: 0944-6524. DOI: 10.1007/s11740-009-0150-8.

Banabic, D., H. J. Bunge, K. Pöhlandt, and A. Tekkaya (2000). *Formability of metallic materials: plastic anisotropy, formability testing, forming limits*. Ed. by D. Banabic. Berlin: Springer Science & Business Media.

Banabic, D., H. Aretz, D. S. Comsa, and L. Paraianu (2005). "An improved analytical description of orthotropy in metallic sheets." In: *International Journal of Plasticity* 21.3, pp. 493–512. ISSN: 07496419. DOI: 10.1016/j.ijplas.2004.04.003.

Bardet, J. P. (1990). "Lode Dependences for Isotropic Pressure-Sensitive Elastoplastic Materials." In: *J. Appl. Mech.* 57.3, p. 498. ISSN: 00218936. DOI: 10.1115/1.2897051.

Barlat, F. and K. Lian (1989). "Plastic behavior and stretchability of sheet metals. Part I: A yield function for orthotropic sheets under plane stress conditions." In: *International Journal of Plasticity* 5.1, pp. 51–66. ISSN: 07496419. DOI: 10.1016/0749-6419(89)90019-3.

Barlat, F., D. J. Lege, and J. C. Brem (1991). "A six-component yield function for anisotropic materials." In: *International Journal of Plasticity* 7.7, pp. 693–712. ISSN: 07496419. DOI: 10.1016/0749-6419(91)90052-Z.

Barlat, F., J. C. Brem, J. W. Yoon, K. Chung, R. Dick, D. Lege, F. Pourboghrat, S.-H. Choi, and E. Chu (2003). "Plane stress yield function for aluminum alloy sheets-part 1: theory." In: *International Journal of Plasticity* 19.9, pp. 1297–1319. ISSN: 07496419. DOI: 10.1016/S0749-6419(02)00019-0.

Barsoum, I. and J. Faleskog (2007). "Rupture mechanisms in combined tension and shear-Experiments." In: *Int. J. Solids Struct.* 44.6, pp. 1768–1786. ISSN: 00207683. DOI: 10.1016/j.ijsolstr.2006.09.031.

Bauschinger, J. (1886). *Über die Veränderung der Elastizitätsgrenze und die Festigkeit des Eisens und Stahls durch Strecken und Quetschen, durch Erwärmen und Abkühlen und durch oftmals wiederholte Beanspruchungen*. Tech. rep. Munich, Germany: Königlich Bayerische Technische Hochschule München.

Bauvineau, L., H. Burlet, C. Eripret, and A. Pineau (1996). "Modelling Ductile Stable Crack Growth in a C-Mn Steel with Local Approaches." In: *Le J. Phys. IV* 6.C6, pp. 33–42. ISSN: 1155-4339. DOI: 10.1051/jp4:1996604.

Beese, A. M. and D. Mohr (2012). "Anisotropic plasticity model coupled with Lode angle dependent strain-induced transformation kinetics law." In: *J. Mech. Phys. Solids* 60.11, pp. 1922–1940. ISSN: 00225096. DOI: 10.1016/j.jmps.2012.06.009.

Behera, A. K. (2013). "Shape Feature Taxonomy Development for Toolpath Optimisation in Incremental Sheet Forming (Ontwikkeling van een taxonomie van vormkenmerken voor optimalisatie van gereedschapsbanen voor incrementeel omvormen)." PhD thesis. Katholieke Universiteit Leuven.

Behera, A. K., H. Vanhove, B. Lauwers, and J. Duflou (2011). "Accuracy Improvement in Single Point Incremental Forming through Systematic Study of Feature Interactions." In: *Key Engineering Materials*. Ed. by J. Duflou, R. Clarke, M. Merklein, F. Micari, B. Shirvani, and K. Kellens. Vol. 473. Leuven, Belgium: Trans Tech Publications, pp. 881–888. DOI: 10.4028/www.scientific.net/KEM.473.881.

Behera, A. K., B. Lauwers, and J. Duflou (2013a). "Tool Path Generation for Single Point Incremental Forming Using Intelligent Sequencing and Multi-Step Mesh Morphing Techniques." In: *Key Engineering Materials*. Ed. by R. J. Alves de Sousa and R. Valente. Vol. 554-557. Aveiro, Portugal: Trans Tech Publications, pp. 1408–1418. DOI: 10.4028/www.scientific.net/KEM.554-557.1408.

Behera, A. K., J. Verbert, B. Lauwers, and J. Duflou (2013b). "Tool path compensation strategies for single point incremental sheet forming using multivariate adaptive regression splines." In: *Computer-Aided Design* 45.3, pp. 575–590. ISSN: 00104485. DOI: 10.1016/j.cad.2012.10.045.

Belchior, J., D. Guines, L. Leotoing, and E. Ragneau (2013). "Force Prediction for Correction of Robot Tool Path in Single Point Incremental Forming." In: *Key Engineering Materials*. Ed. by R. J. Alves de Sousa and R. Valente. Vol. 554-557. Aveiro, Portugal: Trans Tech Publications, pp. 1282–1289. ISBN: 9783037857199. DOI: 10.4028/www.scientific.net/KEM.554-557.1282.

Belytschko, T. and L. Bindeman (1991). "Assumed strain stabilization of the 4-node quadrilateral with 1-point quadrature for nonlinear problems." In: *Computer Methods in Applied Mechanics and Engineering* 88.3, pp. 311–340. ISSN: 00457825. DOI: 10.1016/0045-7825(91)90093-L.

Ben Ayed, L., C. Robert, A. Delamézière, M. Nouari, and J. Batoz (2014). "Simplified numerical approach for incremental sheet metal forming process." In: *Engineering Structures* 62-63, pp. 75–86. ISSN: 01410296. DOI: 10.1016/j.engstruct.2014.01.033.

Ben Bettaieb, A., L. Duchêne, L. Zhang, and A. M. Habraken (2011a). "New solid-shell finite element based on EAS and ANS concepts for sheet metal forming." In: *AIP Conference Proceedings*. Ed. by K. Chung, H. N. Han, H. Huh, F. Barlat, and M. Lee. Vol. 1383. Seoul, Korea, pp. 374–381. ISBN: 9780735409491. DOI: 10.1063/1.3623634.

Ben Bettaieb, A., J. I. V. Sena, R. J. Alves de Sousa, R. Valente, A. M. Habraken, and L. Duchêne (2015). "On the comparison of two solid-shell formulations based on in-plane reduced and full integration schemes in linear and non-linear applications." In: *Finite Elements in Analysis and Design* 107, pp. 44–59. ISSN: 0168874X. DOI: 10.1016/j.finel.2015.08.005.

Ben Bettaieb, M. (2008). *Literature review: state of the art of rupture criteria*. Technical report January. Liège: Université de Liège.

Ben Bettaieb, M., X. Lemoine, O. Bouaziz, A. M. Habraken, and L. Duchêne (2011b). "Numerical modeling of damage evolution of DP steels on the basis of X-ray tomography measurements." In: *Mech. Mater.* 43.3, pp. 139–156. ISSN: 01676636. DOI: 10.1016/j.mechmat.2011.02.005.

Ben Bettaieb, M., X. Lemoine, L. Duchêne, and A. M. Habraken (2011c). "On the numerical integration of an advanced Gurson model." In: *Int. J. Numer. Methods Eng.* 85.8, pp. 1049–1072. ISSN: 00295981. DOI: 10.1002/nme.3010.

Ben Bettaieb, M., O. Débordes, A. Dogui, L. Duchêne, and C. Keller (2012). "On the numerical integration of rate independent single crystal behavior at large strain." In: *International Journal of Plasticity* 32-33, pp. 184–217. ISSN: 07496419. DOI: 10.1016/j.ijplas.2011.10.010.

Benseddiq, N. and A. Imad (2008). "A ductile fracture analysis using a local damage model." In: *Int. J. Press. Vessel. Pip.* 85.4, pp. 219–227. ISSN: 03080161. DOI: 10.1016/j.ijpvp.2007.09.003.

Benzerga, A. A. (2000). "Rupture ductile des tôles anisotropes." PhD. École Nationale Supérieure des Mines de Paris.

Benzerga, A. A. and J. Besson (2001). "Plastic potentials for anisotropic porous solids." In: *Eur. J. Mech. - A/Solids* 20.3, pp. 397–434. ISSN: 09977538. DOI: 10.1016/S0997-7538(01)01147-0.

Benzerga, A. A. and J.-B. Leblond (2010). "Ductile Fracture by Void Growth to Coalescence." In: *Adv. Appl. Mech.* Advances in Applied Mechanics 44. Ed. by H. Aref and E. van der Giessen, pp. 169–305. ISSN: 0065-2156. DOI: 10.1016/S0065-2156(10)44003-X.

Benzerga, A. A., J. Besson, and A. Pineau (2004). "Anisotropic ductile fracture - Part I: experiments." In: *Acta Mater.* 52.15, pp. 4623–4638. ISSN: 13596454. DOI: 10.1016/j.actamat.2004.06.020.

Berdin, C., J. Besson, S. Bugat, R. Desmorat, and F. Feyel (2004). *Local approach to fracture*. Ed. by J. Besson. Paris, France: Presses de l'Ecole des Mines. ISBN: 2-911762-55-X.

Besson, J. (2004). "Model Identification." In: *Local approach to Fract.* Ed. by J. Besson. Paris, France: Presses de l'Ecole des Mines. Chap. XII, pp. 373–394. ISBN: 2-911762-55-X.

Besson, J. (2009). "Continuum Models of Ductile Fracture: A Review." In: *Int. J. Damage Mech.* 19.1, pp. 3–52. ISSN: 1056-7895. DOI: 10.1177/1056789509103482.

Bishop, J. F. W. and R. Hill (1951). "XLVI. A theory of the plastic distortion of a polycrystalline aggregate under combined stresses." In: *Philosophical Magazine Series 7* 42.327, pp. 414–427. DOI: 10.1080/14786445108561065.

Bouaziz, O., É. Maire, M. Giton, J. Lamarre, Y. Salingue, and M. Dimichiele (2008). "A model for initiation and growth of damage in dualphase steels identified by X-ray micro-tomography." In: *Rev. Métallurgie* 105.2, pp. 102–107. ISSN: 0035-1563. DOI: 10.1051/metal:2008021.

Bouchard, P.-O., L. Bourgeon, H. Lachapèle, É. Maire, C. Verdu, R. Forestier, and R. Logé (2008). "On the influence of particle distribution and reverse loading on damage mechanisms of ductile steels." In: *Mater. Sci. Eng. A* 496.1-2, pp. 223–233. ISSN: 09215093. DOI: 10.1016/j.msea.2008.05.033.

Bouffioux, C., C. Henrard, J. Gu, J. Duflou, A. M. Habraken, and H. Sol (2007). "Development of an inverse method for identification of material parameters in the single point incremental forming process." In: *Proceedings of the International Conference of International Deep Drawing Research Group (IDDRG 2007)*. Ed. by M. Tisza. May. Gyor, Hungary.

Bouffioux, C., C. Henrard, P. Eyckens, R. Aerens, A. van Bael, H. Sol, J. Duflou, and A. M. Habraken (2008a). "Comparison of the tests chosen for material parameter identification to predict single point incremental forming forces." In: *Proceedings of the International Conference of International Deep Drawing Research Group (IDDRG 2008)*. Ed. by N. Asnafi. Olofström, Sweden, pp. 133–144.

Bouffioux, C., P. Eyckens, C. Henrard, R. Aerens, A. van Bael, H. Sol, J. Duflou, and A. M. Habraken (2008b). "Identification of material parameters to predict Single Point Incremental Forming forces." In: *Proceedings of the 11th ESAFORM Conference on Material Forming*. Lyon, France: Springer, pp. 1147–1150.

Bouffioux, C., P. Pouteau, L. Duchêne, H. Vanhove, J. Duflou, and A. M. Habraken (2010). "Material data identification to model the single point incremental forming process." In: *International Journal of Material Forming* 3.SUPPL. 1, pp. 979–982. ISSN: 19606206. DOI: 10.1007/s12289-010-0933-7.

Bouffioux, C., C. Lequesne, H. Vanhove, J. Duflou, P. Pouteau, L. Duchêne, and A. M. Habraken (2011). "Experimental and numerical study of an AlMgSc sheet formed by an incremental process." In: *Journal of Materials Processing Technology* 211.11, pp. 1684–1693. ISSN: 09240136. DOI: 10.1016/j.jmatprotec.2011.05.010.

Bouvier, S., H. Haddadi, P. Levée, and C. Teodosiu (2006). "Simple shear tests: Experimental techniques and characterization of the plastic anisotropy of rolled sheets at large strains." In: *Journal of Materials Processing Technology* 172.1, pp. 96–103. ISSN: 09240136. DOI: 10.1016/j.jmatprotec.2005.09.003.

Bridgman, P. W. (1952). *Studies in large plastic flow and fracture with special emphasis on the effects of hydrostatic pressure*. McGraw-Hill.

Bron, F. and J. Besson (2006). "Simulation of the ductile tearing for two grades of 2024 aluminum alloy thin sheets." In: *Eng. Fract. Mech.* 73.11, pp. 1531–1552. ISSN: 00137944. DOI: 10.1016/j.engfracmech.2006.01.024.

Brown, L. and J. Embury (1973). "Initiation and growth of voids at second-phase particles." In: *Microstruct. Des. Alloy.* Cambridge, UK: The Institute of Metals, The Iron, and Steel Institute, pp. 164–169.

Brünig, M., S. Berger, and H. Obrecht (2000). "Numerical simulation of the localization behavior of hydrostatic-stress-sensitive metals." In: *Int. J. Mech. Sci.* 42.11, pp. 2147–2166. ISSN: 00207403. DOI: 10.1016/S0020-7403(00)00002-3.

Brunssen, S. and B. I. Wohlmuth (2009). "An overlapping domain decomposition method for the simulation of elastoplastic incremental forming processes." In: *International Journal for Numerical Methods in Engineering* 77, pp. 1224–1246. DOI: 10.1002/nme.

Cao, T., B. Lu, D. Xu, H. Zhang, J. Chen, H. Long, and J. Cao (2014). "An efficient method for thickness prediction in multi-pass incremental sheet forming." In: *The International Journal of Advanced Manufacturing Technology*. ISSN: 0268-3768. DOI: 10.1007/s00170-014-6489-9.

Carnoy, E. G. (1981). "Mixed finite elements based upon marguerre theory for the study of geometrically nonlinear behavior of thin shells." In: *Computer Methods in Applied Mechanics and Engineering* 29.2, pp. 121–146. ISSN: 00457825. DOI: 10.1016/0045-7825(81)90110-9.

Cazacu, O., B. Plunkett, and F. Barlat (2006). "Orthotropic yield criterion for hexagonal closed packed metals." In: *International Journal of Plasticity* 22.7, pp. 1171–1194. ISSN: 07496419. DOI: 10.1016/j.ijplas.2005.06.001.

Cerro, I., E. Maidagan, J. Arana, A. Rivero, and P. Rodríguez (2006). "Theoretical and experimental analysis of the dieless incremental sheet forming process." In: *Journal of Materials Processing Technology* 177.1-3, pp. 404–408. ISSN: 09240136. DOI: 10.1016/j.jmatprotec.2006.04.078.

Cescotto, S. and R. Charlier (1993). "Frictional contact finite elements based on mixed variational principles." In: *International Journal for Numerical Methods in Engineering* 36.10, pp. 1681–1701. ISSN: 0029-5981. DOI: 10.1002/nme.1620361005.

Chaboche, J.-L. (1977). "Viscoplastic constitutive equations for the description of cyclic and anisotropic behavior of metals." In: *Bulletin de L'Academie Polonaise des Science, Série de Science Techniques* 25.1, pp. 33–42.

Charlier, R. (1987). "Approche Unifiée de Quelques Problèmes Non Linéaires de Mécanique des Milieux Continus par la Méthode des Éléments Finis." PhD thesis. University of Liège.

Charpentier, P. L. (1975). "Influence of punch curvature on the stretching limits of sheet steel." In: *Metallurgical Transactions A* 6.8, pp. 1665–1669. ISSN: 03602133. DOI: 10.1007/BF02641986.

Chu, C. C. and A. Needleman (1980). "Void Nucleation Effects in Biaxially Stretched Sheets." In: *J. Eng. Mater. Technol.* 102.3, p. 249. ISSN: 00944289. DOI: 10.1115/1.3224807.

Considère, M. (1885). "L'emploi du fer et de l'acier dans les constructions." In: *Ann. des ponts chaussées* 1, pp. 574–775.

Coppola, T., L. Cortese, and P. Folgarait (2009). "The effect of stress invariants on ductile fracture limit in steels." In: *Eng. Fract. Mech.* 76.9, pp. 1288–1302. ISSN: 00137944. DOI: 10.1016/j.engfracmech.2009.02.006.

Crisfield, M. A. (1991). *Non-linear finite element analysis of solids and structures: essential topics*. 1st. John Wiley & Sons, Inc. ISBN: 0 471 92956 5.

Cui, Z., Z. Cedric Xia, F. Ren, V. Kiridena, and L. Gao (2013). "Modeling and validation of deformation process for incremental sheet forming." In: *Journal of Manufacturing Processes* 15.2, pp. 236–241. ISSN: 15266125. DOI: 10.1016/j.jmapro.2013.01.003.

Danas, K. and P. Ponte Castañeda (2012). "Influence of the Lode parameter and the stress triaxiality on the failure of elasto-plastic porous materials." In: *Int. J. Solids Struct.* 49.11-12, pp. 1325–1342. ISSN: 00207683. DOI: 10.1016/j.ijsolstr.2012.02.006.

Debongnie, J.-F. (1979). "Physical interpretation and generalization of Marguerre's shallow shell theory." In: *International Journal of Engineering Science* 17.4, pp. 387–399. ISSN: 00207225. DOI: 10.1016/0020-7225(79)90075-2.

Dejardin, S., S. Thibaud, J. Gelin, and G. Micheli (2010). "Experimental investigations and numerical analysis for improving knowledge of incremental sheet forming process for sheet metal parts." In: *Journal of Materials Processing Technology* 210.2, pp. 363–369. ISSN: 09240136. DOI: 10.1016/j.jmatprotec.2009.09.025.

Delamézière, A., Y Yu, C. Robert, L. B. Ayed, M. Nouari, J. Batoz, F. Chinesta, Y. Chastel, and M. El Mansori (2011). "Numerical Simulation of Incremental Sheet Forming by Simplified Approach." In: *AIP Conference Proceedings*. Ed. by F. Chinesta, Y. Chastel, and M. El Mansori. Paris, France: American Institute of Physics, pp. 619–624. DOI: 10.1063/1.3552516.

Drucker, D. and W. Prager (1952). "Soil Mechanics and Plastic Analysis or Limit Design." In: *Quarterly of Applied Mathematics* 10.2, pp. 157–165.

Duchêne, L., F. El Houdaigui, A. M. Habraken, and F Elhoudaigui (2007). "Length changes and texture prediction during free end torsion test of copper bars with FEM and remeshing techniques." In: *International Journal of Plasticity* 23.8, pp. 1417–1438. ISSN: 07496419. DOI: 10.1016/j.ijplas.2007.01.008.

Duchêne, L., A. Ben Bettaieb, and A. M. Habraken (2011). "Assessment of the Enhanced Assumed Strain (EAS) and the Assumed Natural Strain (ANS) techniques in the mechanical behavior of the SSH3D solid-shell element." In: *COMPLAS*. Ed. by E. Oñate, D. Owen, D. Peric, and B. Suárez. Barcelona.

Duchêne, L., C. F. Guzmán, A. K. Behera, J. Duflou, and A. M. Habraken (2013). "Numerical Simulation of a Pyramid Steel Sheet Formed by Single Point Incremental Forming using Solid-Shell Finite Elements." In: *Key Engineering Materials*. Ed. by R. Clarke, A. Leacock, J. R. Duflou, M. Merklein, and F. Micari. Vol. 549. Belfast, United Kingdom: Trans Tech Publications, pp. 180–188. DOI: 10.4028/www.scientific.net/KEM.549.180.

Duflou, J., B. Lauwers, J. Verbert, Y. Tunckol, and H. De Baerdemaeker (2005). "Achievable Accuracy in Single Point Incremental Forming: Case Studies." In: *Proceedings of the 8th ESAFORM Conference on Material Forming*. Ed. by D. Banabic. Vol. 2. Cluj-Napoca, Romania, pp. 675–678.

Duflou, J., B. Callebaut, J. Verbert, and H. De Baerdemaeker (2007). "Laser Assisted Incremental Forming: Formability and Accuracy Improvement." In: *CIRP Annals - Manufacturing Technology* 56.1, pp. 273–276. ISSN: 00078506. DOI: 10.1016/j.cirp.2007.05.063.

Duflou, J., B. Callebaut, J. Verbert, and H. De Baerdemaeker (2008a). "Improved SPIF performance through dynamic local heating." In: *International Journal of Machine Tools and Manufacture* 48.5, pp. 543–549. ISSN: 08906955. DOI: 10.1016/j.ijmachtools.2007.08.010.

Duflou, J., J. Verbert, B. Belkassem, J. Gu, H. Sol, C. Henrard, and A. M. Habraken (2008b). "Process window enhancement for single point incremental forming through multi-step toolpaths." In: *CIRP Annals - Manufacturing Technology* 57.1, pp. 253–256. ISSN: 00078506. DOI: 10.1016/j.cirp.2008.03.030.

Duflou, J., H. Vanhove, J. Verbert, J. Gu, I. Vasilakos, and P. Eyckens (2010). "Twist revisited: Twist phenomena in single point incremental forming." In: *CIRP Annals - Manufacturing Technology* 59.1, pp. 307–310. ISSN: 00078506. DOI: 10.1016/j.cirp.2010.03.018.

Dunand, M. and D. Mohr (2010). "Hybrid experimental-numerical analysis of basic ductile fracture experiments for sheet metals." In: *Int. J. Solids Struct.* 47.9, pp. 1130–1143. ISSN: 00207683. DOI: 10.1016/j.ijsolstr.2009.12.011.

Dunand, M. and D. Mohr (2011a). "On the predictive capabilities of the shear modified Gurson and the modified Mohr-Coulomb fracture models over a wide range of stress triaxialities and Lode angles." In: *J. Mech. Phys. Solids* 59.7, pp. 1374–1394. ISSN: 00225096. DOI: 10.1016/j.jmps.2011.04.006.

Dunand, M. and D. Mohr (2011b). "Optimized butterfly specimen for the fracture testing of sheet materials under combined normal and shear loading." In: *Eng. Fract. Mech.* 78.17, pp. 2919–2934. ISSN: 00137944. DOI: 10.1016/j.engfracmech.2011.08.008.

Durante, M., a. Formisano, a. Langella, and F. Capece Minutolo (2009). "The influence of tool rotation on an incremental forming process." In: *Journal of Materials Processing Technology* 209.9, pp. 4621–4626. ISSN: 09240136. DOI: 10.1016/j.jmatprotec.2008.11.028.

Dvorkin, E. N. and K.-J. Bathe (1984). "A continuum mechanics based four-node shell element for general non-linear analysis." In: *Engineering Computations* 1.1, pp. 77–88. ISSN: 0264-4401. DOI: 10.1108/eb023562.

Elford, M., P. Saha, D. Seong, M. Z. Haque, and J. W. Yoon (2013). "Benchmark 3 - Incremental sheet forming." In: *AIP Conference Proceedings*. Ed. by J. W. Yoon, T. B. Stoughton, B. Rolfe, J. H. Beynon, and P. Hodgson. Vol. 227. Melbourne, Australia: American Institute of Physics, pp. 227–261. ISBN: 9780735411951. DOI: 10.1063/1.4849983.

Emmens, W. C. (2011a). *Formability*. Berlin: Springer Berlin Heidelberg. ISBN: 978-3-642-21903-0. DOI: 10.1007/978-3-642-21904-7.

Emmens, W. C. (2011b). "Shear." In: *Formability*. Ed. by W. C. Emmens. Berlin: Springer Berlin Heidelberg. Chap. 9, pp. 45–50. ISBN: 978-3-642-21903-0. DOI: 10.1007/978-3-642-21904-7.

Emmens, W. C. and A. van den Boogaard (2007). "Strain in Shear, and Material Behaviour in Incremental Forming." In: *Key Engineering Materials*. Ed. by M. Geiger, J. Duflou, B. Shirvani, R. Clarke, R. Di Lorenzo, and L. Fratini. Vol. 344. Palermo, Italy: Trans Tech Publications, pp. 519–526. DOI: 10.4028/www.scientific.net/KEM.344.519.

Emmens, W. C. and A. van den Boogaard (2008). "Tensile tests with bending: A mechanism for incremental forming." In: *International Journal of Material Forming*. Ed. by P. Boisse, F. Morestin, and E. Vidal-Sallé. Vol. 1. S1. Lyon, France: Springer-Verlag, pp. 1155–1158. DOI: 10.1007/s12289-008-0185-y.

Emmens, W. C. and A. van den Boogaard (2009a). "An overview of stabilizing deformation mechanisms in incremental sheet forming." In: *Journal of Materials Processing Technology* 209.8, pp. 3688–3695. ISSN: 09240136. DOI: 10.1016/j.jmatprotec.2008.10.003.

Emmens, W. C. and A. van den Boogaard (2009b). "Incremental Sheet Forming Analysed by Tensile Tests." In: *Key Engineering Materials*. Ed. by B. Shirvani, R. Clarke, J. Duflou, M. Merklein, F. Micari, and J. Griffiths. Vol. 410-411. Birmingham, England: Trans Tech Publications, pp. 347–354. DOI: 10.4028/www.scientific.net/KEM.410-411.347.

Emmens, W. C. and A. van den Boogaard (2009c). "Incremental forming by continuous bending under tension-An experimental investigation." In: *Journal of Materials Processing Technology* 209.14, pp. 5456–5463. ISSN: 0924-0136. DOI: http://dx.doi.org/10.1016/j.jmatprotec.2009.04.023.

Emmens, W. C. and A. van den Boogaard (2010). "Contact Effects in Bending Affecting Stress and Formability." In: *International Journal of Material Forming* 3.S1, pp. 1159–1162. ISSN: 1960-6206. DOI: 10.1007/s12289-010-0978-7.

Emmens, W. C. and A. van den Boogaard (2011). "Cyclic stretch-bending: Mechanics, stability and formability." In: *Journal of Materials Processing Technology* 211.12, pp. 1965–1981. ISSN: 09240136. DOI: 10.1016/j.jmatprotec.2011.06.017.

Essa, K. and P. Hartley (2010). "An assessment of various process strategies for improving precision in single point incremental forming." In: *International Journal of Material Forming* 4.4, pp. 401–412. ISSN: 1960-6206. DOI: 10.1007/s12289-010-1004-9.

Eyckens, P. (2010). "Formability In Incremental Sheet Forming: Generalization of the Marciniak-Kuczynski model." PhD thesis. Katholieke Universiteit Leuven.

Eyckens, P. and A. van Bael (2006). *DL22: Texture analysis of the initial sheets*. Tech. rep. Leuven, Belgium: KULeuven.

Eyckens, P. and A. van Bael (2007). *DL22b: Tensile test results of the initial sheets*. Tech. rep. Leuven, Belgium: KULeuven.

Eyckens, P., S. He, A. van Bael, P. van Houtte, and J. Duflou (2007). "Forming Limit Predictions for the Serrated Strain Paths in Single Point Incremental Sheet Forming." In: *AIP Conference Proceedings*. Vol. 908. Porto, Portugal: AIP, pp. 141–146. DOI: 10.1063/1.2740802.

Eyckens, P., A. van Bael, and P. van Houtte (2008). "An extended Marciniak-Kuczynski forming limit model to assess the influence of through-thickness shear on formability." In: *Proceedings of the 7th International Conference and Workshop on Numerical Simulation od 3D Sheet Metal Forming Processes*. Ed. by P. Hora, pp. 193–198.

Eyckens, P., A. van Bael, and P. van Houtte (2009). "Marciniak-Kuczynski type modelling of the effect of Through-Thickness Shear on the forming limits of sheet metal." In: *International Journal of Plasticity* 25.12, pp. 2249–2268. ISSN: 07496419. DOI: 10.1016/j.ijplas.2009.02.002.

Eyckens, P., B. Belkassem, C. Henrard, J. Gu, H. Sol, A. M. Habraken, J. Duflou, A. Bael, and P. van Houtte (2010). "Strain evolution in the single point incremental forming process: digital image correlation measurement and finite element prediction." In: *International Journal of Material Forming*, pp. 55–71. ISSN: 1960-6206. DOI: 10.1007/s12289-010-0995-6.

Eyckens, P., A. van Bael, and P. van Houtte (2011a). "An extended Marciniak-Kuczynski model for anisotropic sheet subjected to monotonic strain paths with through-thickness shear." In: *International Journal of Plasticity* 27.10, pp. 1577–1597. ISSN: 07496419. DOI: 10.1016/j.ijplas.2011.03.008.

Eyckens, P., H. Vanhove, A. van Bael, J. Duflou, and P. van Houtte (2011b). "Tool Directionality in Contour-Based Incremental Sheet Forming: an Experimental Study on Product Properties and Formability." In: *Key Engineering Materials*. Ed. by J. Duflou, R. Clarke, M. Merklein, F. Micari, B. Shirvani, and K. Kellens. Vol. 473. Leuven, Belgium: Trans Tech Publications, pp. 897–904. DOI: 10.4028/www.scientific.net/KEM.473.897.

Faleskog, J., X. Gao, and C. F. Shih (1998). "Cell model for nonlinear fracture analysis - I. Micromechanics calibration." In: *Int. J. Fract.* 89.4, pp. 355–373. DOI: 10.1023/A:1007421420901.

Fansi, J. (2013). "Prediction of DP steel fracture by FEM simulations using an advanced Gurson model." PhD thesis. Universiy of Liège, Art et Métiers ParisTech.

Fansi, J., T. Balan, X. Lemoine, É. Maire, C. Landron, O. Bouaziz, M. Ben Bettaieb, and A. Marie Habraken (2013). "Numerical investigation and experimental validation of physically-based advanced GTN model for DP steels." In: *Mater. Sci. Eng. A*. ISSN: 09215093. DOI: 10.1016/j.msea.2013.01.019.

Felippa, C. A. (2000). "On the Original Publication of the General Canonical Functional of Linear Elasticity." In: *Journal of Applied Mechanics* 67.1, p. 217. ISSN: 00218936. DOI: 10.1115/1.321170.

Filice, L., L. Fratini, and F. Micari (2002). "Analysis of Material Formability in Incremental Forming." In: *CIRP Annals - Manufacturing Technology* 51.1, pp. 199–202. ISSN: 00078506. DOI: 10.1016/S0007-8506(07)61499-1.

Flores, P. (2003). "Experimental and Theoretical Development of Tensile-Shear Test on Metal Sheets." DEA. University of Liège.

Flores, P. (2005). "Development of Experimental Equipment and Identification Procedures for Sheet Metal Constitutive Laws." PhD thesis. Université de Liège.

Flores, P., L. Duchêne, C. Bouffioux, T. Lelotte, C. Henrard, N. Pernin, A. van Bael, S. He, J. Duflou, and A. M. Habraken (2007). "Model identification and FE simulations: Effect of different yield loci and hardening laws in sheet forming." In: *International Journal of Plasticity* 23.3, pp. 420–449. ISSN: 07496419. DOI: 10.1016/j.ijplas.2006.05.006.

Fraeijs de Veubeke, B. (1951). "Diffusion des inconnues hyperstatiques dans les voilures à longeron couplés." In: *Bulletin du Service Technique de l'Aéronautique* 24, pp. 1–56.

Fraeijs de Veubeke, B. (1965). "Displacement and equilibrium models in the finite element method." In: *Stress Analysis*. Ed. by O. C. Zienkiewicz and G. Holister. London, England: John Wiley & Sons. Chap. 9, pp. 145–197. DOI: 10.1002/nme.339.

François, D., A. Pineau, and A. Zaoui (2012). "Elastoviscoplasticity." In: *Mechanical Behaviour of Materials: Volume 1: Micro- and Macroscopic Constitutive Behaviour*. Vol. 180. Solid Mechanics and Its Applications. Dordrecht: Springer Netherlands. Chap. 4, pp. 363–444. ISBN: 978-94-007-2545-4. DOI: 10.1007/978-94-007-2546-1.

François, D., A. Pineau, and A. Zaoui (2013). "Ductile Fracture." In: *Mech. Behav. Mater.* Vol. 191. Solid Mechanics and Its Applications. Dordrecht: Springer Netherlands. Chap. 4, pp. 193–264. ISBN: 978-94-007-4929-0. DOI: 10.1007/978-94-007-4930-6.

Franklin, A. G. (1969). "Comparison between a quantitative microscope and chemical methods for assessment of non-metallic inclusions." In: *J. Iron Steel Inst.* 207.2, pp. 181–186.

Frederick, C. O. and P. J. Armstrong (2007). "A mathematical representation of the multiaxial Bauschinger effect." In: *Materials at High Temperatures* 24.1, pp. 1–26. ISSN: 09603409. DOI: 10.3184/096034007X207589.

Fu, Z., J. Mo, F. Han, and P. Gong (2013). "Tool path correction algorithm for single-point incremental forming of sheet metal." In: *International Journal of Advanced Manufacturing Technology* 64.9-12, pp. 1239–1248. ISSN: 02683768. DOI: 10.1007/s00170-012-4082-7.

Gao, X., J. Faleskog, and C. F. Shih (1998). "Cell model for nonlinear fracture analysis - II. Fracture-process calibration and verification." In: *Int. J. Fract.* 89.4, pp. 375–398. DOI: 10.1023/A:1007410825313.

Gao, X., G. Zhang, and C. Roe (2009). "A Study on the Effect of the Stress State on Ductile Fracture." In: *Int. J. Damage Mech.* 19.1, pp. 75–94. ISSN: 1056-7895. DOI: 10.1177/1056789509101917.

Garrison, W. and N. Moody (1987). "Ductile fracture." In: *J. Phys. Chem. Solids* 48.11, pp. 1035–1074. ISSN: 00223697. DOI: 10.1016/0022-3697(87)90118-1.

Geuzaine, C. and J.-F. Remacle (2009). "Gmsh: A 3-D finite element mesh generator with built-in pre- and post-processing facilities." In: *International Journal for Numerical Methods in Engineering* 79.11, pp. 1309–1331. ISSN: 00295981. DOI: 10.1002/nme.2579.

Ghosh, A. K. and S. S. Hecker (1974). "Stretching limits in sheet metals: In-plane versus out-of-plane deformation." In: *Metallurgical Transactions* 5.10, pp. 2161–2164. ISSN: 03602133. DOI: 10.1007/BF02643929.

Gilles, G. (2015). "Experimental study and modeling of the quasi-static mechanical behavior of Ti6Al4V at room temperature." PhD thesis. University of Liège.

Gologanu, M., J.-B. Leblond, and J. Devaux (1993). "Approximate models for ductile metals containing non-spherical voids-Case of axisymmetric prolate ellipsoidal cavities." In: *J. Mech. Phys. Solids* 41.11, pp. 1723–1754. ISSN: 00225096. DOI: 10.1016/0022-5096(93)90029-F.

Gologanu, M., J.-B. Leblond, G. Perrin, and J. Devaux (1996). "Recent extensions of Gurson's model for porous ductile materials." In: *Int. Semin. Micromechanics*. Udine, Italy, pp. 61–130.

Goods, S. and L. Brown (1979). "Overview No. 1." In: *Acta Metall.* 27.1, pp. 1–15. ISSN: 00016160. DOI: 10.1016/0001-6160(79)90051-8.

Gotoh, M., T. Chung, and N. Iwata (1995). "Effect of Out-of-Plane Stress on the Forming Limit Strain of Sheet Metals." In: *JSME international journal. Series A, mechanics and material engineering* 38.1, pp. 123–132.

Gurson, A. L. (1975). *Continuum theory of ductile rupture by void nucleation and growth. Part I. Yield criteria and flow rules for porous ductile media*. Technical report. Providence, USA: U.S. Energy Research and Development Administration. DOI: 10.2172/7351470.

Gurson, A. L. (1977a). "Continuum theory of ductile rupture by void nucleation and growth: Part I-Yield criteria and flow rules for porous ductile media." In: *J. Eng. Mater. Technol.* 99.1, pp. 2–15.

Gurson, A. L. (1977b). "Porous Rigid-Plastic Materials Containing Rigid Inclusions - Yield Function, Plastic Potential and Void Nucleation." In: *Proced. Int. Conf. Fract.* Ed. by D. M. R. Taplin. Waterloo, Canada: Pergamon press.

Guzmán, C. F. (2013). *Simulation results of a 70-degree SPIF formed cone*. Internal report. Liège, Belgium: University of Liège.

Guzmán, C. F. (2014). *Extension of the Gurson model for the LAGAMINE code*. Tech. rep. Liège: University of Liège, pp. 1–29.

Guzmán, C. F. and A. M. Habraken (2013). "Towards fracture prediction in single point incremental forming." In: *Key Engineering Materials*. Ed. by R. J. Alves de Sousa and R. Valente. Vol. 554-557. Aveiro, Portugal: Trans Tech Publications, pp. 2355–2362. ISBN: 9783037857199. DOI: 10.4028/www.scientific.net/KEM.554-557.2355.

Guzmán, C. F., A. Ben Bettaieb, J. I. V. Sena, R. J. Alves de Sousa, A. M. Habraken, and L. Duchêne (2012a). "Evaluation of the Enhanced Assumed Strain and Assumed Natural Strain in the SSH3D and RESS3 Solid Shell Elements for Single Point Incremental Forming Simulation." In: *Key Engineering Materials* 504-506. Ed. by M. Merklein and H. Hagenah, pp. 913–918. ISSN: 1662-9795. DOI: 10.4028/www.scientific.net/KEM.504-506.913.

Guzmán, C. F., J. Gu, J. Duflou, H. Vanhove, P. Flores, and A. M. Habraken (2012b). "Study of the geometrical inaccuracy on a SPIF two-slope pyramid by finite element simulations." In: *International Journal of Solids and Structures* 49.25, pp. 3594–3604. ISSN: 00207683. DOI: 10.1016/j.ijsolstr.2012.07.016.

Guzmán, C. F., J. I. V. Sena, L. Duchêne, and A. M. Habraken (2013a). *Accurate Single Point Incremental Forming Simulations using Solid-Shell Elements*. Liège, Belgium.

Guzmán, C. F., T. Mouton, and A. M. Habraken (2013b). *Using Gmsh as a mesh generator and post-processor for LAGAMINE*. Liège, Belgium.

Guzmán, C. F., V. Tuninetti, G. Gilles, and A. M. Habraken (2015). "Assessment of Damage and Anisotropic Plasticity Models to Predict Ti-6Al-4V Behavior." In: *Key Eng. Mater.* 651-653, pp. 575–580. ISSN: 1662-9795. DOI: 10.4028/www.scientific.net/KEM.651-653.575.

Habraken, A. M. and S. Cescotto (1998). "Contact between deformable solids: The fully coupled approach." In: *Mathematical and Computer Modelling* 28.4-8, pp. 153–169. ISSN: 08957177. DOI: 10.1016/S0895-7177(98)00115-0.

Hachez, F. (2008). "Experimental and Numerical Investigation of the Thickness Effect in the Ductile Tearing of Thin Metallic Plates." PhD thesis. Université Catholique de Louvain.

Hadoush, A. and A. van den Boogaard (2009). "Substructuring in the implicit simulation of single point incremental sheet forming." In: *International Journal of Material Forming* 2.3, pp. 181–189. ISSN: 1960-6206. DOI: 10.1007/s12289-009-0402-3.

Hadoush, A. and A. van den Boogaard (2011). "Efficient implicit simulation of incremental sheet forming." In: *International Journal for Numerical Methods in Engineering*, n/a–n/a. ISSN: 00295981. DOI: 10.1002/nme.3334.

Haigh, B. P. (1920a). "Strain-energy Function and the Elastic limit." In: *Report of the Eighty-Seventh Meeting of the British Association for the Advancement of Science*. Bournemouth, England: John Murray, pp. 486–495.

Haigh, B. P. (1920b). "Strain-energy Function and the Elastic limit." In: *Engineering* 109, pp. 158–160.

Ham, M. and J. Jeswiet (2007). "Forming limit curves in single point incremental forming." In: *CIRP Annals - Manufacturing Technology* 56, pp. 277–280. ISSN: 00078506. DOI: 10.1016/j.cirp.2007.05.064.

Hancock, J. and D. Brown (1983). "On the role of strain and stress state in ductile failure." In: *J. Mech. Phys. Solids* 31.1, pp. 1–24. ISSN: 00225096. DOI: 10.1016/0022-5096(83)90017-0.

Hasegawa, T., T. Yakou, and S. Karashima (1975). "Deformation behaviour and dislocation structures upon stress reversal in polycrystalline aluminium." In: *Materials Science and Engineering* 20, pp. 267–276. ISSN: 00255416. DOI: 10.1016/0025-5416(75)90159-7.

Hastings, W. K. (1970). "Monte Carlo Sampling Methods Using Markov Chains and Their Applications." In: *Biometrika* 57.1, pp. 97–109. ISSN: 00063444. DOI: 10.1093/biomet/57.1.97.

He, S., A. van Bael, P. van Houtte, Y. Tunckol, J. Duflou, C. Henrard, C. Bouffioux, and A. M. Habraken (2005a). "Effect of FEM choices in the modelling of incremental forming of aluminium sheets." In: *Proceedings of the 8th ESAFORM Conference on Material Forming*. Ed. by D. Banabic. Cluj-Napoca, Romania: The publishing House of the Romanian Academy, pp. 711–714.

He, S., A. van Bael, P. van Houtte, A. Szekeres, J. Duflou, C. Henrard, and A. M. Habraken (2005b). "Finite Element Modeling of Incremental Forming of Aluminum Sheets." In: *Advanced Materials Research*. Ed. by M. Geiger, J. R. Duflou, H. Kals, B. Shirvani, and M. Singh. Vol. 6/8. Erlangen, Germany: Trans Tech Publications, pp. 525–532. DOI: 10.4028/www.scientific.net/AMR.6-8.533.

Helbert, A., X. Feaugas, and M. Clavel (1998). "Effects of microstructural parameters and back stress on damage mechanisms in α/β titanium alloys." In: *Acta Mater.* 46.3, pp. 939–951. ISSN: 13596454. DOI: 10.1016/S1359-6454(97)00288-7.

Helnwein, P. (2001). "Some remarks on the compressed matrix representation of symmetric second-order and fourth-order tensors." In: *Computer Methods in Applied Mechanics and Engineering* 190.22-23, pp. 2753–2770. ISSN: 00457825. DOI: 10.1016/S0045-7825(00)00263-2.

Henrard, C. (2005). "Development of a Contact Model Adapted to Incremental Forming." DEA graduation work. University of Liège.

Henrard, C. (2008). "Numerical Simulations of the Single Point Incremental Forming Process." PhD thesis. Université de Liege.

Henrard, C., A. M. Habraken, A. Szekeres, J. Duflou, S. He, A. van Bael, and P. van Houtte (2005a). "Comparison of FEM Simulations for the Incremental Forming Process." In: *Advanced Materials Research*. Ed. by M. Geiger, J. R. Duflou, H. Kals, B. Shirvani, and M. Singh. Vol. 6-8. Erlangen, Germany: Trans Tech Publications, pp. 533–542. DOI: 10.4028/www.scientific.net/AMR.6-8.533.

Henrard, C., C. Bouffioux, A. Godinas, and A. M. Habraken (2005b). "Development of a Contact Model Adapted to Incremental Forming." In: *Proceedings of the 8th ESAFORM Conference on Material Forming*. Ed. by D. Banabic. Cluj-Napoca, Romania: The publishing House of the Romanian Academy.

Henrard, C., C. Bouffioux, L. Duchêne, J. Duflou, and A. M. Habraken (2007). "Validation of a New Finite Element for Incremental Forming Simulation Using a Dynamic Explicit Approach." In: *Key Engineering Materials*. Ed. by M. Geiger, J. Duflou, B. Shirvani, R. Clarke, R. Di Lorenzo, and L. Fratini. Vol. 344. Palermo, Italy: Trans Tech Publications, pp. 495–502. DOI: 10.4028/www.scientific.net/KEM.344.495.

Henrard, C., C. Bouffioux, P. Eyckens, H. Sol, J. Duflou, P. van Houtte, A. van Bael, L. Duchêne, and A. M. Habraken (2010). "Forming forces in single point incremental forming: prediction by finite element simulations, validation and sensitivity." In: *Computational Mechanics* 47.5, pp. 573–590. ISSN: 0178-7675. DOI: 10.1007/s00466-010-0563-4.

Hill, R. (1948). "A Theory of the Yielding and Plastic Flow of Anisotropic Metals." In: *Proceedings of the Royal Society A: Mathematical, Physical and Engineering Sciences* 193.1033, pp. 281–297. ISSN: 1364-5021. DOI: 10.1098/rspa.1948.0045.

Hill, R. (1952). "On discontinuous plastic states, with special reference to localized necking in thin sheets." In: *Journal of the Mechanics and Physics of Solids* 1.1, pp. 19–30. ISSN: 00225096. DOI: 10.1016/0022-5096(52)90003-3.

Hirt, G., J. Ames, M. Bambach, and R. Kopp (2004). "Forming strategies and process modelling for CNC incremental sheet forming." In: *CIRP Annals - Manufacturing Technology* 53.1, pp. 203–206. ISSN: 00078506. DOI: 10.1016/S0007-8506(07)60679-9.

Hoferlin, E. (2001). "Incorporation of an accurate model of texture and strain-path induced anisotropy in simulations of sheet metal forming." PhD thesis. Katholieke Universiteit Leuven.

Hosford, W. F. and R. M. Caddell (2007). *Metal forming: mechanics and metallurgy*. 3rd. Cambridge University Press.

Hu, H.-C. (1955). "On some variational principles in the theory of elasticity and the theory of plasticity." In: *Scientia Sinica* 4.1, pp. 33–54.

Huang, Y. (1991). "Accurate Dilatation Rates for Spherical Voids in Triaxial Stress Fields." In: *J. Appl. Mech.* 58.4, p. 1084. ISSN: 00218936. DOI: 10.1115/1.2897686.

Huang, Y., J. W. Hutchinson, and V. Tvergaard (1991). "Cavitation instabilities in elastic-plastic solids." In: *J. Mech. Phys. Solids* 39.2, pp. 223–241. ISSN: 00225096. DOI: 10.1016/0022-5096(91)90004-8.

Hussain, G. and L. Gao (2007). "A novel method to test the thinning limits of sheet metals in negative incremental forming." In: *International Journal of Machine Tools and Manufacture* 47.3-4, pp. 419–435. ISSN: 08906955. DOI: 10.1016/j.ijmachtools.2006.06.015.

Hussain, G., L. Gao, and N. Dar (2007). "An experimental study on some formability evaluation methods in negative incremental forming." In: *Journal of Materials Processing Technology* 186.1-3, pp. 45–53. ISSN: 09240136. DOI: 10.1016/j.jmatprotec.2006.12.005.

ISO 6892-1:2009 (2009). *Matériaux métalliques - Essai de traction - Partie 1: Méthode d'essai à température ambiante*. Norm.

Iseki, H., K Kazunori, and S Sakamoto (1993). "Forming limit of flexible and incremental sheet metal bulging with a spherical roller." In: *Advanced Technology of Plasticity* 3, pp. 1635–1640.

Jackson, K. and J. M. Allwood (2009). "The mechanics of incremental sheet forming." In: *Journal of Materials Processing Technology* 209.3, pp. 1158–1174. ISSN: 09240136. DOI: 10.1016/j.jmatprotec.2008.03.025.

Jackson, K., J. M. Allwood, and M. Landert (2008). "Incremental forming of sandwich panels." In: *Journal of Materials Processing Technology* 204.1-3, pp. 290–303. ISSN: 09240136. DOI: 10.1016/j.jmatprotec.2007.11.117.

Jeswiet, J. and D. Young (2005). "Forming limit diagrams for single-point incremental forming of aluminium sheet." In: *Proceedings of the Institution of Mechanical Engineers, Part B: Journal of Engineering Manufacture* 219.4, pp. 359–364. ISSN: 0954-4054. DOI: 10.1243/095440505X32210.

Jeswiet, J., E. Hagan, and A. Szekeres (2002). "Forming parameters for incremental forming of aluminium alloy sheet metal." In: *Proceedings of the Institution of Mechanical Engineers, Part B: Journal of Engineering Manufacture* 216.10, pp. 1367–1371. ISSN: 0954-4054. DOI: 10.1243/095440502320405458.

Jeswiet, J., F. Micari, G. Hirt, A. Bramley, J. Duflou, and J. M. Allwood (2005). "Asymmetric Single Point Incremental Forming of Sheet Metal." In: *CIRP Annals - Manufacturing Technology* 54.2, pp. 88–114. ISSN: 00078506. DOI: 10.1016/S0007-8506(07)60021-3.

Jetteur, P. and F. Frey (1986). "A four node Marguerre element for non-linear shell analysis." In: *Engineering Computations* 3.4, pp. 276–282. ISSN: 0264-4401. DOI: 10.1108/eb023667.

Ji, Y. and J.-J. Park (2008). "Formability of magnesium AZ31 sheet in the incremental forming at warm temperature." In: *Journal of Materials Processing Technology* 201.1-3, pp. 354–358. ISSN: 09240136. DOI: 10.1016/j.jmatprotec.2007.11.206.

Jones, R. M. (2009). *Deformation theory of plasticity*. Bull Ridge Corporation. ISBN: 978-0-9787223-1-9.

Karypis, G. and V. Kumar (1998). "A Fast and High Quality Multilevel Scheme for Partitioning Irregular Graphs." In: *SIAM Journal on Scientific Computing* 20.1, pp. 359–392. ISSN: 1064-8275. DOI: 10.1137/S1064827595287997.

Keeler, S. P. and W. A. Backofen (1963). "Plastic instability and fracture in sheets stretched over rigid punches." In: *Transactions of the American Society for Metals* 56, pp. 25–28.

Khan, A. S. and S. Huang (1995). *Continuum theory of plasticity*. New York: Wiley-Interscience. ISBN: 978-0471310433.

Kim, J. and X. Gao (2005). "A generalized approach to formulate the consistent tangent stiffness in plasticity with application to the GLD porous material model." In: *Int. J. Solids Struct.* 42.1, pp. 103–122. ISSN: 00207683. DOI: 10.1016/j.ijsolstr.2004.07.011.

Kim, J., X. Gao, and T. S. Srivatsan (2004). "Modeling of void growth in ductile solids: effects of stress triaxiality and initial porosity." In: *Eng. Fract. Mech.* 71.3, pp. 379–400. ISSN: 00137944. DOI: 10.1016/S0013-7944(03)00114-0.

Kim, T. and D. Yang (2000). "Improvement of formability for the incremental sheet metal forming process." In: *International Journal of Mechanical Sciences* 42.7, pp. 1271–1286. ISSN: 00207403. DOI: 10.1016/S0020-7403(99)00047-8.

Kim, Y. and J.-J. Park (2002). "Effect of process parameters on formability in incremental forming of sheet metal." In: *Journal of Materials Processing Technology* 130, pp. 42–46. ISSN: 09240136. DOI: 10.1016/S0924-0136(02)00788-4.

Kitting, D., A. Ofenheimer, H. Pauli, and E. T. Till (2011). "Experimental characterization of stretch-bending formability of ahss sheets." In: *AIP Conference Proceedings*. Ed. by G. Menary. Vol. 1353. Belfast, United Kingdom: American Institute of Physics, pp. 1589–1594. ISBN: 9780735409118. DOI: 10.1063/1.3589743.

Kobayashi, S., I. Hall, and E. Thomsen (1961). "A theory of shear spinning of cones." In: *Transactions of the ASME, Journal of Engineering for Industry* 81, pp. 485–495.

Kojic, M., I. Vlastelica, and M. Zivkovic (2002). "Implicit stress integration procedure for small and large strains of the Gurson material model." In: *Int. J. Numer. Methods Eng.* 53.12, pp. 2701–2720. ISSN: 0029-5981. DOI: 10.1002/nme.410.

Kopač, J. and Z. Kampus (2005). "Incremental sheet metal forming on CNC milling machine-tool." In: *Journal of Materials Processing Technology* 162-163.SPEC. ISS. Pp. 622–628. ISSN: 09240136. DOI: 10.1016/j.jmatprotec.2005.02.160.

Koplik, J. and A. Needleman (1988). "Void growth and coalescence in porous plastic solids." In: *Int. J. Solids Struct.* 24.8, pp. 835–853. ISSN: 00207683. DOI: 10.1016/0020-7683(88)90051-0.

Kurra, S. and S. P. Regalla (2014). "Experimental and numerical studies on formability of extra-deep drawing steel in incremental sheet metal forming." In: *Journal of Materials Research and Technology* 3.2, pp. 158–171. ISSN: 2238-7854. DOI: 10.1016/j.jmrt.2014.03.009.

Landron, C., O. Bouaziz, É. Maire, and J. Adrien (2010). "Characterization and modeling of void nucleation by interface decohesion in dual phase steels." In: *Scr. Mater.* 63.10, pp. 973–976. ISSN: 13596462. DOI: 10.1016/j.scriptamat.2010.07.021.

Landron, C., É. Maire, O. Bouaziz, J. Adrien, L. Lecarme, and A. Bareggi (2011). "Validation of void growth models using X-ray microtomography characterization of damage in dual phase steels." In: *Acta Mater.* 59.20, pp. 7564–7573. ISSN: 13596454. DOI: 10.1016/j.actamat.2011.08.046.

Lankford, W. T., S. C. Snyder, and J. A. Bauscher (1950). "New criteria for predicting the press performance of deep drawing sheets." In: *Transactions of the American Society for Metals* 42, p. 1197.

Lassance, D, D Fabregue, F Delannay, and T. Pardoen (2007). "Micromechanics of room and high temperature fracture in 6xxx Al alloys." In: *Prog. Mater. Sci.* 52.1, pp. 62–129. ISSN: 00796425. DOI: 10.1016/j.pmatsci.2006.06.001.

Leblond, J.-B., G. Perrin, and J. Devaux (1995). "An improved Gurson-type model for hardenable ductile metals." In: *Eur. J. Mech. A. Solids* 14.4, pp. 499–527.

Leblond, J.-b. and G. Perrin (1996). *Introduction à la mécanique de la rupture ductile des métaux*. Palaiseau, France: Cours de l'École Polytechnique.

Lemaitre, J. (1985). "A Continuous Damage Mechanics Model for Ductile Fracture." In: *J. Eng. Mater. Technol.* 107.1, p. 83. ISSN: 00944289. DOI: 10.1115/1.3225775.

Lequesne, C., C. Henrard, C. Bouffioux, J. Duflou, and A. M. Habraken (2008). "Adaptive remeshing for incremental forming simulation." In: *Proceedings of the 7th International Conference and Workshop on Numerical Simulation od 3D Sheet Metal Forming Processes*. Ed. by P. Hora. Interlaken, Switzerland.

Levenberg, K. (1944). "A method for the solution of certain problems in least squares." In: *Quarterly of applied mathematics* 2, pp. 164–168.

Li, H., M. Fu, J. Lu, and H. Yang (2011). "Ductile fracture: Experiments and computations." In: *Int. J. Plast.* 27.2, pp. 147–180. ISSN: 07496419. DOI: 10.1016/j.ijplas.2010.04.001.

Li, J.-c., C. Li, and T.-g. Zhou (2012). "Thickness distribution and mechanical property of sheet metal incremental forming based on numerical simulation." In: *Transactions of Nonferrous Metals Society of China* 22, s54–s60. ISSN: 10036326. DOI: 10.1016/S1003-6326(12)61683-5.

Li, K. (1995). "Contribution to the Finite Element Simulation of three-dimensional sheet metal forming." PhD Thesis. University of Liège.

Li, K. and S. Cescotto (1997). "An 8-node brick element with mixed formulation for large deformation analyses." In: *Computer Methods in Applied Mechanics and Engineering* 141.1-2, pp. 157–204. ISSN: 00457825. DOI: 10.1016/S0045-7825(96)01071-7.

Lievers, W., A. Pilkey, and D. Lloyd (2004). "Using incremental forming to calibrate a void nucleation model for automotive aluminum sheet alloys." In: *Acta Materialia* 52.10, pp. 3001–3007. ISSN: 13596454. DOI: 10.1016/j.actamat.2004.03.002.

Lode, W. (1926). "Versuche über den Einflußder mittleren Hauptspannung auf das Fließen der Metalle Eisen, Kupfer und Nickel." In: *Zeitschrift für Physik* 36.11-12, pp. 913–939. ISSN: 1434-6001. DOI: 10.1007/BF01400222.

Maire, É. (2004). "Quantitative Measurement of Damage." In: *Local approach to Fract.* Ed. by J. Besson. Paris, France: Presses de l'Ecole des Mines. Chap. III, pp. 79–108. ISBN: 2-911762-55-X.

Maire, É., O. Bouaziz, M. Di Michiel, and C. Verdu (2008). "Initiation and growth of damage in a dual-phase steel observed by X-ray microtomography." In: *Acta Mater.* 56.18, pp. 4954–4964. ISSN: 13596454. DOI: 10.1016/j.actamat.2008.06.015.

Malcher, L., F. M. Andrade Pires, and J. César de Sá (2012). "An assessment of isotropic constitutive models for ductile fracture under high and low stress triaxiality." In: *Int. J. Plast.* 30-31, pp. 81–115. ISSN: 07496419. DOI: 10.1016/j.ijplas.2011.10.005.

Malcher, L., F. M. Andrade Pires, and J. César de Sá (2014). "An extended GTN model for ductile fracture under high and low stress triaxiality." In: *Int. J. Plast.* 54, pp. 193–228. ISSN: 07496419. DOI: 10.1016/j.ijplas.2013.08.015.

Malhotra, R., L. Xue, T. Belytschko, and J. Cao (2012). "Mechanics of fracture in single point incremental forming." In: *Journal of Materials Processing Technology* 212.7, pp. 1573–1590. ISSN: 09240136. DOI: 10.1016/j.jmatprotec.2012.02.021.

Mansouri, L. (2014). "Analyse des instabilités plastiques dans les matériaux ductiles endommageables: application à la prediction de la striction et de la formabilité des tôles métalliques." PhD thesis. Arts et Métiers ParisTech.

Marciniak, Z. and K. Kuczynski (1967). "Limit strains in the processes of stretch-forming sheet metal." In: *International Journal of Mechanical Sciences* 9.9, pp. 609–620. ISSN: 00207403. DOI: 10.1016/0020-7403(67)90066-5.

Marguerre, K. (1938). "Zur theorie der gekrümmten platte grosser formänderung." In: *Proceedings of the 5th International Congress for Applied Mechanics*. Cambridge, Massachusetts: Wiley, pp. 93–101.

Marquardt, D. W. (1963). "An Algorithm for Least-Squares Estimation of Nonlinear Parameters." In: *Journal of the Society for Industrial and Applied Mathematics* 11.2, pp. 431–441. ISSN: 0368-4245. DOI: 10.1137/0111030.

Martins, P., N. Bay, M. Skjoedt, and M. Silva (2008). "Theory of single point incremental forming." In: *CIRP Annals - Manufacturing Technology* 57.1, pp. 247–252. ISSN: 00078506. DOI: 10.1016/j.cirp.2008.03.047.

Martins, P., L. Kwiatkowski, V. Franzen, A. Tekkaya, and M. Kleiner (2009). "Single point incremental forming of polymers." In: *CIRP Annals - Manufacturing Technology* 58.1, pp. 229–232. ISSN: 00078506. DOI: 10.1016/j.cirp.2009.03.095.

Mathonet, V. (2003). *Manuel D'Utilisation Du Programme D'Identification Paramétrique Optim.* Tech. rep. Liège: Université de Liège.

McClintock, F. A. (1968). "A Criterion for Ductile Fracture by the Growth of Holes." In: *J. Appl. Mech.* 35.2, p. 363. ISSN: 00218936. DOI: 10.1115/1.3601204.

McClintock, F. A., S. M. Kaplan, and C. A. Berg (1966). "Ductile fracture by hole growth in shear bands." In: *Int. J. Fract. Mech.* 2.4. ISSN: 0020-7268. DOI: 10.1007/BF00184558.

Mear, M. and J. W. Hutchinson (1985). "Influence of yield surface curvature on flow localization in dilatant plasticity." In: *Mech. Mater.* 4.3-4, pp. 395–407. ISSN: 01676636. DOI: 10.1016/0167-6636(85)90035-3.

Meier, H., B. Buff, R. Laurischkat, and V. Smukala (2009). "Increasing the part accuracy in dieless robot-based incremental sheet metal forming." In: *CIRP Annals - Manufacturing Technology* 58.1, pp. 233–238. ISSN: 00078506. DOI: 10.1016/j.cirp.2009.03.056.

Meier, H., S. Reese, Y. Kiliclar, and R. Laurischkat (2013). "Increase of the Dimensional Accuracy of Sheet Metal Parts Utilizing a Model-Based Path Planning for Robot-Based Incremental Forming." In: *Process Machine Interactions*. Ed. by B. Denkena and F. Hollmann. Lecture Notes in Production Engineering. Berlin, Heidelberg: Springer Berlin Heidelberg. Chap. 21, pp. 459–473. ISBN: 978-3-642-32447-5. DOI: 10.1007/978-3-642-32448-2.

Mertens, A., C. F. Guzmán, A. M. Habraken, A. K. Behera, and J. Lecomte-Beckers (2012). *Experimental Characterisation of Damage Occuring during Single Point Incremental Forming of a Ferritic Steel*. Tech. rep. Dortmund, Germany: Université de Liège.

Metropolis, N., A. W. Rosenbluth, M. N. Rosenbluth, A. H. Teller, and E. Teller (1953). "Equation of State Calculations by Fast Computing Machines." In: *The Journal of Chemical Physics* 21.6, pp. 1087–1092. ISSN: 00219606. DOI: doi:10.1063/1.1699114. arXiv: 5744249209.

Micari, F., G. Ambrogio, and L. Filice (2007). "Shape and dimensional accuracy in Single Point Incremental Forming: State of the art and future trends." In: *Journal of Materials Processing Technology* 191.1-3, pp. 390–395. DOI: 2010.1016/j.jmatprotec.2007.03.066.

Mirnia, M. J., B. Mollaei Dariani, H. Vanhove, and J. Duflou (2013). "An investigation into thickness distribution in single point incremental forming using sequential limit analysis." In: *International Journal of Material Forming* 7.4, pp. 469–477. ISSN: 1960-6206. DOI: 10.1007/s12289-013-1143-x.

Mohammadi, A., H. Vanhove, A. Van Bael, and J. Duflou (2014). "Towards accuracy improvement in single point incremental forming of shallow parts formed under laser assisted conditions." In: *International Journal of Material Forming*. ISSN: 1960-6206.

Montleau, P. D., J. M. Cela, and S. Moto Mpong (2002). "A Parallel Computing Model for the Acceleration of a Finite Element Software." In: *ISHPC*. Ed. by H. Zima, K. Joe, M. Sato, Y. Seo, and M. Shimasaki. Kansai science city: Springer-Verlag Berlin Heidelberg, pp. 449–456. DOI: 10.1007/3-540-47847-7{_}41.

Moto Mpong, S. and P. D. Montleau (2002). "Acceleration of finite element analysis by parallel processing." In: *Proceedings of the 5th International ESAFORM Conference on Material Forming*. Ed. by M. Pietrzyk, Z. Mitura, and J. Kaczmar. Kraków, Poland, pp. 47–50.

Moto Mpong, S., P. D. Montleau, A. Godinas, and A. M. Habraken (2002). "A parallel computing model for the acceleration of a finite element software." In: *Parallel and Distributed Processing Techniques and Applications*. Ed. by H. R. Arabnia. Las Vegas, USA: CSREA Press, pp. 185–191.

Mühlich, U. and W. Brocks (2003). "On the numerical integration of a class of pressure-dependent plasticity models including kinematic hardening." In: *Comput. Mech.* 31.6, pp. 479–488. ISSN: 0178-7675. DOI: 10.1007/s00466-003-0454-z.

Nagtegaal, J. C. (1982). "On the implementation of inelastic constitutive equations with special reference to large deformation problems." In: *Computer Methods in Applied Mechanics and Engineering* 33.1-3, pp. 469–484. ISSN: 00457825. DOI: 10.1016/0045-7825(82)90120-7.

Nahshon, K. and J. W. Hutchinson (2008). "Modification of the Gurson Model for shear failure." In: *Eur. J. Mech. - A/Solids* 27.1, pp. 1–17. ISSN: 09977538. DOI: 10.1016/j.euromechsol.2007.08.002.

Nahshon, K. and Z. Xue (2009). "A modified Gurson model and its application to punch-out experiments." In: *Eng. Fract. Mech.* 76.8, pp. 997–1009. ISSN: 00137944. DOI: 10.1016/j.engfracmech.2009.01.003.

Ndip-Agbor, E., J. Smith, H. Ren, Z. Jiang, J. Xu, N. Moser, W. Chen, Z. C. Xia, and J. Cao (2015). "Optimization of relative tool position in accumulative double sided incremental forming using finite element analysis and model bias correction." In: *International Journal of Material Forming*. ISSN: 1960-6206. DOI: 10.1007/s12289-014-1209-4.

Needleman, A. and J. R. Rice (1978). "Limits to ductility set by plastic flow localization." In: *Mech. sheet Met. Form.* Ed. by D. P. Koistinen and N.-M. Wang. Springer, pp. 237–267.

Nielsen, K. L. and V. Tvergaard (2009). "Effect of a shear modified Gurson model on damage development in a FSW tensile specimen." In: *Int. J. Solids Struct.* 46.3-4, pp. 587–601. ISSN: 00207683. DOI: 10.1016/j.ijsolstr.2008.09.011.

Nielsen, K. L. and V. Tvergaard (2010). "Ductile shear failure or plug failure of spot welds modelled by modified Gurson model." In: *Eng. Fract. Mech.* 77.7, pp. 1031–1047. ISSN: 00137944. DOI: 10.1016/j.engfracmech.2010.02.031.

Ortiz, M. and E. P. Popov (1985). "Accuracy and stability of integration algorithms for elastoplastic constitutive relations." In: *International Journal for Numerical Methods in Engineering* 21.9, pp. 1561–1576. ISSN: 0029-5981. DOI: 10.1002/nme.1620210902.

Pardoen, T. (2006). "Numerical simulation of low stress triaxiality ductile fracture." In: *Comput. Struct.* 84.26-27, pp. 1641–1650. ISSN: 00457949. DOI: 10.1016/j.compstruc.2006.05.001.

Pardoen, T. and J. Besson (2004). "Micromechanics-based constitutive models of ductile fracture." In: *Local approach to Fract.* Ed. by J. Besson. Paris, France: Presses de l'Ecole des Mines. Chap. VIII, pp. 221–264. ISBN: 2-911762-55-X.

Pardoen, T. and Y. Brechet (2004). "Influence of microstructure-driven strain localization on the ductile fracture of metallic alloys." In: *Philos. Mag.* 84.3-5, pp. 269–297. ISSN: 1478-6435. DOI: 10.1080/14786430310001610366.

Pardoen, T. and F. Delannay (1998). "Assessment of void growth models from porosity measurements in cold-drawn copper bars." In: *Metall. Mater. Trans. A* 29.7, pp. 1895–1909. ISSN: 1073-5623. DOI: 10.1007/s11661-998-0014-4.

Pardoen, T. and J. W. Hutchinson (2000). "An extended model for void growth and coalescence." In: *J. Mech. Phys. Solids* 48.12, pp. 2467–2512. ISSN: 00225096. DOI: 10.1016/S0022-5096(00)00019-3.

Peirs, J., P. Verleysen, W. Van Paepegem, and J. Degrieck (2011). "Determining the stress-strain behaviour at large strains from high strain rate tensile and shear experiments." In: *International Journal of Impact Engineering* 38.5, pp. 406–415. ISSN: 0734743X. DOI: 10.1016/j.ijimpeng.2011.01.004.

Picart, P, G Piechel, and J Oudin (1997). "Damage influence in the finite element computations for large strains elasto-plastic mechanical structures." In: *Adv. Methods Mater. Process. Defects*. Ed. by M Predeleanu and P Gilormini. Vol. 45. Studies in Applied Mechanics. Elsevier, pp. 175–184. DOI: http://dx.doi.org/10.1016/S0922-5382(97)80019-0.

Pineau, A. (2004). "Physical mechanisms of Damage." In: *Local approach to Fract.* Ed. by J. Besson. Paris, France: Presses de l'Ecole des Mines. Chap. II, pp. 33–78. ISBN: 2-911762-55-X.

Pineau, A. and T. Pardoen (2007). "Failure mechanisms of metals." In: *Compr. Struct. Integr. Encycl.* 2.

Prager, W. (1955). "The theory of plasticity: a survey of recent achievements." In: *Proceedings of the Institution of Mechanical Engineers* 169.1, pp. 41–57.

Ratcliffe, R. T. (1965). "The measurement of small density changes in solids." In: *British Journal of Applied Physics* 16.8, pp. 1193–1196. ISSN: 0508-3443. DOI: 10.1088/0508-3443/16/8/319.

Rauch, M., J.-Y. Hascoet, J.-C. Hamann, and Y. Plenel (2009). "Tool path programming optimization for incremental sheet forming applications." In: *Computer-Aided Design* 41.12, pp. 877–885. ISSN: 00104485. DOI: 10.1016/j.cad.2009.06.006.

Reddy, N. V., R. Lingam, and J. Cao (2015). "Incremental Metal Forming Processes in Manufacturing." In: *Handbook of Manufacturing Engineering and Technology*. Ed. by A. Y. C. Nee. London: Springer London. Chap. 9, pp. 411–452. ISBN: 978-1-4471-4669-8. DOI: 10.1007/978-1-4471-4670-4.

Rice, J. R. and D. Tracey (1969). "On the ductile enlargement of voids in triaxial stress fields." In: *J. Mech. Phys. Solids* 17.3, pp. 201–217. ISSN: 00225096. DOI: 10.1016/0022-5096(69)90033-7.

Robert, C., L. Ben Ayed, A. Delamézière, P. Dal Santo, and J. Batoz (2010). "Development of a simplified approach of contact for incremental sheet forming." In: *International Journal of Material Forming* 3.S1, pp. 987–990. ISSN: 1960-6206. DOI: 10.1007/s12289-010-0935-5.

Robert, C., A. Delamézière, P. Dal Santo, and J. Batoz (2012). "Comparison between incremental deformation theory and flow rule to simulate sheet-metal forming processes." In: *Journal of Materials Processing Technology*. ISSN: 09240136. DOI: 10.1016/j.jmatprotec.2011.12.021.

Salençon, J. (2005). *Mécanique des milieux continus, Tome I: Concepts généraux*. Palaiseau, France: Éditions de l'École Polytechnique.

Sawada, T., G. Fukuhara, and M. Sakamoto (2001). "Deformation Mechanism of Sheet Metal in Stretch Forming with Computer Numerical Control Machine Tools." In: *Journal of the Japan Society for Technology of Plasticity* 42.489, pp. 1067–1069.

Schneider, C. A., W. S. Rasband, and K. W. Eliceiri (2012). "NIH Image to ImageJ: 25 years of image analysis." In: *Nature Methods* 9.7, pp. 671–675. ISSN: 1548-7091. DOI: 10.1038/nmeth.2089.

Sebastiani, G., A. Brosius, A. Tekkaya, W. Homberg, and M. Kleiner (2007). "Decoupled simulation method for incremental sheet metal forming." In: *AIP Conference Proceedings*. Ed. by J. César de Sá and A. D. Santos. Vol. 908. Porto, Portugal: American Institute of Physics, pp. 1501–1506. ISBN: 9780735404151. DOI: 10.1063/1.2741021.

Sena, J. I. V. (2015). "Advanced numerical framework to simulate Incremental Forming Processes." PhD thesis. University of Aveiro, University of Liège.

Sena, J. I. V., C. F. Guzmán, L. Duchêne, A. M. Habraken, R. A. F. Valente, and R. J. Alves de Sousa (2013). "Numerical simulation of a conical shape made by single point incremental." In: *AIP Conference Proceedings*. Ed. by J. W. Yoon, T. B. Stoughton, B. Rolfe, J. H. Beynon, and P. Hodgson. Melbourne, Australia: American Institute of Physics, pp. 852–855. ISBN: 9780735411951. DOI: 10.1063/1.4850104.

Sena, J. I. V., C. F. Guzmán, L. Duchêne, A. M. Habraken, A. K. Behera, J. Duflou, R. Valente, and R. J. Alves de Sousa (2015). "Simulation of a two-slope pyramid made by SPIF using an adaptive remeshing method with solid-shell finite element." In: *International Journal of Material Forming*. ISSN: 1960-6206. DOI: 10.1007/s12289-014-1213-8.

Seong, D., M. Z. Haque, J. B. Kim, T. B. Stoughton, and J. W. Yoon (2014). "Suppression of necking in incremental sheet forming." In: *International Journal of Solids and Structures* 51.15-16, pp. 2840–2849. ISSN: 0020-7683. DOI: 10.1016/j.ijsolstr.2014.04.007.

Sezgin, M. and B. Sankur (2004). "Survey over image thresholding techniques and quantitative performance evaluation." In: *Journal of Electronic Imaging* 13.1, p. 146. ISSN: 1017-9909. DOI: 10.1117/1.1631315.

Shanmuganatan, S. and V. Senthil Kumar (2012). "Experimental investigation and finite element modeling on profile forming of conical component using Al 3003(O) alloy." In: *Materials & Design* 36, pp. 564–569. ISSN: 02613069. DOI: 10.1016/j.matdes.2011.11.066.

Silva, M., M. Skjoedt, P. Martins, and N. Bay (2008). "Revisiting the fundamentals of single point incremental forming by means of membrane analysis." In: *International Journal of Machine Tools and Manufacture* 48.1, pp. 73–83. ISSN: 08906955. DOI: 10.1016/j.ijmachtools.2007.07.004.

Silva, M., P. S. Nielsen, N. Bay, and P. Martins (2011). "Failure mechanisms in single-point incremental forming of metals." In: *The International Journal of Advanced Manufacturing Technology* 56.9-12, pp. 893–903. ISSN: 0268-3768. DOI: 10.1007/s00170-011-3254-1.

Simo, J. C. and T. J. R. Hughes (1986). "On the Variational Foundations of Assumed Strain Methods." In: *Journal of Applied Mechanics* 53.1, p. 51. ISSN: 00218936. DOI: 10.1115/1.3171737.

Simo, J. C. and T. J. R. Hughes (1998). *Computational Inelasticity*. Vol. 7. Interdisciplinary Applied Mathematics. New York: Springer-Verlag. ISBN: 0-387-97520-9. DOI: 10.1007/b98904.

Simo, J. C. and R. L. Taylor (1985). "Consistent tangent operators for rate-independent elastoplasticity." In: *Computer Methods in Applied Mechanics and Engineering* 48.1, pp. 101–118. ISSN: 00457825. DOI: 10.1016/0045-7825(85)90070-2.

Soyarslan, C., M. Malekipour Gharbi, and A. Tekkaya (2012). "A combined experimental-numerical investigation of ductile fracture in bending of a class of ferritic-martensitic steel." In: *Int. J. Solids Struct.* 49.13, pp. 1608–1626. ISSN: 00207683. DOI: 10.1016/j.ijsolstr.2012.03.009.

Stören, S. and J. R. Rice (1975). "Localized necking in thin sheets." In: *Journal of the Mechanics and Physics of Solids* 23.6, pp. 421–441. ISSN: 00225096. DOI: 10.1016/0022-5096(75)90004-6.

Stoughton, T. B. and J. W. Yoon (2011). "A new approach for failure criterion for sheet metals." In: *Int. J. Plast.* 27.3, pp. 440–459. ISSN: 07496419. DOI: 10.1016/j.ijplas.2010.07.004.

Swift, H. (1952). "Plastic instability under plane stress." In: *Journal of the Mechanics and Physics of Solids* 1.1, pp. 1–18. ISSN: 00225096. DOI: 10.1016/0022-5096(52)90002-1.

Taylor, G. I. (1938). "Plastic Strain in Metals." In: *Journal Institute of Metals* 62, pp. 307–324.

Tekoglu, C., J. W. Hutchinson, and T. Pardoen (2015). "On localization and void coalescence as a precursor to ductile fracture." In: *Philos. Trans. R. Soc. A Math. Phys. Eng. Sci.* 373.2038, pp. 20140121–20140121. ISSN: 1364-503X. DOI: 10.1098/rsta.2014.0121.

Teodosiu, C. and Z Hu (1995). "Evolution of the intragranular microstructure at moderate and large strains: modelling and computational significance." In: *NUMIFORM '95 : Simulation of materials processing: theory, methods and applications*. Ed. by S.-F.S.P. R. Dawson. Vol. 95. Ithaca, New York, USA: A.A. Balkema, Rotterdam, pp. 173–182.

Thomason, P. (1968). "A theory for ductile fracture by internal necking of cavities." In: *J. Inst. Met.* 96.12, pp. 360–365.

Thomason, P. (1993). *Ductile fracture by the growth and coalescence of microvoids of non-uniform size and spacing*. DOI: 10.1016/0956-7151(93)90382-3.

Tisza, M. (2012). "General overview of sheet incremental forming." In: *Journal of Achievements in Materials and Manufacturing Engineering* 55.1, pp. 113–120.

Tuninetti, V. (2014). "Experimental and Numerical Study of the Quasi-Static Behavior of Ti-6Al-4V." PhD thesis. University of Liège.

Tuninetti, V. and A. M. Habraken (2014). "Impact of anisotropy and viscosity to model the mechanical behavior of Ti-6Al-4V alloy." In: *Materials Science and Engineering: A* 605, pp. 39–50. ISSN: 09215093. DOI: 10.1016/j.msea.2014.03.009.

Tuninetti, V., G. Gilles, O. Milis, T. Pardoen, and A. M. Habraken (2015). "Anisotropy and tension-compression asymmetry modeling of the room temperature plastic response of Ti-6Al-4V." In: *International Journal of Plasticity* 67, pp. 53–68. ISSN: 07496419. DOI: 10.1016/j.ijplas.2014.10.003.

Tvergaard, V. (1981). "Influence of voids on shear band instabilities under plane strain conditions." In: *Int. J. Fract.* 17.4, pp. 389–407. ISSN: 0376-9429. DOI: 10.1007/BF00036191.

Tvergaard, V. (1982). "Material failure by void coalescence in localized shear bands." In: *Int. J. Solids Struct.* 18.8, pp. 659–672. ISSN: 00207683. DOI: 10.1016/0020-7683(82)90046-4.

Tvergaard, V. (1989). "Material Failure by Void Growth to Coalescence." In: *Adv. Appl. Mech.* Advances in Applied Mechanics 27. Ed. by J. W. Hutchinson and T. Y. Wu, pp. 83–151. ISSN: 0065-2156. DOI: 10.1016/S0065-2156(08)70195-9.

Tvergaard, V. and A. Needleman (1984). "Analysis of the cup-cone fracture in a round tensile bar." In: *Acta Metall.* 32.1, pp. 157–169. ISSN: 00016160. DOI: 10.1016/0001-6160(84)90213-X.

Tvergaard, V. and K. L. Nielsen (2010). "Relations between a micro-mechanical model and a damage model for ductile failure in shear." In: *J. Mech. Phys. Solids* 58.9, pp. 1243–1252. ISSN: 00225096. DOI: 10.1016/j.jmps.2010.06.006.

Van Houtte, P. (2004). *The MTM-FHM Software System manual, Version 2*. Tech. rep. Leuven, Belgium: KULeuven.

Van Bael, A., P. Eyckens, S. He, C. Bouffioux, C. Henrard, A. M. Habraken, J. Duflou, and P. Van Houtte (2007a). "Forming Limit Predictions for Single-Point Incremental Sheet Metal Forming." In: *AIP Conference Proceedings*. Ed. by E. Cueto and F. Chinesta. Vol. 907. Zaragoza, Spain: American Institute of Physics, pp. 309–314. DOI: 10.1063/1.2729530.

Van Bael, A., P. Eyckens, S. He, J. Duflou, and P. Van Houtte (2007b). "The prediction of forming limits in incremental sheet metal forming." In: *Proceedings of the 13th International Symposium on Plasticity & its Current Applications*. Vol. 35. Alaska, USA: Neat Press, pp. 229–231.

Vasilakos, I., J. Gu, B. Belkassem, H. Sol, J. Verbert, and J. Duflou (2009). "Investigation of Deformation Phenomena in SPIF Using an In-Process DIC Technique." In: *Key Engineering Materials*. Ed. by B. Shirvani, R. Clarke, J. R. Duflou, M. Merklein, F. Micari, and J. Griffiths. Vol. 410-411. Birmingham, England: Trans Tech Publications, pp. 401–409. DOI: 10.4028/www.scientific.net/KEM.410-411.401.

Vasilakos, I., J. Gu, H. Vanhove, H. Sol, and J. Duflou (2011). "Deviations between FE Simulation and Experiments in the SPIF Process." In: *Key Engineering Materials*. Ed. by J. Duflou, R. Clarke, M. Merklein, F. Micari, B. Shirvani, and K. Kellens. Vol. 473. Leuven, Belgium: Trans Tech Publications, pp. 937–946. ISBN: 978-3-03785-083-1. DOI: 10.4028/www.scientific.net/KEM.473.937.

Vegter, H., C. ten Horn, and M. Abspoel (2009). "The Corus-Vegter Lite material model: Simplifying advanced material modelling." In: *International Journal of Material Forming* 2.SUPPL. 1, pp. 511–514. ISSN: 19606206. DOI: 10.1007/s12289-009-0640-4.

Verbert, J. (2010). "Computer Aided Process Planning for Rapid Prototyping With Incremental Sheet Forming Techniques (Computer ondersteunde proces planning voor rapid prototyping met incrementele plaatvormtechnieken)." PhD thesis. Katholieke Universiteit Leuven.

Verbert, J., J. Duflou, and B. Lauwers (2007). "Feature Based Approach for Increasing the Accuracy of the SPIF Process." In: *Key Engineering Materials*. Ed. by M. Geiger, J. Duflou, B. Shirvani, R. Clarke, R. Di Lorenzo, and L. Fratini. Vol. 344. Palermo, Italy: Trans Tech Publications, pp. 527–534. DOI: 10.4028/www.scientific.net/KEM.344.527.

Verbert, J., R. Aerens, H. Vanhove, E. Aertbeliën, and J. Duflou (2009). "Obtainable Accuracies and Compensation Strategies for Robot Supported SPIF." In: *Key Engineering Materials*. Ed. by B. Shirvani, R. Clarke, J. R. Duflou, M. Merklein, F. Micari, and J. Griffiths. Vol. 410-411. Birmingham, England: Trans Tech Publications, pp. 679–687. DOI: 10.4028/www.scientific.net/KEM.410-411.679.

Voce, E. (1948). "The relationship between stress and strain for homogeneous deformation." In: *Journal Institute of Metals* 74, pp. 537–562.

Voce, E. (1955). "A Practical Strain Hardening Function." In: *Metallurgica* 51, pp. 219–226.

Von Mises, R. (1913). "Mechanik der festen Körper im plastisch-deformablen Zustand." In: *Nachrichten von der Gesellschaft der Wissenschaften zu Göttingen, Mathematisch-Physikalische Klasse*, pp. 582–592.

Voyiadjis, G. Z., S. Hoseini, and G. Farrahi (2012). "Effects of stress invariants and reverse loading on ductile fracture initiation." In: *Int. J. Solids Struct.* 49.13, pp. 1541–1556. ISSN: 00207683. DOI: 10.1016/j.ijsolstr.2012.02.030.

Wang, J. and R. H. Wagoner (2004). "A New Hexahedral Solid Element for 3D FEM Simulation of Sheet Metal Forming." In: *AIP Conference Proceedings*. Vol. 712. AIP, pp. 2181–2186. DOI: 10.1063/1.1766858.

Wang, X. (1989). *La localisation de la déformation en bandes de cisaillement dans les matériaux poreux ductiles, modélisation par élements finis*. Internal report no. 196. Liège: University of Liège.

Wang, X. (1993). "Modélisation numérique des problèmes avec localisation de la déformation en bandes de cisaillement." PhD thesis. University of Liège.

Washizu, K. (1955). *On the variational principles of elasticity and plasticity*. Technical report. Massachusetts Institute of Technology.

Weck, A. and D. S. Wilkinson (2008). "Experimental investigation of void coalescence in metallic sheets containing laser drilled holes." In: *Acta Mater.* 56.8, pp. 1774–1784. ISSN: 13596454. DOI: 10.1016/j.actamat.2007.12.035.

Weck, A., D. S. Wilkinson, H. Toda, and É. Maire (2006). "2D and 3D Visualization of Ductile Fracture." In: *Adv. Eng. Mater.* 8.6, pp. 469–472. ISSN: 1438-1656. DOI: 10.1002/adem.200600034.

Westergaard, H. (1920). "On the resistance of ductile materials to combined stresses in two or three directions perpendicular to one another." In: *Journal of the Franklin Institute* 189.5, pp. 627–640. ISSN: 00160032. DOI: 10.1016/S0016-0032(20)90373-3.

Wierzbicki, T., Y. Bao, Y.-W. Lee, and Y. Bai (2005). "Calibration and evaluation of seven fracture models." In: *Int. J. Mech. Sci.* 47.4-5, pp. 719–743. ISSN: 00207403. DOI: 10.1016/j.ijmecsci.2005.03.003.

Wikipedia (2014). *Voigt notation — Wikipedia, The Free Encyclopedia*.

Wilkins, M. (1964). "Calculation of elastic-plastic flow." In: *Methods in Computational Physics* 3, pp. 211–263.

Xue, L. (2007). "Damage accumulation and fracture initiation in uncracked ductile solids subject to triaxial loading." In: *Int. J. Solids Struct.* 44.16, pp. 5163–5181. ISSN: 00207683. DOI: 10.1016/j.ijsolstr.2006.12.026.

Xue, L. (2008). "Constitutive modeling of void shearing effect in ductile fracture of porous materials." In: *Eng. Fract. Mech.* 75.11, pp. 3343–3366. ISSN: 00137944. DOI: 10.1016/j.engfracmech.2007.07.022.

Xue, L. (2012). *The Introduction of Shear Modification to Gurson Model*.

Xue, L. and T. Belytschko (2010). "Fast methods for determining instabilities of elastic-plastic damage models through closed-form expressions." In: *Int. J. Numer. Methods Eng.* 84.12, pp. 1490–1518. ISSN: 00295981. DOI: 10.1002/nme.2947. arXiv: 1010.1724.

Xue, Z., M. Pontin, F. Zok, and J. W. Hutchinson (2010). "Calibration procedures for a computational model of ductile fracture." In: *Eng. Fract. Mech.* 77.3, pp. 492–509. ISSN: 00137944. DOI: 10.1016/j.engfracmech.2009.10.007.

Yamashita, M., M. Gotoh, and S.-Y. Atsumi (2008). "Numerical simulation of incremental forming of sheet metal." In: *Journal of Materials Processing Technology* 199.1-3, pp. 163–172. ISSN: 09240136. DOI: 10.1016/j.jmatprotec.2007.07.037.

Yang, X., J. Zhou, and X. Ling (2012). "Study on plastic damage of AISI 304 stainless steel induced by ultrasonic impact treatment." In: *Mater. Des.* 36, pp. 477–481. ISSN: 02613069. DOI: 10.1016/j.matdes.2011.11.023.

Yao, H. and J. Cao (2002). "Prediction of forming limit curves using an anisotropic yield function with prestrain induced backstress." In: *International Journal of Plasticity* 18.8, pp. 1013–1038. ISSN: 07496419. DOI: 10.1016/S0749-6419(01)00022-5.

Yen, J.-C., F.-J. Chang, and S. Chang (1995). "A new criterion for automatic multilevel thresholding." In: *IEEE Transactions on Image Processing* 4.3, pp. 370–378. ISSN: 10577149. DOI: 10.1109/83.366472.

Yoshida, F. and T. Uemori (2002). "A model of large-strain cyclic plasticity describing the Bauschinger effect and workhardening stagnation." In: *International Journal of Plasticity* 18.5-6, pp. 661–686. ISSN: 07496419. DOI: 10.1016/S0749-6419(01)00050-X.

Zhang, K., J. Bai, and D. François (2001). "Numerical analysis of the influence of the Lode parameter on void growth." In: *Int. J. Solids Struct.* 38.32-33, pp. 5847–5856. ISSN: 00207683. DOI: 10.1016/S0020-7683(00)00391-7.

Zhang, Z., C. Thaulow, and J. Ødegård (2000). "A complete Gurson model approach for ductile fracture." In: *Eng. Fract. Mech.* 67.2, pp. 155–168. ISSN: 00137944. DOI: 10.1016/S0013-7944(00)00055-2.

Zhu, Y. (1992). "Contribution to the local approach of fracture in solid dynamics." PhD thesis. University of Liège.

Zhu, Y. and S. Cescotto (1994). *Transient thermal and thermomechanical analysis by mixed FEM.* DOI: 10.1016/0045-7949(94)90202-X.

Zienkiewicz, O. C. and R. L. Taylor (2006). *The finite element method for solid and structural mechanics.* 6th. Elsevier Butterworth-Heinemann. ISBN: 0 7506 6321 9.

de Souza Neto, E. A., D. Peri, and D. R. J. Owen (2008). *Computational Methods for Plasticity.* Chichester, UK: John Wiley & Sons, Ltd. ISBN: 9780470694626. DOI: 10.1002/9780470694626.

Curriculum Vitae

Education

2011–2016	PhD in Engineering Sciences	University of Liège (Belgium)
2010–2012	Master in Engineering Sciences	University of Concepción (Chile)
2009	Vibration Analyst, ISO 18436-2	University of Concepción (Chile)
2005–2011	Bachelor in Engineering Sciences	University of Concepción (Chile)

List of publications

C. F. Guzmán et al. (2015). "Assessment of Damage and Anisotropic Plasticity Models to Predict Ti-6Al-4V Behavior." In: *Key Eng. Mater.* 651-653, pp. 575–580. ISSN: 1662-9795. DOI: 10.4028/www.scientific.net/KEM.651-653.575

J. I. V. Sena et al. (2015). "Simulation of a two-slope pyramid made by SPIF using an adaptive remeshing method with solid-shell finite element." In: *International Journal of Material Forming.* ISSN: 1960-6206. DOI: 10.1007/s12289-014-1213-8

Guzman2014b

L. Duchêne et al. (2013). "Numerical Simulation of a Pyramid Steel Sheet Formed by Single Point Incremental Forming using Solid-Shell Finite Elements." In: *Key Engineering Materials.* Ed. by R. Clarke et al. Vol. 549. Belfast, United Kingdom: Trans Tech Publications, pp. 180–188. DOI: 10.4028/www.scientific.net/KEM.549.180

C. F. Guzmán and A. M. Habraken (2013). "Towards fracture prediction in single point incremental forming." In: *Key Engineering Materials.* Ed. by R. J. Alves de Sousa and R. Valente. Vol. 554-557. Aveiro, Portugal: Trans Tech Publications, pp. 2355–2362. ISBN: 9783037857199. DOI: 10.4028/www.scientific.net/KEM.554-557.2355

C. F. Guzmán et al. (2013b). *Using Gmsh as a mesh generator and post-processor for LAGAMINE.* Liège, Belgium

C. F. Guzmán et al. (2013a). *Accurate Single Point Incremental Forming Simulations using Solid-Shell Elements.* Liège, Belgium

J. I. V. Sena et al. (2013). "Numerical simulation of a conical shape made by single point incremental." In: *AIP Conference Proceedings.* Ed. by J. W. Yoon et al. Melbourne, Australia: American Institute of Physics, pp. 852–855. ISBN: 9780735411951. DOI: 10.1063/1.4850104

C. F. Guzmán et al. (2012a). "Evaluation of the Enhanced Assumed Strain and Assumed Natural Strain in the SSH3D and RESS3 Solid Shell Elements for Single Point Incremental Forming Simulation." In: *Key Engineering Materials* 504-506. Ed. by M. Merklein and H. Hagenah, pp. 913–918. ISSN: 1662-9795. DOI: 10.4028/www.scientific.net/KEM.504-506.913

C. F. Guzmán et al. (2012b). "Study of the geometrical inaccuracy on a SPIF two-slope pyramid by finite element simulations." In: *International Journal of Solids and Structures* 49.25, pp. 3594–3604. ISSN: 00207683. DOI: 10.1016/j.ijsolstr.2012.07.016